University of Wollongong

Research Online

University of Wollongong Thesis Collection 2017+

University of Wollongong Thesis Collections

2017

Investigation into Performance of Bulk Heterojunction Organic Solar Cells

Ali Aghassi
University of Wollongong

Follow this and additional works at: https://ro.uow.edu.au/theses1

University of Wollongong

Copyright Warning

You may print or download ONE copy of this document for the purpose of your own research or study. The University does not authorise you to copy, communicate or otherwise make available electronically to any other person any copyright material contained on this site.

You are reminded of the following: This work is copyright. Apart from any use permitted under the Copyright Act 1968, no part of this work may be reproduced by any process, nor may any other exclusive right be exercised, without the permission of the author. Copyright owners are entitled to take legal action against persons who infringe their copyright. A reproduction of material that is protected by copyright may be a copyright infringement. A court may impose penalties and award damages in relation to offences and infringements relating to copyright material. Higher penalties may apply, and higher damages may be awarded, for offences and infringements involving the conversion of material into digital or electronic form.

Unless otherwise indicated, the views expressed in this thesis are those of the author and do not necessarily represent the views of the University of Wollongong.

Recommended Citation

Aghassi, Ali, Investigation into Performance of Bulk Heterojunction Organic Solar Cells, Doctor of Philosophy thesis, School of Chemistry, University of Wollongong, 2017. https://ro.uow.edu.au/theses1/360

Research Online is the open access institutional repository for the University of Wollongong. For further information contact the UOW Library: research-pubs@uow.edu.au

UNIVERSITY
OF WOLLONGONG
AUSTRALIA

Investigation into Performance of Bulk Heterojunction Organic Solar Cells

Ali Aghassi

This thesis is presented as part of the requirements for the conferral of the degree:

Doctor of Philosophy

Supervisors:
Attila J. Mozer
Peter Innis

The University of Wollongong
School of Chemistry

August 2017

This research has been conducted with the support of an Australian Government Research Training Program Scholarship.

Declaration

I, *Ali Aghassi*, declare that this thesis is submitted in partial fulfillment of the requirements for the conferral of the degree *Doctor of philosophy*, from the University of Wollongong, is wholly my own work unless otherwise referenced or acknowledged. This document has not been submitted for qualifications at any other academic institution.

Ali Aghassi

August 30, 2017

Abstract

Despite the continuous improvement of bulk heterojunction solar cell performance, their power conversion efficiency lags far behind inorganic counterparts. A better understanding of underlying mechanisms that limit the device performance allows the development of strategies to improve the power conversion efficiency of the devices. Of particular importance is the dynamics of charge carriers (generation, transportation, collection, and recombination) within the bulk heterojunction or at interfaces with electrodes. Within this body of work, charge carrier dynamics of bulk heterojunction solar cells were investigated as a function of (i) the use of electron transport layer poly[(9,9-bis(3′-(N,N-dimethylamino)-propyl)-2,7-fluorene)-alt-2,7-(9,9-dioctyl)-fluorene] (PFN), (ii) altering dielectric constant by considering Clausius-Mossotti relation, and (iii) the appearance of the S-shaped current density-voltage curve.

While PFN has been extensively used as electron transport layer to modify the interface, a number of issues over the optimum PFN film can be found in the literature. To address the issues, the modification of the interface between the cathode electrode and bulk heterojunction compose of Poly[N-9′-heptadecanyl-2,7-carbazole-alt-5,5-(4′,7′-di-2-thienyl-2′,1′,3′-benzothiadiazole)] and 1-[3-(Methoxycarbonyl)propyl]-1-phenyl-[6.6]C_{71} (PCDTBT:PCBM) were studied. It was determined that for a range of PFN solutions (from 0.5 to 0.2 mg/ml) cast at a wide range of spin speed (from 1000 to 8000 rpm), the performance of the solar cell devices is lower or similar to the control devices. Further investigation of devices revealed no substantial alteration in recombination or mobility of charge carriers upon incorporation of PFN interlayer. It was proposed that PFN interlayer is unable to modify the interface and therefore charge carrier dynamics of the solar cell devices, contrary to what has been reported in the literature.

Secondly, increasing dielectric constant of the bulk heterojunction was considered as an alternative path to influence recombination of charge carriers. Based on the Clausius-Mossotti

relationship, the polymeric dielectric constant has consisted of two parts, i.e., polarization and free volume. It was speculated that replacing air in the free volume of bulk heterojunction with an organic filler may enhance the dielectric constant. A series of materials with higher dielectric constant than air (PFN = 2.16, rhodamine 101 = 4.73, Isopropyl alcohol:17.9) was incorporated to the bulk heterojunction. Then, the dielectric constant of the bulk was measured as a function of the incorporated materials. The bulk heterojunction was composed of either polymer (PCDTBT) or small molecule 7,7′-[4,4-Bis(2-ethylhexyl)-4H-silolo[3,2-b:4,5-b′]dithiophene-2,6-diyl]bis[6-fluoro-4-(5′-hexyl-[2,2′-bithiophen]-5-yl)benzo[c][1,2,5]thiadiazole] (p-DTS(FBTTh$_2$)$_2$) as donor and PC$_{60}$BM as acceptor. It was determined that the dielectric constant varied only slightly depending on the bulk system and the used materials. In addition, the photovoltaic performance of the solar cell devices is affected, mostly due to the interference of the incorporated materials with the generation and collection of charge carriers. These results imply that free volume of the bulk heterojunction may not be readily accessible to modify and Clausius-Mossotti relation cannot be thus employed to enhance BHJ dielectric constant.

Thirdly, the charge carrier dynamics of solution-processed small molecule bulk heterojunction (p-DTS(FBTTh$_2$)$_2$:PC$_{70}$BM) was investigated when it was influenced by S-shaped current-voltage phenomena. The power conversion efficiency of the S-curve devices was considerably decreased, mostly due to the reduction of fill factor and short-circuit current. It was proposed that the formation of a thin layer of the small molecule near cathode electrode was responsible for the occurrence of the S-shaped curve. It was determined that the thin layer not only participates in photogeneration process but also hinders the collection of charge carriers via introducing an additional energy barrier. In addition, charge carrier recombination was found to be faster in S-curve devices. A novel method was examined to recover device performance and a normal diode-like current-voltage curve was accomplished when PCBM content of the bulk heterojunction was increased.

Table of Contents

List of Figures

Chapter 1: Introduction

1.1. ORGANIC PHOTOVOLTAICS: A CASE FOR FUTURE ENERGY

In a world where the engine of economic growth and human development is driven by the energy, supplying a clean, sustainable, reliable and affordable source of energy is a great challenge of our time and expected for the foreseeable future. The economic growth - indicated by the gross domestic product (GDP) – is the key determinant for energy demands around the world. With a projected 3.3%/year GDP from 2012 to 2040 particularly led by countries outside the Organization of Economic Corporation and Development (OECD), it comes as no surprise that the global demand for energy will continue to increase over the coming decades. Indeed, estimates by U.S. Energy Administration Information (EIA) anticipate that total world energy consumption will rise from 549 quadrillions Btu[1] in 2012 to 815 quadrillion Btu by 2040.[1] This huge expansion of projected energy use raises questions such as i) what are sources to supply this amount of energy, ii) what are the consequences regarding utilization of these energy sources. Such questions are amongst the most significant challenges facing humanity and how to address said questions will shape the future of human and other life forms for generations.

1.1.1. Energy Sources and Global Warming

Before addressing future energy challenges, it is informative to survey the current energy supply sources, see Figure 1.1a. The British Petroleum (bp) company estimates that the primary source of energy in 2016 was fossil fuels which include petroleum, coal and natural gas, amounting to 85% of the world's energy consumption (Figure 1.1a).[2] On the contrary, non-fossil fuel based energy sources in 2016 consisted of nuclear 4%, hydroelectric 7% and Climate

---

[1]- Btu is acronym for British thermal unit. A quadrillion Btu is about equal to amount of energy of 45 million tons of coal, 1 trillion feet cubic of natural gas and 170 million barrels of crude oil.

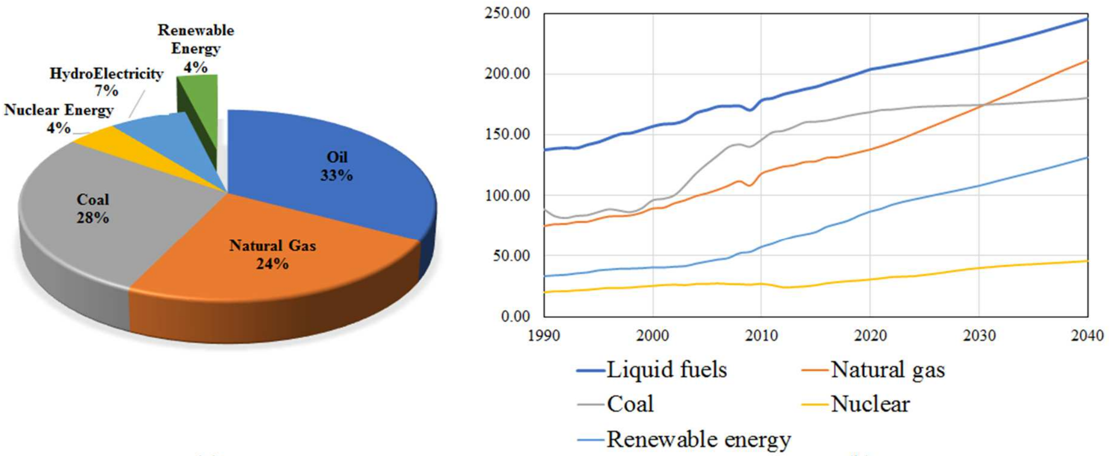

(a) (b)

Figure 1.1. (a) Global energy consumption breakdown by energy source in 2016 taken from bp statistical reference case,[2] (b) total energy consumption by energy source, 1990-2040 (quadrillion Btu) from EIA reference case.[1]

renewable (solar, wind, tidal, geothermal, wood and waste) 4%. This demonstrates the dominance of the fossil fuel in the energy marketplace, which can be mostly due to their abundance, industrial demands, research and a long history of heavy investment by governing body across the globe. It is even projected by the EIA that fossil fuels will still account for the 78% of energy consumption by 2040 (Figure 1.1b). Although liquid fossil fuel (petroleum) remains the main source of energy for world energy consumption, natural gas is on the rise expected to surpass coal (the slowest-growing energy source) by 2030.[1]

Given the projection of world energy consumption, serious concerns have been raised in the scientific community and public domain regarding the impact of using of fossil fuel, on a massive scale for such a prolonged period of time, in addition to the effect(s) on the quality of the human life and on planet earth. Even though the global reserve of the fossil fuel will be eventually depleted, the current stockpiles are more than ample to inflict an irreversible climate catastrophe. Multiple lines of scientific evidence have indicated the rise of average temperature of Earth's climate system, known as global warming.[3-4] The Intergovernmental Panel on Climate Change (IPCC) has concluded the following in its Fifth Assessment Report:[5]

“*It is extremely likely that human influence has been the dominant cause of the observed warming since the mid-20th century*.”

The human influence is primarily related to the release of greenhouse gasses (GHG) such as carbon dioxide (CO_2), methane, and nitrous oxide (N_2O), among others. It is generally accepted that the combustion of fossil fuels is one of the main sources of GHG emissions. An estimation by the EIA has projected a 34% increase in world energy-related CO_2 emission from 32.2 million metrics tons at 2012 to 35.6 million metrics tons by 2040.[1] Unless a substantial reduction of GHG emissions occurs, the climate disruption can take an immense toll on natural and socioeconomic system including i) more frequent extreme weather events (droughts, floods, wildfires) resulting in the death of thousands,[6-9] ii) rising sea levels causing the gradual submergence of low-level coastal area,[10-11] iii) power outages,[12] iv) crop failure.[13] A significant shift in energy sources from fossil fuels toward a less polluting is indispensable. Renewable energy potentially offers clean, yet sustainable sources of energy for the future.

1.1.2. Renewable Energy

Renewable energy is energy sources that originate from nature and continuously replenished by natural processes on a human timescale. The renewable energy can be harnessed from different natural sources such as sunlight, wind, plant growth, tidal, and geothermal which are widespread over geographical areas. Figure 1.2 represents various kinds of renewable energy resources. It is believed that the rapid deployment of the renewable energy will not only improve public health,[14-15] create jobs,[16-17] and contain financial benefits,[18] but also mitigate global warming by reducing GHG emission arising from the burning of fossil fuel. However, the feasibility of implementation and degree of limitation associated with the use of renewable energy sources should be considered.

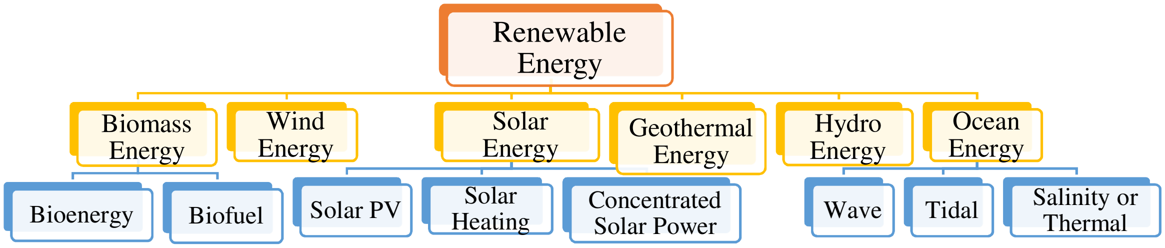

Figure 1.2. Overview of renewable energy resources.

Hydropower is the power that can be harnessed from moving water. It is a reliable, well-advanced technology with more than a century of practical advancement which already supplies 0.5 terawatts (TW) electricity worldwide.[19] However, hydropower technology is extremely site-specific and the majority of feasible locations (rivers) have already been identified and exploited, thereby leaving small room for more expansion of utilization of the energy. In addition, it brings about substantial changes to lands, rivers and the ecosystem.[20]

Geothermal energy exploits the heat energy within the Earth which is generated via the temperature difference between the planet core and its surface.[21] Geothermal energy is cost-effective, reliable and sustainable, yet have some limitation including i) limit to specific areas (near tectonic boundaries), ii) require advanced technology to drill through the planet's crust, iii) releasing greenhouse gases and toxic elements.[22-23]

Biomass energy is the energy from the Sun which is collected and stored in the plants, trees, and crops through photosynthesis processes.[21] The energy of biomass can be directly obtained via burning or can be converted into biofuel. Although it may play a role in the context of liquid fuel, there are some challenges to overcome for practical electricity production from biomass sources including low energy density, and costly storage and transportation. Moreover, there is a competition between biomass farming and food production arising from the global shortage of productive land, water, and fertilizer.[21]

Wind power is the conversion of flowing air via wind turbines into electricity. It is one of the main sustainable energy sources that emit no greenhouse gases and use no water during its operation. The advancement of technology within the turbine wind has paved the way for the deployment of multiple wind farms during the past decades. However, power production varies significantly especially in short time frames, making it supplement to other power supply sources.[21]

Ocean energy refers to energy that can be harnessed from waves, tides, salinity and difference temperature in the oceans to produce electricity.[21] While ocean energy technology is at the early development stage, however, serious concerns have been raised regarding side effects on the marine systems.[24]

The renewable energy sources above are almost indirect branches of solar energy. This is the energy of the Sun that drives winds and ocean currents, evaporates water and produces clouds, and stores it in the plants through photosynthesis. An abundant amount of the solar energy reaches the surface of the Earth every day in the form of irradiation and heat. This widely available energy can be directly exploited to produce useful outputs. The International Energy Agency (IEA) has said:[25]

> "*The development of affordable, inexhaustible and clean solar energy technologies will have huge longer-term benefits. It will increase countries 'energy security through reliance on an indigenous, inexhaustible and mostly import-independent resource, enhance sustainability, reduce pollution, lower the costs of mitigating global warming, and keep fossil fuel prices lower than otherwise. These advantages are global.*"

Despite numerous advantages of solar energy, there are a few limitations including i) solar radiation level is very low at night, ii) The amount of sunlight fluctuates, depending on geographical location and weather condition. In addition, there are some concerns regarding health and environmental impact of manufacturing processes of photovoltaic solar cells.[26]

1.1.3. Photovoltaic Solar Cells

Several approaches have been adopted to capture the solar energy including photovoltaic solar cell (PV),[27] concentrated solar panels (CSP),[28] solar thermal heating,[29] and solar fuels.[30] The Photovoltaic cells are the leading technology for solar energy and seem to be the backbone of solar power generation for forthcoming decades. Seth *et al.* have shown that if 2% of Earth's land is covered by photovoltaic solar panels with an average power conversion efficiency of 12%, an approximation of 67 TW of electricity can be supplied which is twice than that of total projected energy demand in 2050.[19] As of 2016, the global capacity of the installed solar photovoltaic was 303 gigawatts (GW).[31] The fast deployment of the solar PV is attributed to advances in the technologies which increase the effici[ency of installed photovoltaics together with the reduction of the costs owing to massive scale production.[32] In addition, PV is highly modular technology which allows for the economy of scales and ease of deployment.[33] Of noteworthy importance is solar PV technology is environmentally benign and once installed no greenhouse gases, in particular, are emitted.

The photovoltaic solar cell refers to a device that directly converts sunlight into electricity. The device is comprised of a semiconducting material which generates electrical power upon exposure to the light. This involves the absorption of the light and the generation of charge carriers which are then separated and collected at respective electrodes. A wide variety of materials have been employed to fabricate photovoltaic solar cells. Figure 1.3 exhibits the major PV solar cells categorized based on semiconducting materials. These semiconducting materials differ from each other in terms of light absorption, power conversion efficiency, production cost and manufacturing technology.

Figure 1.3. Various types of photovoltaic solar cells. Abbreviation: DSSC: Dye-synthesized Solar Cell; PSC: Perovskite Solar Cells; OSC: Organic Solar Cells; QDSC: Quantum-Dot Solar Cells; GaAs: Gallium Arsenide; InP: Indium Phosphide; sc-Si: Monocrystalline silicon; mc-Si: multi-crystalline silicon; CdTe: Cadmium Telluride; CIS: Copper Indium di-Selenide; CIGS: Copper Indium Gallium di-selenide; CZTS: Copper Zinc Tin Sulfide; CZTSS: Copper Zinc Tin Sulfide Selenide; a-Si: Amorphous Silicon, μ-Si: microcrystalline Silicon. The efficiencies have been taken from Green *et al.*[34], *: the efficiency was not reported in the ref [34].

The most prevalent PV solar cells on the market are crystalline silicon (c-Si) (also known as the first generation) which are made of monocrystalline (sc-Si) and polycrystalline (mc-Si) silicon. The sc-Si solar cells are fabricated from a single crystal of silicon (sliced from a big size ingot) by a process known as Czochralski process.[35] The sc-Si solar cells are highly reliable and their efficiency lies around 26-27%.[34, 36] However, the manufacturing process of sc-Si solar cells is costly and time-consuming.[37] The polycrystalline solar cells, on the other hand, are composed of a number of different crystals attached to each other on a single crystal. The manufacturing process of mc-Si is cheaper and requires fewer materials compared to sc-Si solar cells, yet compensate with lower power conversion efficiency (21%).[34, 36]

Thin film solar cells are the next generation of the solar cells which consist of a thin layer of photovoltaic materials deposited on a supporting substrate such as metal, glass or plastic coil.[38-41] The thickness of PV layer in thin film solar cells is in the range of few micrometers which is due to higher absorptivity of the PV materials compared to the crystalline materials. Since fewer materials are used and simpler techniques (spray coating) are employed to fabricate the thin film solar cells, the manufacturing cost is reduced. Examples are cadmium telluride (CdTe), copper zinc gallium di-selenide (CIGS) and amorphous silicon (a-Si). The efficiency of the CdTe and CIGS are comparable and close to the mc-Si solar cell (21% and 21.7%, respectively),[34] making them appealing options for further commercialization.

The newest generation of the photovoltaic solar cell on the verge of commercialization is organic photovoltaics. The light-sensitive layers in this type of solar cell are organic materials such as conjugated polymers or small molecules. Examples of these classes of solar cells are organic solar cells,[42-43] dye-synthesized solar cells,[44] perovskite solar cells,[45] and quantum-dot solar cells.[46] There are advantages associated with employing the organic photovoltaics including i) semiconducting properties of the organic materials can be tuned via engineering of chemical structures, ii) organic materials have high absorption coefficient (~ 1000 times higher than polycrystalline silicon), enabling a thin layer of few hundred nanometers to absorb a large portion of incident light, iii) the organic photovoltaics are lightweight, flexible and visually aesthetic which can be integrated within current infrastructure,[43, 47-48] iv) the manufacturing process of organic photovoltaics is simpler and cheaper than crystalline silicone which benefits bulk scale production.[49] However, several challenges need to be addressed in order to make the solar cell commercially viable. Some of the challenges are 1) the power conversion efficiency of organic photovoltaic module remains very low, 2) the operational lifetime of OPV devices is far shorter than inorganic counterpart, 3) variation in batch-to-batch production of organic material seems to be a difficulty for performance consistency.[19, 50] Noteworthy that a transition from a small scale, spin-coated laboratory-based solar cell to a flexible large-scale coupled with roll-to-roll printing technique and environmentally friendly formulation must take place to achieve scalable manufacturing.

1.2. ORGANIC SOLAR CELLS

Among organic photovoltaic technologies, organic solar cells (OSC) have made a significant contribution to the research filed over the past 15 years. The prospect of cost-effective throughput fabrication using roll-to-roll printing technology has inspired a great deal of research which has advanced our knowledge about organic electronics and paved the way future commercialization of organic solar cells. Organic solar cells consist of a photoactive layer which is sandwiched between two electrodes with different work functions. While the photoactive layer is responsible for transforming part of the solar electromagnetic spectrum (radiation) into charge carriers (electricity), the electrodes are responsible for collecting those charge carriers. The photoactive layer has composed of two major compounds; so-called electron donor and electron acceptor material. The donor and acceptor materials govern fundamental processes that determine the performance of organic solar cells. These fundamental processes are i) photon absorption by electron donor and exciton (electron-hole pair) generation, ii) exciton diffusion to donor-acceptor interface, iii) exciton dissociation to free charge carriers at the interface, and iv) charge carrier transport and collection at the respective electrodes. The processes are discussed in details in the following section. The efficiency of the abovementioned steps and consequently device overall performance is dependent crucially on the morphology of the photoactive layer, i.e., how donor and acceptor materials dwell throughout the active layer.

The donor and acceptor can be both polymers, small molecules and/or combination of polymer and small molecule (Figure 1.4). A characteristic that all donor and acceptor materials have in common is a large conjugated system, i.e., the alternation of single and double bonds between the carbon atoms. The ground state configuration of a carbon atom is $1s^2\,2s^2\,2p^2$.[47, 51] The s orbital interact with P_x and P_y orbitals and form three sp^2 orbitals which then form the σ bonds. But, the P_z orbital which is perpendicular to the plane of sp^2 orbitals does not participate in σ bond. Instead, the overlap of P_z orbital electron wavefunction leads to the formation of two new orbitals called bonding (π) and antibonding ($\pi*$). The charge in these orbitals are delocalized which is the reason for conductivity in the carbon-based semiconductor. The bonding and antibonding orbital also known as highest occupied molecular orbital (HOMO) and the lowest unoccupied molecular orbital (LUMO), respectively. The band gap in organic semiconductors refers to the energy difference between the HOMO and LUMO level which is in order of 1-3 eV.[47] These HOMO and LUMO energy levels can be used to obtain many properties of organic semiconductors including open-circuit voltage,[52] ionization energy, electron affinity,[53] electronic band gap, and the driving force for charge separation.[54]

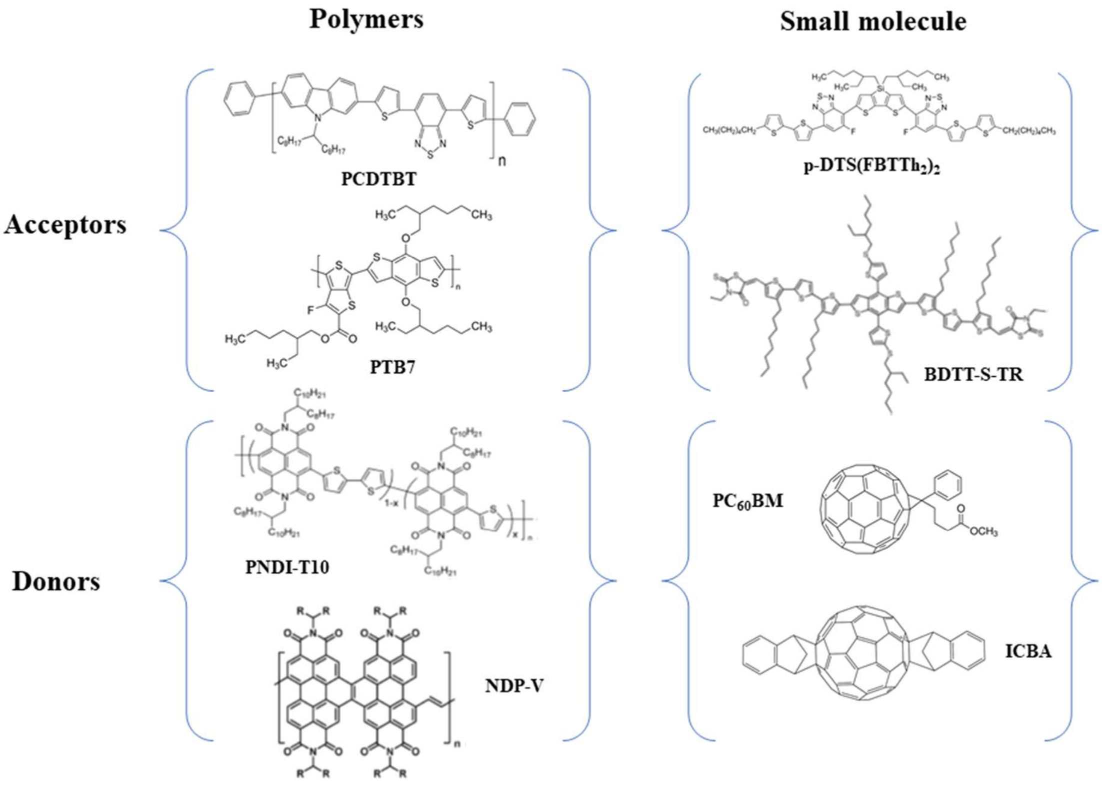

Figure 1.4. Chemical structures of some polymers and small molecule used as either acceptor or donor.

1.2.1. Bulk Heterojunction

The performance of organic solar cells is largely dependent on the distribution and interaction of donor and acceptor materials within the photoactive layer. In the case of most efficient OSC, donor and acceptor materials are intimately mixed to form a bicontinuous interpenetrating network known as bulk heterojunction (BHJ). The idea of bulk heterojunction was first introduced by Heeger *et al.*[55] in 1995 to overcome the low rate generation of free charge carriers in the planar structure OSC. Due to short exciton lifetime (and therefore diffusion length), the efficiency of the devices is inherently limited. The exciton is Coulombic-bound electron-hole pair with no net charge. The binding energy between electron and hole in the organic semiconductor is much large than that of thermal energy ($k_BT = 0.025\ eV$). As such, dissociation of exciton to free electron and hole requires an additional driving force to overcome the binding energy.

The bulk heterojunction facilitates scavenging exciton to free charge carriers by providing the driving force at donor-acceptor interface. The concept of bulk heterojunction has the advantage of exciton dissociation all over the photoactive layer, thereby leading to dramatic enhancement of charge carrier generation. In addition, it contains large enough percolating path that allows free charge carriers to reach their respective electrode. However, difficulty to control the exact nature of BHJ morphology has made it necessary to use some pre- or posttreatment techniques such as thermal/annealing or processing additives to further fine-tune 3D nanostructure of BHJ morphology.[56] The BHJ morphology is the most dominant active layer geometry in OSC offering advantages including low-cost, large-scale fabrication process over silicon solar cells.[57]

1.2.2. Device Physics

Figure 1.5 presents a simplified overview of photoinduced processes happens within the bulk heterojunction solar cells following photoexcitation. First, absorption of photon produces excitons. The exciton then diffuses to the interface of donor/acceptor phase. Once at the interface, a charge transfer (CT) state is formed with an electron in acceptor phase and the hole in the donor phase. If the binding energy of the electron and hole (CT state) can be overcome, the electron will be transferred to the LUMO level of acceptor and the hole to the HOMO level of the donor. These free charge carriers are described as charge separate (CS) state that can travel through pure domain phase of donor and acceptor to be collected by their respective electrodes.[58-59] Noteworthy, it is believed that these free charges can distort the position surroundings their nuclei and form a pseudo particle known as polaron which is comprised of charge and phonon.[47]

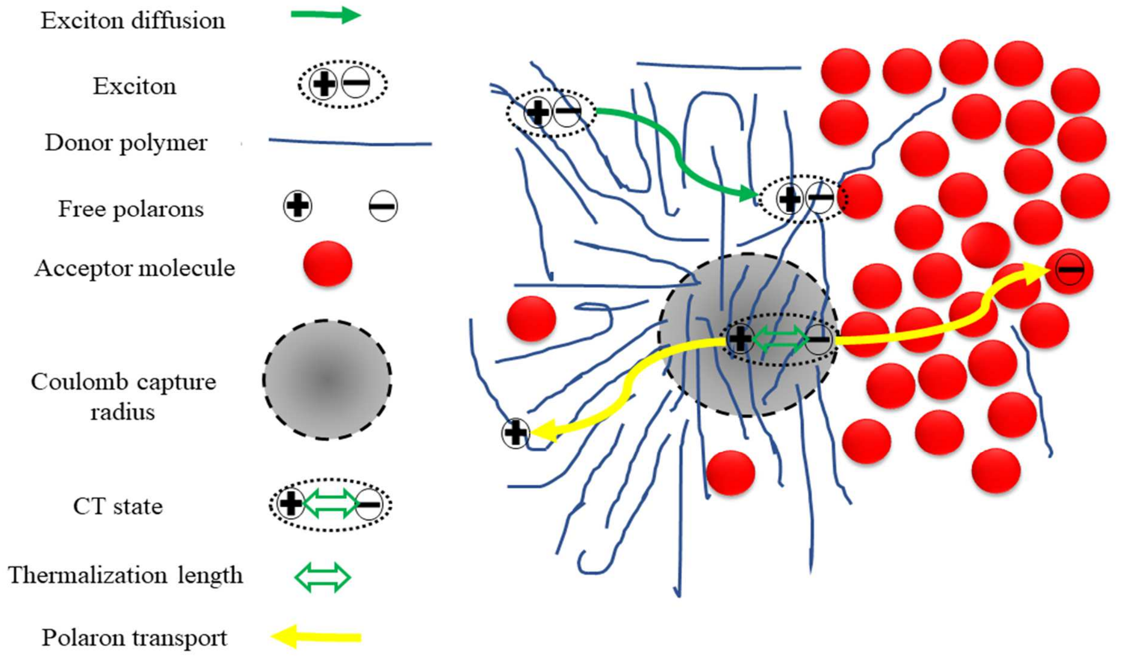

Figure 1.5. Schematics of charge carrier generation in polymer-PCBM bulk heterojunction active layer from exciton formation to free charge carrier collection (for the case of donor phase absorption) consider Braun-Onsager model.

1.2.2.1. Exciton generation and dissociation

The primary product of the light interaction with semiconductors is an exciton. Exciton is a pair of electron and hole which are bound to each other by the electrostatic Coulomb force. The low dielectric constant of organic materials (e.g. benzol = 2.28) leads to the formation of Frenkel-type excitons.[60] The binding energy of electron and hole in Frenkel-type exciton is around 0.5-1 eV. The exciton usually has a certain lifetime (around 1 ns) and afterward recombines radiatively. As mentioned earlier, the exciton binding energy by far exceeds thermal energy ($k_BT = 0.025\ eV$) at room temperature. Before dissociation of the exciton can take place, it must travel to the donor/acceptor interface. Since the exciton is a neutral species, its motion cannot be influenced by an electric field and therefore they randomly diffuse. Hence, donor/acceptor interface must be in the range of exciton diffusion length. Various diffusion lengths have been reported in the literature, ranging from 3-30 nm.[47] For example, the diffusion length of P3HT and C60 excitons are reported to be around 4 and 12 nm, respectively.[61-62] Upon arrival to the donor/acceptor interface, the exciton can transfer its electron to the electronegative acceptor. Many studies have shown that the charge transport is extremely fast and on the order of tens of femtoseconds (< 100 fs).[63-66] The exciton dissociation takes place when energy gain is larger than the binding energy of electron and hole. Only then, charge transfer process generates an electron in acceptor phase and a hole in donor phase. The energy gain has been related to the energy offset between the LUMO of the donor and the LUMO of the acceptor. Several studies have reported a universal prerequisite of 0.3 *eV* offset energy between donor and acceptor for the efficient exciton dissociation. However, the theoretical basis regarding the assumption is limited [59] and some exceptions have been observed.[67-68] Moreover, limited the dissociation to energy offset between LUMO of donor and acceptor appears to be a rough estimate as some other factors have been identified that could have contributed to the exciton dissociation including doping,[69] mixed phases,[70] charge defects,[71] and entropy gains from increased electron and hole separation.[59, 72]

1.2.2.2. Charge transfer (CT) state

It is shown that after transfer of electron and hole to the acceptor and donor phases, respectively, electron and holes are still Coulombically bound together.[54, 59, 73-75] This intermediate state is called charge transfer (CT) state and exists at the interface of donor and acceptor phases. The binding energy of electron and hole in CT state has been estimated to be around a few hundred millielectronvolts which is still large than the thermal energy available at room temperature.[73, 76-77] Once the CT state form, there is a competition between separation into free charge carriers and recombination (geminate) into ground state or triplet state (if energetically suitable). As such, an excess energy is needed to separate this electron-hole pair (polaron pair) into free charge carriers. In addition to factors mentioned in the previous section causing exciton dissociation, the role of electronic delocalization has been also explored. Several studies have reported that short-lived hot and delocalized CT states can help to overcome the Coulomb attraction by increasing effective separation of an electron-hole pair.[54, 59, 73, 78-80] It has been also reported that the excess energy arising from absorbing above bandgap photon can lead to faster and efficient free charge carrier generation in some polymer/fullerene systems which are consistent with hot CT concept.[78, 80] However, the role of hot CT state regarding charge carrier generation process has been found to be insignificant in several other polymer/system.[81-83] Nevertheless, recent studies have shown that in the efficient bulk heterojunction the charge generation doesn't pass through the bottleneck of CT states and the majority of free charge carriers are directly produced via delocalized states.[74, 84] Hence, this field of study still remains a matter of research and debate.

1.2.2.3. Charge carrier transport/mobility

Following exciton dissociation and CT state separation, transportation of charge carriers toward their respective electrode takes place. Charge carrier mobility in the crystalline semiconductor is in order of 10^2 - 10^3 cm^2 V^{-1} s^{-1} due to 3D rigid lattice ensuring wide valence and conduction bands. In contrast, organic semiconductor suffering from weakness of the electronic coupling, large electron-vibration coupling, and disorder which give rise to the localization of charge carriers and formation of polaron.[73] As such, charge carrier transport is limited to thermally assisted hoping process from one localized state to another across the different molecule. As a result, charge carrier mobility strongly relies upon the morphology of the active layer (bulk heterojunction) and varies largely over ranges from 10^{-6}-10^{-3} cm^2 V^{-1} s^{-1} in highly disorder materials to > 1 cm^2 V^{-1} s^{-1} in highly ordered materials.[73]

In the most BHJ system, the mobility of the electron is governed by the transport through the LUMO level of acceptor toward the cathode electrode, whereas the hole mobility originates from transport through the HOMO level of donor toward the anode electrode. The fact that bulk heterojunction composes of a disordered blend of donor and acceptor materials, the mobility of individual charge carrier is heavily influenced by the ratio of donor/acceptor and the morphology of the bulk heterojunction.[85-86] For example, the hole mobility of pristine P3HT (donor) is around 1.4×10^{-4} cm^2 V^{-1} s^{-1}, whereas a four order of magnitude drops when it is blended with PCBM (acceptor). The other factor can influence charge carrier mobility are temperature, energetic disorder (trap density), and electric field.[87-91]

The performance of the OSC is largely dependent on the collection of photogenerated charge carriers at the electrodes. This process competes with recombination (nongeminate) loss mechanisms and mostly depends upon the mobility of charge carriers within the bulk heterojunction. The higher the charge carrier mobility is, the more charge carrier can be extracted. On the other hand, low charge carrier mobility results in accumulation of charge carrier within the bulk heterojunction due to less efficient extraction, leading to more recombination (nongeminate) and consequently low efficient devices. Therefore, some studies have indicated that 10^{-4} cm^2 V^{-1} s^{-1} as a minimum mobility required for the efficient solar cell devices.[92-95]

1.2.2.4. Charge carrier extraction/collection

Charge extraction/collection is the last step that charge carriers undergo to produce a photocurrent. The electron is extracted through the cathode electrode and the hole via anode electrode and the extracted charge carries thus generate the resulting photocurrent. An efficient charge carrier extraction is complementary to an efficient charge generation which should take place before charge carrier concentration can be significantly reduced by recombination processes. It is shown that at short-circuit conditions (strong internal electric field) the charge carriers are swept-out of the bulk heterojunction on the order of 100 ns.[96-97] In the swept-out process, the free charge carriers are extracted via drift transport under influence of built-in electric field. The swept-out process competes with recombination processes (nongeminate) such that charge carriers can be efficiently collected at the electrodes. It is shown that charge carrier sweep-out is proportional to the magnitude of the internal electric field and is restricted by the charge carrier mobility.[84, 96] Noteworthy, at the voltage near open-circuit condition where internal electric field approaches zero, the drift current contribution to the charge extraction is in insignificant and diffusion current may play a significant role.[84]

It should be noted that the contact between the electrode and the active layer plays a large role in the extraction/collection of charge carriers into the electrodes. Various metals including aluminum, gold, silver together with transparent conducting oxide, conducting polymer, graphene, and carbon nanotube are commonly employed to make contact in OSC devices. As mentioned above, efficient charge collection is due to a drift electric field (it is assumed that there is no sufficient charge carrier density or mobility that can compensate the applied field) which is set up by the metallic and semiconducting contacts.[84, 96, 98-99] Given the thickness of the active layer, the drift electric field should be uniform in the efficient solar cell devices. Other important factors of contact that can influence device performance are contact workfunction, stability, the ability to block opposing charge, and favorable chemical interaction with the active layer.[84] For example, it is shown that PSS dopant of PEDOT:PSS layer migrates to the active layer and significantly reduce the lifetime of the devices.[100]

Some other factors have also been reported that significantly influence the extraction/collection of charge carriers. For instance, imbalanced mobility between electron and hole and space charge formation can locally screen electric field near electrodes, leading to significant suppression of drift current and consequently charge carrier collection.[101] Another issue is the occurrence of the S-shaped current density-voltage curve which seriously undermines the collection of charge carriers. Several explanations have been reported in the literature for the S-shaped characteristics including the formation of a dipole at the interface,[102] or reduction of charge transfer rate over the interface or by the surface recombination.[47, 103-104]

1.2.3. Energy Loss Mechanisms

Recombination of charge carriers reduces the short-circuit current, open-circuit potential, and fill factor in BHJ solar cells, thereby limiting power conversion efficiency (PCE) of the organic solar cells. Hence, identifying recombination mechanism would help to develop strategies preventing charge carriers annihilation and therefore enhances the PCE. In an ideal scenario, every absorbed photon by active layer would be converted into free charge carriers which are collected at the electrodes. However, under real circumstances, every step from exciton generation to charge carrier collection is prone to lose mechanisms. Once exciton is generated, it has only a few nanoseconds to reach a donor/acceptor interface prior to relaxing to the ground state. If nanoscale domain sizes are larger than exciton diffusion length, it is more likely that exciton recombine. Once CT state form, there is still the possibility of recombination of the electron-hole pair rather than dissociating into free charge carriers. After successful dissociation of CT states into free charge carriers, the charge carrier must travel to their respective electrode. A possible route of recombination is to encounter an oppositely charged free carrier on their way to the electrodes. Charge carrier recombination in organic solar cells has been categorized into two major group, i.e., geminate and non-geminate recombination. The geminate term refers to recombination of electron and hole (pair) which originates from a single photon, while non-geminate considers recombination whose electron and hole are created by different photons.

1.2.3.1. Geminate recombination

The process of recombination of an electron-hole pair originated from some photon is known as geminate recombination. The driven force for the geminate recombination is the strong Coulomb attraction between the electron-hole pair in the organic semiconductor. This recombination process includes excitons which are lost to ground state before reaching to the interface and electron-hole pair that recombines at the donor/acceptor interface before separate into free charge carriers. Numerous factors have been reported that affect the geminate recombination including nanoscale domain size of the active layer, energy offset between donor and acceptor, delocalization of CT state, the energy of triplet exciton, electric field, and phase purity.[92] The photocurrent of bulk heterojunction system can be significantly limited y the geminate recombination in some systems. It is also shown that geminate recombination can be increased by the applied bias, thereby affecting fill factor.[105-107] However, it is shown that geminate recombination does not play a significant role in recombination of charge carriers and the efficiency is mainly limited by the non-geminate recombination.[84, 97, 108-109]

1.2.3.2. Nongeminate recombination

The nongeminate recombination encompasses recombination of charge carriers that have not been originated from absorption of a single photon. The order of nongeminate recombination can be classified based on the number of the participant into three categories: monomolecular (trap-assisted) recombination, bimolecular recombination, and trimolecular (Auger) recombination.[92] Recombination of free charge carriers with trapped carriers considered first order process, especially when the concentration of trapped charges exceeds mobile's one. If two free and independent charge carriers recombine, bimolecular recombination rate describes electron-hole recombination. Higher order recombination process is well established in the inorganic solar cell where three particles are involved such as Auger recombination. However, this has been rarely observed in organic solar cells.[92, 110-112]

The nongeminate recombination can effectively eliminate charge carriers that could otherwise contribute to the photocurrent. As a result, photocurrent could be significantly reduced by the recombination. This is mostly dependent on the thickness of the active layer, the mobility of charge carriers, and degree of phase separation between donor and acceptor.[92]

The nongeminate recombination becomes significant at the open-circuit conditions where the applied bias and injection of dark carriers screen the internal electric field within the bulk heterojunction. Hence, fill factor of the devices could also be affected. Establish an efficient and balanced charge carrier mobility in conjunction with strong internal electric field can help to reduce the effect of the nongeminate recombination on the photocurrent and fill factor. It is also reported that nongeminate recombination could influence the open-circuit potential of the solar cell.[113-114]

1.2.3.2.1. Bimolecular recombination

The most common type of recombination observed in the organic solar cell is bimolecular recombination. Bimolecular recombination involves recombination of two free mobile charge carriers. The bimolecular recombination in the disordered organic semiconductor with localized states depends on the rate at which opposite charge carriers meet each other. As a result, the rate of bimolecular recombination is proportional to the mobility of charge carriers in organic semiconductors. The most widely used model to describe bimolecular recombination rate is Langevin which correlate the rate to the charge carrier density, mobility of charge carrier and dielectric constant of the medium as follow:[84, 92]

$$\mathrm{R} = \mathrm{e}\ \mathrm{n_e n_h} \frac{\mu_h + \mu_e}{\varepsilon_r \varepsilon_0} \qquad (1\text{-}1)$$

where e is elementary charge, n_e and n_h represents electron and hole density, μ_h and μ_e are mobility of electron and hole and $\varepsilon_r \varepsilon_0$ stands for effective dielectric constant of medium. Considering Langevin model, one may expect that increasing mobility of charge carriers would eventually enhance bimolecular recombination in organic solar cells. This is not generally the case as some studies have shown that increasing mobility reduce the bimolecular recombination yield in OSC.[104, 115] This is due to enhance charge extraction, leading to decrease the density of charge carriers within the device. Although bimolecular recombination in organic solar cells has been satisfactorily described by the Langevin model, the strength of this model in many BHJ system has been found less pronounced. This is commonly referred to reduced Langevin recombination and several reasons for the reduction of the rate have been reported in the literature.[92, 105, 116-120] It should be noted that bimolecular recombination is charge carrier density- and bias dependent and is responsible for the majority of recombination from short-circuit to open-circuit conditions.[84, 97, 109]

1.2.3.2.2. Trap-assisted recombination

Trap-assisted recombination is a first-order recombination process in which a free charge carrier recombines with opposite charge through a localized energetic trap. The rate of trap-assisted recombination depends on traps density and how fast the free charge carrier finds the trap. A model for the trap-assisted recombination was developed for the inorganic solar known as Shockley-Read-Hall (SRH) which has been lately applied to organic solar cells.[121-123] The trap-assisted recombination in the organic semiconductor is controlled by the diffusion of free charge carrier toward the trapped-charge. As a result, trap-assisted recombination is governed by the charge carrier transport.[124] In most BHJ systems, donor materials or impurities are the main culprits for the trap-assisted recombination as it is known that acceptor materials (mainly fullerene) are trap free. It is shown that any materials with LUMO level above approximately 3.6 eV are expected to include electron-trapping, thereby inducing trap-assisted recombination.[92, 125]

1.2.4. OSC Challenges & Motivation

It is generally accepted that OSCs are currently facing a number of ‘grand challenges’ before achieving their practical use in society. Some examples include overcoming low efficiencies,[126-127] low operational lifetimes under ambient conditions,[84, 128] improvements of the manufacturing processing methods,[84] amongst others. More specific challenges associated with bulk heterojunction based solar cells can include the design new of materials with high efficiency, increased stability, resistance to unwanted environmental conditions, and compatible with the processing of large volumes, understanding/characterization of the photophysical mechanisms resulting in device failure, reduction energy loss during charge carrier photogeneration and collection, fine-tuning of bulk heterojunction morphology, and spectral sensitivity.[43, 47-48, 50, 84] To address some of these issues, this section outlines the challenges associated with (a) dielectric constant, (b) interfacial layer, and (c) low efficiencies associated with the occurrence of the S-shaped current density-voltage curve.

It is believed that the dielectric constant can have a profound effect on the efficiency of OSCs. Koster *et al.*[129] have argued that enhancing dielectric constant properties of the bulk heterojunction can lead to a reduction of the exciton binding energy, the singlet-triplet energy splitting, the reorganization energy, the Coulomb attraction within the CT exciton, the geminate recombination back to the CT state, the bimolecular and trap-assisted recombination and space-charge effects. It was proposed that if one changed the dielectric constant from a low constant of e.g. 3 to a higher constant of e.g. 10, an increase in efficiency of up to 21% can result. While this is theoretically based, the possibility of achieving this is an intuitively attractive proposition to explore. It is therefore surprising to find that little attention has been given to the pursuit of this concept. The major challenge here involves maintaining the delicate balance between many aspects, e.g. if one changes the chemical structure, the morphology will change as a result.

Modification of the interface between the bulk heterojunction and the electrodes has been one of the most important methods to improve in both efficiency and stability of solar cells. Numerous materials have been explored as the interfacial layer including metal, metal oxide, inorganic, organic, self-assembled monolayers, and salts.[130-132] One of the most widely used interfacial layers is PFN. It has been claimed that the interface modification by PFN can simultaneously enhance open-circuit potential, short-circuit current and fill factor altogether, thereby improving the efficiency of the devices.[133] However, an extensive review of the literature was revealed a number of discrepancies. For example, while it was claimed that PFN prevents Fermi level pinning at the interface,[133] another study showed that this is not true and pinning occurred, which concluded with the message that PFN did not introduce any significant changes to the device.[134] These results confirmed the need for the further investigation of the effect(s) of PFN on the performance of the solar cells. The challenge here is to investigate fundamental assumptions appearing within the literature and discrepancies/disagreements between accepted published articles.

S-shaped current density-voltage curve has been known for its devastating impact on the performance of the organic solar cells. Generally, the appearance of the S-curve phenomenon is related to the inefficient charge carrier extraction due to non-ideal morphological or interfacial issues. While several studies have been carried out on polymer-based BHJ solar cells, there are very few or no studies related to addressing the S-curve phenomenon in solution-processed small molecule (SM) BHJ devices. Given the fact that small molecules are an emerging alternative to polymer-based systems, it is important to examine solutions for resolving the S-curve characteristics in SM BHJ solar cells.

1.3. HYPOTHESES

The main goal of this thesis was to enhance dielectric constant of the BHJ solar cells. However, prior to investigating this hypothesis, two issues were encountered, which required examination before proceeding.

The first issue which took place at the early stage of this study was the use of PFN as the interfacial layer. It was noticed that the more efficient a solar cell device is, the better mechanistic results can be obtained. To achieve this, modification of the interface between the bulk heterojunction and the electrodes was considered. The most widely adopted material in use by far for the interfacial layer is PFN. Following a literature review in addition to ascertaining preliminary results, some questions were raised regarding the capability of PFN to modify the interface. This interestingly develops into a whole new study warranting investigation resulting in the first hypothesis:

"*Modification of the interface by means of a PFN electron transport layer can affect charge carrier generation, transportation, recombination and/or collection, and therefore affect the efficiency of BHJ solar cells*."

In order to improve power conversion efficiency in organic solar cells, one major influencing factor is their inherently low dielectric constant. According to the Clausius-Mossotti relationship, the dielectric constant of polymeric materials is determined by its polarization (a partial separation of charges due to the different electronegativity of atoms) and free volume (a spaced not occupied by polymeric materials). While polarization is an inherent characteristic of the material and therefore cannot be changed, it is possible to tune the free volume. This allows for the formulation of the second hypothesis, which is as follows:

"*Incorporation of materials with a higher dielectric constant than air set to occupy the free volume of the bulk can enhance the dielectric constant and consequently the efficiency of the bulk heterojunction solar cells*."

The second issue encountered was the appearance of the S-shaped current-voltage curve in high-performance solution-processed small molecule bulk heterojunction. The whole study of the dielectric constant of the small molecule was contingent upon solving the S-curve behavior. The S-curve phenomenon is generally the result of an energy barrier at the interface or within the bulk heterojunction, which gives rise to significant recombination of charge carriers and therefore reduction of efficiency. The rectification of S-curve phenomenon requires an additional treatment which varies depending on the BHJ system and source of the S-curve. Finding a solution for the phenomenon affected performance of the small molecule bulk heterojunction led therefore to the third hypothesis:

"*Alteration of the ratio between donor and acceptor may resolve the S-shaped current density-voltage curve in solution-processed small molecule bulk heterojunction solar cells*."

1.3.1. Research Questions

To evaluate the aforementioned hypotheses, the following research questions will be addressed within the working chapters:

1. PFN electron transport layer (Chapter 3)
    - Can a PFN interfacial layer modify the interface between the bulk heterojunction and the cathode electrodes?
    - What is the effect of PFN on the photovoltaic performance of OSC devices?
    - What is the effect of PFN film on the generation of charge carriers?
    - Can recombination of charge carriers be suppressed in the presence of a PFN interlayer?
    - Can mobility of charge carriers be enhanced by modification of interface by PFN?

2. Dielectric Constant (Chapters 4 & 5)

- Can the Clausius-Mossotti relation be applied to bulk heterojunction solar cells?
- What are the impacts of the incorporated materials on the performance of the device?
- Does the dielectric constant of devices differ before and after the introduction of these materials into the bulks?
- Does recombination and mobility of charge carriers change following doping of the bulk with these materials?

3. S-shaped current density-voltage curve (Chapter 6)

- What is the reason for the appearance of the S-shaped current density-voltage curve?
- What is the origin of the S-curve phenomenon?
- How can a normal diode-like curve be revived?
- What is the difference between a normal device and device showing S-curve in terms of charge carrier generation, collection or recombination?
- Does charge carrier mobility of the S-curve devices differ from the normal device?

1.3.2. Thesis Overview

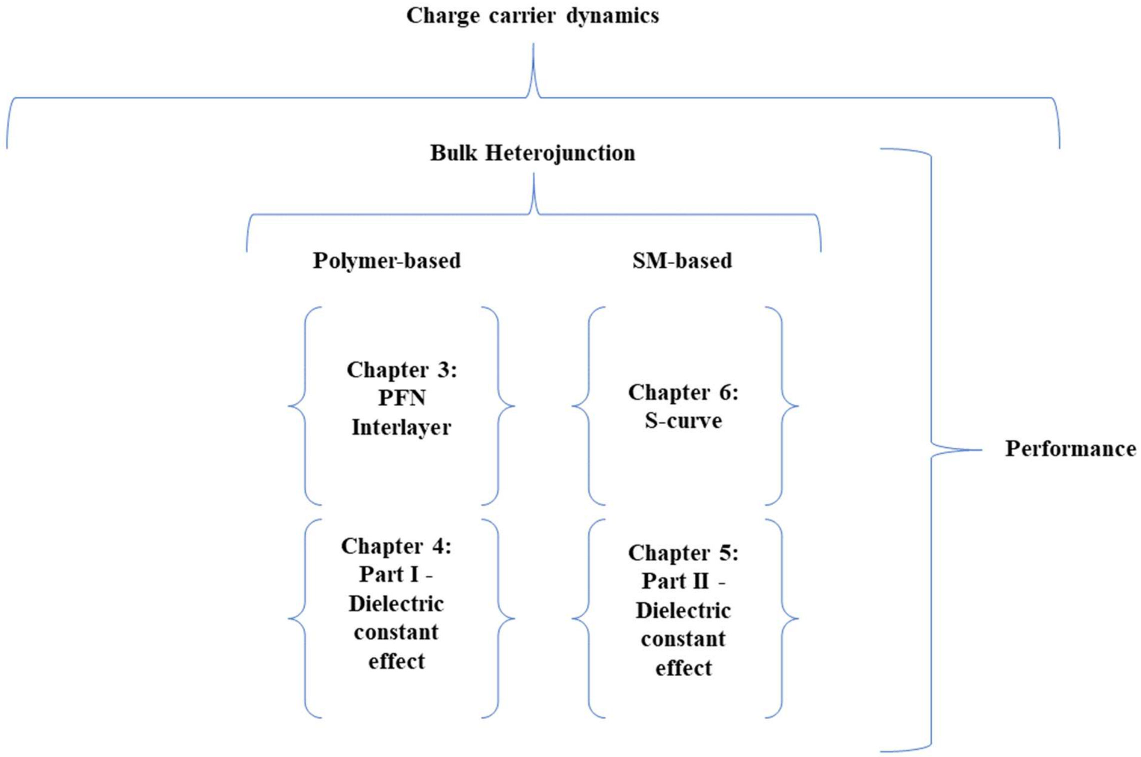

Figure 1.6. The overarching theme of the thesis.

Figure 1.6 illustrated the structure of this thesis. An overview of each chapter is as follow:

Chapter 1: This current chapter introduces the need for renewable energy sources and technologies that are helping to meet the need and their limitations. Following an overview of photovoltaic technologies, a survey of literature in relation to the principal operation of the organic solar cells as well as limitations are provided. Subsequently, hypotheses and associated research questions are presented.

Chapter 2: This chapter provides general information about fabrication processes of the organic solar cell. In addition, the details of steady-state and transient techniques employed to study solar cell devices are also outlined.

Chapter 3: This chapter responses to the questions regarding the use of PFN electron transport layer. The interface between the active layer and the cathode electrode is modified with a range of PFN films and photovoltaic parameters of the solar cell devices are investigated as a function of PFN films. Furthermore, the effect of the interlayer on the charge carrier dynamics of the devices is also studied.

Chapter 4: This chapter relates to the questions regarding dielectric constant. The focus of this study was to alter dielectric constant of the polymer-based bulk heterojunction. The addition of materials to bulk heterojunction and their impact on the dielectric constant and photovoltaic characteristics of the devices are demonstrated. In addition, charge carrier generation, recombination, and mobility of the devices are investigated with regard to the added materials.

Chapter 5: This chapter expands similar concept presented in chapter 4, except the focus of the study is solution-processed small molecule bulk heterojunction.

Chapter 6: In this chapter, the research questions related to the S-shaped current density-voltage curve are answered. Several parameters that could revive normal current density-voltage curve in solution-processed small molecule solar cells are probed and the origin of the S-curve is identified. The performance discrepancy between normal and S-curve devices is studied using steady-state techniques. A surface morphology study of the active layers is carried out. An equivalent circuit considering an energy barrier is discussed. The charge carrier recombination and mobility of normal and S-curve devices are compared. Some suggestions for further examination are suggested.

Chapter 7: The outcomes of each chapter are summarized and overall conclusion regarding research hypotheses are presented.

1.4. REFERENCES

1. *International Energy Outlook 2016*; U.S. Energy Information Administration: 2016.

2. *Bp Statistical Review of World Energy*; British Petroleum Oil Industry Company: 2017.

3. Mauritsen, T.; Pincus, R., Committed Warming Inferred from Observations. *Nature Clim. Change* **2017**, *advance online publication*.

4. Raftery, A. E.; Zimmer, A.; Frierson, D. M. W.; Startz, R.; Liu, P., Less Than 2[Thinsp][Deg]C Warming by 2100 Unlikely. *Nature Clim. Change* **2017**, *advance online publication*.

5. *Climate Change 2014 Synthesis Report Summary for Policymakers*; Intergovernmental Panel on Climate Change (IPCC): 2014.

6. Forzieri, G.; Cescatti, A.; e Silva, F. B.; Feyen, L., Increasing Risk over Time of Weather-Related Hazards to the European Population: A Data-Driven Prognostic Study. *The Lancet Planetary Health* **2017**, *1*, e200-e208.

7. Poumadère, M.; Mays, C.; Le Mer, S.; Blong, R., The 2003 Heat Wave in France: Dangerous Climate Change Here and Now. *Risk Analysis* **2005**, *25*, 1483-1494.

8. Desantis, L. R. G.; Bhotika, S.; Williams, K.; Putz, F. E., Sea-Level Rise and Drought Interactions Accelerate Forest Decline on the Gulf Coast of Florida, USA. *Global Change Biology* **2007**, *13*, 2349-2360.

9. Carnicer, J.; Coll, M.; Ninyerola, M.; Pons, X.; Sánchez, G.; Peñuelas, J., Widespread Crown Condition Decline, Food Web Disruption, and Amplified Tree Mortality with Increased Climate Change-Type Drought. *Proceedings of the National Academy of Sciences* **2011**, *108*, 1474-1478.

10. Moorhead, K. K.; Brinson, M. M., Response of Wetlands to Rising Sea Level in the Lower Coastal Plain of North Carolina. *Ecological Applications* **1995**, *5*, 261-271.

11. Frihy, O. E., The Nile Delta-Alexandria Coast: Vulnerability to Sea-Level Rise, Consequences and Adaptation. *Mitigation and Adaptation Strategies for Global Change* **2003**, *8*, 115-138.

12. Vine, E., Adaptation of California’s Electricity Sector to Climate Change. *Climatic Change* **2012**, *111*, 75-99.

13. D'Amato, G.; Cecchi, L., Effects of Climate Change on Environmental Factors in Respiratory Allergic Diseases. *Clinical & Experimental Allergy* **2008**, *38*, 1264-1274.

14. Rabl, A.; Spadaro, J. V., Public Health Impact of Air Pollution and Implications for the Energy System. *Annual Review of Energy and the Environment* **2000**, *25*, 601-627.

15. Haines, A.; Kovats, R. S.; Campbell-Lendrum, D.; Corvalan, C., Climate Change and Human Health: Impacts, Vulnerability and Public Health. *Public Health* **2006**, *120*, 585-596.

16. Eric Martinot; Akanksha Chaurey; Debra Lew; José Roberto Moreira; Wamukonya, N., Renewable Energy Markets in Developing Countries. *Annual Review of Energy and the Environment* **2002**, *27*, 309-348.

17. Yi, H., Clean Energy Policies and Green Jobs: An Evaluation of Green Jobs in U.S. Metropolitan Areas. *Energy Policy* **2013**, *56*, 644-652.

18. Branker, K.; Pathak, M. J. M.; Pearce, J. M., A Review of Solar Photovoltaic Levelized Cost of Electricity. *Renewable and Sustainable Energy Reviews* **2011**, *15*, 4470-4482.

19. Darling, S. B.; You, F., The Case for Organic Photovoltaics. *RSC Advances* **2013**, *3*, 17633-17648.

20. Mohtasham, J., Review Article-Renewable Energies. *Energy Procedia* **2015**, *74*, 1289-1297.

21. Ellabban, O.; Abu-Rub, H.; Blaabjerg, F., Renewable Energy Resources: Current Status, Future Prospects and Their Enabling Technology. *Renewable and Sustainable Energy Reviews* **2014**, *39*, 748-764.

22. Amponsah, N. Y.; Troldborg, M.; Kington, B.; Aalders, I.; Hough, R. L., Greenhouse Gas Emissions from Renewable Energy Sources: A Review of Lifecycle Considerations. *Renewable and Sustainable Energy Reviews* **2014**, *39*, 461-475.

23. Bargagli, R.; Cateni, D.; Nelli, L.; Olmastroni, S.; Zagarese, B., Environmental Impact of Trace Element Emissions from Geothermal Power Plants. *Archives of Environmental Contamination and Toxicology* **1997**, *33*, 172-181.

24. Zhang, J.; Kitazawa, D.; Taya, S.; Mizukami, Y., Impact Assessment of Marine Current Turbines on Fish Behavior Using an Experimental Approach Based on the Similarity Law. *Journal of Marine Science and Technology* **2017**, *22*, 219-230.

25. *Solar Energy Prospectives*; International Energy Agency: 2011.

26. Bakhiyi, B.; Labrèche, F.; Zayed, J., The Photovoltaic Industry on the Path to a Sustainable Future — Environmental and Occupational Health Issues. *Environment International* **2014**, *73*, 224-234.

27. Parida, B.; Iniyan, S.; Goic, R., A Review of Solar Photovoltaic Technologies. *Renewable and Sustainable Energy Reviews* **2011**, *15*, 1625-1636.

28. Gil, A.; Medrano, M.; Martorell, I.; Lázaro, A.; Dolado, P.; Zalba, B.; Cabeza, L. F., State of the Art on High Temperature Thermal Energy Storage for Power Generation. Part 1—Concepts, Materials and Modellization. *Renewable and Sustainable Energy Reviews* **2010**, *14*, 31-55.

29. Thirugnanasambandam, M.; Iniyan, S.; Goic, R., A Review of Solar Thermal Technologies. *Renewable and Sustainable Energy Reviews* **2010**, *14*, 312-322.

30. Gust, D.; Moore, T. A.; Moore, A. L., Solar Fuels Via Artificial Photosynthesis. *Accounts of Chemical Research* **2009**, *42*, 1890-1898.

31. *Renewables 2017 Global Status Report*; Renewable Energy Policy Network for the 21st Century: 2017.

32. Swanson, R. M., Photovoltaics Power Up. *Science* **2009**, *324*, 891-892.

33. Pearce, J. M., Photovoltaics — a Path to Sustainable Futures. *Futures* **2002**, *34*, 663-674.

34. Green, M. A.; Hishikawa, Y.; Warta, W.; Dunlop, E. D.; Levi, D. H.; Hohl-Ebinger, J.; Ho-Baillie, A. W. H., Solar Cell Efficiency Tables (Version 50). *Progress in Photovoltaics: Research and Applications* **2017**, *25*, 668-676.

35. Wurfel, P.; Wurfel, U., *Physics of Solar Cells: From Basic Principles to Advanced Concepts.*; John Wiley & Sons, 2009.

36. Lee, Y.; Park, C.; Balaji, N.; Lee, Y.-J.; Dao, V. A., High-Efficiency Silicon Solar Cells: A Review. *Israel Journal of Chemistry* **2015**, *55*, 1050-1063.

37. Louwen, A.; van Sark, W.; Schropp, R.; Faaij, A., A Cost Roadmap for Silicon Heterojunction Solar Cells. *Solar Energy Materials and Solar Cells* **2016**, *147*, 295-314.

38. Chopra, K. L.; Paulson, P. D.; Dutta, V., Thin-Film Solar Cells: An Overview. *Progress in Photovoltaics: Research and Applications* **2004**, *12*, 69-92.

39. Green, M. A., Thin-Film Solar Cells: Review of Materials, Technologies and Commercial Status. *Journal of Materials Science: Materials in Electronics* **2007**, *18*, 15-19.

40. Lee, T. D.; Ebong, A. In *Thin Film Solar Technologies: A Review*, 2015 12th International Conference on High-capacity Optical Networks and Enabling/Emerging Technologies (HONET), 21-23 Dec. 2015; 2015; pp 1-10.

41. Shah, A. V.; Schade, H.; Vanecek, M.; Meier, J.; Vallat-Sauvain, E.; Wyrsch, N.; Kroll, U.; Droz, C.; Bailat, J., Thin-Film Silicon Solar Cell Technology. *Progress in Photovoltaics: Research and Applications* **2004**, *12*, 113-142.

42. Yeh, N.; Yeh, P., Organic Solar Cells: Their Developments and Potentials. *Renewable and Sustainable Energy Reviews* **2013**, *21*, 421-431.

43. Li, G.; Zhu, R.; Yang, Y., Polymer Solar Cells. *Nat Photon* **2012**, *6*, 153-161.

44. Hagfeldt, A.; Boschloo, G.; Sun, L.; Kloo, L.; Pettersson, H., Dye-Sensitized Solar Cells. *Chemical Reviews* **2010**, *110*, 6595-6663.

45. Yang, S.; Fu, W.; Zhang, Z.; Chen, H.; Li, C.-Z., Recent Advances in Perovskite Solar Cells: Efficiency, Stability and Lead-Free Perovskite. *Journal of Materials Chemistry A* **2017**, *5*, 11462-11482.

46. Choi, H.; Nahm, C.; Kim, J.; Kim, C.; Kang, S.; Hwang, T.; Park, B., Review Paper: Toward Highly Efficient Quantum-Dot- and Dye-Sensitized Solar Cells. *Current Applied Physics* **2013**, *13*, S2-S13.

47. Carsten, D.; Vladimir, D., Polymer–Fullerene Bulk Heterojunction Solar Cells. *Reports on Progress in Physics* **2010**, *73*, 096401.

48. Nelson, J., Polymer:Fullerene Bulk Heterojunction Solar Cells. *Materials Today* **2011**, *14*, 462-470.

49. Lo, V.; Landrock, C.; Kaminska, B.; Maine, E. In *Manufacturing Cost Modeling for Flexible Organic Solar Cells*, 2012 Proceedings of PICMET '12: Technology Management for Emerging Technologies, July 29 2012-Aug. 2 2012; 2012; pp 2951-2956.

50. Chidichimo, G.; Filippelli, L., Organic Solar Cells: Problems and Perspectives. *International Journal of Photoenergy* **2010**, *2010*.

51. Pope, M.; Swenberg, C. E., *Electronic Processes in Organic Crystals and Polymers 2nd Edn*; New York: Oxford University Press, 1999.

52. Scharber, M. C.; Mühlbacher, D.; Koppe, M.; Denk, P.; Waldauf, C.; Heeger, A. J.; Brabec, C. J., Design Rules for Donors in Bulk-Heterojunction Solar Cells—Towards 10 % Energy-Conversion Efficiency. *Advanced Materials* **2006**, *18*, 789-794.

53. Risko, C.; McGehee, M. D.; Bredas, J.-L., A Quantum-Chemical Perspective into Low Optical-Gap Polymers for Highly-Efficient Organic Solar Cells. *Chemical Science* **2011**, *2*, 1200-1218.

54. Ohkita, H., et al., Charge Carrier Formation in Polythiophene/Fullerene Blend Films Studied by Transient Absorption Spectroscopy. *Journal of the American Chemical Society* **2008**, *130*, 3030-3042.

55. Yu, G.; Gao, J.; Hummelen, J. C.; Wudl, F.; Heeger, A. J., Polymer Photovoltaic Cells: Enhanced Efficiencies Via a Network of Internal Donor-Acceptor Heterojunctions. *Science* **1995**, *270*, 1789-1791.

56. Huang, Y.; Kramer, E. J.; Heeger, A. J.; Bazan, G. C., Bulk Heterojunction Solar Cells: Morphology and Performance Relationships. *Chemical Reviews* **2014**, *114*, 7006-7043.

57. Kang, H.; Kim, G.; Kim, J.; Kwon, S.; Kim, H.; Lee, K., Bulk-Heterojunction Organic Solar Cells: Five Core Technologies for Their Commercialization. *Advanced Materials* **2016**, *28*, 7821-7861.

58. Pelzer, K. M.; Darling, S. B., Charge Generation in Organic Photovoltaics: A Review of Theory and Computation. *Molecular Systems Design & Engineering* **2016**, *1*, 10-24.

59. Clarke, T. M.; Durrant, J. R., Charge Photogeneration in Organic Solar Cells. *Chemical Reviews* **2010**, *110*, 6736-6767.

60. Muntwiler, M.; Yang, Q.; Tisdale, W. A.; Zhu, X. Y., Coulomb Barrier for Charge Separation at an Organic Semiconductor Interface. *Physical Review Letters* **2008**, *101*, 196403.

61. Lüer, L.; Egelhaaf, H. J.; Oelkrug, D.; Cerullo, G.; Lanzani, G.; Huisman, B. H.; de Leeuw, D., Oxygen-Induced Quenching of Photoexcited States in Polythiophene Films. *Organic Electronics* **2004**, *5*, 83-89.

62. Stübinger, T.; Brütting, W., Exciton Diffusion and Optical Interference in Organic Donor–Acceptor Photovoltaic Cells. *Journal of Applied Physics* **2001**, *90*, 3632-3641.

63. Jespersen, K. G.; Zhang, F.; Gadisa, A.; Sundström, V.; Yartsev, A.; Inganäs, O., Charge Formation and Transport in Bulk-Heterojunction Solar Cells Based on Alternating Polyfluorene Copolymers Blended with Fullerenes. *Organic Electronics* **2006**, *7*, 235-242.

64. Bakulin, A. A.; Hummelen, J. C.; Pshenichnikov, M. S.; van Loosdrecht, P. H. M., Ultrafast Hole-Transfer Dynamics in Polymer/Pcbm Bulk Heterojunctions. *Advanced Functional Materials* **2010**, *20*, 1653-1660.

65. Brabec, C. J.; Zerza, G.; Cerullo, G.; De Silvestri, S.; Luzzati, S.; Hummelen, J. C.; Sariciftci, S., Tracing Photoinduced Electron Transfer Process in Conjugated Polymer/Fullerene Bulk Heterojunctions in Real Time. *Chemical Physics Letters* **2001**, *340*, 232-236.

66. Hwang, I. W.; Soci, C.; Moses, D.; Zhu, Z.; Waller, D.; Gaudiana, R.; Brabec, C. J.; Heeger, A. J., Ultrafast Electron Transfer and Decay Dynamics in a Small Band Gap Bulk Heterojunction Material. *Advanced Materials* **2007**, *19*, 2307-2312.

67. Vandewal, K.; Ma, Z.; Bergqvist, J.; Tang, Z.; Wang, E.; Henriksson, P.; Tvingstedt, K.; Andersson, M. R.; Zhang, F.; Inganäs, O., Quantification of Quantum Efficiency and Energy Losses in Low Bandgap Polymer:Fullerene Solar Cells with High Open-Circuit Voltage. *Advanced Functional Materials* **2012**, *22*, 3480-3490.

68. Gong, X.; Tong, M.; Brunetti, F. G.; Seo, J.; Sun, Y.; Moses, D.; Wudl, F.; Heeger, A. J., Bulk Heterojunction Solar Cells with Large Open-Circuit Voltage: Electron Transfer with Small Donor-Acceptor Energy Offset. *Advanced Materials* **2011**, *23*, 2272-2277.

69. Liu, A.; Zhao, S.; Rim, S. B.; Wu, J.; Könemann, M.; Erk, P.; Peumans, P., Control of Electric Field Strength and Orientation at the Donor–Acceptor Interface in Organic Solar Cells. *Advanced Materials* **2008**, *20*, 1065-1070.

70. Groves, C., Suppression of Geminate Charge Recombination in Organic Photovoltaic Devices with a Cascaded Energy Heterojunction. *Energy & Environmental Science* **2013**, *6*, 1546-1551.

71. Gregg, B. A., Charged Defects in Soft Semiconductors and Their Influence on Organic Photovoltaics. *Soft Matter* **2009**, *5*, 2985-2989.

72. Gregg, B. A., Entropy of Charge Separation in Organic Photovoltaic Cells: The Benefit of Higher Dimensionality. *The Journal of Physical Chemistry Letters* **2011**, *2*, 3013-3015.

73. Brédas, J.-L.; Norton, J. E.; Cornil, J.; Coropceanu, V., Molecular Understanding of Organic Solar Cells: The Challenges. *Accounts of Chemical Research* **2009**, *42*, 1691-1699.

74. Bakulin, A. A.; Rao, A.; Pavelyev, V. G.; van Loosdrecht, P. H. M.; Pshenichnikov, M. S.; Niedzialek, D.; Cornil, J.; Beljonne, D.; Friend, R. H., The Role of Driving Energy and Delocalized States for Charge Separation in Organic Semiconductors. *Science* **2012**, *335*, 1340-1344.

75. Clarke, T. M.; Ballantyne, A. M.; Nelson, J.; Bradley, D. D. C.; Durrant, J. R., Free Energy Control of Charge Photogeneration in Polythiophene/Fullerene Solar Cells: The Influence of Thermal Annealing on P3ht/Pcbm Blends. *Advanced Functional Materials* **2008**, *18*, 4029-4035.

76. Gélinas, S.; Paré-Labrosse, O.; Brosseau, C.-N.; Albert-Seifried, S.; McNeill, C. R.; Kirov, K. R.; Howard, I. A.; Leonelli, R.; Friend, R. H.; Silva, C., The Binding Energy of Charge-Transfer Excitons Localized at Polymeric Semiconductor Heterojunctions. *The Journal of Physical Chemistry C* **2011**, *115*, 7114-7119.

77. Zhu, X. Y.; Yang, Q.; Muntwiler, M., Charge-Transfer Excitons at Organic Semiconductor Surfaces and Interfaces. *Accounts of Chemical Research* **2009**, *42*, 1779-1787.

78. Grancini, G.; Maiuri, M.; Fazzi, D.; Petrozza, A.; Egelhaaf, H. J.; Brida, D.; Cerullo, G.; Lanzani, G., Hot Exciton Dissociation in Polymer Solar Cells. *Nat Mater* **2013**, *12*, 29-33.

79. Jailaubekov, A. E., et al., Hot Charge-Transfer Excitons Set the Time Limit for Charge Separation at Donor/Acceptor Interfaces in Organic Photovoltaics. *Nat Mater* **2013**, *12*, 66-73.

80. Dimitrov, S. D.; Bakulin, A. A.; Nielsen, C. B.; Schroeder, B. C.; Du, J.; Bronstein, H.; McCulloch, I.; Friend, R. H.; Durrant, J. R., On the Energetic Dependence of Charge

Separation in Low-Band-Gap Polymer/Fullerene Blends. *Journal of the American Chemical Society* **2012**, *134*, 18189-18192.

81. Zhou, Y.; Tvingstedt, K.; Zhang, F.; Du, C.; Ni, W. X.; Andersson, M. R.; Inganäs, O., Observation of a Charge Transfer State in Low-Bandgap Polymer/Fullerene Blend Systems by Photoluminescence and Electroluminescence Studies. *Advanced Functional Materials* **2009**, *19*, 3293-3299.

82. Lee, J.; Vandewal, K.; Yost, S. R.; Bahlke, M. E.; Goris, L.; Baldo, M. A.; Manca, J. V.; Voorhis, T. V., Charge Transfer State Versus Hot Exciton Dissociation in Polymer–Fullerene Blended Solar Cells. *Journal of the American Chemical Society* **2010**, *132*, 11878-11880.

83. Hofstad, T. G. J. v. d.; Nuzzo, D. D.; Berg, M. v. d.; Janssen, R. A. J.; Meskers, S. C. J., Influence of Photon Excess Energy on Charge Carrier Dynamics in a Polymer-Fullerene Solar Cell. *Advanced Energy Materials* **2012**, *2*, 1095-1099.

84. *Organic Solar Cells Fundamentals, Devices, and Upscaling*; Taylor & Francis Group, 2014

85. Walker, B.; Tamayo, A. B.; Dang, X. D.; Zalar, P.; Seo, J. H.; Garcia, A.; Tantiwiwat, M.; Nguyen, T. Q., Nanoscale Phase Separation and High Photovoltaic Efficiency in Solution-Processed, Small-Molecule Bulk Heterojunction Solar Cells. *Advanced Functional Materials* **2009**, *19*, 3063-3069.

86. Guo, X.; Zhang, M.; Tan, J.; Zhang, S.; Huo, L.; Hu, W.; Li, Y.; Hou, J., Influence of D/a Ratio on Photovoltaic Performance of a Highly Efficient Polymer Solar Cell System. *Advanced Materials* **2012**, *24*, 6536-6541.

87. Ebenhoch, B.; Thomson, S. A. J.; Genevičius, K.; Juška, G.; Samuel, I. D. W., Charge Carrier Mobility of the Organic Photovoltaic Materials Ptb7 and Pc71bm and Its Influence on Device Performance. *Organic Electronics* **2015**, *22*, 62-68.

88. Mozer, A. J.; Sariciftci, N. S.; Lutsen, L.; Vanderzande, D.; Österbacka, R.; Westerling, M.; Juška, G., Charge Transport and Recombination in Bulk Heterojunction Solar Cells Studied by the Photoinduced Charge Extraction in Linearly Increasing Voltage Technique. *Applied Physics Letters* **2005**, *86*, 112104.

89. Mozer, A. J.; Dennler, G.; Sariciftci, N. S.; Westerling, M.; Pivrikas, A.; Österbacka, R.; Juška, G., Time-Dependent Mobility and Recombination of the Photoinduced Charge Carriers in Conjugated Polymer/Fullerene Bulk Heterojunction Solar Cells. *Physical Review B* **2005**, *72*, 035217.

90. Mozer, A. J.; Sariciftci, N. S.; Pivrikas, A.; Österbacka, R.; Juška, G.; Brassat, L.; Bässler, H., Charge Carrier Mobility in Regioregular Poly(3-Hexylthiophene) Probed by Transient Conductivity Techniques: A Comparative Study. *Physical Review B* **2005**, *71*, 035214.

91. Mendil, N.; Daoudi, M.; Berkai, Z.; Belghachi, A., Disorder Effect on Carrier Mobility in Fullerene Organic Semiconductor. *Journal of Physics: Conference Series* **2015**, *647*, 012057.

92. Proctor, C. M.; Kuik, M.; Nguyen, T.-Q., Charge Carrier Recombination in Organic Solar Cells. *Progress in Polymer Science* **2013**, *38*, 1941-1960.

93. Mandoc, M. M.; Koster, L. J. A.; Blom, P. W. M., Optimum Charge Carrier Mobility in Organic Solar Cells. *Applied Physics Letters* **2007**, *90*, 133504.

94. Baumann, A.; Lorrmann, J.; Rauh, D.; Deibel, C.; Dyakonov, V., A New Approach for Probing the Mobility and Lifetime of Photogenerated Charge Carriers in Organic Solar Cells under Real Operating Conditions. *Advanced Materials* **2012**, *24*, 4381-4386.

95. Deibel, C.; Wagenpfahl, A.; Dyakonov, V., Influence of Charge Carrier Mobility on the Performance of Organic Solar Cells. *physica status solidi (RRL) – Rapid Research Letters* **2008**, *2*, 175-177.

96. Cowan, S. R.; Street, R. A.; Cho, S.; Heeger, A. J., Transient Photoconductivity in Polymer Bulk Heterojunction Solar Cells: Competition between Sweep-out and Recombination. *Physical Review B* **2011**, *83*, 035205.

97. Kniepert, J.; Schubert, M.; Blakesley, J. C.; Neher, D., Photogeneration and Recombination in P3ht/Pcbm Solar Cells Probed by Time-Delayed Collection Field Experiments. *The Journal of Physical Chemistry Letters* **2011**, *2*, 700-705.

98. Barker, J. A.; Ramsdale, C. M.; Greenham, N. C., Modeling the Current-Voltage Characteristics of Bilayer Polymer Photovoltaic Devices. *Physical Review B* **2003**, *67*, 075205.

99. Mihailetchi, V. D.; Koster, L. J. A.; Hummelen, J. C.; Blom, P. W. M., Photocurrent Generation in Polymer-Fullerene Bulk Heterojunctions. *Physical Review Letters* **2004**, *93*, 216601.

100. Lloyd, M. T.; Peters, C. H.; Garcia, A.; Kauvar, I. V.; Berry, J. J.; Reese, M. O.; McGehee, M. D.; Ginley, D. S.; Olson, D. C., Influence of the Hole-Transport Layer on the Initial Behavior and Lifetime of Inverted Organic Photovoltaics. *Solar Energy Materials and Solar Cells* **2011**, *95*, 1382-1388.

101. Mihailetchi, V. D.; Wildeman, J.; Blom, P. W. M., Space-Charge Limited Photocurrent. *Physical Review Letters* **2005**, *94*, 126602.

102. Kumar, A.; Sista, S.; Yang, Y., Dipole Induced Anomalous S-Shape I-V Curves in Polymer Solar Cells. *Journal of Applied Physics* **2009**, *105*, 094512.

103. Nelson, J.; Kirkpatrick, J.; Ravirajan, P., Factors Limiting the Efficiency of Molecular Photovoltaic Devices. *Physical Review B* **2004**, *69*, 035337.

104. Wagenpfahl, A.; Deibel, C.; Dyakonov, V., Organic Solar Cell Efficiencies under the Aspect of Reduced Surface Recombination Velocities. *IEEE Journal of Selected Topics in Quantum Electronics* **2010**, *16*, 1759-1763.

105. Albrecht, S.; Schindler, W.; Kurpiers, J.; Kniepert, J.; Blakesley, J. C.; Dumsch, I.; Allard, S.; Fostiropoulos, K.; Scherf, U.; Neher, D., On the Field Dependence of Free Charge Carrier Generation and Recombination in Blends of Pcpdtbt/Pc70bm: Influence of Solvent Additives. *The Journal of Physical Chemistry Letters* **2012**, *3*, 640-645.

106. Credgington, D.; Jamieson, F. C.; Walker, B.; Nguyen, T. Q.; Durrant, J. R., Quantification of Geminate and Non-Geminate Recombination Losses within a Solution-Processed Small-Molecule Bulk Heterojunction Solar Cell. *Advanced Materials* **2012**, *24*, 2135-2141.

107. Dibb, G. F. A.; Jamieson, F. C.; Maurano, A.; Nelson, J.; Durrant, J. R., Limits on the Fill Factor in Organic Photovoltaics: Distinguishing Nongeminate and Geminate Recombination Mechanisms. *The Journal of Physical Chemistry Letters* **2013**, *4*, 803-808.

108. Koster, L. J. A.; Kemerink, M.; Wienk, M. M.; Maturová, K.; Janssen, R. A. J., Quantifying Bimolecular Recombination Losses in Organic Bulk Heterojunction Solar Cells. *Advanced Materials* **2011**, *23*, 1670-1674.

109. Mauer, R.; Howard, I. A.; Laquai, F., Effect of External Bias on Nongeminate Recombination in Polythiophene/Methanofullerene Organic Solar Cells. *The Journal of Physical Chemistry Letters* **2011**, *2*, 1736-1741.

110. Juška, G.; Genevičius, K.; Nekrašas, N.; Sliaužys, G.; Dennler, G., Trimolecular Recombination in Polythiophene: Fullerene Bulk Heterojunction Solar Cells. *Applied Physics Letters* **2008**, *93*, 143303.

111. Shuttle, C. G.; O'Regan, B.; Ballantyne, A. M.; Nelson, J.; Bradley, D. D. C.; Mello, J. d.; Durrant, J. R., Experimental Determination of the Rate Law for Charge Carrier Decay in a Polythiophene: Fullerene Solar Cell. *Applied Physics Letters* **2008**, *92*, 093311.

112. Deibel, C.; Baumann, A.; Dyakonov, V., Polaron Recombination in Pristine and Annealed Bulk Heterojunction Solar Cells. *Applied Physics Letters* **2008**, *93*, 163303.

113. Blakesley, J. C.; Neher, D., Relationship between Energetic Disorder and Open-Circuit Voltage in Bulk Heterojunction Organic Solar Cells. *Physical Review B* **2011**, *84*, 075210.

114. Credgington, D.; Durrant, J. R., Insights from Transient Optoelectronic Analyses on the Open-Circuit Voltage of Organic Solar Cells. *The Journal of Physical Chemistry Letters* **2012**, *3*, 1465-1478.

115. Deibel, C.; Wagenpfahl, A.; Dyakonov, V., Influence of Charge Carrier Mobility on the Performance of Organic Solar Cells. *physica status solidi (RRL) - Rapid Research Letters* **2008**, *2*, 175-177.

116. Pivrikas, A.; Sariciftci, N. S.; Juška, G.; Österbacka, R., A Review of Charge Transport and Recombination in Polymer/Fullerene Organic Solar Cells. *Progress in Photovoltaics: Research and Applications* **2007**, *15*, 677-696.

117. Albrecht, S., et al., Fluorinated Copolymer Pcpdtbt with Enhanced Open-Circuit Voltage and Reduced Recombination for Highly Efficient Polymer Solar Cells. *Journal of the American Chemical Society* **2012**, *134*, 14932-14944.

118. Mauer, R.; Howard, I. A.; Laquai, F., Effect of Nongeminate Recombination on Fill Factor in Polythiophene/Methanofullerene Organic Solar Cells. *The Journal of Physical Chemistry Letters* **2010**, *1*, 3500-3505.

119. Proctor, C. M.; Kim, C.; Neher, D.; Nguyen, T. Q., Nongeminate Recombination and Charge Transport Limitations in Diketopyrrolopyrrole-Based Solution-Processed Small Molecule Solar Cells. *Advanced Functional Materials* **2013**, *23*, 3584-3594.

120. Koster, L. J. A.; Mihailetchi, V. D.; Blom, P. W. M., Bimolecular Recombination in Polymer/Fullerene Bulk Heterojunction Solar Cells. *Applied Physics Letters* **2006**, *88*, 052104.

121. Cowan, S. R.; Roy, A.; Heeger, A. J., Recombination in Polymer-Fullerene Bulk Heterojunction Solar Cells. *Physical Review B* **2010**, *82*, 245207.

122. Wetzelaer, G. A. H.; Kuik, M.; Lenes, M.; Blom, P. W. M., Origin of the Dark-Current Ideality Factor in Polymer:Fullerene Bulk Heterojunction Solar Cells. *Applied Physics Letters* **2011**, *99*, 153506.

123. Wetzelaer, G. J. A. H.; Kuik, M.; Blom, P. W. M., Identifying the Nature of Charge Recombination in Organic Solar Cells from Charge-Transfer State Electroluminescence. *Advanced Energy Materials* **2012**, *2*, 1232-1237.

124. Street, R. A.; Krakaris, A.; Cowan, S. R., Recombination through Different Types of Localized States in Organic Solar Cells. *Advanced Functional Materials* **2012**, *22*, 4608-4619.

125. Lenes, M.; Shelton, S. W.; Sieval, A. B.; Kronholm, D. F.; Hummelen, J. C.; Blom, P. W. M., Electron Trapping in Higher Adduct Fullerene-Based Solar Cells. *Advanced Functional Materials* **2009**, *19*, 3002-3007.

126. Scharber, M. C., On the Efficiency Limit of Conjugated Polymer:Fullerene-Based Bulk Heterojunction Solar Cells. *Advanced Materials* **2016**, *28*, 1994-2001.

127. Scharber, M. C.; Sariciftci, N. S., Efficiency of Bulk-Heterojunction Organic Solar Cells. *Progress in Polymer Science* **2013**, *38*, 1929-1940.

128. Cheng, P.; Zhan, X., Stability of Organic Solar Cells: Challenges and Strategies. *Chemical Society Reviews* **2016**, *45*, 2544-2582.

129. Koster, L. J. A.; Shaheen, S. E.; Hummelen, J. C., Pathways to a New Efficiency Regime for Organic Solar Cells. *Advanced Energy Materials* **2012**, *2*, 1246-1253.

130. Yip, H.-L.; Jen, A. K. Y., Recent Advances in Solution-Processed Interfacial Materials for Efficient and Stable Polymer Solar Cells. *Energy & Environmental Science* **2012**, *5*, 5994-6011.

131. Steim, R.; Kogler, F. R.; Brabec, C. J., Interface Materials for Organic Solar Cells. *Journal of Materials Chemistry* **2010**, *20*, 2499-2512.

132. Yin, Z.; Wei, J.; Zheng, Q., Interfacial Materials for Organic Solar Cells: Recent Advances and Perspectives. *Advanced Science* **2016**, *3*.

133. He, Z.; Zhong, C.; Huang, X.; Wong, W. Y.; Wu, H.; Chen, L.; Su, S.; Cao, Y., Simultaneous Enhancement of Open-Circuit Voltage, Short-Circuit Current Density, and Fill Factor in Polymer Solar Cells. *Advanced Materials* **2011**, *23*, 4636-4643.

134. Hu, Z.; Zhong, Z.; Chen, Y.; Sun, C.; Huang, F.; Peng, J.; Wang, J.; Cao, Y., Energy-Level Alignment at the Organic/Electrode Interface in Organic Optoelectronic Devices. *Advanced Functional Materials* **2015**, *26*, 129-136.

Chapter 2: General Experiments

2.1. MATERIALS AND SOLVENTS

PCDTBT (Poly[N-9′-heptadecanyl-2,7-carbazole-alt-5,5-(4′,7′-di-2-thienyl-2′,1′,3′-benzothiadiazole)]) (purity of > 99.5%, Solaris Chem. Inc.), $PC_{70}BM$ ([6,6]-Phenyl C71 butyric acid methyl ester) (purity of > 99.5%, Solaris Chem. Inc.), PFN (Poly[(9,9-bis(3'-(N,N-dimethylamino)propyl)-2,7-fluorene)-alt-2,7-(9,9–dioctylfluorene)) (Solaris Chem. Inc.), p-DTS$(FBTTh_2)_2$ (7,7′-(4,4-bis(2-ethylhexyl)-4H-silolo[3,2-b:4,5-b′]dithiophene-2,6-diyl)bis(6-fluoro-4-(5′-hexyl-[2,2′-bithiophen]-5-yl) benzo[c][1,2,5]thiadiazole)) (purity of > 99%, 1-Material), Rhodamine 101 (Sigma-Aldrich), $PC_{60}BM$ ([6,6]-Phenyl C61 butyric acid methyl ester) (purity of > 99.5%, Solaris Chem. Inc.) were purchased commercially and used without further purification.

Chlorobenzene (CB) (anhydrous, purity of > 99.9%, Sigma-Aldrich), 1,8-diiodooctane (DIO) (Sigma-Aldrich), Methanol (purity of > 99.9%, Sigma-Aldrich), 1,2-dichlorobenzene (o-DCB) (anhydrous, purity of > 99.9%, Sigma-Aldrich), isopropyl alcohol (IPA) (Sigma-Aldrich) Acetic Acid (purity of > 99.5%, Sigma-Aldrich), dimethyl sulfoxide (DMSO) (anhydrous, purity of > 99.9%, Sigma-Aldrich) and N,N-Dimethylformamide (DMF) (purity of > 99.9%, Sigma-Aldrich) were commercially available and used as received. Poly(3,4-ethylenedioxythiophene)-poly(styrenesulfonate) solution (PEDOT:PSS) (Clevios^{TM} P VP AI 4083) was supplied by "Heraeus Deutschland GmbH & Co." and kept in the dark and under ambient temperature and pressure.

Pre-patterned indium tin oxide (ITO) coated glasses ($R_s \leq 15\ \Omega\ sq^{-1}$) were purchased from "Xin Yan Technology LTD". Aluminum with high purity was bought from "AVT Services".

2.2. SOLAR CELL DEVICES FABRICATION

2.2.1. Architecture of the Solar Cell Devices

An organic bulk heterojunction solar cell comprises a multilayer structure which is sandwiched between two metal electrodes of two different work functions. The multilayer structure includes a hole transport layer (HTL), photoactive layer and an electron transport layer (ETL). Different techniques could be used to deposit each layer, depending on the size of the substrate and the amount of materials, such as spin coating, spray coating, doctor blading, screen printing, inject printing etc.[1] It should be noted that there are two architectures for bulk heterojunction solar cells: conventional and inverted. In the conventional geometry, the anode electrode is ITO and cathode is a low work function metal (aluminum). Conversely, in the inverted architecture, the ITO electrode is modified to be used as an anode and a high work function metal (gold or silver) is deposited as a cathode electrode.

A conventional architecture was chosen for studying the solar cell devices throughout this thesis. The general structure of the devices is glass/indium tin oxide (ITO)/HTL/ active layer (bulk heterojunction)/ETL/cathode electrode. The general procedure of solar cell fabrication is provided in this chapter and fabrication details of each set of solar cell devices are mentioned in the associated chapters.

2.2.2. Active Layer Solution

Active layer solutions were prepared inside a glovebox (Innovative Technology) with monitored oxygen (≤ 5 ppm) and humidity (≤ 1 ppm) levels. An exact amount of donor materials and acceptor materials (based on the ratio) were measured by a scale separately and added to a bottle. Then, one milliliter (ml) of an appropriate solvent was poured into the bottle. Finally, the solution was stirred and heated during the night for several hours. The temperature of the hotplate (IKA RCT basic) was controlled by a thermocouple.

2.2.3. ITO Substrate Cleaning

The first step of cleaning procedure was to remove the presence of any dust and dirt on the substrates. The substrates were loaded into a beaker filled with deionized (DI) water and the beaker was placed into a sonicator for 20 minutes sonication. Thereafter, the substrates were thoroughly dried with nitrogen gas to remove remaining DI water. To further clean the substrates and to remove any organic residual, the substrates were sonicated in acetone and IPA each for 20 minutes successively whereas the substrates were dried by the nitrogen gas between each step. Eventually, in order to prepare the ITO surface for deposition of PEDOT:PSS film, the substrates were treated by a “Novascan” UV ozone cleaner for another 20 min. In Figure 2.1(top left), an ITO substrate after the cleaning process is shown.

2.2.4. Hole Transport Layer - PEDOT:PSS Film

The PEDOT:PSS solution was filtered through a 0.45 µm syringe filter (Sigma-Aldrich) prior to spin casting. A 40 µl of PEDOT:PSS solution was deposited by a pipette on top of the substrate and spun cast at 5000 rpm for 40 s. The thickness of PEDOT:PSS film was measured by a surface profiler (Veeco, Dektak 150) and found to be approximately 30-40 nm. The quality of the PEDOT:PSS film was inspected visually and any substrate with defects on the film was discarded from further processing. The last step before active solution casting was to anneal the PEDOT:PSS film for 10 min at 140 C°, in order to remove residual water from the film.

2.2.5. Bulk Heterojunction Active Layer

A spin casting technique was employed in this thesis to make bulk heterojunction (BHJ) films from the active layer solution. The thickness of the BHJ film was controlled by several parameters in the spin casting process e.g. active layer solution concentration (viscosity) and temperature, spin speed and acceleration and spinning time. The substrate was held onto a digitally-controlled spinner by vacuum. In order to accelerate evaporation of the solvent and obtain a homogeneous film, the active layer solution temperature was set at 60-70 ˚C prior to casting. The active layer solution was dropped then onto the substrate by a pipette (30-40 µl) and the substrate was spun at a determined spin and acceleration for a given time. Duration of the spinning was different based on the solvent e.g. for CB was less than 1 minutes, whereas it was more than 1 min for o-DCB. A dried film with a given thickness was attained. The final thickness of BHJ film was measured by stylus surface profiler (Veeco, Dektak 150). Figure 2.1 (top right) shows an ITO substrate fully covered by the active layer film. Finally, the active layer film on top of the cathode strip was wiped clean by a cotton bud dipped in toluene.

2.2.6. Thermal Evaporation of Cathode Electrode

The completion of the solar cell device structure was achieved by thermal evaporation (AVT Services thermal evaporator) of 100 nm of aluminum (Al) as the cathode electrode. The substrates were placed face down in an evaporation shadow mask and were kept in place by Kapton tape (Ted Pella Inc.). The evaporation shadow mask was then adhered upside-down to a plate by Kapton tape. The plate was positioned above clamps that hold a tungsten filament (Ted Pell Inc.) and rotating at a constant speed throughout the evaporation. A high purity of cathode material (aluminum wire) was cut into small pieces and hung onto the filament. After that, the ambient pressure was gradually decreased to the 10^{-6} bar. Then, a high-voltage radiofrequency current was applied to the filament, causing temperature elevation enough to vaporize the aluminum pieces. The evaporation rate was held at 0.1 $\overset{\circ}{A}$/s and monitored through a quartz crystal microbalance (QCM). The solar cell device area after deposition of cathode electrode was 0.06 cm^2.

2.2.7. Encapsulation

Encapsulation is an important step in the fabrication of organic solar cells and is required to protect them from moisture and oxygen and to increase their lifetime under ambient conditions. To encapsulate the solar cell devices, a piece of glass cut into a proper size and a UV curable encapsulation epoxy (Ossilla Ltd.) were employed to encapsulate the devices. A single drop of UV curable epoxy was dropped onto the middle of the cathode and the glass piece was placed on top of it. After thorough spreading of resin underneath the glass, a UV gun was used to cure the epoxy over the course of 60 s. The encapsulation process was performed inside the glovebox.

2.2.8. Soldering onto ITO

Any residual of active layer materials that remained on the ITO parts of the substrates was thoroughly removed by toluene and acetone. A thin layer of soldering (MBR Cerasolzer) was deposited by an ultrasonic soldering on top of the ITO stripes. A complete solar cell device was shown in Figure 2.1 (bottom left and bottom right).

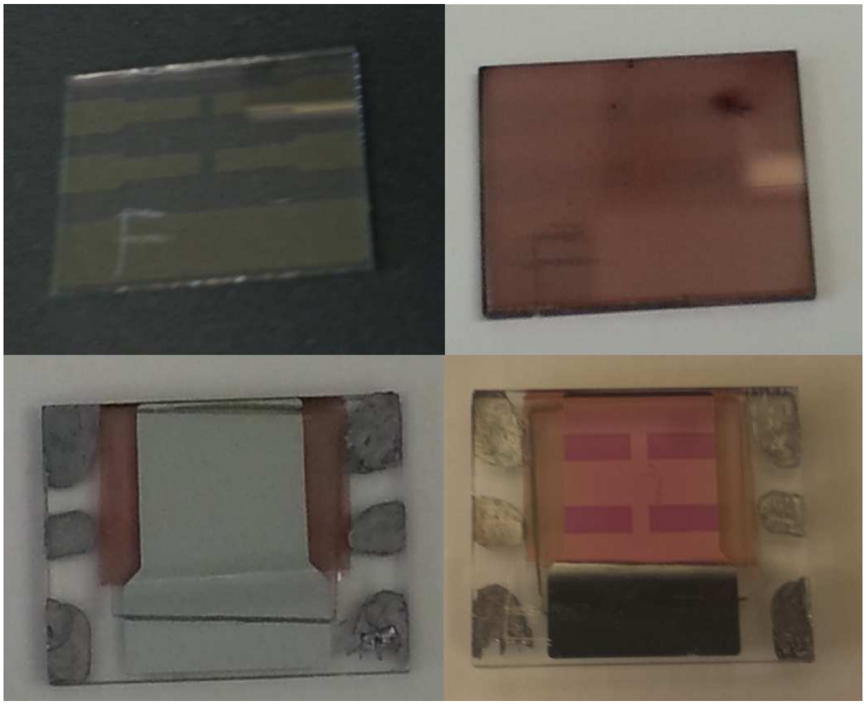

Figure 2.1. Photos of (Top left) an ITO substrate. The yellow strips are ITO parts. (top right) the ITO substrate after spin casting of active layer materials. (bottom left) A complete solar cell device from cathode electrode side. The excess active layer film on sides and bottom was wiped out. (bottom right) A complete solar cell device from ITO side.

2.3. CHARACTERIZATION TECHNIQUES

2.3.1. UV-Visible Spectroscopy

UV-Vis absorption spectra of the BHJ films were obtained in the wavelength range of 300 to 800 nm. Absorption of BHJ film was recorded on a Shimadzu UV-3600 spectrophotometer connected to a PC running UV probe software. The films were cast on a microscope glass slide for absorption measurement. The baseline was corrected for glass absorption and single point absorption at 800 nm.

2.3.2. Current-Voltage Characterization

The most prevalent technique to measure the performance of a solar cell is current-voltage (I-V) measurement. The measurement is based on sweeping a range of potential across the solar cell and record the current response of the device, while the solar cell is illuminated. The intensity of the lamp for routine measurement (1 sun) is 100 $mW\ cm^{-2}$. Figure 2.1 represents current-voltage characteristics of a typical solar cell under operational conditions. Power conversion efficiency (PCE) is the primary parameter obtained from the current-voltage measurement. PCE indicates the overall efficiency of a solar cell and is calculated by dividing electrical power output (P_{out}) of solar cell device by incident light power (P_{in}) multiplied by 100. The formula of PCE is as follow [2]:

$$\text{PCE}\ (\%) = \frac{\text{P}_{\text{out}}}{\text{P}_{\text{in}}} \times 100 \qquad (2\text{-}1)$$

The short-circuit current (I_{sc}) is defined as the current produced by the cell when the applied potential is zero. Open-circuit potential (V_{oc}), on the other hand, is the voltage delivered by the cell at a given light intensity when the current flow through the cell is zero. At these two special conditions, the power output of the cell is zero. The power output of a solar cell is the

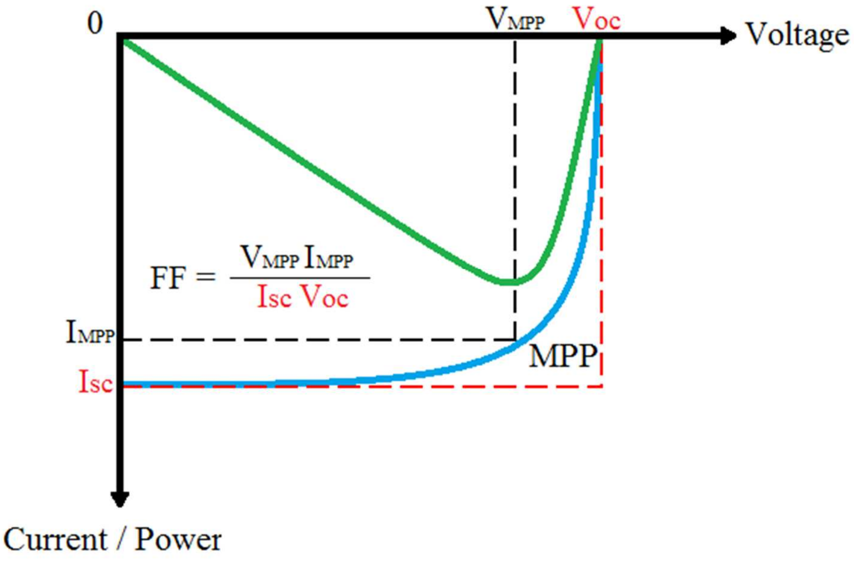

Figure 2.2. Typical current-voltage curve a solar cell under operation condition with output parameters: J_{sc} (short-circuit current), V_{oc} (open-circuit potential), FF (fill factor), MPP (maximum power point), IMPP (current at maximum power point) and VMPP (voltage at maximum power point).

product of the voltage and current at each point of the I-V curve. Hence, there is a point between I_{sc} and V_{oc} where the maximum value of electrical power is delivered to the external load. This point is called the maximum power point (MPP) and the ideal operation of a solar cell is therefore taken place at the MPP. The corresponding values of the MPP on the current and voltage axes are I_{MPP} and V_{MPP}, respectively. The last determining factor in the overall behavior of a solar cell performance is the fill factor (FF). The FF is calculated as follow [3]:

$$\mathrm{FF} = \frac{P_{max}}{I_{sc}\,V_{oc}} = \frac{I_{MPP}\ V_{MPP}}{I_{sc}\,V_{oc}} \qquad (2\text{-}2)$$

The fill factor determines the shape of the I-V curve and it ideally should reach 1.0. However, recombination of charge carriers throughout the cell always causes values less than 1.0. It should be noted that the I-V curve of devices having high FF (>50%) is convex-shaped ($d^2I/dV^2 > 0$), whereas low fill factor devices with (<12.5%) show concaved-shaped ($d^2I/dV^2 < 0$) characteristics.[4]

The performance of the solar cell devices was probed by using a PV Measurement Inc. solar simulator (Class ABA) or Newport solar simulator (Class ABA) equipped with an Air Mass (AM) 1.5G filter as white light illumination source (100 $mW\ cm^{-2}$). The irradiance was calibrated with a standard silicon photovoltaics certified by National Renewable Energy Laboratory. A Keithley 2400 source meter unit connected to PC running software (PV Measurements I-V Measurement Software) was used to apply potential and record the current response of the solar cell devices in the dark and under illumination conditions. The potential was swept from +1.5 V to -1.5 V. All encapsulated solar cells were tested in ambient conditions. All solar cell devices were masked to ensure a well-defined active area. In addition, efforts were made to ensure repeatability of the measurements, including using a darkroom throughout the experiment, examining room temperature (25 ± 3 ℃), maintaining a constant vertical distance between the lamp and the devices throughout the experiment, in addition to other standard setup considerations such as similar potential window, identical swept rate, etc.

2.3.3. Light Intensity-dependency Measurement

Light intensity-dependency measurement has been widely used to study dynamics of charge carriers under steady-state conditions. In this experiment, the intensity of the incident light was decreased gradually and photovoltaic parameters of the solar cell devices recorded as a function of light intensity. As such, the dynamics of charge carriers can be understood at both short-circuit conditions and open-circuit conditions. It is shown that charge carriers dynamics evolves from extraction at the short-circuit conditions to recombination around the open-circuit potential.[5]

Under short-circuit conditions, charge carriers are collected at electrodes via a drift current due to the high internal electric field (built-in potential). The drift current is defined as $J_d = e\mu n_e E$, which e is elementary charge, μ is mobility of charge carrier, n_e stands for density of electrons (assuming density of hole is the same) and E is internal electric field.[2, 6] It is predicted based on the drift current equation that there is a linear proportionality between short-circuit current and density of the photo-generated charge carriers. Therefore, the relationship between the short-circuit current (J_{sc}) and the intensity of incident light (I) can be expressed as $J_{sc} \propto I^{\alpha}$.[7] There are a few common interpretations for values of fitting parameters α in the literature. $\alpha = 1$ is attributed to first order (monomolecular) recombination, whereas $\alpha = 0.75$ and $\alpha = 0.5$ are related to space charge effects.[2, 5, 7] and second order (bimolecular) recombination, respectively. Moreover, It is shown that there is a small bimolecular current loss at the short-circuit conditions which cause a small deviation in the linearity relation of light intensity-dependency of short-circuit current.[2, 8]

Under recombination regime under open-circuit conditions, charge carriers dynamics are mostly described by bimolecular recombination as results of increased charge carrier density in the device. As such, recombination dynamics of charge carriers is examined by studying V_{oc} as a function of light intensity. In the presence of bimolecular recombination, V_{oc} of the solar cell is given by [9]:

$$V_{oc} = \frac{E_{gap}}{e} - \frac{kT}{e} \ln \left[\frac{(1 - P_D)\gamma N_c^2}{G P_D}\right] \qquad (2\text{-}3)$$

where E_{gap} is the energy difference between the highest occupied molecular orbital (HUMO) of the donor and the lowest unoccupied molecular orbital (LUMO) of the acceptor, e is elementary charge, k stands for Boltzmann constant, T is temperature in Kelvin, P_D is dissociation probability of the electron-hole pair, γ is Langevin recombination constant, N_C is the effective density of states and G is generation rate of bond electron-hole pair.[9] Given that G is the only term that can be related to light intensity, the slope of V_{oc} versus natural logarithm of the incident light intensity is predicted to be kT/e. It has been shown that bigger values than *kT/e* appear when trap-assisted (Shockley-Red-Hall) recombination competes with bimolecular recombination, resulting in a stronger dependency on the light intensity.[5, 10]

In order to study device light intensity dependency, solar cells were subjected to different incident light intensities. A series of neutral density (ND) filters were employed to attenuate the light intensity from 100 $mW\ cm^{-2}$ to 1 $mW\ cm^{-2}$. The photovoltaic parameters of the devices were recorded by the same solar simulator described at 2.3.2 section.

2.3.4. Quantum Efficiency Measurement

Quantum efficiency (QE) is the spectral distribution of the short-circuit current and indicates the amount of current that can be produced by photons of a particular wavelength when absorbed by a solar cell. In order to obtain QE of a device, two parameters must be determined: the intensity (power) of monochromatic light incident reaching the device and the generated current at each wavelength by the device. To perform the QE measurement, a monochromatic light beam scans over a given wavelength range for both solar cell devices and a calibrated reference detector (usually silicon) separately or simultaneously. The ratio between the current produced by the devices ($I_{dev}(\lambda)$) and the reference detector ($I_{ref}(\lambda)$) is called the cell responsivity. Thus, the QE of the solar cell devices can be calculated by the equation below [11]:

$$\mathrm{QE} = \frac{\mathrm{hc}}{\mathrm{e}\lambda} \times \frac{\mathrm{I_{dev}}(\lambda)}{\mathrm{I_{ref}}(\lambda)\times \mathrm{R}(\lambda)} \times 100\% \qquad (2\text{-}4)$$

where h stands for Plank's constant, c is the speed of light, e is elementary charge, λ is wavelength, and $R(\lambda)$ is known as responsivity value of the calibrated reference detector.

The quantum efficiency can be expressed in two ways: external quantum efficiency (EQE) and internal quantum efficiency (IQE). The EQE is the ratio of the number of collected free charge carriers to the number of incident photons of a given energy. Therefore, it represents the efficiency of three processes in photovoltaic devices: absorption efficiency (η_{Abs}), charge separation efficiency (η_{CS}) and charge collection efficiency (η_{CC}). A range of EQE from 60%

to 80% has been reported in the literature for various types of photovoltaic devices which indicate 85 to 95% efficiency for each of individual steps.[2]

External quantum efficiency (EQE) was measured using a QEX10 quantum efficiency measurement system (PV Measurement Inc.). The EQE system was calibrated for spectral response via a reference photodiode prior to any measurement. AC mode was chosen for both calibration and measurement. The rate of the mechanical chopper to modulate light was 100 Hz. The wavelength range of 300 – 800 nm was set to record photocurrent response of the devices. The wavelength interval was 10 nm. Focused beam size is about 1 mm x 5 mm independent of wavelength. The solar cell devices were kept in the dark (inside a black box) throughout the measurement.

2.3.5. Photo-Voltage Decay (PVD)

The open-circuit potential (V_{oc}) decay or photo-voltage decay technique is a simple measurement to observe decay of voltage over the course of the time. Having kept device under open-circuit conditions throughout the measurement, an excess voltage is generated by illumination and decay the photo-voltage is monitored over the time. This technique was initially adapted to the dye-synthesized solar cell (DSSC) [12-13] and was then extended to the BHJ solar cells.

In order to perform photo-voltage decay technique, the solar cell devices were held at open-circuit conditions (2.2 mΩ) by using a nanosecond switch (Asama Lab). A laser pulse (6 ns, repetition rate 10 Hz) generated by Nd:YAG laser (Spectra-Physics, INDI-40-10) with a pump wavelength of 532 nm was used to excite the devices. Then, the photogenerated voltage decay was monitored over the time by a digital oscilloscope (Tektronix, DPO4054). The intensity of the laser pulse was adjusted by ND filters and measured repeatedly throughout the experiments. The devices were illuminated through ITO side.

2.3.6. Time-resolved Charge Extraction Technique

The charge extraction (CE) technique was introduced by Shuttle *et al.* to determine the charge carrier density of organic solar cells under steady-state operational conditions. In CE technique, a solar cell is initially held at a potential (bias) away from short-circuit conditions (zero bias) under dark or illumination. Then the device is switched to short-circuit conditions, at which a current transient is produced as charge carriers are extracted. It is assumed that recombination of charge carriers is insignificant during extraction and therefore integral of the current transient is given a number of charge carriers at that particular potential prior to extraction.[14] An established similar technique to the CE techniques is time-resolved charge extraction (TRCE) measurement, by which charge carrier extraction can be accomplished as a function of light intensity and time delay between photo-generation and extraction of charge carriers. It is principally similar to CE technique and involves three steps: 1) holding the device at open-circuit conditions, 2) photo-generation of charge carrier with a nanosecond laser pulse, 3) switching device to short-circuit conditions after a well-defined, adjustable delay time following photo-generation.[15-16] The schematic representation of the TRCE setup and typical charge extraction curves as a function of delay time are shown in Figure 2.3.

Given the time dependency of charge carriers extraction and subsequently charge carriers density (n), bimolecular recombination coefficient (β) and bimolecular recombination lifetime (τ) were calculated by the following equations [17]:

$$\beta(t) = -\frac{dn}{dt}\frac{1}{n^2} \qquad (2\text{-}5)$$

$$\tau = \frac{1}{n\beta} = -\, n\,\left(\frac{dn}{dt}\right)^{-1} \qquad (2\text{-}6)$$

It was assumed that β is dependent on charge carriers density and charge carrier density of holes (p) is equivalent to the charge carrier density of electrons (n).[17]

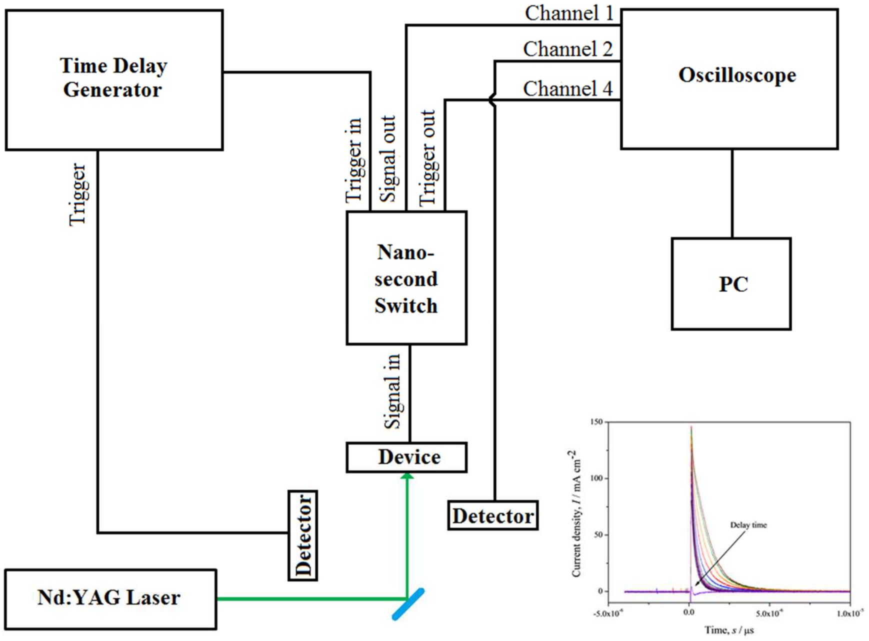

Figure 2.3. Schematic representation of time-resolved charge extraction setup and (bottom right) charge extraction curves as a function of delay time between photo-generation and extraction of charge carriers at a fixed excitation laser energy. Integration of each curve provides charge carrier density for the specified conditions.

TRCE measurement was performed using a nanosecond switch (Asama Lab.). The rolemi of the switch is to hold the device at open-circuit conditions (2.2 MΩ impedance) for a well-defined, adjustable delay time after charge carrier generation. The devices were illuminated by the laser pulse as above. The photogenerated charge carriers were kept at a high impedance (open-circuit condition) by the nanosecond switch. After a given time set by a digital time delay generator (Stanford research DG 535, 250 ns switching time), the impedance is switched to low, allowing extraction of photogenerated charge carriers take place under the built-in potential. The resulting photocurrent transient is recorded by a digital oscilloscope (Tektronix, DPO4054). The photocurrent transient curve was integrated to obtain the number of the charge carriers. Then, charge carriers density was calculated by dividing the number of charge carriers with the active layer film volume. The charge carrier density associated with switch and dark capacitive response was also subtracted to ascertain photo-generated charge carriers density at each delay time.

2.3.7. Photo-induced Charge Extraction by Linearly Increasing Voltage

The charge extraction by linearly increasing voltage (CELIV) technique is developed to study charge carrier transport and recombination in organic and inorganic solar cells.[18-19] The CELIV technique can be performed without and with a light source. The light source is required to generate charge carriers for less conductive, undoped organic semiconducting film. As such the technique is called photo-CELIV. Typically, the photo-CELIV is a two-step measurement. First, charge carriers are generated within the photoactive layer by a laser pulse. Then, the photo-generated charge carriers are extracted by a linearly increasing voltage pulse. A schematic diagram of applied voltage and subsequent current response versus time in photo-CELIV measurement is shown in Figure 2.4. Upon illumination of the device and after an adjustable delay time, a triangle shape voltage pulse with a slope of $A = \frac{\mathrm{U}}{\mathrm{t_{pulse}}}$ is applied to extract the charge carriers. Initially, the capacitive current response (j_0) of the devices appeared. Thereafter, the current (Δj) started rising due to the transportation of charge carriers within the active layer and increased conductivity. The current steadily increased as a result of increasing applied voltage until all the charge carriers were extracted. Next, the current declined to the capacitive current step provided that the electrodes had a good blocking property (prevent injection of charge carriers into the film) and the pulse duration was long enough. In the case of moderately conductive film and $\Delta j \ll j_0$, the mobility of the charge carriers was obtained from the following equation [15, 20-22]:

$$\mu = \frac{2d^2}{3A\, t_{max}^2[1+0.36\frac{\Delta j}{j_0}]} \qquad (2\text{-}7)$$

where d is the active layer thickness, A stands for voltage pulse ($\frac{\Delta U}{\Delta t}$), t_{max} account for time that the photocurrent response reaches its maximum value, Δj is the photo-generated current response and j_0 (= CU) is the capacitive current response of the devices in the dark.

To perform a photo-CELIV experiment, the solar cell devices were illuminated by the nanosecond laser pulse and held at open-circuit conditions as described in section 2.3.6. After an adjustable delay time, the extraction of the photo-generated charge carriers was accomplished by applying a linearly increasing voltage pulse produced by a function generator. The current transient was recorded by the oscilloscope. To compensate for the built-in voltage, an offset potential equal to V_{oc} of the devices was applied. It should be noted that the nanosecond switch was used for the all photo-CELIV experiments. Clarke *et al.* have mentioned that due to the high impedance of the circuit, using the nanosecond switch causes reduction of normal photocurrent response prior to $t = 0$ and V_{oc} conditions are therefore present.

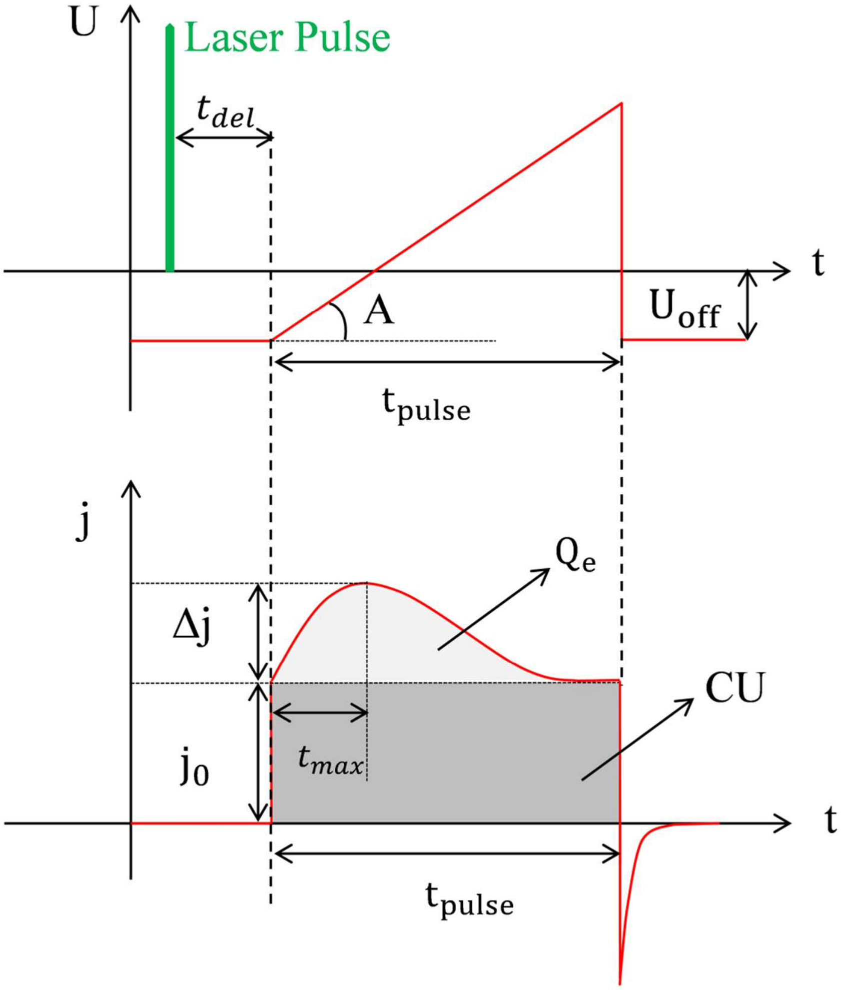

Figure 2.4. (top) Applied triangle voltage pulse versus time and (bottom) current response of the device versus time. j_0 (= CU) is the capacitive current response of the device in the dark. Δjis photogenerated current response overlay on j_0 upon illumination. t_{max} represents the time that the highest value of the photocurrent acquired. t_{del} is the delay time between when the device is illuminated and when the voltage pulse is applied. t_{pulse} stands for the duration of time that the voltage pulse is applied. U_{off} is the offset potential applied to compensate for the built-in potential after illumination.

2.4. REFERENCES

1. Krebs, F. C., Fabrication and Processing of Polymer Solar Cells: A Review of Printing and Coating Techniques. *Solar Energy Materials and Solar Cells* **2009**, *93*, 394-412.

2. Rand, B. P., Richter H.,, *Organic Solar Cells Fundamentals, Devices, and Upscaling*; CRC Press, Taylor & Francis Group, 2014.

3. Qi, B.; Wang, J., Fill Factor in Organic Solar Cells. *Physical Chemistry Chemical Physics* **2013**, *15*, 8972-8982.

4. Kumar, P.; Chand, S., Recent Progress and Future Aspects of Organic Solar Cells. *Progress in Photovoltaics: Research and Applications* **2012**, *20*, 377-415.

5. Cowan, S. R.; Roy, A.; Heeger, A. J., Recombination in Polymer-Fullerene Bulk Heterojunction Solar Cells. *Physical Review B* **2010**, *82*, 245207.

6. Cowan, S. R.; Street, R. A.; Cho, S.; Heeger, A. J., Transient Photoconductivity in Polymer Bulk Heterojunction Solar Cells: Competition between Sweep-out and Recombination. *Physical Review B* **2011**, *83*, 035205.

7. Koster, L. J. A.; Mihailetchi, V. D.; Xie, H.; Blom, P. W. M., Origin of the Light Intensity Dependence of the Short-Circuit Current of Polymer/Fullerene Solar Cells. *Applied Physics Letters* **2005**, *87*, 203502.

8. Mauer, R.; Howard, I. A.; Laquai, F., Effect of External Bias on Nongeminate Recombination in Polythiophene/Methanofullerene Organic Solar Cells. *The Journal of Physical Chemistry Letters* **2011**, *2*, 1736-1741.

9. Koster, L. J. A.; Mihailetchi, V. D.; Ramaker, R.; Blom, P. W. M., Light Intensity Dependence of Open-Circuit Voltage of Polymer:Fullerene Solar Cells. *Applied Physics Letters* **2005**, *86*, 123509.

10. Kyaw, A. K. K.; Wang, D. H.; Gupta, V.; Leong, W. L.; Ke, L.; Bazan, G. C.; Heeger, A. J., Intensity Dependence of Current–Voltage Characteristics and Recombination in High-Efficiency Solution-Processed Small-Molecule Solar Cells. *ACS Nano* **2013**, *7*, 4569-4577.

11. Standard Test Method for Determination of the Spectral Mismatch Parameter between a Photovoltaic Device and a Photovoltaic Reference Cel. *ASTM standard E973 & E973M* **1996**.

12. Bisquert, J.; Zaban, A.; Greenshtein, M.; Mora-Seró, I., Determination of Rate Constants for Charge Transfer and the Distribution of Semiconductor and Electrolyte Electronic Energy Levels in Dye-Sensitized Solar Cells by Open-Circuit Photovoltage Decay Method. *Journal of the American Chemical Society* **2004**, *126*, 13550-13559.

13. Zaban, A.; Greenshtein, M.; Bisquert, J., Determination of the Electron Lifetime in Nanocrystalline Dye Solar Cells by Open-Circuit Voltage Decay Measurements. *ChemPhysChem* **2003**, *4*, 859-864.

14. Shuttle, C. G.; Maurano, A.; Hamilton, R.; O'Regan, B.; Mello, J. C. d.; Durrant, J. R., Charge Extraction Analysis of Charge Carrier Densities in a Polythiophene/Fullerene Solar Cell: Analysis of the Origin of the Device Dark Current. *Applied Physics Letters* **2008**, *93*, 183501.

15. Clarke, T. M.; Lungenschmied, C.; Peet, J.; Drolet, N.; Sunahara, K.; Furube, A.; Mozer, A. J., Photodegradation in Encapsulated Silole-Based Polymer: Pcbm Solar Cells Investigated Using Transient Absorption Spectroscopy and Charge Extraction Measurements. *Advanced Energy Materials* **2013**, *3*, 1473-1483.

16. Clarke, T. M.; Peet, J.; Denk, P.; Dennler, G.; Lungenschmied, C.; Mozer, A. J., Non-Langevin Bimolecular Recombination in a Silole-Based Polymer:Pcbm Solar Cell Measured by Time-Resolved Charge Extraction and Resistance-Dependent Time-of-Flight Techniques. *Energy & Environmental Science* **2012**, *5*, 5241-5245.

17. Clarke, T. M.; Lungenschmied, C.; Peet, J.; Drolet, N.; Mozer, A. J., A Comparison of Five Experimental Techniques to Measure Charge Carrier Lifetime in Polymer/Fullerene Solar Cells. *Advanced Energy Materials* **2015**, *5*, 1401345-n/a.

18. Juška, G.; Arlauskas, K.; Viliūnas, M.; Kočka, J., Extraction Current Transients: New Method of Study of Charge Transport in Microcrystalline Silicon. *Physical Review Letters* **2000**, *84*, 4946-4949.

19. Lorrmann, J.; Badada, B. H.; Inganäs, O.; Dyakonov, V.; Deibel, C., Charge Carrier Extraction by Linearly Increasing Voltage: Analytic Framework and Ambipolar Transients. *Journal of Applied Physics* **2010**, *108*, 113705.

20. Mozer, A. J.; Dennler, G.; Sariciftci, N. S.; Westerling, M.; Pivrikas, A.; Österbacka, R.; Juška, G., Time-Dependent Mobility and Recombination of the Photoinduced Charge Carriers in Conjugated Polymer/Fullerene Bulk Heterojunction Solar Cells. *Physical Review B* **2005**, *72*, 035217.

21. Mozer, A. J.; Sariciftci, N. S.; Pivrikas, A.; Österbacka, R.; Juška, G.; Brassat, L.; Bässler, H., Charge Carrier Mobility in Regioregular Poly(3-Hexylthiophene) Probed by Transient Conductivity Techniques: A Comparative Study. *Physical Review B* **2005**, *71*, 035214.

22. Pivrikas, A.; Sariciftci, N. S.; Juška, G.; Österbacka, R., A Review of Charge Transport and Recombination in Polymer/Fullerene Organic Solar Cells. *Progress in Photovoltaics: Research and Applications* **2007**, *15*, 677-696.

Chapter 3: Investigation into the performance of PCDTBT-based bulk heterojunction solar cells through incorporation of a PFN interfacial layer

3.1. INTRODUCTION

It is well established that the overall performance of the organic photovoltaic device is significantly dependent upon the nature of the electrical contact between the active layer and the electrodes [1-4]. Hence, for an efficient charge carrier collection/extraction, an ohmic contact is required. In recent years, a thin layer of alcohol-soluble conjugated polyelectrolyte, [(9,9-bis(3'-(N,N-dimethylamino)propyl)-2,7-fluorene)-alt-2,7-(9,9–dioctylfluorene) (PFN) has been proposed to provide an ohmic contact between the bulk heterojunction and the cathode electrode, giving rise to simultaneous enhancement of the photovoltaic parameters of solar cell devices[5,6]. The underlying mechanism is believed to be attributable to the deposition of the PFN film, which causes the formation of a permanent electrical dipole at the interface due to the strong interaction of the amino group at the side chain of the PFN and cathode electrode (aluminum). It is therefore claimed that a higher built-in potential is achievable based on the alignment of the electric dipole with the direction of the built-in potential. Consequently, the fill factor of solar cell devices is shown to be improved and higher values for both open-circuit potential and short-circuit current are obtainable. The enhancement of the photovoltaic parameters is attributed to higher charge carrier mobility, balanced charge carrier mobility, superior diode quality and the reduction of charge carriers recombination. Furthermore, it is believed that the PFN interlayer prevents Fermi level pinning between PCBM component of the active layer and the cathode electrodes, resulting in contact selectivity for the electrons and blocking hole transfer across the interface. Conversely, it is shown that generation of charge carriers upon insertion of the PFN layer is not affected, however, the collection of charge carriers around maximum power output condition is increased [5].

Although PFN as an interfacial layer for polymer solar cells was introduced in 2010,[7] it was just a year later that a report was published on the substantial improvement of solar cell performance upon the insertion of a thin layer of PFN.[5] Since then the PFN interlayer has been widely used in the conventional and inverted structures of solar cell devices i.e., as an electron transport layer. However, after reviewing the literature, one can identify a vast variability of the conditions under which the PFN interlayer is applied onto the active layers. Primarily, there is a huge discrepancy reported over the concentration of the PFN solution and its casting condition onto the active layer.[8-22] This is an important factor in determining the thickness of the film. Nevertheless; an overwhelming majority of the publications has stated the thickness of their film to be 5 nm. In one study, it was reported that the thickness of the interlayer was measured by means of a surface profiler in combination with extrapolation from an absorbance-thickness curve which assumes a linear relationship between absorption of the PFN film at 380 nm and the film thickness.[5,7,23] However, experimental proof to verify the exact thickness of the PFN film independently is not evident in the literature. Instead, there is a long line of citation propagating back to the original study.[24-36] Yet it is worth noting that other techniques have been used to determine the thickness of PFN film, but precision and film preparation procedure are still questionable e.g. Long *et al.*[37] measured PFN film thickness (20, 10 and 5 nm) by atomic force microscopy (AFM) technique and Srinivasan *et al.*[38] used 3D laser scanning microscope to estimate the thickness of PFN film cast by spray coating and spin coating. However, no details of film preparation procedure (PFN solution, substrate) or methods (masking substrate or scratching the film to measure z-step) was provided. It should be also mentioned that the amount of the acetic acid used to dissolve the PFN in the polar solvents (mostly methanol) also differs within the literature. Eventually, it was shown by Hu *et al.* that the introduction of PFN to solar cell devices does not modify energy levels at the interface. It was also shown that the work function of the cathode electrode pins to the fullerene energy levels ($\mathrm{E}_{\mathrm{ICT}}^{-}$), which implies that open circuit potential of solar cell devices is independent of the work function of the cathode electrode.[39]

The first aim of this study was to realize the condition to achieve an optimal PFN film as an electron transport layer in the conventional architecture of the BHJ solar cells. Hence, a series of PFN solutions with difference concentrations, i.e. 0.5, 0.4, 0.3, 0.2 mg/ml were prepared. The solutions were spun cast on top of the active layer, with the spin speed varying from 1000 to 8000 rpm. Subsequently, the photovoltaic parameters of the solar cell devices were recorded as a function of the PFN film. Noteworthy that the preparation procedure (solution concentration and spin speed) encompasses a variety ranges of PFN film (thickness), however, PFN film thicknesses were undetermined. The second aim was to understand the extent to which the PFN film contributes to the charge carrier dynamics of the solar cell devices. Thus, the influence of the PFN interlayer on the recombination processes of the charge carriers was investigated by a combination of steady state and transient techniques. This involved the employment of the light intensity dependency measurement in addition to charges extraction, photovoltage decay, and photo-CELIV techniques. The light intensity dependency measurement was used to examine recombination dynamics of the device under the operational condition, whereas the transient techniques provide information about the influence of PFN on the lifetime and bimolecular recombination rate and mobility of the charge carriers. It should be noted that choosing PCDTBT as donor polymer in this study were based on the facts that it is a low-bandgap, high-performance, well-characterized polymer which commercially available (inexpensive) and does not require special treatments (pre- or post-treatment) in the bulk heterojunction. Moreover, it has been claimed that PFN effectively increases the performance of BHJ solar cell made of polymers containing N-heterocycle structure.[40]

3.2. EXPERIMENTAL

3.2.1 Materials

[6,6]-Phenyl C61 butyric acid methyl ester ($PC_{60}BM$) with a purity of > 99.5%, Poly[N-9′-heptadecanyl-2,7-carbazole-alt-5,5-(4′,7′-di-2-thienyl-2′,1′,3′-benzothiadiazole)] (PCDTBT), [6,6]-Phenyl C71 butyric acid methyl ester ($PC_{70}BM$) with a purity of > 99.5% and Poly [(9,9-bis(3'-(N,N-dimethylamino)propyl)-2,7-fluorene)-alt-2,7-(9,9–dioctylfluorene) (PFN) were sourced from Solaris Chem. Inc. (Qc, Canada). Methanol (HPLC grade), 1,2-dichlorobenzene (o-DCB) and Acetic Acid were also sourced from Sigma-Aldrich. All materials were of analytical grade and used as received without further purification.

3.2.2. Film and Device Fabrication

Solar cell devices were fabricated with an architecture consisting of ITO/PEDOT:PSS/PCDTBT:PCBM/PFN/Al. Patterned ITO-coated glasses were cleaned by sequential sonication in DI water, Acetone, and Isopropanol (IPA) and then treated with UV-Ozone for 20 min. PEDOT:PSS solution was spin-coated on the substrate at 5000 rpm for 40 s to form a 30~40 nm thick film. After that, the substrates were annealed at 150 °C for 10 min in ambient air. The active layer was coated on top of the PEDOT:PSS film from a solution of 1,2-dichlorobenzene containing PCDTBT:$PC_{70}BM$ or PCDTBT:$PC_{60}BM$ (1:4 ratio) at an overall concentration of 20 mg/ml. The final thickness of the active layer was 80 nm (± 5) as measured by a surface profiler (Dektak 150, Veeco). PFN solutions at 4 different concentrations were prepared, i.e., at 0.5, 0.4, 0.3 and 0.2 mg/ml by adding PFN into 1cc methanol in the presence of 1µL acetic acid. PFN solutions were spin-coated onto active layer at various spin speed, i.e., 1000 to 8000 rpm. Finally, the cathode electrode was deposited by thermal evaporation of 100 nm of aluminum. The device active area was 0.06 cm^2. It should be noted in both reference and PFN-based devices cast from 0.5, 0.4, and 0.3 mg/ml solutions, $PC_{70}BM$ was used as acceptor, whereas $PC_{60}BM$ was used as acceptor in both reference and PFN-based devices cast from 0.2 mg/ml solution. $PC_{70}BM$ has a relatively bigger size and stronger absorption than $PC_{60}BM$. Therefore, it is expected that the performance of the device using $PC_{70}BM$ would be higher compared to PC60BM. In addition, LUMO energy levels of both $PC_{70}BM$ and $PC_{60}BM$ are comparable. Thus, electrons may experience similar energy cascade (electrons travel from LUMO of acceptor to the cathode electrode) regardless of which molecule is used as acceptor. Nevertheless, both $PC_{70}BM$ and $PC_{60}BM$ do not contain N-heterocycle function group - the cardinal factor for PFN to interact with.[40] As such, the mechanism with which PFN interlayer influences the performance of the devices is independent of which molecule is used as acceptor in the bulk heterojunction.

3.2.3. Chemical Structure and Device Architecture

The chemical structures of the polymer donor PCDTBT, fullerene-derivative acceptors $PC_{70}BM$, $PC_{60}BM$, PFN molecule and the schematic illustration of the solar cell energy levels in the conventional structure are shown in Figure 3.1.

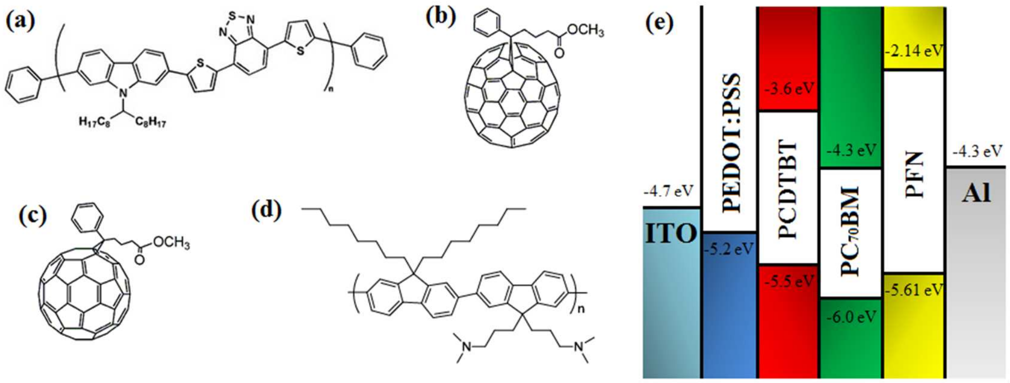

Figure 3.1. Chemical structures of (a) PCDTBT, (b) $PC_{70}BM$, (c) $PC_{60}BM$, (d) PFN and (e) the schematic representation of the solar cell energy levels. The energy levels were obtained from ref. [8].

3.3. RESULTS AND DISCUSSION

3.3.1. Current density-Voltage Measurements

Figure 3.2 shows comparison of power conversion efficiency (PCE) of the PCDTBT-based bulk heterojunction solar cell devices without (reference) and with PFN interlayer (PFN-based) as a function of spin speed of PFN solution casting (The full set of data including statistics, current density-voltage curves, external quantum efficiency, dark current and photocurrent analysis for both the reference devices and PFN-based devices are shown in Appendix). The PFN solutions were spin-coated on top of the active layer from PFN solutions with different concentrations and the spin speed was increased from 1000 to 8000 rpm. It is clear that for the whole range of PFN solutions and spin speed no substantial enhancement was observed in the overall performance of the PFN-based solar cell devices compared to reference devices. Moreover, the PCE of the devices are conversely degraded (Appendix) upon introduction of the PFN interlayer at some spin speeds (PFN film thickness). Generally, PFN film (thickness) effect (based on spin speed) on the overall performance of the solar cell devices can be categorized into three regions, i.e., i) low spin speed (1000 to 3000 rpm), ii) moderate spin speed (4000 to 6000 rpm), and iii) high spin speed (7000 and 8000 rpm). It can be seen that at low spin speed region, poor performance device compared to the reference devices become apparent which can be related to the formation of a thick PFN film at the interface that significantly blocks passages of the charge carriers to the cathode electrode. While at the moderate spin speed region PFN-based devices with similar efficiencies compared to reference devices appears, PCE of the PFN-based devices varies at the high spin speed region. It should be noted that PCE of reference devices in section b (0.4 mg/mg PFN) of Figure 3.2 is slightly lower than that of devices in sections a and c (0.5 and 0.3 mg/ml PFN). This is mostly due to the lower molecular weight of PCDTBT used in these series of experiments, resulting in lower V_{oc} and J_{sc} (Appendix, Table 3.6.2) and consequently lower PCE. Nevertheless, this does not

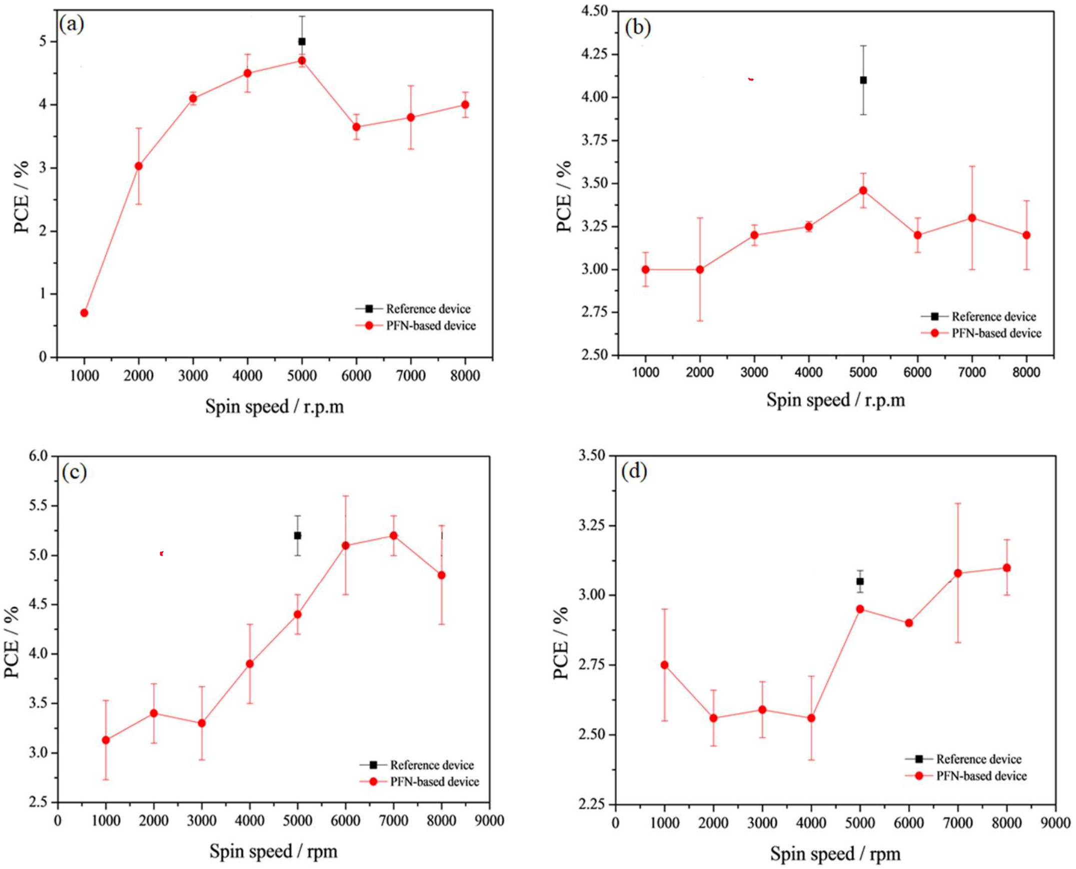

Figure 3.2. Comparison of the power conversion efficiency (PCE) of the PCDTBT-based bulk heterojunction solar cells in the absence (black) and presence (red) of the PFN interlayer spin coated from PFN solutions with concentration of (a) 0.5 mg/ml, (b) 0.4 mg/ml, (c) 0.3 mg/ml, and (d) 0.2 mg/ml as a function of spin speed. The acceptor molecule in the bulk heterojunction for all device was $PC_{70}BM$, except the reference and PFN-based device with 0.2 mg/ml which $PC_{60}BM$ is used.

affect the fact that the PFN interlayer has not shown the ability to modify the interface and thereby improving solar cell devices efficiency. In the following, the effect of the PFN film (thickness) on each photovoltaic parameter of the solar cell devices is discussed.

The open-circuit potential of the PFN-based devices remained independent of the PFN film (thickness) regardless of the concentration of PFN solutions or solution casting velocity, i.e. the V_{oc} values before and after deposition of the PFN interlayer are comparable (Appendix, Table 3.6.1, Table 3.6.2, Table 3.6.3 and Table 3.6.4). This implies that the interface between the cathode electrode and the active layer was not modified by insertion of the PFN interlayer. This might be due to deposition process of the cathode electrode (aluminum), Fermi level pinning between the cathode electrode and PCBM or band bending of the active layer. For example, deposition of aluminum is done through thermal evaporation. Given the thickness of the PFN layer, the hot particles of aluminum could penetrate the ultra-thin layer and either destroy the PFN film or result in the pinning of the Fermi level of the cathode electrode to the LUMO level of PCBM molecules. Under these circumstances, the V_{oc} of the devices is independent of the PFN interlayer and determined by the work function of the aluminum. It should be noted that a thick PFN layer could resist either above-mentioned scenarios as the existence of such a thick film can be proved through its detrimental impact on the photovoltaic characteristics of the devices (Appendix, Table 3.6.1, 1000 rpm PFN-based devices).

Zhang *et al.*[6] has reported the improvement of the open-circuit potential of the PCDTBT:$PC_{70}BM$ BHJ solar cells upon incorporation of the PFN interlayer. However, it is apparent that there was only 0.01 V difference between V_{oc} of the devices treated with methanol (0.92 ± 0.01 *V*) and the device containing PFN (0.93 ± 0.01 *V*). Moreover, the open-circuit potential of the control devices (without PFN interlayer or methanol treatment) is relatively low (0.8 *V*) compared to those reported in the literature (0.9 *V*). He *et al.*[5] also report improving V_{oc} from 0.7 *V* to 0.9 *V* following the addition of PFN interlayer and calcium. It is also shown by Guo *et al.*[15] that V_{oc} slightly increases from 0.845 *V* to 0.890 *V* after incorporation of PFN film. Therefore, it could be understood that the PFN interlayer has no and/or a small impact on the V_{oc} of the devices which were already acquired the highest possible open-circuit potential. This conclusion has been reflected in the results presented here where V_{oc} remains almost unchanged following deposition of the PFN interfacial layer. A similar trend can also be found in solar cell consisted of other donor materials such as P3HT, PTB7, etc.

The short-circuit current of the PFN-based devices fluctuates over values less than that of the reference devices (Appendix, Table 3.6.1, Table 3.6.2, Table 3.6.3 and Table 3.6.4) across the whole range of spin speeds and concentrations. The external quantum efficiency of the best devices with PFN interlayer (Appendix, Figures 3.6.3, 3.6.7, 3.6.11, and 3.6.15) also shows a slight decrease (devices fabricated with PFN solutions 0.5, 0.4 and 0.3 mg/ml) or increase (devices fabricated with 0.2 mg/ml) compared to the respective reference devices. These results are consistent with current density-voltage measurement and imply that the conversion efficiency of the incoming photon to collected electron has not been altered following the introduction of PFN interlayer. In other words, generation, transportation, collection and recombination of charge carriers are likely to be similar in the absence and presence of the PFN film.

He *et al.*[5] show that PFN/Ca interlayer can moderately increases (0.7 $mA\ cm^{-2}$) the short-circuit current. Zhang *et al.*[6] report PFN interlayer film cast from methanol solvent enhances J_{sc} around 0.5 $mA\ cm^{-2}$. Guo *et al.*[15], on the other hand, demonstrated that methanol solely increases the J_{sc} more than that of PFN. The other BHJ solar cells have also demonstrated an increase in the short-circuit current upon methanol treatment.[41,42] As such, it would be difficult to exclude the contribution of the methanol into the enhancement of the J_{sc}, since PFN has been always cast from methanol solvent. However, no considerable changes in the short-circuit current were observed here upon the inclusion of PFN interlayer.

The impact of PFN interlayer was observed to be on the fill factor of PFN-based devices (Appendix, Table 3.6.1, Table 3.6.2, Table 3.6.3 and Table 3.6.4). The *FF* of PFN-based devices were reduced significantly at the low spin speeds compared to the reference devices. This perhaps was due to the formation of a relatively thick film at the interface which would hamper collection of charge carriers (electrons) at the cathode electrode. As a result, charge carriers recombine which would lead to a subsequently lower fill factor. At the moderate speed spin region, the fill factor started rising whereas at the high-speed spin region it fluctuates with values close to or less than that of the reference devices. Thus, improvement of the fill factor is not observed here upon introduction of the PFN layer between the active layer and the cathode electrode. It is worth pointing out that fill factor of the devices (references) reported in this chapter is slightly smaller (~0.52) than those that are reported in the literature (vide infra), which could be due to inherent impurity containing within the active materials. Nevertheless, the FF of the PFN-based devices was lower or remained almost unchanged compared to the reference devices. FF is an indicator of competition between extraction and recombination which is dependent on the mobility of charge carriers. Hence, one may conclude that PFN interlayer unable to modify either the mobility of charge carriers or interface characteristics (in terms of recombination) between the active layer and the cathode electrode.

It has been reported that PFN interlayer could improve the *FF* of the solar cell devices. He *et al.*[5] reported a 26% increase in the *FF* (from 0.49 to 0.62) due to PFN interlayer. A more balanced and increased mobility of charge carriers were accounted for the enhancement. Zhang *et al.*[6] claimed that FF increases 17% (from 53.6 to 62.8) upon insertion of PFN film. This increase was related to better diode quality of devices due to hole-blocking characteristics of the amino groups of the PFN side chain. A similar improvement of the FF (from 0.57 to 0.67) was reported by Guo *et al.*[15] and correlated to the effect of PFN in the reduction of space-charge build-up and charge carrier recombination. Such an enhancement on fill factor was not observed here.

3.3.2. Dark Current Measurement

To gain more understanding of the effect of the PFN interlayer on the electrical characteristics of the solar cell devices, the current-voltage characteristics of the devices were measured in the dark condition. Figure 3.3 exhibits dark current characteristics of the solar cell devices without and with PFN interlayer. For the purpose of comparison, only the best devices were compared here, however, the full sets of dark current measurement containing all spin speed are presented in the Appendix (Figures 3.6.2, 3.6.6, 3.6.10, and 3.6.14). It is clear that there is only quite small difference between dark currents characteristics of the solar cell devices in the absence and presence of the PFN interlayer. The key characteristics of the devices in the dark such as turn-on voltage or rectification ratio have not been significantly altered. It is

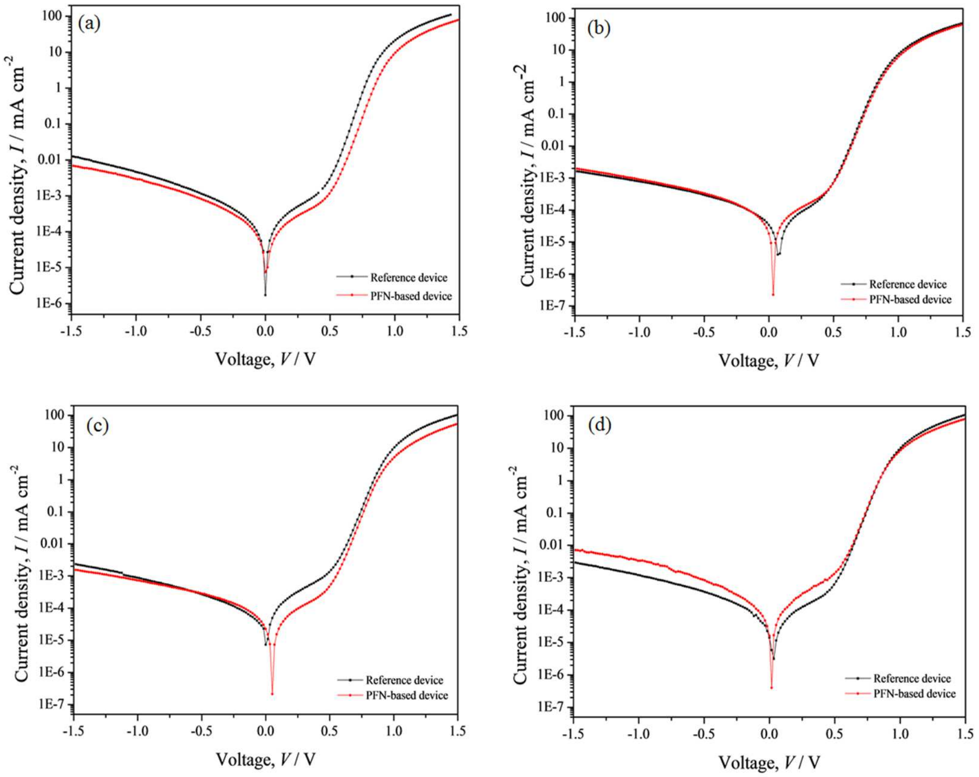

Figure 3.3. Comparison of the dark current density of PCDTBT:PCBM solar cell devices without (black line) and with (red line) the PFN interlayer as a function applied voltage. The concentration of the PFN solutions were (a) 0.5 mg/ml, (b) 0.4 mg/ml, (c) 0.3 mg/ml, and (d) 0.2 mg/ml.

claimed that PFN interlayer results in a reduced current density in the reverse bias (known as leakage current region).[7] This reduction is ascribed to increasing of contact barrier for hole injection at the semiconductor/metal interface and subsequently lower reverse dark current saturation. Such a reduction in the reverse bias (-1.5 *V*) for the majority of the PFN-based devices fabricated with 0.2, 0.3 and 0.4 mg/ml PFN solutions was not observed (Appendix, Figures 3.6.6, 3.6.10, and 3.6.14), whereas devices with PFN interlayer casted from 0.5 mg/ml solution exhibit the reduction (Appendix, Figure 3.6.2). On the other hand, the current density in forward bias bigger than 1*V* (known as space charge limited current region) is at the same level or decreases in devices containing PFN interfacial layer compared to the control devices (Appendix, Figures 3.6.2, 3.6.6, 3.6.10, and 3.6.14). The current is an indication of series resistance in solar cell devices and demonstrates the injection of electrons from the cathode electrode (flowing electrons from the cathode to anode).[43,44] Therefore, it could be surmised that series resistance has not been changed or even increased following the deposition of PFN interlayer. This possible increase in series resistance could stem from the bulk resistance of the PFN layer (thick PFN film) or interfacial resistance at the PFN/Al interface (thin PFN film).

As mentioned earlier, the turn-on voltage of the solar cell devices has not been significantly modified following the addition of PFN interlayer. The turn-on voltage is an indication of built-in voltage (V_{bi}) that influences the internal electric field in BHJ solar cells and determines the maximum attainable V_{oc} provided that difference of electrodes' work functions is larger than the offset between HOMO-donor and acceptor-LUMO.[42] He *et al.*[5] has mentioned enhancement of V_{bi} and consequently the open-circuit potential of PCDTBT:PC$_{70}$BM BHJ is primarily due to the formation of a dipole (originating from amino group in side chain of PFN) and its alignment with internal electric field. Furthermore, the authors claimed that turn-on voltage increase to 0.8 – 1*V* from pristine values of 0.5 - 0.6 *V* (toward higher voltage) upon incorporation of PFN as interlayer. Such a drastic enhancement in the turn-on voltage is not clearly observed here. In addition, similar to turn-on voltage, V_{bi} remained also unaltered. Therefore, the fact that open-circuit potential of the solar cell devices has not been enhanced after addition of PFN interfacial layer can be ascribed to the unchanged turn-on voltage and subsequent V_{bi}.

3.3.3. Charge Generation and Collection

Figure 3.4 and 3.5 compares the photocurrent density (J_{ph}) and charge collection probability (P_c) of the PCDTBT:PCBM devices without and with PFN interlayer cast from different PFN solutions as a function of effective voltage (V_{int}). Given PFN solution concentrations and spin speed, PFN-based devices showing highest PCE were chosen to be compared to the reference devices here. In addition, the photocurrent density and charge collection probability for the lowest and highest rpm for each PFN solution concentration are shown in the Appendix (Figures 3.6.4, 3.6.8, 3.6.12 and 3.6.16). Generally, the photocurrent density in the devices containing PFN interfacial layer is lower compared to the reference device (Figure 3.4a-d). The photocurrent density flowing through a solar cell can be expressed as a function of charge generation rate and charge collection probability. Hence, it can be written as below [45,46]:

$$J_{ph} = edG_{max}P_c \qquad (1)$$

where e is elementary charge, d is the thickness of the active layer, G_{max} is the maximum photo-induced charge carrier generation rate per unit volume and P_c is the charge collection probability. The charge collection probability approaches unity ($P_C = 1$) at saturated photocurrent ($J_{ph,sat} = qLG_{max}$) when the internal electric field within the device is strong enough to sweep out all charge carriers. Thereby the P_c can be determined as below [45,46]:

$$P_c = \frac{J_{ph}}{J_{ph,sat}} \qquad (2)$$

The G_{max} values of the devices for both reference and PFN-based solar cell devices are shown in Table 3.1. It is clear that G_{max} values for the PFN-based devices are slightly smaller than that of the reference counterparts. The G_{max} corresponds to the maximum number of the photons absorbed by the active layer. Therefore, the G_{max} results imply that the absorption of the light has not been enhanced following insertion of the PFN layer between the active layer

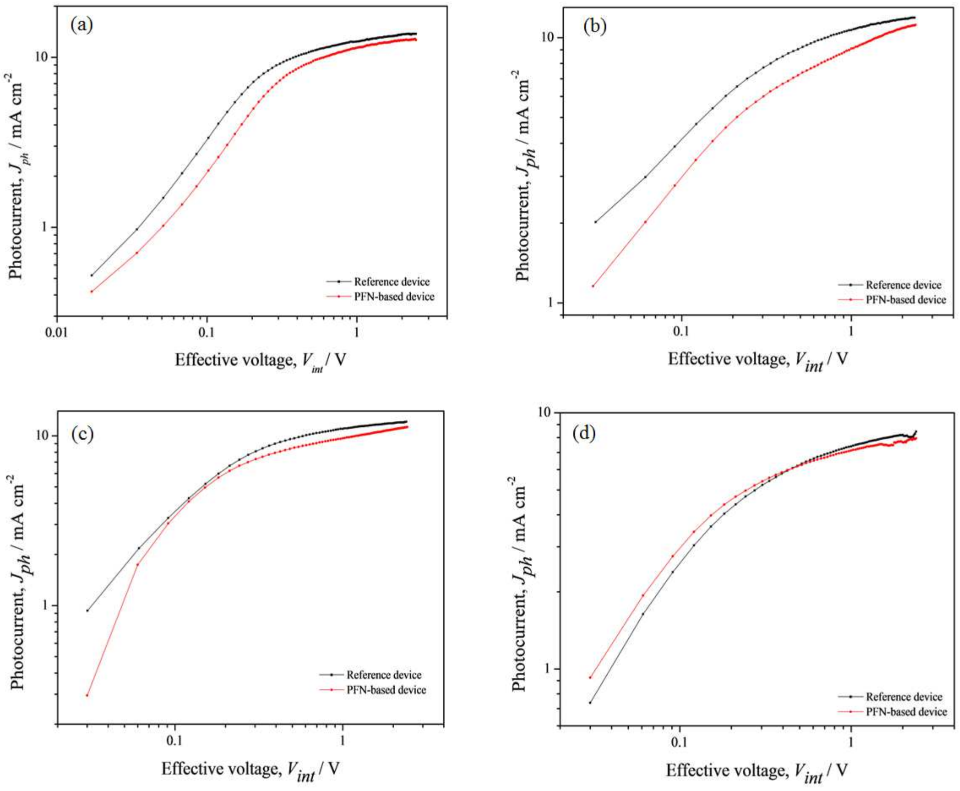

Figure 3.4. Comparison photocurrent density of the best efficient PCDTBT:PCBM solar cell devices as a function of the effective voltage without (black line) and with (red line) the PFN interlayer casted from solution with concentration of (a) 0.5 mg/ml (donor is $PC_{70}BM$), (b) 0.4 mg/ml (donor is $PC_{70}BM$), (c) 0.3 mg/ml (donor is $PC_{70}BM$), and (d) 0.2 mg/ml (donor is $PC_{60}B$).

Table 3.1. The calculated G_{max} values for the devices without and with PFN interlayer cast from PFN solution with different concentration.

PFN solution concentration (mg/ml)	Spin speed (rpm)	G_{max} (m^{-3} s^{-1}) (PFN-based device)	G_{max} (m^{-3} s^{-1}) (Reference device)
0.5	5000	9.5×10^{27}	1.0×10^{28}
0.4	5000	8.7×10^{27}	9.3×10^{27}
0.3	6000	8.8×10^{27}	9.4×10^{27}
0.2	8000	6.2×10^{27}	6.6×10^{27}

and the cathode electrode. Indeed, it appears that PFN has a small negative impact on the generation rate of the charge carrier (Table 3.1). The above-mentioned negative effect is even more pronounced in the PFN containing devices cast at lowest spin speed, e.g. 1000 rpm (Appendix, Figures 3.6.4, 3.6.8, 3.6.12 and 3.6.16). This may indicate the PFN film does not have characteristics of an optical spacer. The optical spacer gives rise to a better spatial distribution of incident light throughout the bulk heterojunction, leading to increase light absorption and subsequent photo-generated charge carriers. Thus, one may conclude that PFN interfacial layer not only contributes to the spatial distribution of the incident light but also interferes with bulk heterojunction absorption.

The charge collection probability (P_c) of the devices is also compared in Figure 3.5a-d. There are no appreciable changes in the P_c values before and after deposition of the interlayer at the high effective voltage ($V_{int} > 0.3\ V$). Besides, the P_c values of PFN-based devices are lower compared to the reference devices at low V_{int} ($< 0.3\ V$). The exception is the devices with PFN interlayer cast from 0.2 mg/ml solution (Figure 3.5d). The observed reduction of charge collection in PFN-based BHJ devices at low effective voltage (close to open-circuit conditions) where the internal electric field is weak, may indicate the enhancement of charge carrier recombination.

Generally, it could be concluded that both charge carrier generation and collection of the PCDTBT:PCBM BHJ devices have been declined after incorporation of the PFN interlayer. As such, this may explain the reduction of the short-circuit current and fill factor of the PFN-based devices.

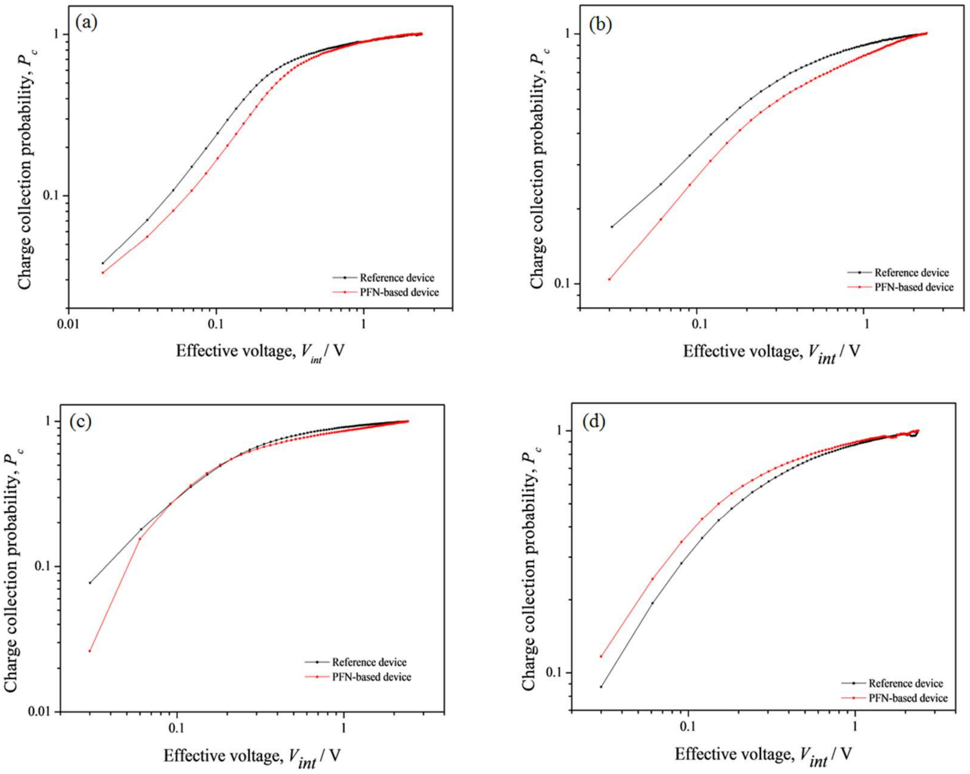

Figure 3.5. Comparison charge collection probability of the best efficient PCDTBT:PCBM solar cell devices as a function of the effective voltage without (black line) and with (red line) the PFN interlayer casted from solution with concentration of (a) 0.5 mg/ml (acceptor is $PC_{70}BM$), (b) 0.4 mg/ml (acceptor is $PC_{70}BM$), (c) 0.3 mg/ml (acceptor is $PC_{70}BM$), and (d) 0.2 mg/ml (acceptor is $PC_{60}BM$).

3.3.4. Light-Intensity Dependency Measurement

To study the effect of the PFN interfacial layer on the charge carrier recombination kinetics, the dependency of the short-circuit current and open-circuit potential as a function of the illumination intensity is examined. Given that PFN interlayer did not substantially enhance the performance of the BHJ devices, the highest achieved PCE of PFN-based devices cast at 5000 rpm from 0.5 mg/ml solution was selected for comparison with its respective reference device for this study. In Figure 3.6a, the short-circuit currents of the device are plotted against the incident light intensity on a log-log scale and fitted to a power law based one the $J_{sc} \propto I^{\alpha}$ relationship, where α is indicative of the recombination dynamics.[45-48] The α values for the reference and PFN-based devices are 0.945 and 0.943, respectively. These values suggest that recombination dynamics of the charge carriers at the short-circuit conditions has not been altered upon insertion of the PFN film between the active layer and the cathode electrode. Similar results were reported by He *et al.* [5] It is pointed out that a sole monomolecular recombination at short-circuit conditions gives rise to an α value close to unity, whereas deviation from unity could be due to strong bimolecular recombination, space charge effect and different in mobility of the charge carriers [45,48]. Considering the mobility measurement results (Section 3.3.8), the deviation from unity could result from the bimolecular recombination of the charge carriers.

In order to further investigate the impact of the PFN interlayer on the recombination dynamics of the charge carriers at the low effective voltage, the open circuit potential of the solar cell devices is studied as a function of the incident light intensity (Figure 3.6b). According to equation 2-3 and given the fact that all charge carriers are recombined at the open-circuit condition via bimolecular recombination, the slope of V_{oc} versus the natural logarithm of the light intensity is kT/e.[45-48] The slope values for the reference and PFN-based devices are 1.44

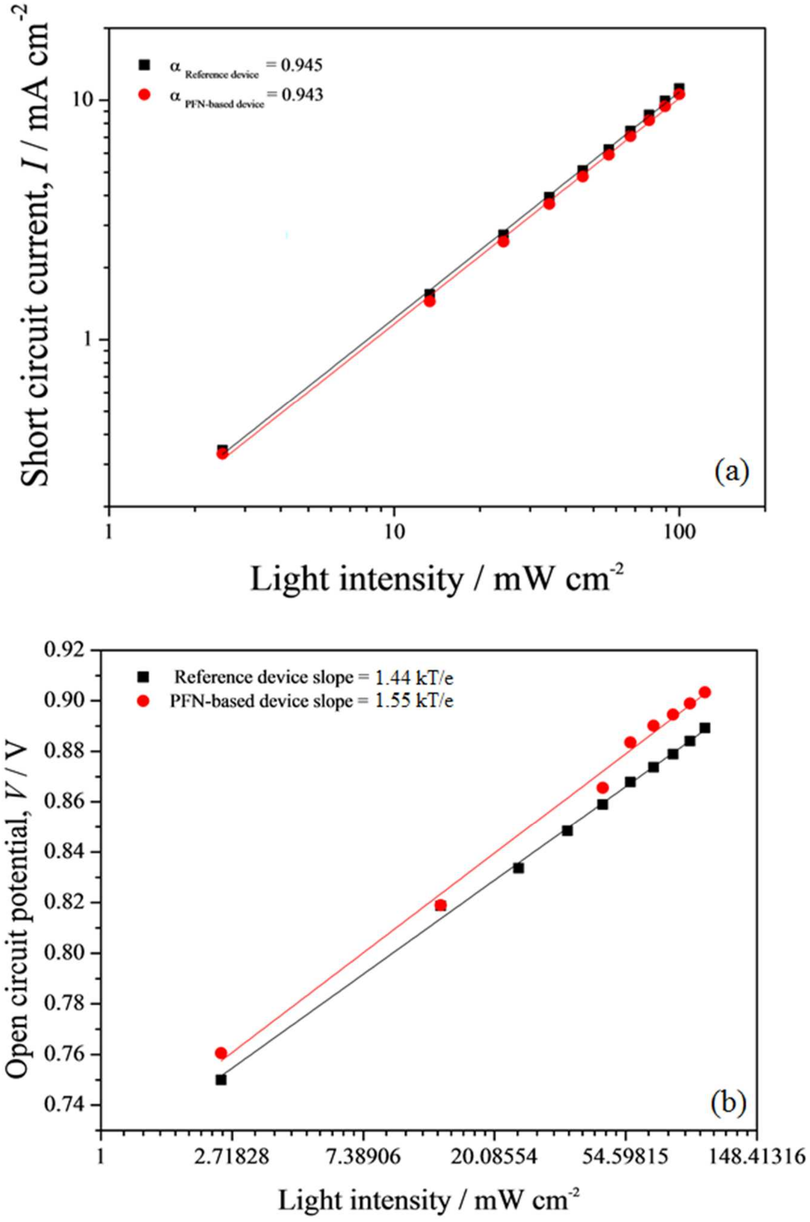

Figure 3.6. (a) Short circuit currents and (b) open circuit potentials plot against light intensity for the PCDTBT: $PC_{70}BM$ solar cell devices without (black line) and with (red line) the PFN interlayer. The adjacent R^2 for fitting parameters are more than 0.99. PFN solution concentration was 0.5 mg/ml and was cast at 5000 rpm.

kT/e and 1.55 *kT/e*, respectively. Although the difference between the slopes is not huge, the slope values suggest that recombination dynamics at the open-circuit is not purely bimolecular and the addition of the PFN interfacial layer results in the stronger dependency of the open-circuit potential to the incident light intensity. According to Kway *et al.* [45,46], interfacial trap states are responsible for the stronger dependency of the open-circuit potential to the light intensity and subsequent deviation of the slope from *kT/e*. The authors have shown that interfacial trap states can be mitigated by insertion of an interfacial layer between the active layer and the cathode electrode. Thus it can be inferred that both bimolecular recombination and trap-assisted recombination are present at the open-circuit condition. Moreover, charge carrier recombination via trap states enhanced in devices with the interlayer. Hence, reduction of charge collection in PFN-based devices, especially at low effective voltage (close to open-circuit conditions), can be attributed to the enhancement of trap-assisted recombination (also known as monomolecular or Shockley-Read-Hall recombination). The reason for such an enhancement remains unclear. One possible explanation can be that PFN acts as a recombination center and facilitate the monomolecular recombination as it has been claimed that amino group in PFN side chain are the hole trapping center.[6]

3.3.5. Photovoltage Decay Measurement

To study the effect of the interlayer on the recombination dynamics of the charge carriers, the decay of photovoltage over the time for the BHJsolar cell devices in the absence and presence of the PFN interlayer is examined. Figure 3.7 compares the photovoltage decay of the PCDTBT:PC$_{70}$BM BHJ solar cells without and with PFN interlayer cast at 5000 rpm from 0.5 mg/ml solution. It is clear that both devices possess similar V_{oc} initially, which are close to the open-circuit potential values obtained from the current density-voltage measurement. This implies that the open-circuit potential of the PFN-based device is independent of the interlayer. Moreover, the photovoltage of the device with PFN interlayer decays faster than that of the control devices. This means charge carriers recombine faster in the presence of the PFN in particular at the longer time. This finding is consistent with light intensity dependency results.

It should be noted that V_{oc} in BHJ solar cells is determined by quasi-Fermi level splitting that is obtained when available electronic states are occupied by a certain amount of the charge carriers. The charge carriers density, on the other hand, at the open circuit conditions is determined by a competition between generation and recombination of the charge carriers, considering recombination term has a charge carriers dependency. Therefore, any change in either the generation or recombination rates could affect charge carrier density and subsequently the V_{oc}.[49] Maurano *et al.* [50] have also shown that V_{oc} is determined by the energy levels of the donor and acceptor materials as well as recombination dynamics of the charge carriers. All in all, it could be rationalized that neither recombination dynamics nor generation rates of the charge carriers at the open-circuit conditions were influenced by the introduction of PFN interlayer. Two possible scenarios for this can be i) the contact between active layer and the cathode electrode is ideal and ohmic which cannot be further improve by PFN interlayer, ii) the PFN interfacial layer would have been destroyed during thermal evaporation of cathode electrode such that there is no longer an intact interfacial layer on top of the active layer to

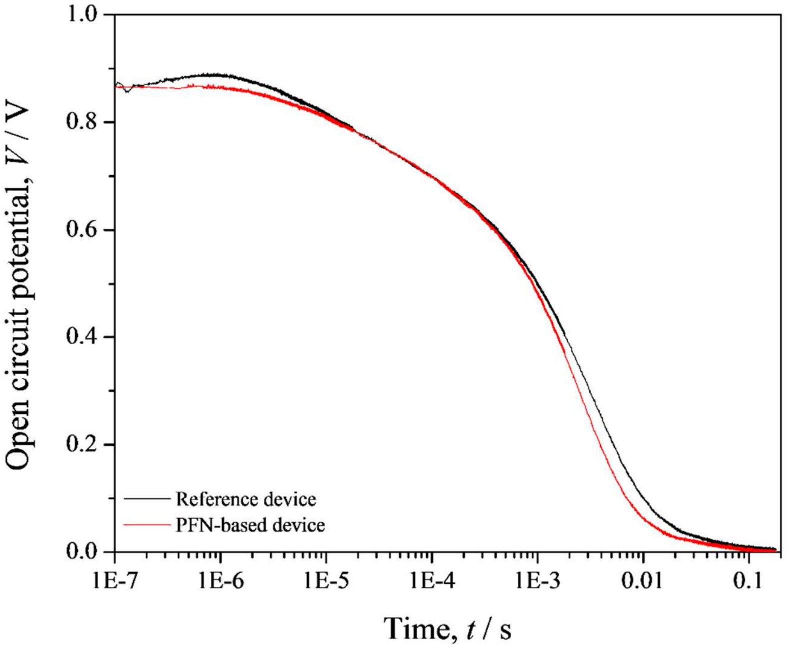

Figure 3.7. The decay of photovoltage over time of the PCDTBT:$PC_{70}BM$ solar cell devices without (black line) and with (red line) the PFN interlayer. PFN solution concentration was 0.5 mg/ml and was cast at 5000 rpm.

modify the interface. Given the second scenario, Hu *et al.*[39] have reported that cathode electrode (Al) diffuses into the PFN film and the interface is a mixture of Al, PFN, and fullerene. The above-mentioned findings are not in agreement with findings report by He *et al.*[5] that suggest incorporation of the PFN film results in the reduction of the bimolecular recombination and therefore increase of V_{oc}.

3.3.6. Charge Extraction Measurement

The dynamics of the charge carrier over the time for the solar cell devices in the absence and presence of the PFN interfacial layer were measured and presented in Figure 3.8. The best efficient devices without an with PFN interlayer (0.5 mg/ml cast at 5000 rpm) were chosen for this study. As shown in Figure 3.8a, the amount of charge carrier density at the early time acquired by both reference and PFN-based devices is comparatively similar. However, charge carrier density is lower in the device with PFN interfacial layer at the longer time. This means that the decay of the charge carriers in the PFN-base devices are faster compared to the control device. The charge carrier bimolecular recombination coefficient (β) and bimolecular recombination lifetime (τ) were calculated based on equation (2-5) and (2-6), respectively. It can be seen that β is slightly higher in the presence of the PFN interfacial layer (Figure 3.8c). Nevertheless, τ for both devices is almost identical over the course of the time (Figure 3.8b). These findings suggest that recombination of charge carriers is enhanced following the inclusion of PFN interlayer. This may result from recombination through interfacial trap states. The bimolecular recombination at the longer time is attributed to the bimolecular recombination of the charge carrier in the presence of the exponentially distributed localized (trap) states.[51] Given the higher value of β in the PFN-based devices (especially at the longer time), one may conclude that recombination via trap states has been enhanced in the presence of the PFN. The charge extraction results are in good agreement with light-intensity dependency as well as photovoltage decay results.

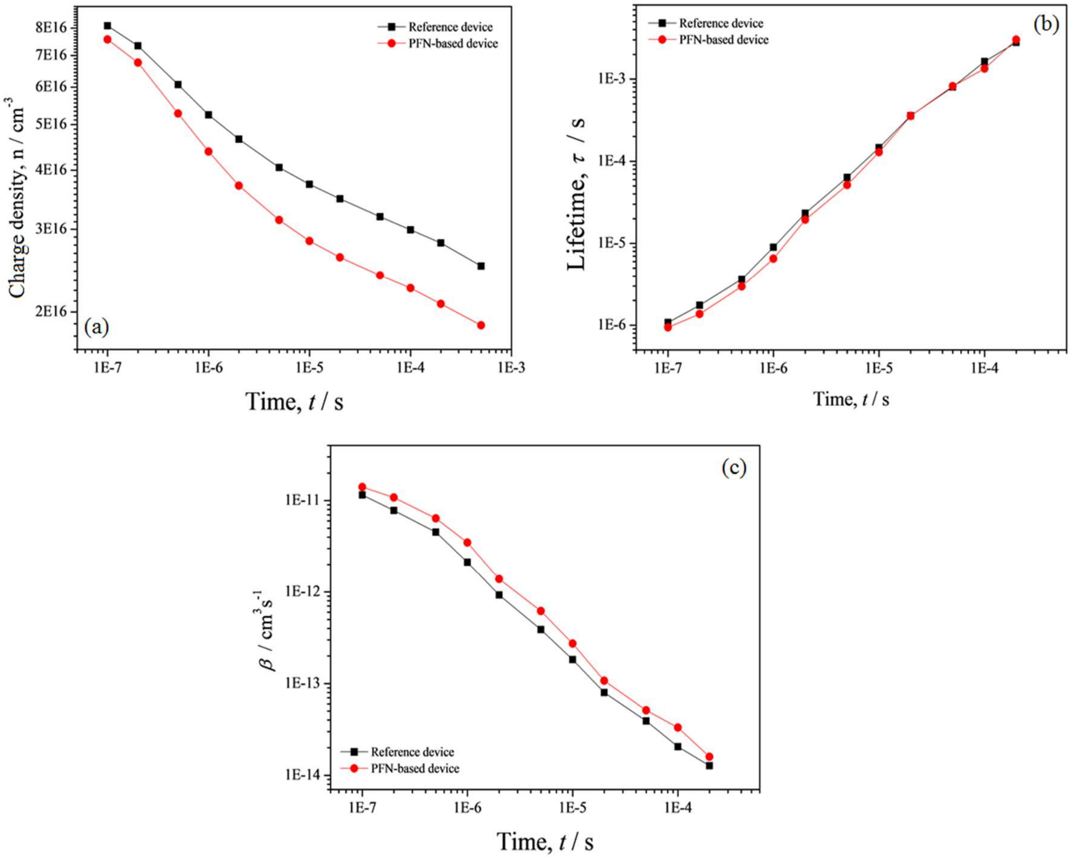

Figure 3.8. (a) Charge density and (b) bimolecular recombination lifetime and (c) bimolecular recombination coefficient (β) as a function of time of the PCDTBT:PC$_{70}$BM solar cell devices without (black line) and with (red line) the PFN interlayer. The concentration of PFN solution was 0.5 mg/ml. The PFN solution was cast at 5000 rpm.

3.3.7. Photo-CELIV Measurement

In order to study the effect of the PFN interfacial layer on the transportation of the charge carriers, the mobility of the PCDTBT:PC$_{70}$BM BHJ solar cell devices before and after insertion of the PFN interlayer is measured by photo-CELIV technique. The photo-CELIV curves of the devices under illumination and in the dark are shown in Figure 3.9. the calculated mobility based on equation (2-7) is 1.2×10^{-5} cm^2 V^{-1} s^{-1} prior to insertion of the PFN interlayer. Once the interlayer is introduced, the mobility is calculated to be 1.01×10^{-5} cm^2 V^{-1} s^{-1}. The mobility values are quite similar and imply that mobility of the charge carriers has not improved by the inclusion of the PFN interlayer between the active layer and the cathode electrode. Given that, similar values of short-circuit current and fill factor can be attributed to the almost equal charge carrier mobility before and after the incorporation of the PFN interlayer.

He *et al.*[5] claimed that the introduction of the PFN gives rise to a more balanced as well as increased charge carrier mobility. The results showed that electron mobility was slightly increased, whereas hole mobility was enhanced by almost one order of magnitude (from 3.2×10^{-4} cm^2 V^{-1} s^{-1} to 1.7×10^{-3} cm^2 V^{-1} s^{-1}) following incorporation of the PFN interlayer. The authors claim that increased charge carrier mobility is due to boost of V_{bi} across the device and strong local field at the interface which cause the charge carriers escape shallow traps and acquire subsequently higher mobility. As mentioned earlier, PFN did not rise to enhancement of V_{bi} here. Notably, there are some reports that show methanol treatment can enhance the mobility of charge carriers.[41,42,52] For example, Zhang *et al.*[6] claimed that upon methanol treatment of the PCDTBT:PC$_{70}$BM film, no change in electron mobility was observed whereas the hole mobility was improved. Given that the PFN cast from methanol solvent, the observed enhanced mobility with PFN may come from methanol treatment. Nevertheless, no change on the charge carrier mobility was observed here. Noteworthy that the charge carrier mobility in the abovementioned publications was measured by space charge limited current (SCLC) model in conjunction with Mott-Gurney law. In the SCLC regime, the current characteristic is quadratic ($I \sim V^2$) and depends only on the charge carrier mobility. Hence, the mobility can be estimated by the Mott-Gurney law from a simple current-voltage measurement.[53] Given that mobility is charge density dependent, the difference between mobility results reported here and those reported in the literature may come from variation of charge density across the devices. It should also be mentioned that operational devices are used in photo-CELIV measurement, whereas SCLC technique can be only performed on electron-only or hole-only devices.

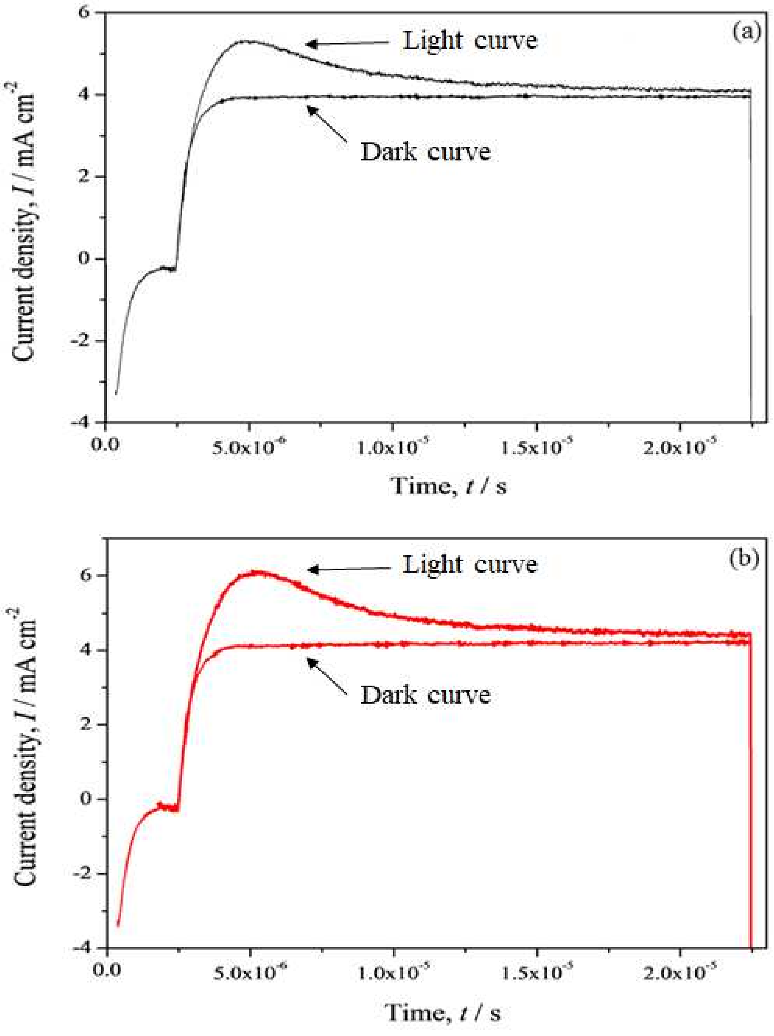

Figure 3.9. Light and dark photo-CELIV curves of the PCDTBT:$PC_{70}BM$ solar cell devices (a) without and (b) with PFN interlayer. The applied voltage was 2 *V* with a width of 5 µs. The delay time between photogeneration and extraction was set 2 µs. The laser intensity was 10 µj.

3.4. CONCLUSION

The interface between the PCDTBT:PC$_{70}$BM bulk heterojunction and the cathode electrode (aluminum) was modified by the insertion of PFN as an electron transport layer. Several solutions with various concentration of PFN were prepared and the solutions were spin-coated on top the BHJ active layer by varying the spin velocity from 1000 to 8000 rpm. The photovoltaic characteristics of the solar cell devices were investigated as a function of PFN interlayer. Upon incorporation of the PFN interlayer, no significant enhancement regarding the overall performance of the BHJ solar cell devices was observed contradictory to the published work.[5,6] Charge carrier dynamics of the devices including generation, recombination, and mobility were examined and found to be quite similar or slightly degraded after deposition of the PFN interlayer. It is concluded that either the contact between BHJ and the cathode electrode is ideal and ohmic that can no longer be boosted by the interlayer or the PFN film would have been destroyed during thermal evaporation of the cathode electrode.

3.5. FUTURE WORK

While the body of the work presented in this chapter has disputed the impact of the PFN on improving the performance of the BHJ solar cell, a few aspects could be further examined. Firstly, establish a procedure to determine the thickness of the optimal PFN film (if any) accurately rather than inferring PFN thickness through extrapolation technique and changing concentration and deposition speed rates. This includes using different techniques such as AFM, SEM and/or TEM simultaneously to verify the thickness fo the PFN on both bare glass and BHJ active layer. Another aspect is to examine the effect of the PFN (if any) on different BHJ systems such as small molecules and polymer-polymer.

3.6. APPENDIX

PFN solution concentration - 0.5 mg / 1 cc

Table 3.6.1. Photovoltaic parameters of the PCDTBT:$PC_{70}BM$ solar cell devices without and with the PFN interlayer. The concentration of the PFN solution was 0.5 mg/ml. The results are average of 12 devices.

	V_{oc} (*mV*)	**J_{sc} (*mA cm*$^{-2}$)**	**FF**	**PCE (%)**
Reference	886.33 ± 5.2	10.82 ± 0.96	0.52 ± 0.05	5 ± 0.4
1000 rpm	400.5 ± 74.2	0.8 ± 0.1	0.21 ± 0.01	0.07 ± 0.02
2000 rpm	892 ± 8.8	9.5 ± 0.9	0.36 ± 0.04	3.03 ± 0.6
3000 rpm	881.4 ± 8.3	8.7 ± 3.4	0.46 ± 0.02	4.1 ± 0.1
4000 rpm	892.7 ± 8.8	9.9 ± 0.3	0.50 ± 0.02	4.5 ± 0.3
5000 rpm	899.1 ± 8.5	10.2 ± 0.1	0.52 ± 0.01	4.7 ± 0.1
6000 rpm	892.7 ± 8.8	9.5 ± 0.6	0.43 ± 0.02	3.65 ± 0.2
7000 rpm	873.5 ± 25.5	8.9 ± 0.8	0.49 ± 0.03	3.8 ± 0.5
8000 rpm	886.35 ± 2.1	9.9 ± 0.79	0.45 ± 0.01	4 ± 0.2

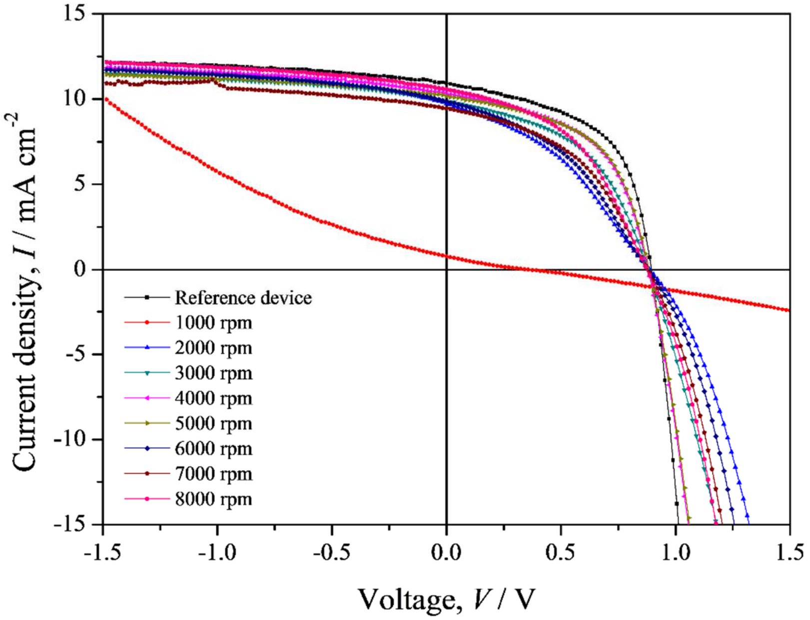

Figure 3.6.1. Comparison of the current density-voltage curves of PCDTBT:$PC_{70}BM$ solar cell devices without and with the PFN interlayer as a function of the spin speed of the PFN solution casting. The concentration of the PFN solution was 0.5 mg/ml.

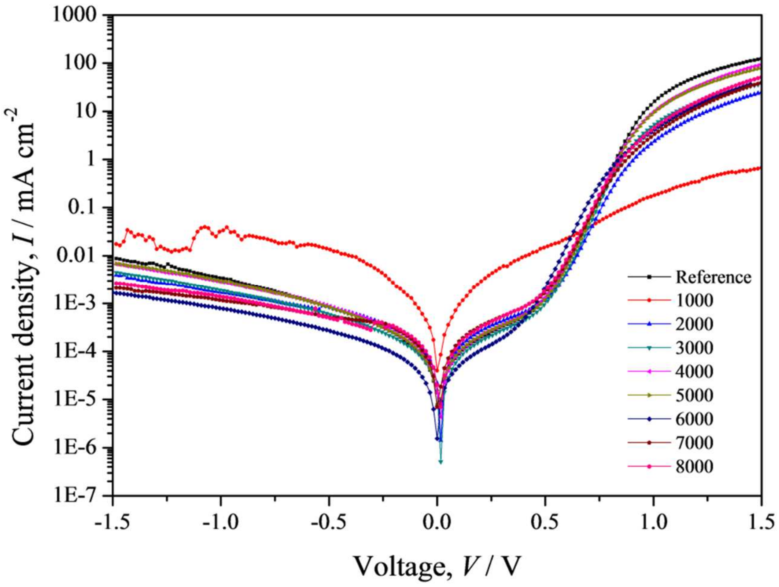

Figure 3.6.2. Comparison of the dark current density of PCDTBT:PC$_{70}$BM solar cell devices without (black line) and with (red line) the PFN interlayer as a function of the spin speed of the PFN solution casting. The concentration of the PFN solution was 0.5 mg/ml.

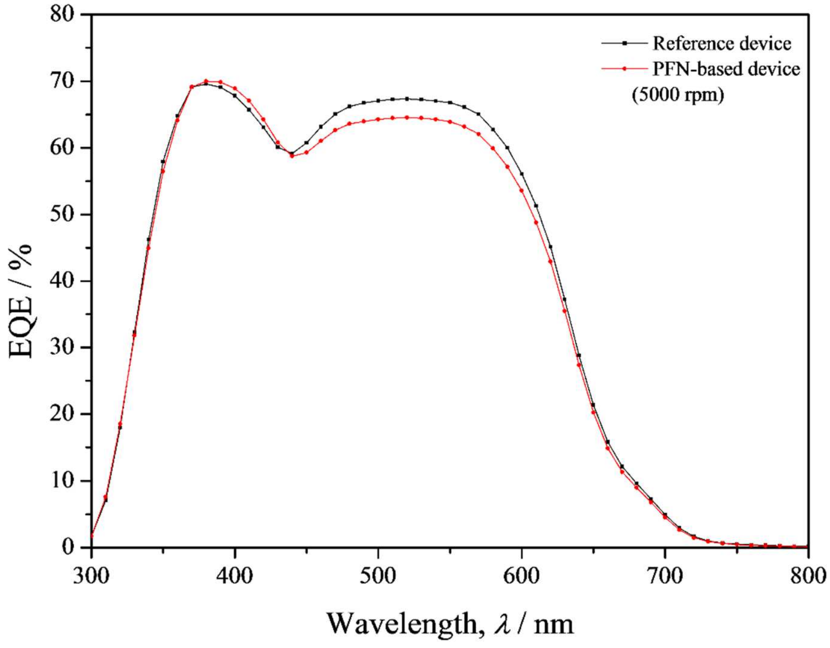

Figure 3.6.3. External quantum efficiency of PCDTBT:PC$_{70}$BM solar cells without and with the PFN interlayer cast at the spin speed of 5000 rpm. The concentration of the PFN solution was 0.5 mg/ml. The J_{sc} obtained from EQE for reference and PFN-based devices are 10.37, and 10.01 $mA\ cm^{-2}$, respectively.

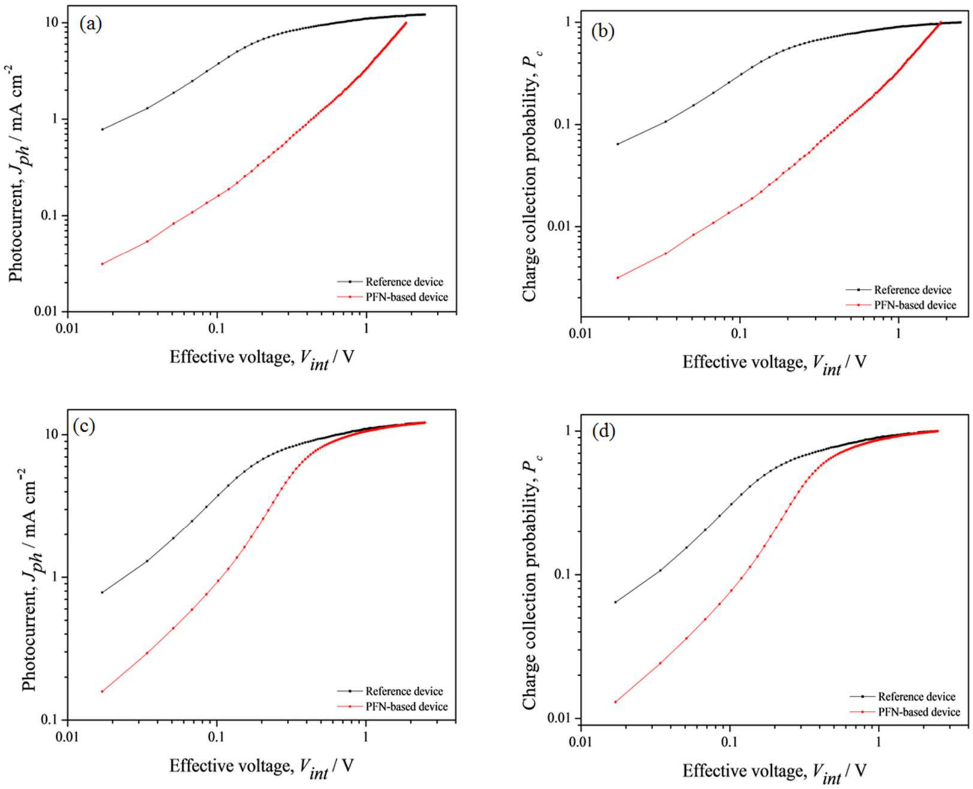

Figure 3.6.4. (a) & (c) Photocurrent density and (b) & (d) charge collection probability as a function of the effective voltage of PCDTBT:$PC_{70}BM$ solar cell devices without (black line) and with (red line) the PFN interlayer. The spin speed for (a) & (b) devices is 1000 rpm. The spin speed for (c) & (d) is 8000 rpm. The concentration of PFN solution was 0.5 mg/ml.

PFN solution concentration - 0.4 mg / cc

Table 3.6.2. Photovoltaic parameters of the PCDTBT:$PC_{70}BM$ solar cell devices without and with the PFN interlayer. The concentration of the PFN solution was 0.4 mg/ml. Eight devices were measured and averaged.

	V_{oc} (mV)	J_{sc} (mA/cm^2)	FF	PCE (%)
Reference	854.1 ± 5.7	10.02 ± 0.6	0.48 ± 0.02	4.1 ± 0.2
1000 rpm	855.7 ± 3.2	7.3 ± 0.2	0.47 ± 0.005	3 ± 0.1
2000 rpm	860.2 ± 2.8	8.03 ± 0.7	0.42 ± 0.03	3 ± 0.3
3000 rpm	857 ± 5.2	8.7 ± 0.07	0.43 ± 0.01	3.2 ± 0.06
4000 rpm	864.2 ± 5.5	9 ± 0.2	0.42 ± 0.01	3.25 ± 0.03
5000 rpm	863.7± 4.5	8.95 ± 0.1	0.45 ± 0.02	3.46 ± 0.1
6000 rpm	856.3 ± 3.5	8.2 ± 0.4	0.46 ± 0.01	3.20 ± 0.1
7000 rpm	862.3 ± 5.1	8.6 ± 0.8	0.44 ± 0.01	3.3 ± 0.3
8000 rpm	855.2 ± 2.5	7.9 ± 0.3	0.47 ± 0.01	3.2 ± 0.2

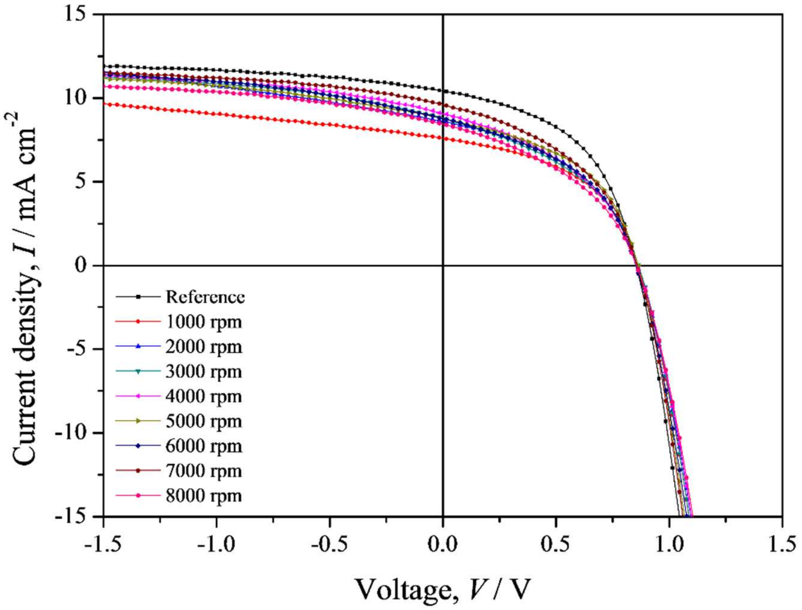

Figure 3.6.5. Comparison of the current density-voltage curves of PCDTBT:$PC_{70}BM$ solar cell devices without and with the PFN interlayer as a function of the spin speed of the PFN solution casting. The concentration of the PFN solution was 0.4 mg/ml.

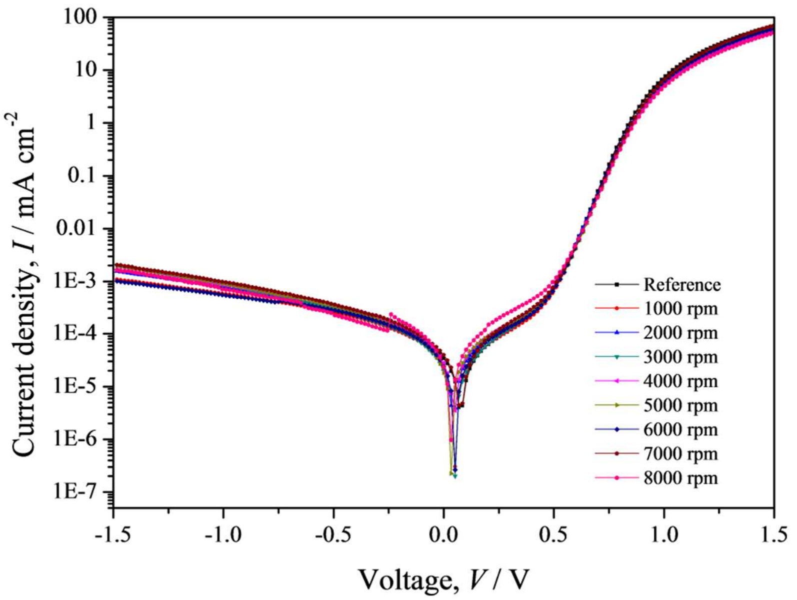

Figure 3.6.6. Comparison of the dark current density of PCDTBT:PC$_{70}$BM solar cell devices without and with the PFN interlayer as a function of the spin speed of the PFN solution casting. The concentration of the PFN solution was 0.4 mg/ml.

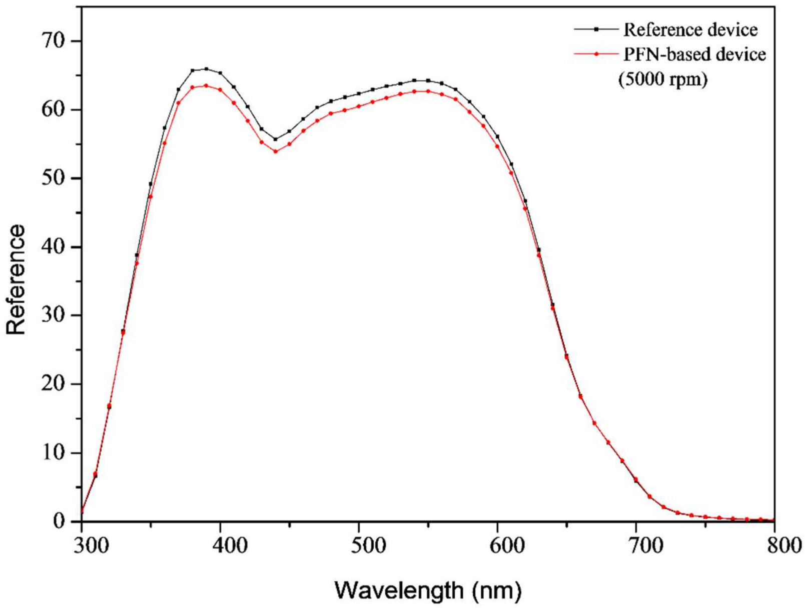

Figure 3.6.7. External quantum efficiency of PCDTBT:PC$_{70}$BM solar cells without and with the PFN interlayer cast at the spin speed of 5000 rpm. The concentration of the PFN solution was 0.4 mg/ml. The obtained J_{sc} from EQE for the reference and PFN-based devices are 10.08, and 9.13 $mA\ cm^{-2}$.

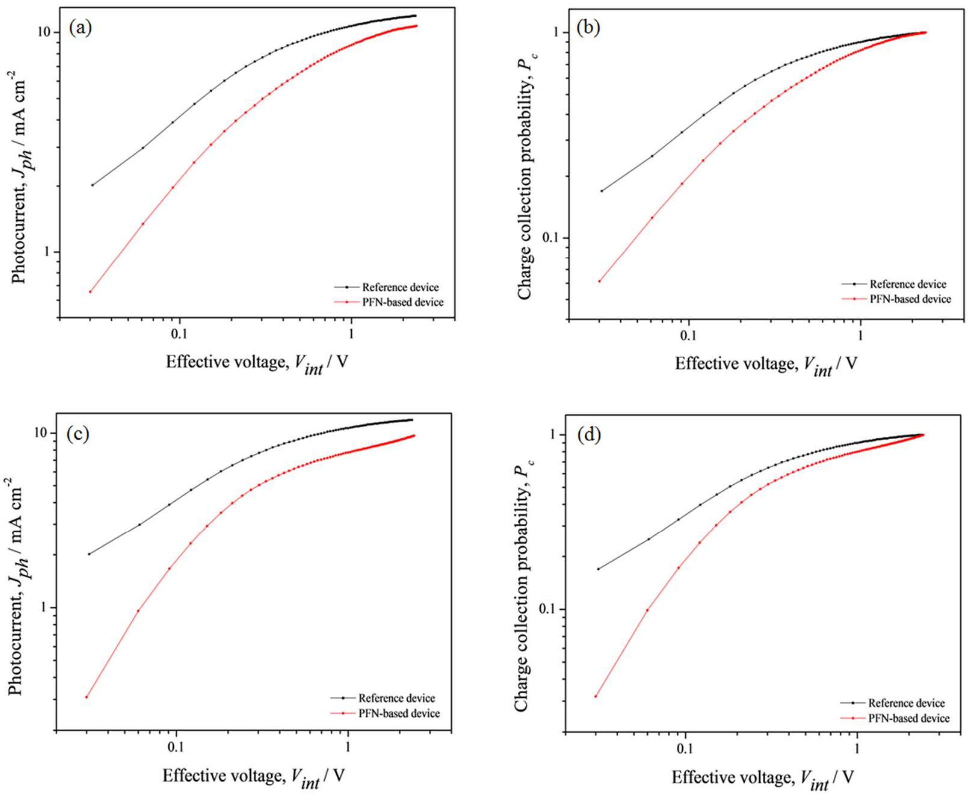

Figure 3.6.8. (a) & (c) Photocurrent density and (b) & (d) charge collection probability as a function of the effective voltage of PCDTBT:PC$_{70}$BM solar cell devices without (black line) and with (red line) the PFN interlayer. The spin speed for (a) & (b) devices is 1000 rpm. The spin speed for (c) & (d) is 8000 rpm. The concentration of PFN solution was 0.4 mg/ml.

PFN solution concentration - 0.3 mg / cc

Table 3.6.3. Photovoltaic parameters of the PCDTBT:$PC_{70}BM$ solar cell devices without and with the PFN interlayer. The concentration of the PFN solution was 0.3 mg/ml. The results are average of 8 devices.

	V_{oc} (mV)	J_{sc} ($mA\ cm^{-2}$)	FF	PCE (%)
Reference	890.6 ± 8	10.7 ± 0.25	53.3 ± 0.01	5.1 ± 0.25
1000	890.5 ± 9.9	9.53 ± 0.6	36.7 ± 2.7	3.13 ± 0.4
2000	891.1 ± 4.8	10.1 ± 0.3	37.6 ± 1.9	3.4 ± 0.3
3000	893.7 ± 5.7	9.66 ± 0.2	38.3 ± 3.5	3.3 ± 0.37
4000	897.9 ± 6.4	9.8 ± 0.4	44 ± 4	3.9 ± 0.4
5000	889.8 ± 1.8	9.6 ± 0.4	0.51 ± 0.01	4.4 ± 0.2
6000	881.5 ± 16	10.8 ± 0.6	53 ± 0.03	5.1 ± 0.5
7000	886.4 ± 4	10.7 ± 0.6	54.7 ± 0.01	5.2 ± 0.2
8000	876.1 ± 9.3	10.8 ± 0.4	51 ± 0.05	4.8 ± 0.5

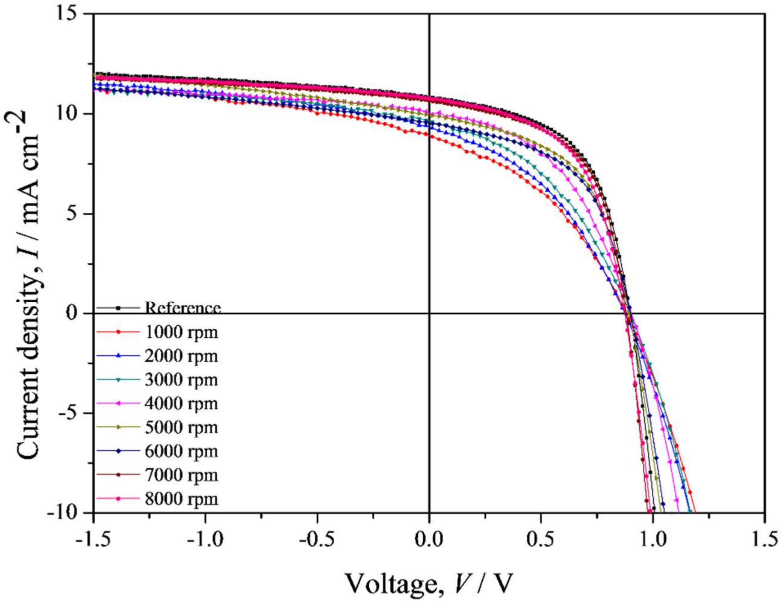

Figure 3.6.9. Current density-voltage curves of PCDTBT:$PC_{70}BM$ solar cell devices without and with the PFN interlayer cast at different spin speeds. The concentration of the PFN solution was 0.3 mg/ml.

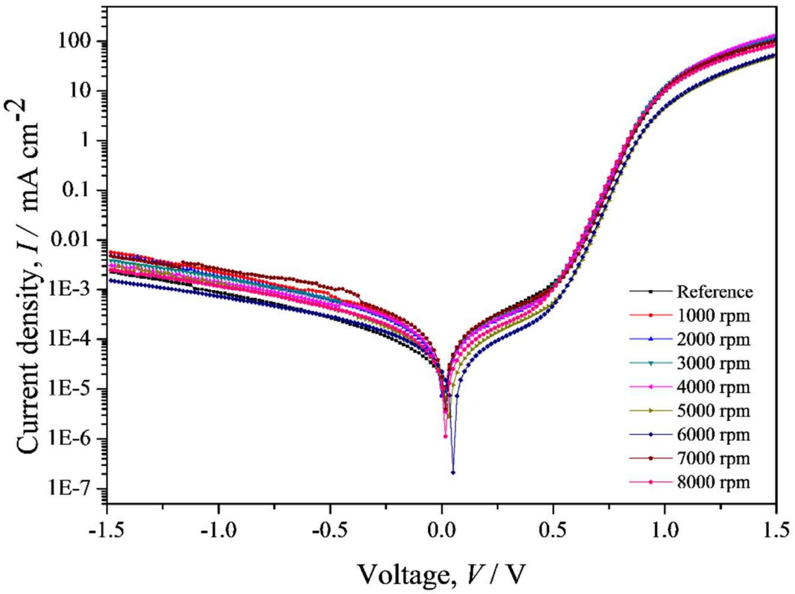

Figure 3.6.10. Comparison of the dark current density of PCDTBT:$PC_{70}BM$ solar cell devices without and with the PFN interlayer as a function of the spin speed of the PFN solution casting. The concentration of the PFN solution was 0.3 mg/ml.

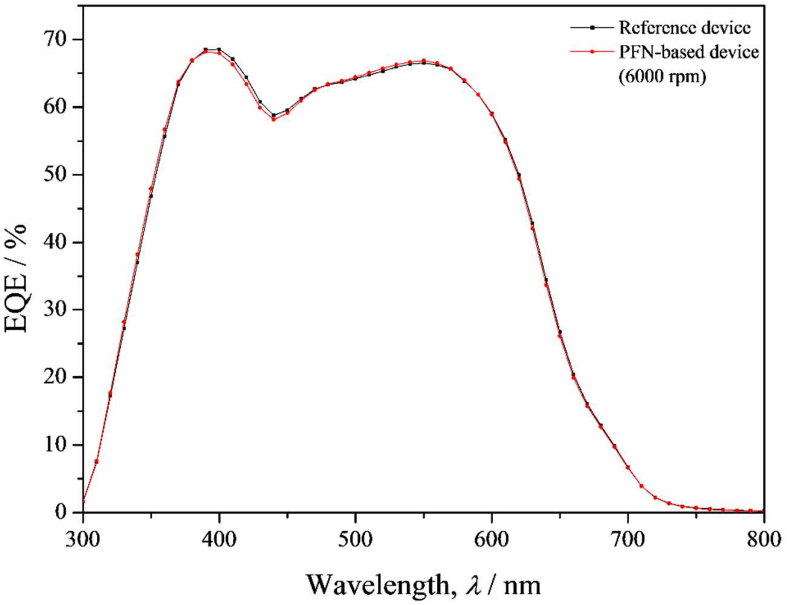

Figure 3.6.11. External quantum efficiency of PCDTBT:$PC_{70}BM$ solar cells without and with the PFN interlayer cast at the spin speed of 6000 rpm. The concentration of the PFN solution was 0.3 mg/ml. The obtained J_{sc} from EQE for the reference and PFN-based devices are 10.57, and 10.53 $mA\ cm^{-2}$, respectively.

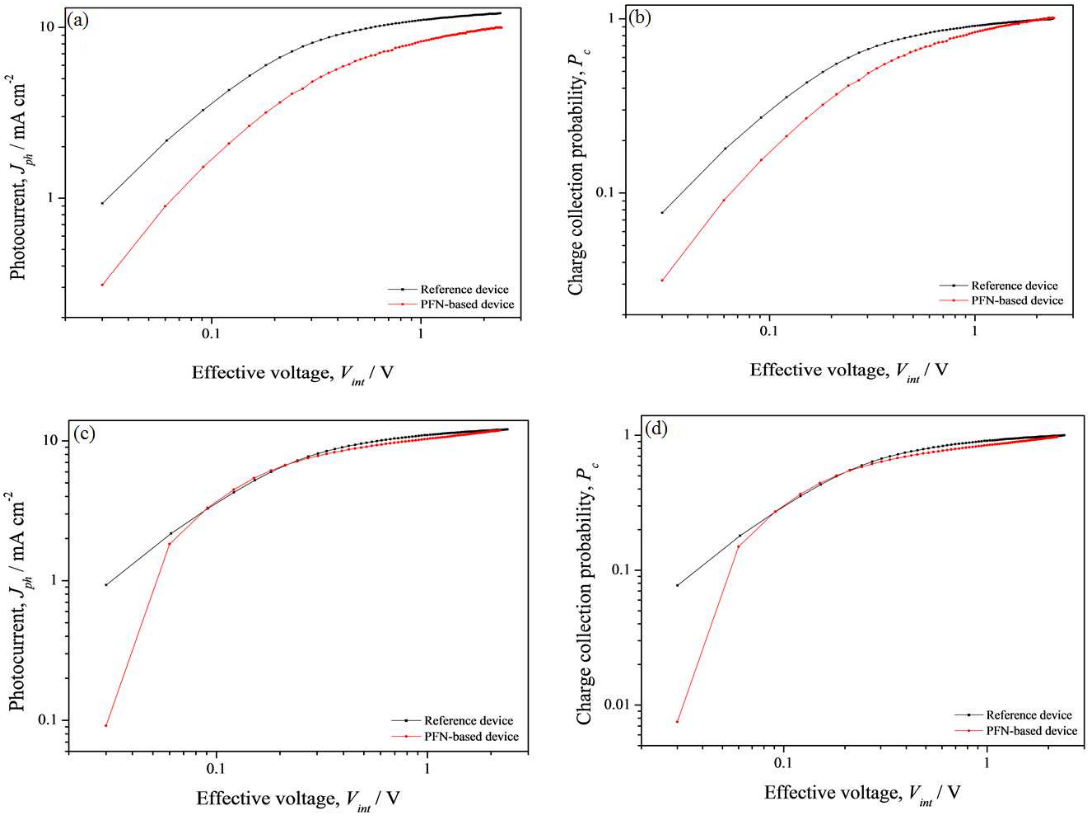

Figure 3.6.12. (a) & (c) Photocurrent density and (b) & (d) charge collection probability as a function of the effective voltage of PCDTBT:PC$_{70}$BM solar cell devices without (black line) and with (red line) the PFN interlayer. The spin speed for (a) & (b) devices is 1000 rpm. The spin speed for (c) & (d) is 8000 rpm. The concentration of PFN solution was 0.3 mg/ml.

PFN solution concentration - 0.2 mg / cc

Table 3.6.4. Photovoltaic parameters of the PCDTBT:PC$_{60}$BM solar cell devices without and with the PFN interlayer. The concentration of the PFN solution was 0.2 mg/ml. The results are average of 8 devices. The acceptor is PC$_{60}$BM.

	V_{oc} (*mV*)	J_{sc} (*mAcm*$^{-2}$)	FF	PCE (%)
Reference	847.8 ± 4.5	6.81 ± 0.42	0.51 ± 0.006	2.93 ± 0.14
1000 rpm	855.8 ± 7.6	6.51 ± 0.55	0.49 ± 0.009	2.75 ± 0.2
2000 rpm	846.3 ± 8.6	6.34 ± 0.13	0.47 ± 0.002	2.56 ± 0.12
3000 rpm	850.8 ± 4.3	6.5 ± 0.3	0.48 ± 0.03	2.7 ± 0.09
4000 rpm	831 ± 7.9	6.6 ± 0.22	0.47 ± 0.03	2.6 ± 0.15
5000 rpm	837 ± 3.8	7.11 ± 0.4	47.9 ± 0.006	2.85 ± 0.2
6000 rpm	844.3 ± 5.1	6.61 ± 0.25	0.52 ± 0.016	2.9 ± 0.06
7000 rpm	854.25 ± 8.5	6.9 ± 0.6	0.5 ± 0.42	2.94 ± 0.3
8000 rpm	857 ± 6.3	6.53 ± 0.4	0.55 ± 0.09	3.1 ± 0.1

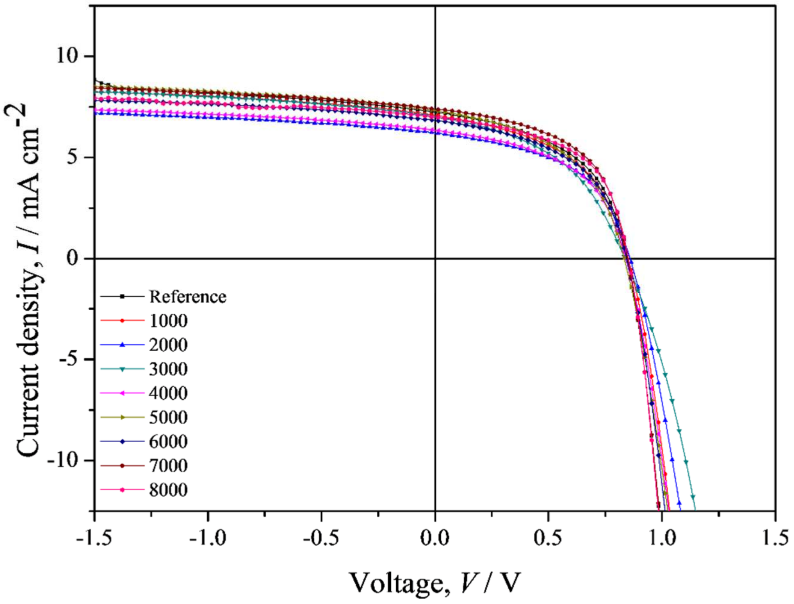

Figure 3.6.13. Comparison of the current density-voltage curves of PCDTBT:PC$_{60}$BM solar cell devices without and with the PFN interlayer as a function of the spin speed of the PFN solution casting. The concentration of the PFN solution was 0.2 mg/ml. The acceptor is PC$_{60}$BM.

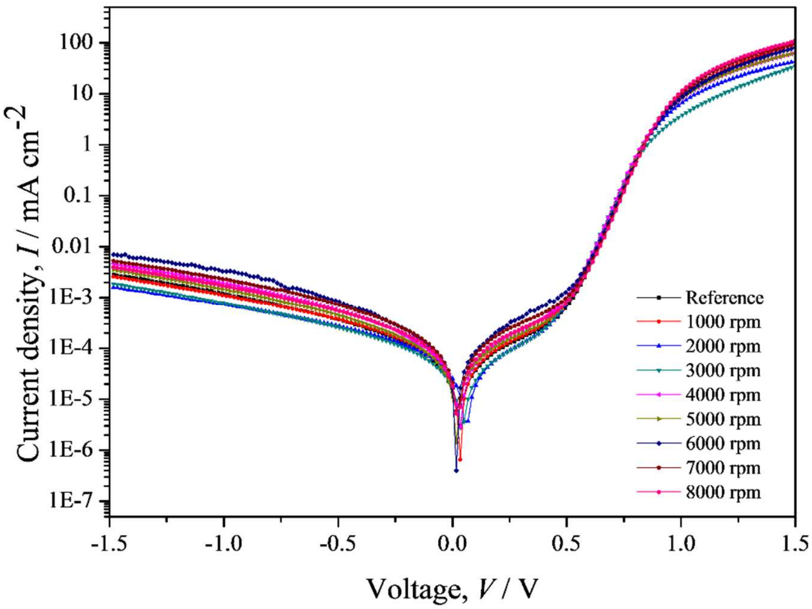

Figure 3.6.14. Comparison of the dark current density of PCDTBT:$PC_{60}BM$ solar cell devices without and with the PFN interlayer cast at different rpm. The concentration of the PFN solution was 0.2 mg/ml.

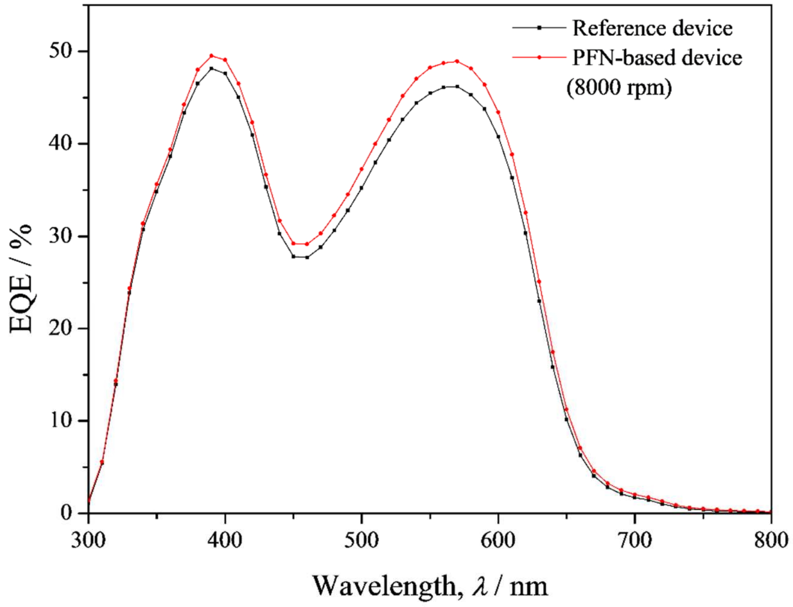

Figure 3.6.15. External quantum efficiency of PCDTBT:$PC_{60}BM$ solar cells without and with the PFN interlayer cast at the spin speed of 8000 rpm. The concentration of the PFN solution was 0.2 mg/ml. The acceptor is $PC_{60}BM$. The obtained J_{sc} from EQE for the reference and PFN-based devices are 6.25 and 6.62 $mA\ cm^{-2}$, respectively.

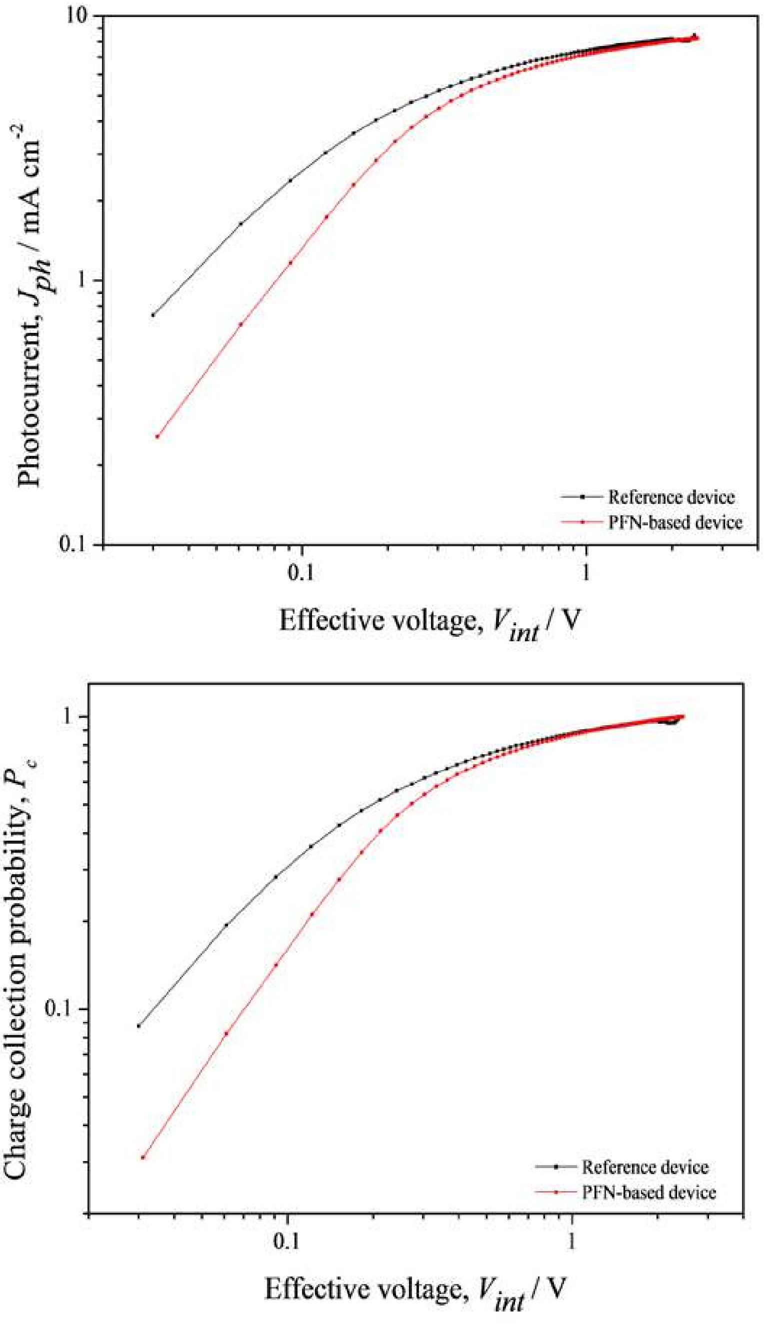

Figure 3.6.16. (a) Photocurrent density and (b) charge collection probability as a function of the effective voltage of PCDTBT:PC$_{60}$BM solar cell devices without (black line) and with (red line) the PFN interlayer. The spin speed was 1000 rpm. The concentration of PFN solution was 0.2 mg/ml.

3.7. REFERENCES

(1) Park, J. H.; Lee, T.-W.; Chin, B.-D.; Wang, D. H.; Park, O. O. Roles of Interlayers in Efficient Organic Photovoltaic Devices. *Macromolecular Rapid Communications* **2010,** *31* (24), 2095.

(2) Steim, R.; Kogler, F. R.; Brabec, C. J. Interface materials for organic solar cells. *Journal of Materials Chemistry* **2010,** *20* (13), 2499.

(3) Po, R.; Carbonera, C.; Bernardi, A.; Camaioni, N. The role of buffer layers in polymer solar cells. *Energy & Environmental Science* **2011,** *4* (2), 285.

(4) Yin, Z.; Wei, J.; Zheng, Q. Interfacial Materials for Organic Solar Cells: Recent Advances and Perspectives. *Adv Sci (Weinh)* **2016,** *3* (8), 1500362.

(5) He, Z.; Zhong, C.; Huang, X.; Wong, W.-Y.; Wu, H.; Chen, L.; Su, S.; Cao, Y. Simultaneous Enhancement of Open-Circuit Voltage, Short-Circuit Current Density, and Fill Factor in Polymer Solar Cells. *Advanced Materials* **2011,** *23* (40), 4636.

(6) Kai, Z.; Zhicheng, H.; Chunhui, D.; Lei, Y.; Fei, H.; Yong, C. The effect of methanol treatment on the performance of polymer solar cells. *Nanotechnology* **2013,** *24* (48), 484003.

(7) He, C.; Zhong, C.; Wu, H.; Yang, R.; Yang, W.; Huang, F.; Bazan, G. C.; Cao, Y. Origin of the enhanced open-circuit voltage in polymer solar cells via interfacial modification using conjugated polyelectrolytes. *Journal of Materials Chemistry* **2010,** *20* (13), 2617.

(8) He, Z.; Zhong, C.; Su, S.; Xu, M.; Wu, H.; Cao, Y. Enhanced power-conversion efficiency in polymer solar cells using an inverted device structure. *Nat Photon* **2012,** *6* (9), 591.

(9) Li, S.; He, Z.; Yu, J.; Chen, S. a.; Zhong, A.; Tang, R.; Wu, H.; Qin, J.; Li, Z. How the linkage positions affect the performance of bulk-heterojunction polymer solar cells. *Journal of Materials Chemistry* **2012,** *22* (25), 12523.

(10) Kazuya, T. Effect of conjugated polyelectrolyte interlayer at cathode in bulk heterojunction photocells based on neat C 70 and low-energy-gap polymer prepared with halogen-free solvent. *Applied Physics Express* **2014,** *7* (5), 051601.

(11) Qin, H.; Li, L.; Guo, F.; Su, S.; Peng, J.; Cao, Y.; Peng, X. Solution-processed bulk heterojunction solar cells based on a porphyrin small molecule with 7% power conversion efficiency. *Energy & Environmental Science* **2014,** *7* (4), 1397.

(12) Lee, B. H.; Lee, J.-H.; Jeong, S. Y.; Park, S. B.; Lee, S. H.; Lee, K. Broad Work-Function Tunability of p-Type Conjugated Polyelectrolytes for Efficient Organic Solar Cells. *Advanced Energy Materials* **2015,** *5* (5), 1401653.

(13) Shi, H.; Fu, W.; Shi, M.; Ling, J.; Chen, H. A solution-processable bipolar diketopyrrolopyrrole molecule used as both electron donor and acceptor for efficient organic solar cells. *Journal of Materials Chemistry A* **2015,** *3* (5), 1902.

(14) Ai, L.; Ouyang, X.; Liu, Z.; Peng, R.; Mi, D.; Kakimoto, M.-a.; Ge, Z. Multi-channel interface dipole of hyperbranched polymers with quasi-immovable hydrion to modification of cathode interface for high-efficiency polymer solar cells. *Progress in Photovoltaics: Research and Applications* **2016,** *24* (8), 1044.

(15) Guo, B.; Zhou, W.; Wu, M.; Lv, J.; Yu, C.; Li, F.; Hu, Z. Improving the efficiency of polymer solar cells via a treatment of methanol : water on the active layers. *Journal of Materials Chemistry A* **2016,** *4* (24), 9644.

(16) Huang, L.; Chen, L.; Huang, P.; Wu, F.; Tan, L.; Xiao, S.; Zhong, W.; Sun, L.; Chen, Y. Triple Dipole Effect from Self-Assembled Small-Molecules for High Performance Organic Photovoltaics. *Advanced Materials* **2016,** *28* (24), 4852.

(17) Li, S.; Liu, W.; Shi, M.; Mai, J.; Lau, T.-K.; Wan, J.; Lu, X.; Li, C.-Z.; Chen, H. A spirobifluorene and diketopyrrolopyrrole moieties based non-fullerene acceptor for

efficient and thermally stable polymer solar cells with high open-circuit voltage. *Energy & Environmental Science* **2016,** *9* (2), 604.

(18) Li, S.; Yan, J.; Li, C.-Z.; Liu, F.; Shi, M.; Chen, H.; Russell, T. P. A non-fullerene electron acceptor modified by thiophene-2-carbonitrile for solution-processed organic solar cells. *Journal of Materials Chemistry A* **2016,** *4* (10), 3777.

(19) Liu, W.; Liang, T.; Chen, Q.; Yu, Z.; Zhang, Y.; Liu, Y.; Fu, W.; Tang, F.; Chen, L.; Chen, H. Solution-Processed 8-Hydroquinolatolithium as Effective Cathode Interlayer for High-Performance Polymer Solar Cells. *ACS Applied Materials & Interfaces* **2016,** *8* (14), 9254.

(20) Wang, H.; Xiao, L.; Yan, L.; Chen, S.; Zhu, X.; Peng, X.; Wang, X.; Wong, W.-K.; Wong, W.-Y. Structural engineering of porphyrin-based small molecules as donors for efficient organic solar cells. *Chemical Science* **2016,** *7* (7), 4301.

(21) Wang, J.; Zhang, F.; An, Q.; Zhang, M.; Zhang, J.; Tang, W. Adjusting acceptor redistribution for highly efficient solvent additive-free polymer solar cells. *Journal of Materials Chemistry C* **2016,** *4* (15), 3202.

(22) Yu, Z.; Liu, W.; Fu, W.; Zhang, Z.; Yang, W.; Wang, S.; Li, H.; Xu, M.; Chen, H. An aqueous solution-processed CuOX film as an anode buffer layer for efficient and stable organic solar cells. *Journal of Materials Chemistry A* **2016,** *4* (14), 5130.

(23) Wu, H.; Huang, F.; Mo, Y.; Yang, W.; Wang, D.; Peng, J.; Cao, Y. Efficient Electron Injection from a Bilayer Cathode Consisting of Aluminum and Alcohol-/Water-Soluble Conjugated Polymers. *Advanced Materials* **2004,** *16* (20), 1826.

(24) Jun Song, H.; Hun Kim, D.; Hee Choi, M.; Won Heo, S.; Young Lee, J.; Yong Lee, J.; Kyung Moon, D. Self-organization polymer consisting of quinacridone and quaterthiophene units: Coplanar structure between benzene and thiophene linkage. *Solar Energy Materials and Solar Cells* **2013,** *117*, 285.

(25) Kesters, J.; Ghoos, T.; Penxten, H.; Drijkoningen, J.; Vangerven, T.; Lyons, D. M.; Verreet, B.; Aernouts, T.; Lutsen, L.; Vanderzande, D.et al. Imidazolium-Substituted Polythiophenes as Efficient Electron Transport Materials Improving Photovoltaic Performance. *Advanced Energy Materials* **2013,** *3* (9), 1180.

(26) Kim, J.-H.; Song, C. E.; Kim, H. U.; Grimsdale, A. C.; Moon, S.-J.; Shin, W. S.; Choi, S. K.; Hwang, D.-H. High Open Circuit Voltage Solution-Processed Tandem Organic Photovoltaic Cells Employing a Bottom Cell Using a New Medium Band Gap Semiconducting Polymer. *Chemistry of Materials* **2013,** *25* (13), 2722.

(27) Li, S.; Zhao, B.; He, Z.; Chen, S. a.; Yu, J.; Zhong, A.; Tang, R.; Wu, H.; Li, Q.; Qin, J.et al. Synthesis, characterization and photovoltaic performances of D-A copolymers based on BDT and DBPz: the largely improved performance caused by additional thiophene blocks. *Journal of Materials Chemistry A* **2013,** *1* (14), 4508.

(28) Song, H.-J.; Kim, D.-H.; Lee, E.-J.; Moon, D.-K. Conjugated polymers consisting of quinacridone and quinoxaline as donor materials for organic photovoltaics: orientation and charge transfer properties of polymers formed by phenyl structures with a quinoxaline derivative. *Journal of Materials Chemistry A* **2013,** *1* (19), 6010.

(29) Cheng, X.; Sun, S.; Chen, Y.; Gao, Y.; Ai, L.; Jia, T.; Li, F.; Wang, Y. A water-soluble metallophthalocyanine derivative as a cathode interlayer for highly efficient polymer solar cells. *Journal of Materials Chemistry A* **2014,** *2* (31), 12484.

(30) Fu, W.; Wang, L.; Zhang, Y.; Ma, R.; Zuo, L.; Mai, J.; Lau, T.-K.; Du, S.; Lu, X.; Shi, M.et al. Improving Polymer/Nanocrystal Hybrid Solar Cell Performance via Tuning Ligand Orientation at CdSe Quantum Dot Surface. *ACS Applied Materials & Interfaces* **2014,** *6* (21), 19154.

(31) Zhang, Z.-G.; Qi, B.; Jin, Z.; Chi, D.; Qi, Z.; Li, Y.; Wang, J. Perylene diimides: a thickness-insensitive cathode interlayer for high performance polymer solar cells. *Energy & Environmental Science* **2014,** *7* (6), 1966.

(32) Zhu, E.; Luo, G.; Liu, Y.; Yu, J.; Zhang, F.; Che, G.; Wu, H.; Tang, W. Design and photovoltaic characterization of dithieno[3,2-b:2[prime or minute],3[prime or minute]-d]silole copolymers with positioning phenyl groups. *Physical Chemistry Chemical Physics* **2014,** *16* (48), 26893.

(33) Xie, Z.; Xiao, B.; He, Z.; Zhang, W.; Wu, X.; Wu, H.; Wurthner, F.; Wang, C.; Xie, F.; Liu, L.et al. Self-assembled perylene bisimide J-aggregates as promising cathode modifiers for highly efficient inverted polymer solar cells. *Materials Horizons* **2015,** *2* (5), 514.

(34) Zhang, Q.; Kan, B.; Liu, F.; Long, G.; Wan, X.; Chen, X.; Zuo, Y.; Ni, W.; Zhang, H.; Li, M.et al. Small-molecule solar cells with efficiency over 9%. *Nat Photon* **2015,** *9* (1), 35.

(35) Wang, J.-L.; Xiao, F.; Yan, J.; Liu, K.-K.; Chang, Z.-F.; Zhang, R.-B.; Wu, H.-B.; Cao, Y. Toward high performance indacenodithiophene-based small-molecule organic solar cells: investigation of the effect of fused aromatic bridges on the device performance. *Journal of Materials Chemistry A* **2016,** *4* (6), 2252.

(36) Xu, W.; Liu, Y.; Huang, X.; Jiang, L.; Li, Q.; Hu, X.; Huang, F.; Gong, X.; Cao, Y. Solution-processed VOx prepared using a novel synthetic method as the hole extraction layer for polymer solar cells. *Journal of Materials Chemistry C* **2016,** *4* (10), 1953.

(37) Long, G.; Wan, X.; Kan, B.; Hu, Z.; Yang, X.; Zhang, Y.; Zhang, M.; Wu, H.; Huang, F.; Su, S.et al. Impact of the Electron-Transport Layer on the Performance of Solution-Processed Small-Molecule Organic Solar Cells. *ChemSusChem* **2014,** *7* (8), 2358.

(38) Srinivasan, M. V.; Ito, M.; Kumar, P.; Abhirami, K.; Tsuda, N.; Yamada, J.; Shin, P.-K.; Ochiai, S. Performance Evaluation of an Organic Thin-Film Solar Cell of PTB7:PC71BM with an Alcohol-Soluble Polyelectrolyte Interlayer Prepared Using the Spray-Coating Method. *Industrial & Engineering Chemistry Research* **2015,** *54* (1), 181.

(39) Hu, Z.; Zhong, Z.; Chen, Y.; Sun, C.; Huang, F.; Peng, J.; Wang, J.; Cao, Y. Energy-Level Alignment at the Organic/Electrode Interface in Organic Optoelectronic Devices. *Advanced Functional Materials* **2016,** *26* (1), 129.

(40) He, Z.; Zhang, C.; Xu, X.; Zhang, L.; Huang, L.; Chen, J.; Wu, H.; Cao, Y. Largely Enhanced Efficiency with a PFN/Al Bilayer Cathode in High Efficiency Bulk Heterojunction Photovoltaic Cells with a Low Bandgap Polycarbazole Donor. *Advanced Materials* **2011,** *23* (27), 3086.

(41) Lv, M.; Li, S.; Jasieniak, J. J.; Hou, J.; Zhu, J.; Tan, Z. a.; Watkins, S. E.; Li, Y.; Chen, X. A Hyperbranched Conjugated Polymer as the Cathode Interlayer for High-Performance Polymer Solar Cells. *Advanced Materials* **2013,** *25* (47), 6889.

(42) Zhou, H.; Zhang, Y.; Seifter, J.; Collins, S. D.; Luo, C.; Bazan, G. C.; Nguyen, T.-Q.; Heeger, A. J. High-Efficiency Polymer Solar Cells Enhanced by Solvent Treatment. *Advanced Materials* **2013,** *25* (11), 1646.

(43) Servaites, J. D.; Ratner, M. A.; Marks, T. J. Organic solar cells: A new look at traditional models. *Energy & Environmental Science* **2011,** *4* (11), 4410.

(44) Liu, S.; Zhang, G.; Lu, J.; Jia, J.; Li, W.; Huang, F.; Cao, Y. An alcohol soluble amino-functionalized organoplatinum(ii) complex as the cathode interlayer for highly efficient polymer solar cells. *Journal of Materials Chemistry C* **2015,** *3* (17), 4372.

(45) Kyaw, A. K. K.; Wang, D. H.; Gupta, V.; Leong, W. L.; Ke, L.; Bazan, G. C.; Heeger, A. J. Intensity Dependence of Current–Voltage Characteristics and Recombination in

High-Efficiency Solution-Processed Small-Molecule Solar Cells. *ACS Nano* **2013,** *7* (5), 4569.

(46) Kyaw, A. K. K.; Wang, D. H.; Wynands, D.; Zhang, J.; Nguyen, T.-Q.; Bazan, G. C.; Heeger, A. J. Improved Light Harvesting and Improved Efficiency by Insertion of an Optical Spacer (ZnO) in Solution-Processed Small-Molecule Solar Cells. *Nano Letters* **2013,** *13* (8), 3796.

(47) Koster, L. J. A.; Mihailetchi, V. D.; Ramaker, R.; Blom, P. W. M. Light intensity dependence of open-circuit voltage of polymer:fullerene solar cells. *Applied Physics Letters* **2005,** *86* (12), 123509.

(48) Cowan, S. R.; Roy, A.; Heeger, A. J. Recombination in polymer-fullerene bulk heterojunction solar cells. *Physical Review B* **2010,** *82* (24), 245207.

(49) Heumueller, T.; Burke, T. M.; Mateker, W. R.; Sachs-Quintana, I. T.; Vandewal, K.; Brabec, C. J.; McGehee, M. D. Disorder-Induced Open-Circuit Voltage Losses in Organic Solar Cells During Photoinduced Burn-In. *Advanced Energy Materials* **2015,** *5* (14), 1500111.

(50) Maurano, A.; Hamilton, R.; Shuttle, C. G.; Ballantyne, A. M.; Nelson, J.; O'Regan, B.; Zhang, W.; McCulloch, I.; Azimi, H.; Morana, M.et al. Recombination Dynamics as a Key Determinant of Open Circuit Voltage in Organic Bulk Heterojunction Solar Cells: A Comparison of Four Different Donor Polymers. *Advanced Materials* **2010,** *22* (44), 4987.

(51) Clarke, T. M.; Peet, J.; Denk, P.; Dennler, G.; Lungenschmied, C.; Mozer, A. J. Non-Langevin bimolecular recombination in a silole-based polymer:PCBM solar cell measured by time-resolved charge extraction and resistance-dependent time-of-flight techniques. *Energy & Environmental Science* **2012,** *5* (1), 5241.

(52) Wang, Y.; Liu, Y.; Chen, S.; Peng, R.; Ge, Z. Significant Enhancement of Polymer Solar Cell Performance via Side-Chain Engineering and Simple Solvent Treatment. *Chemistry of Materials* **2013,** *25* (15), 3196.

(53) Karl, N. Charge carrier transport in organic semiconductors. *Synthetic Metals* **2003,** *133–134*, 649.

Chapter 4: A study of dielectric constant effect on the performance of bulk heterojunction solar cells Part I: Polymer-based solar cells

4.1. INTRODUCTION

To achieve high performance organic solar cells, it is necessary to suppress the recombination losses of charge carriers throughout the bulk heterojunction. It is proposed that enhancing dielectric constant properties of the bulk heterojunction can lead to reduction of the exciton binding energy, the singlet-triplet energy splitting, the reorganization energy, the Coulomb attraction within the CT exciton, the geminate recombination back to the CT state, the bimolecular and trap-assisted recombination and space-charge effects.[1] It is predicted that if one changed the dielectric constant from a low constant of e.g. 3 to a higher constant of e.g. 10, an increase in efficiency of up to 21% can result. In practice, a few attempts have been made to design and synthesize organic semiconductors (mostly polymer) with high dielectric constant. The approach was based upon structural changes of polymers by incorporation of new functional groups. For instance, Cho *et al.*[2] claimed that the dielectric constant of the PIDT-DPP-Alkyl polymer was improved from 3.5 to 5 upon incorporation a nitrile-side chain. It was further discussed that the structural change resulted in the suppression of the non-geminate recombination losses in planar heterojunction solar cell and subsequent enhancement of the performance (from 0.75% to 1.44%).[2] However, it was mentioned such a structural modification had not had any impact on the crucial properties of the polymers such as energy level or charge carrier mobility. Torabi *et al.*[3] reported a 46% increase in $PC_{60}BM$ dielectric constant (from 3.9 to 5.7) upon adding an ethylene glycol (EG) functional unit. They showed the new product had a similar electron mobility to the pristine $PC_{60}BM$, although no current-voltage results of solar cell devices with the new product were provided. On the other hand, it is shown that however, the current approach increases the dielectric constant, it is more likely give rise to lower efficient devices due to the significant suboptimal morphology of the bulk heterojunction.[4] Therefore, new approaches are necessary to improve the dielectric constant of the bulk heterojunction.

Quantitative description of dielectric constant in an electric field can be shown using Clausius-Mossotti relation:[5]

$$\mathrm{P} = \frac{\varepsilon_r - 1}{\varepsilon_r - 2} \cdot \frac{M}{\rho} = \frac{N_A \alpha}{3\varepsilon_0} \qquad (6\text{-}1)$$

where P stands for molar polarizability, ε_r is the relative permittivity, ε_0 is the permittivity in vacuum, M stands for molecular weight of a repeat unit, ρ is density, α is polarizability, and N_A is the Avogadro constant.[6] According to the Clausius-Mossotti relation, the dielectric constant of the polymeric materials is determined by the polarizability and free volume of the constituent element. The polarization term refers to the ability of the atom or molecule to form a dipole under the influence of an electric field. The free volume, on the other hand, is defined as a volume which is not occupied by the polymeric materials.[6] It is shown that the amount of free volume, and its distribution throughout the matrix have a significate influence on the polymer properties. The fact that the free volume within the polymer is filled with air whose dielectric constant is about one will result in a decrease of the dielectric constant.[6] It is indeed reported that the augmentation of the polymer free volume via introducing different functional units decreases the dielectric constant of the polymers.[7] Thus, it may be possible to increase the dielectric constant of the polymer by replacing the air within the matrix of polymers with high dielectric constant materials.

The aim of this chapter is to explore the idea of increasing dielectric constant of the bulk heterojunction by the introduction of materials with dielectric constant higher than air and investigate the subsequent impact on the charge carrier dynamics of the BHJ solar cells. It was assumed that there is a limit to the packing density of the donor and acceptor that can be achieved and some fraction of the bulk heterojunction 3D labyrinth are free and occupied with low dielectric constant gas like air. A range value of 0.11 to 0.23 fractional free volume was reported for variety (glassy) polymers,[8,9] however, it would be technically difficult to estimate the free volume of the BHJ structure. For this study, PCDTBT:PC$_{60}$BM were chosen as polymer-based bulk heterojunction and the introduced materials to the bulk were PFN, rhodamine 101 and isopropyl alcohol (IPA). The reasons for choosing PFN and rhodamine 101 are i) they have conjugated structure backbone similar to the BHJ systems, ii) they are soluble in polar solvents such as CB and o-DCB, iii) their dielectric constant can be determined via simple diode-like structure. In addition, IPA has relatively high dielectric constant and can easily penetrate into bulk heterojunction. Hence, the PFN and rhodamine 101 was incorporated directly into the bulk, whereas the bulk was treated with the IPA. It is expected a slight or moderate increase in the dielectric constant of the BHJ may be achieved upon introduction of the materials (based on the free volume of the BHJ). As such, recombination of charge carriers in the bulk heterojunction is expected to decrease, causing improvement of the overall performance of the BHJ solar cell devices. Thus, the photovoltaic characteristics of the devices are studied before and after the introduction of the materials along with dielectric constant. Then, further investigation of charge carrier recombination dynamics is carried out using techniques such as photo-CELIV, TRCE, and photo-voltage decay.

4.2. EXPERIMENTAL

4.2.1. PFN-diode like Devices

The dielectric constant of the PFN was measured using a diode-like device structure consisting of ITO/PFN/Al. The ITO substrates were thoroughly cleaned according to procedures described in chapter 2. The PFN film was processed from 250 μL CB containing 10 mg PFN. The solution was cast at 3000 rpm for 60 s to form a film. The thickness of the film was measured by the surface profiler (Dektak 150, Veeco) to be around142 ± 4 nm. The 100-nm aluminum was then deposited on top of the PFN film. The devices were encapsulated by UV-curable epoxy and a glass slide for testing in the air.

4.2.2. Rhodamine 101-diode like Devices

A diode-like structure of ITO/rhodamine 101/Al was used to measure the dielectric constant of the rhodamine 101. A similar procedure to PFN was used to fabricate the rhodamine 101-diode like devices. The rhodamine 101 solution was prepared by dissolving 10 mg rhodamine 101 in 250 μL chlorobenzene. The solution was cast at 3000 rpm for 60 s to form a film with thickness around 121 ± 3 (measured by surface profiler Dektak 150 (Veecom)). Then, the device was completed by evaporation of 100 nm aluminum on top of the pure film.

4.2.3. PFN-incorporated BHJ Devices

The BHJ solar cell devices were fabricated based on the general procedures presented in detail in chapter 2. The solar cell structure was ITO/PEDOT:PSS/Active Layer/Al. The incorporation of the PFN into the active layer was accomplished by dissolving PFN in 1,2 dichlorobenzene (o-DCB). First, 0.1 mg PFN was dissolved in 1 cc o-DCB. Then 100, 200 and 500 μl PFN-contained o-DCB solutions were mixed with the pure o-DCB solution to prepare 1 mL solution altogether. After that, the active material solutions were accomplished by adding

PCDTBT (donor) and $PC_{60}BM$ (acceptor) at a weight ratio of 1:4 at an overall concentration of 20 mg mL^{-1}. Thus, the weight percentage of PFN relative to active materials were 0.05%, 0.1% and 0.25% wt.

4.2.4. Rhodamine 101-incorporated BHJ Devices

The structure of the solar cell devices was ITO/PEDOT:PSS/Active Layer/Al. The active layer composed of PCDTBT and $PC_{60}BM$ as donor and acceptor, respectively. A similar process described in section 4.2.3 was used to incorporate rhodamine 101 into the active layer. The weight ratios of the rhodamine 101 to the active materials were 0.0025%, 0.005%, and 0.025%. The chemical structure of the Rhodamine 101 is shown in Figure 1a.

4.2.5. Isopropyl alcohol-treated BHJ Devices

The PCDTBT:$PC_{60}BM$ BHJ was treated with 20 µl of the Isopropyl alcohol (IPA). It was dropped on top of the active layer and was then spin cast at 2000 rpm for the 60s. The chemical structure of the IPA is presented in Figure 1b.

4.2.6. Dielectric Constant Measurement

The dielectric constant of the solar cell devices was measured using dark CELIV technique. In this technique, the solar cell device is considered a capacitor, i.e. the active layer is sandwiched between two electrodes at $x = 0$ (blocking contact) and $x = d$. The d is the thickness of the active layer. Upon applying a negative ramp, an initial current step (J_0) arises (Figure 2-4). The current step stems from the geometrical capacitance (capacitive current response) of the solar cell device and is defined as below:[10]

$$J_0 = \frac{A\varepsilon\varepsilon_0}{d} \qquad (4\text{-}1)$$

which A (= $\frac{\Delta U}{\Delta t}$) is voltage rise speed ($V\ s^{-1}$), ε is dielectric constant of the active layer, ε_0 stands for the vacuum permittivity ($8.854 \times 10^{-12}\ F\ m^{-1}$) and d is the thickness of the active layer.

4.2.7. Solar Cell Device Characterization

The current density-voltage, EQE, photovoltage decay, time-resolved charge extraction and photo-CELIV measurements were carried out according to the procedure described in chapter 2.

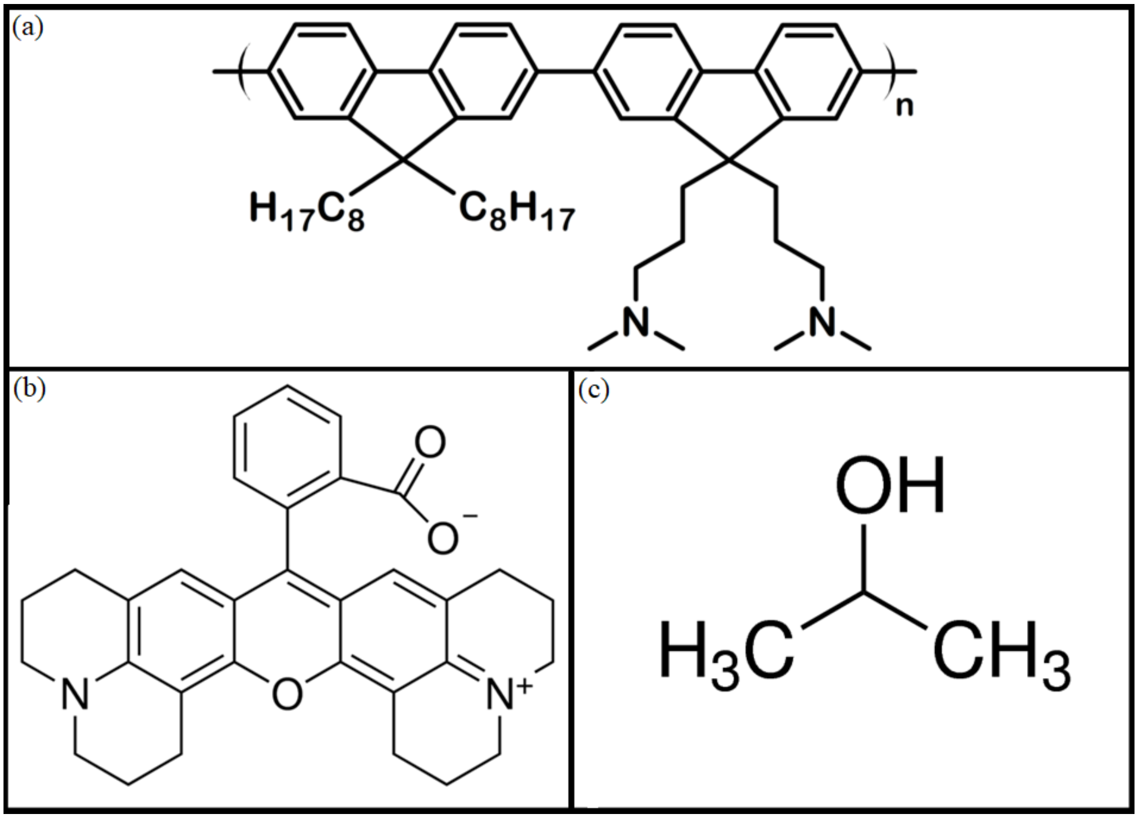

Figure 4.1. Chemical structures of (a) PFN, (b) rhodamine 101, and (c) isopropyl alcohol (IPA).

4.3. RESULT AND DISCUSSION

4.3.1. PCDTBT:PC$_{60}$BM:PFN-Incorporated

4.3.1.1. PFN dielectric constant

It is required to determine the dielectric constant of the PFN. Hence, diode-like devices with a PFN film (measured thickness by surface profiler was 142 ± 4 nm) sandwiched between ITO and aluminum were fabricated. The dark-CELIV technique was employed to measure the dielectric constant of the PFN devices. Figure 4.2 shows the dark CELIV current response of the PFN diode-like device after a triangle-shaped increasing voltage (2 *V* together with 50000 Hz rise time) was applied. The dielectric constant of the PFN film is calculated according to equation 4-1 and estimated to be 2.16 ± 0.09. The value indicates that PFN meets the requirement of having dielectric constant bigger than air (1.0005 at 25 °C).[11]

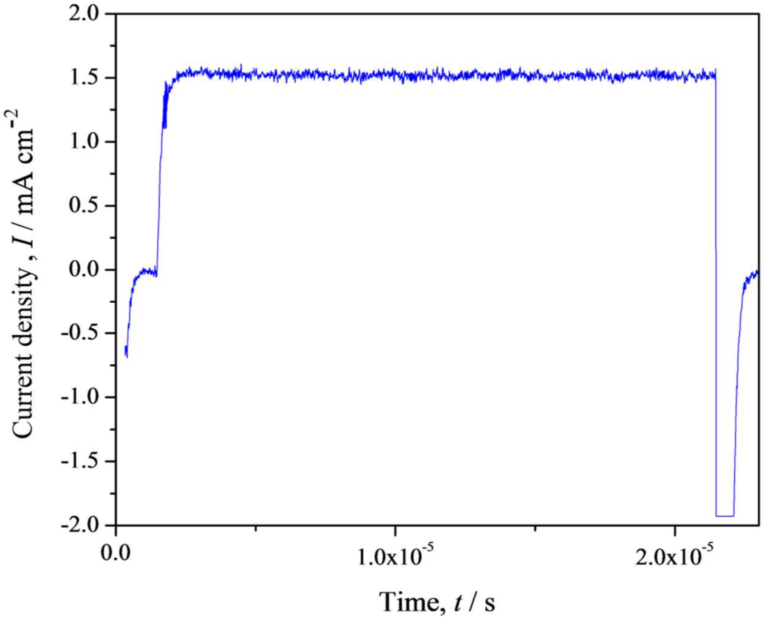

Figure 4.2. The measured dark-CELIV curve of the diode-like PFN-only device with a structure of ITO/PFN (142 ± 4 nm)/Al. The applied voltage was 2 *V* coupled with 50000 Hz rise time (A = 100000 $V\,s^{-1}$).

4.3.1.2. Photovoltaic characteristics

To demonstrate the effect of PFN on the photovoltaic characteristics, solar cell devices were fabricated with an active layer composed of PCDTBT:PC_{60}BM or PFN-doped PCDTBT:PC_{60}BM. The photovoltaic characteristics of the fabricated devices are summarized in Table 4.1. Figure 4.3 shows the current density-voltage curves of the devices before and after containing PFN. The PFN is added in mass fraction to the dissolved PCDTBT:PC_{60}BM in chlorobenzene solution, i.e. 0.05%, 0.1% and 0.25% wt. It is observed that the efficiency of the solar cell devices is reduced after PFN was introduced to PCDTBT:PC_{60}BM bulk heterojunction. Devices fabricated with 0.05% PFN shows a small but appreciable reduction in V_{oc}, J_{sc} and FF. When the PFN concentration increased to 0.1% and 0.25% wt, the photovoltaic parameters were significantly reduced and an S-shaped current density-voltage curve becomes apparent. Moreover, PFN-loaded devices exhibit lower charge carrier photogeneration compared to the reference devices especially at the low effective voltage (Figure 4.5.1a, Appendix). A similar impact on charge collection probability is also observed for devices with more than 0.1% PFN-loaded (Figure 4.5.1b, Appendix). Although morphology evidences were not provided, changes in BHJ morphology upon incorporation of the PFN would be expected particularly at the high concentration. Thus, the performance reduction in the PFN-loaded devices may come from the influence of the PFN on the BHJ morphology and enhanced recombination loss of charge carrier. Nian *et al.*[12] have reported that performance of P3HT:PCBM BHJ devices deteriorate after incorporation of the PFN. The deterioration was attributed to degradation of the bulk morphology (less aggregation and crystallization of P3HT) and phase separation between P3HT and PCBM. An increase in the series resistance and decrease of shunt resistance was also reported. The authors proposed that energy level of the PFN (low HOMO and high LUMO) as well as the presence of PFN on top of the PEDOT:PSS would be origins of the increased series resistance, whereas conductivity enhancement

Table 4.1. Photovoltaic parameters of PCDTBT:$PC_{60}BM$ BHJ solar cell devices without and with PFN-embedded into bulk heterojunction. The results of an average of 8 devices.

Devices	V_{oc} (*mV*)	J_{sc} (*mA cm^{-2}*)	FF	PCE (%)
Reference	881.0 ± 19	7.3 ± 0.7	0.53 ± 0.04	3.42 ± 0.5
0.05% PFN-Inc.	877.3 ± 17	7.2 ± 0.36	0.50 ± 0.06	3.17 ± 0.5
0.1% PFN-Inc.	842.0 ± 46	7.0 ± 0.82	0.42 ± 0.04	2.56 ± 0.4
0.25% PFN-Inc.	327.0 ± 32	3.5 ± 0.78	0.20 ± 0.03	0.25 ± 0.1

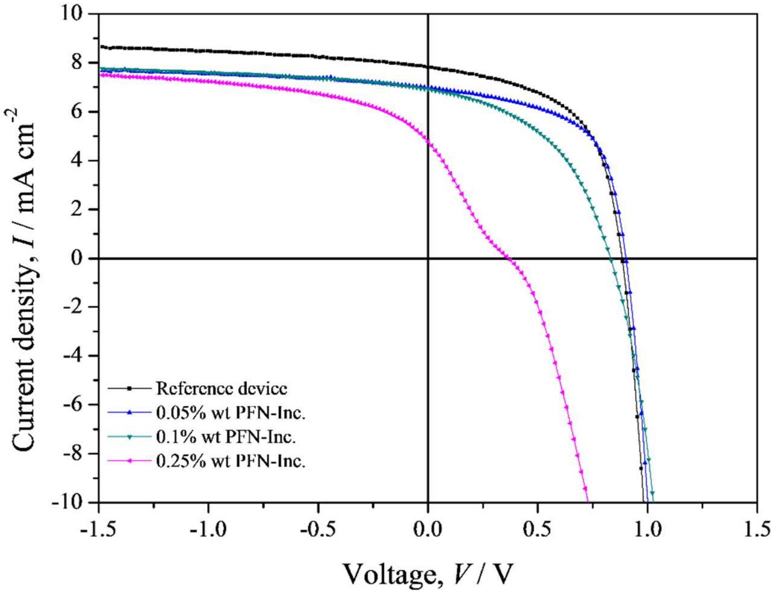

Figure 4.3. Comparison of current density-voltage characteristics of PCDTBT:$PC_{60}BM$ BHJ solar cell devices without and with the incorporation of the PFN into bulk heterojunction.

(due to the polarization of PFN) may be the reason for the shunt resistance reduction. Noteworthy that it has been claimed that PFN is a hole blocking layer and its amino group acts like traps.[13] Therefore, the S-shaped current-voltage curve of the 0.25% wt PFN-loaded devices may be attributed to the accumulation and subsequent recombination of the holes in the bulk or at the interface of the bulk-anode electrode.

4.3.1.3. Dielectric constant and mobility measurement

To study the effect of the PFN on the dielectric constant of the PCDTBT:PC$_{60}$BM BHJ, it is first necessary to obtain the dark CELIV response of the devices. The dark CELIV responses of the devices are shown in Figure 4.4. The dielectric constant of the PCDTBT:PC$_{60}$BM devices containing PFN is calculated according to equation 4-1 and summarized in Table 4.2. Devices made with 0.05% and 0.1% wt PFN show slightly lower or similar dielectric constant compared to the reference device. But, increase the concentration of PFN to 0.25% reduce the dielectric constant. According to Clausius–Mossotti relation, polarization and free volume determine the dielectric constant of a polymer.

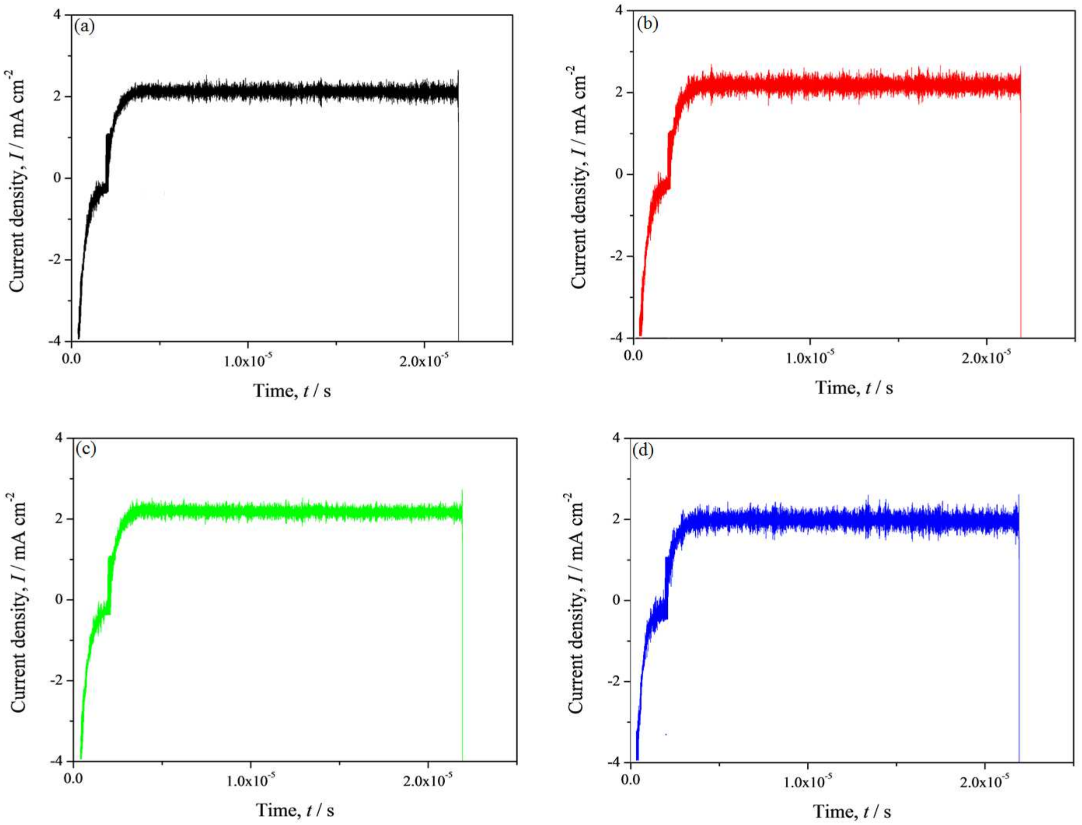

Figure 4.4. Dark CELIV response of the PCDTBT:PC$_{60}$BM BHJ solar cell devices (a) without, and with (b) 0.05% wt, (c) 0.1% wt, and (c) 0.25% wt PFN- loaded. The applied voltage was 1 *V* coupled with 50000 Hz rise time (A = 50000 $V\ s^{-1}$). The thickness of the active layer for all devices was 80 ± 5.

Table 4.2. Calculated dielectric constant and charge carrier mobility of the PCDTBT:PC$_{60}$BM BHJ solar cell devices before and after incorporation of PFN into bulk heterojunction. The results are average of 2 devices.

Device	Dielectric constant	Mobility (cm^2 V^{-1} s^{-1})
Reference	3.9 ± 0.2	1.88×10^{-5}
0.05% wt PFN-Inc.	3.8 ± 0.2	2.10×10^{-5}
0.1% wt PFN-Inc.	3.9 ± 0.2	1.34×10^{-5}
0.25% wt PFN-Inc.	3.6 ± 0.2	1.11×10^{-5}

Given that polarization is an intrinsic characteristic of atoms and molecules, it is speculated that the slight reduction of the dielectric constant upon incorporation of 0.25% PFN in the PCDTBT:PC$_{60}$BM bulk heterojunction may be the result of an increase in the free volume compared to the free-PFN bulk heterojunction.

Constantinou *et al.*[14] reported that dielectric constant of PCDTBT:PC$_{70}$BM was enhanced from 3.32 to 3.87 by thermal annealing. As a result, a higher degree of CT state delocalized resulted in slightly higher photocurrent at reverse bias. It was mentioned that the alteration of the bulk morphology was not substantial after thermal annealing. However, the performance of the annealed devices decreases due to higher recombination of charge carrier through Shockley-Read-Hall (SRH) recombination. As such, considerable reduction of solar cell's performance upon incorporation of PFN may be attributed to i) the deterioration of fundamental processes of the devices such as generation, transportation, and collection of charge carrier or ii) enhancement of the charge carrier recombination in the presence of the PFN and/or iii) combination of both. To study the effect of the incorporated PFN on the transportation, charge carrier mobility of the devices is measured using the photo-CELIV technique. The mobility results are shown in Table 4.2 (Figure 4.5.2 shows photo-CELIV curves, Appendix A). The mobility of the devices slightly increases with the inclusion of 0.05% PFN, whereas increasing concentration of PFN gives rise to slightly lower charge carrier mobility. Noteworthy that several parameters could be responsible for the reduction of mobility in the PFN-loaded devices including increased disorder, impurity and trap effects, and degraded molecular packing.

4.3.2. PCDTBT:PC$_{60}$BM:Rhodamine 101-loaded

4.3.2.1. Rhodamine 101 dielectric constant

To establish the dielectric constant of the rhodamine 101, the rhodamine 101 diode-like devices composed of ITO/rhodamine101 (121 ± 3 nm)/Al were fabricated. A 2 *V* triangle-shaped voltage associated with 50000 Hz rise time is applied and the dark CELIV current response of the devices is recorded (Figure 4.3). According to equation 4-1, the dielectric constant of the rhodamine 101 is 4.73 ± 0.08. The rhodamine 101 is a zwitterion which is a neutral molecule carrying both positive and negative electrical charges (Figure 4.1a). The rhodamine 101 has been used as interfacial electron transport layer in solar cell devices. It is said that formation of dipoles at the interface reduces the work function of the electrode, giving rise to enhancement of the solar cell performance.[15,16]

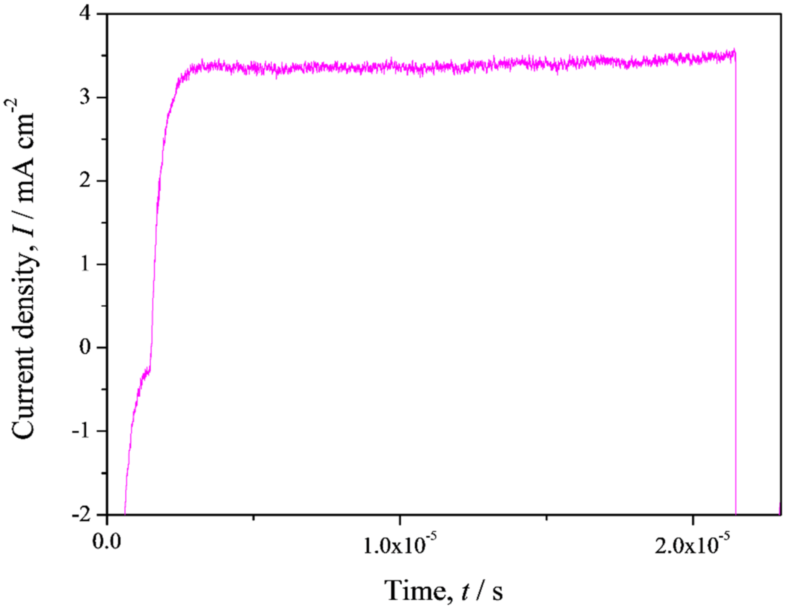

Figure 4.5. Dark CELIV curve of diode-like Rhodamine 101 device with structure of ITO/rhodamine101 (121 ± 3 nm)/Al. The voltage speed rise (A) was set to 100000 $V\ s^{-1}$.

4.3.2.2. Photovoltaic characteristic

The photovoltaic performance of the PCDTBT:PC$_{60}$BM BHJ solar cell devices when various concentrations of rhodamine 101 were introduced to the bulk are studied by the current density-voltage measurement. The current density-voltage curves of the devices are shown in Figure 4.6. The photovoltaic parameters of the devices are also summarized in Table 4.3. It is observed that the increase of the concentration of the rhodamine 101 from 0 to 0.025% wt results in a decrease of the power conversion efficiency of devices from 3.7 ± 0.2% to 2.6 ± 0.4%. The external quantum efficiency of the device is shown in Figure 4.7. The J_{sc} of the devices obtained from EQE for 0%, 0.0025%, 0.005% and 0.025% wt rhodamine 101-embedded devices are 7.8, 7.6, 7.38 and 7.08 *mA cm*$^{-2}$, respectively. These currents are in good agreement with J_{sc} obtained from the current density-voltage measurement. The EQE data shows that the addition of rhodamine 101 to the bulk reduces the efficiency of photon-to-electron conversion, especially between 500 to 650 nm. Hence, the reduction of the

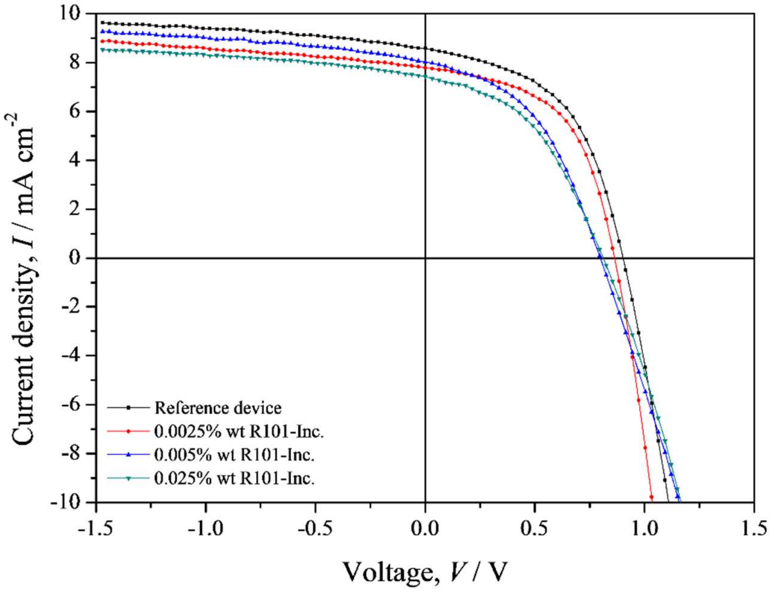

Figure 4.6. Current density-voltage curves of the PCDTBT:PC$_{60}$BM BHJ solar cell devices before and after incorporation of various concentration of rhodamine 101 in the bulk heterojunction.

Table 4.3. Photovoltaic parameters of the PCDTBT:$PC_{60}BM$ BHJ solar cell devices before and after adding rhodamine 101 into the bulk heterojunction. The results are average of 8 devices.

Devices	V_{oc} (*mV*)	J_{sc} (*mA cm*$^{-2}$)	FF	PCE (%)
Reference	891.0 ± 7	8.1 ± 0.4	51.5 ± 1.95	3.7 ± 0.2
0.0025% wt R101-Inc.	869.0 ± 14	7.6 ± 0.3	53.1± 0.9	3.5 ± 0.4
0.005% wt R101-Inc.	833.0 ± 34	7.5 ± 0.6	45.1 ± 1.54	2.8 ± 0.3
0.025% wt R101-Inc.	785.0 ± 28	7.4 ± 0.4	45.0 ± 3.9	2.62 ± 0.4

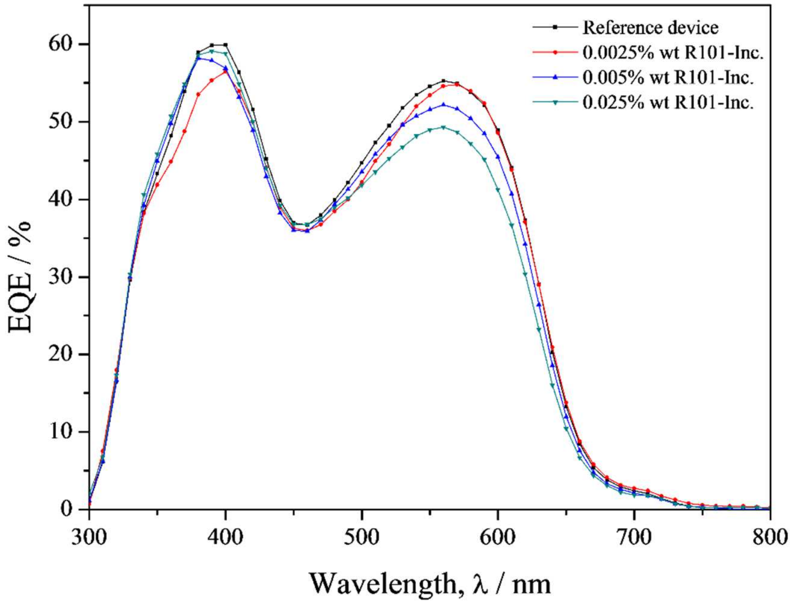

Figure 4.7. EQE curves of the PCDTBT:$PC_{60}BM$ BHJ solar cell devices without and with incorporation various concentrations of rhodamine 101 into the bulk.

performance in rhodamine 101-doped solar cell devices perhaps come from the enhancement of the charge carrier recombination.

4.3.2.3. Dielectric constant, mobility and TRCE measurements

The dark CELIV response of PCDTBT:$PC_{60}BM$ solar cell devices before and after the introduction of the rhodamine 101 are shown in Figure 4.8. The calculated dielectric constants of the solar cell devices are presented in Table 4.4. It can be seen that the dielectric constant of the bulk heterojunction has not been altered upon introduction of the rhodamine 101. This indicates that the parameters determine the dielectric constant of the bulk, i.e. polarization and free volume, has not been affected by the presence of the rhodamine 101. Nevertheless, photovoltaic characteristics of the devices are influenced significantly.

Further investigation of the devices was accomplished using TRCE techniques. Figure 4.9a compare the charge carrier density of the solar cell devices before and after incorporation of the rhodamine 101. The charge carrier density of 0.0025% wt-loaded rhodamine 101 BHJ device is initially quite similar to the reference device but slightly decreases at the longer time, whereas both 0.005% wt- and 0.025% wt-loaded devices possess lower charge density over the course of the time in comparison with reference device. In addition, bimolecular recombination coefficient increased in devices with 0.005% and 0.025% wt loaded rhodamine 101. However, bimolecular recombination lifetimes of the solar cell devices are quite comparable except at the longer time (Figure 4.9b). These results imply that the addition of the rhodamine 101 into PCDTBT:$PC_{60}BM$ BHJ intensifies recombination of the charge carriers. Hence, the performance reduction of the rhodamine 101-loaded solar cell devices could be related to the enhanced charge carrier recombination. Cowan *et al.*[17] report that the addition small amount of impurity like $PC_{84}BM$ into the PCDTBT:$PC_{60}BM$ BHJ solar cells alters the electronic characteristics of devices, leading to the reduction of V_{oc}, J_{sc}, FF, and PCE. The authors describe that $PC_{84}BM$ acts like trap states and subsequently give rise to enhanced recombination of charge carriers, especially via the trap-assisted mechanism.

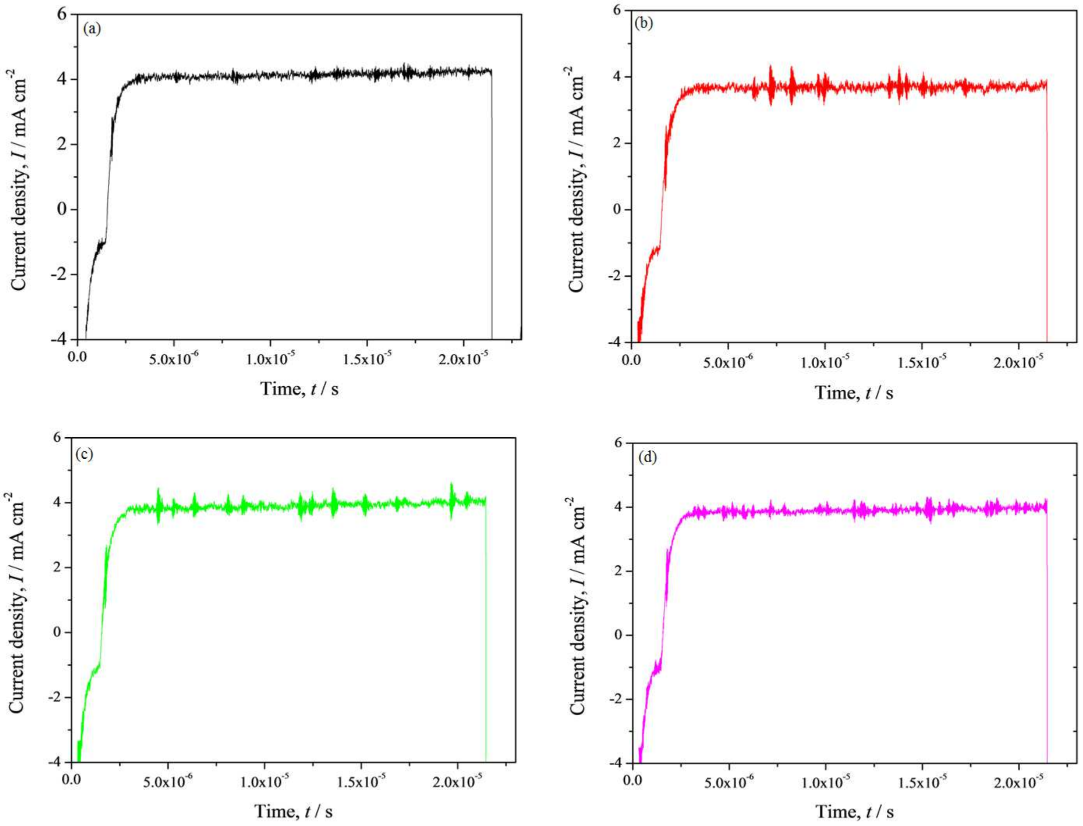

Figure 4.8. Measured dark CELIV of the PCDTBT:PC$_{60}$BM solar cell devices (a) without, (b) 0.0025% , (c) 0.005%, and (d) 0.025% wt rhodamine 101 loaded-bulk heterojunction.. The voltage speed rise (A) was 100000 $V\,s^{-1}$. The resistance used on oscilloscope was 10 Ω. The thickness of the bulk film was 80 ± 5 nm.

Table 4.4. The calculated dielectric constant and charge carrier mobility of the PCDTBT:PC$_{60}$BM BHJ solar cell devices before and after incorporation of rhodamine 101. Three devices were measured and averaged.

Device	**Dielectric constant**	**Mobility ($cm^2\ V^{-1}\ s^{-1}$)**
Reference	3.7 ± 0.2	1.77×10^{-5}
0.0025%-loaded rhodamine 101	3.7 ± 0.1	1.52×10^{-5}
0.005%-loaded Rhodamine 101	3.5 ± 0.2	2.11×10^{-5}
0.025%-loaded Rhodamine 101	3.5 ± 0.2	1.1×10^{-5}

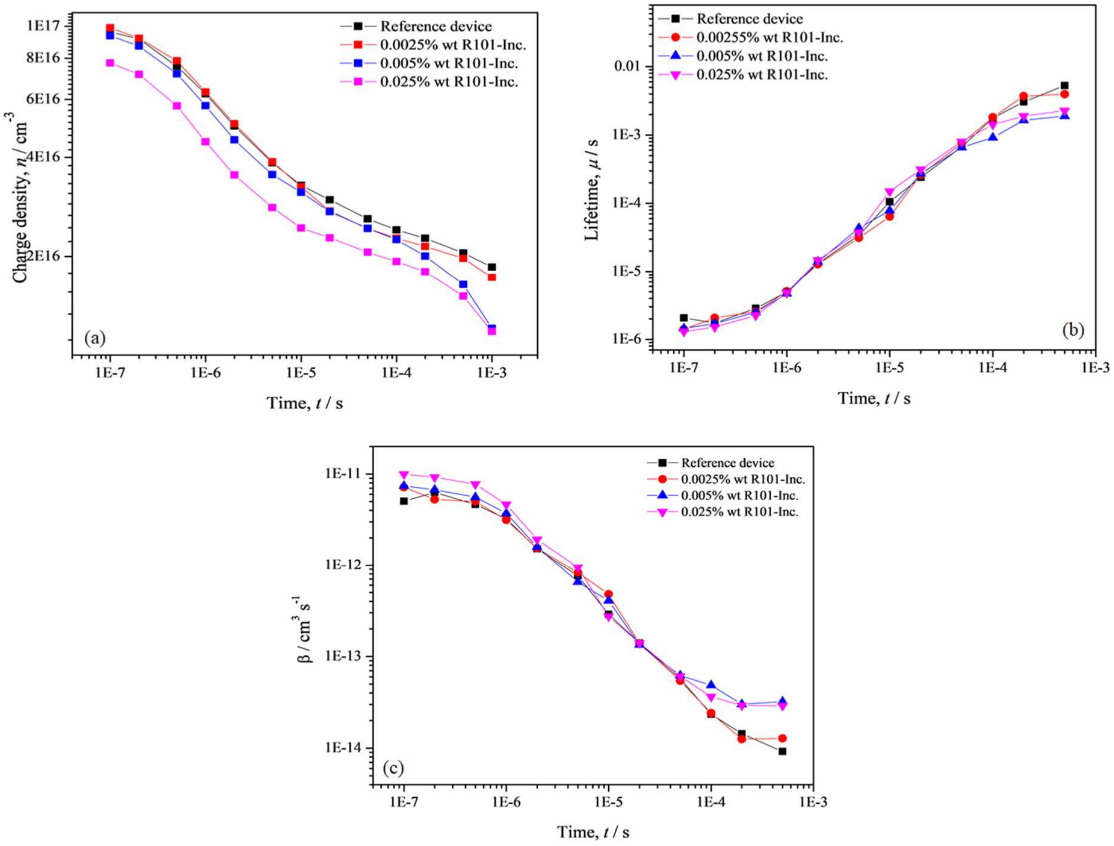

Figure 4.9. (a) Charge carrier density, (b) bimolecular lifetime, and (c) bimolecular recombination coefficient as a function of time of PCDTBT:PC$_{60}$BM BHJ solar cell devices without and with various concentrations rhodamine 101 introduced to the bulk heterojunction. The energy of laser was 10 µj.

Charge carrier mobility of the solar cell devices with and without rhodamine 101 are reported in Table 4.4 (the associated photo-CELIV curves are shown in Figure 4.6.3). The charge carrier mobility of rhodamine-incorporated devices is close to the reference device, though slightly higher for 0.005% and 0.025% wt-loaded devices. It is predicted that traps enhance energy disorder in P3HT:PCBM bulk heterojunction system which hampers charge carrier transport and therefore reduce the mobility of charge carriers around two orders of magnitude.[18] Given that the rhodamine 101 may have introduced trap into the PCDTBT:PCBM bulk, such a decrease in the charge carrier mobility is not observed in the rhodamine-loaded devices. Clarke *et al.*[19] have studied the mobility of the KP115:PCBM solar cell before and after photodegradation using the photo-CELIV technique. While the photodegradation introduces traps into the system, no sign of mobility reduction was observed. The authors propose two possible reasons i) recombination of charge carrier within the duration of the laser pulse or during actual charge carrier extraction, ii) only free, delocalized charge carriers that are being extracted are visible in photo-CELIV technique and deeply trapped charges may not be observable.[19]

4.3.3. PCDTBT:PC$_{60}$BM:IPA-treated

4.3.3.1. Photovoltaic characteristics

It is observed that the introduction of PFN and rhodamine 101 have not altered the dielectric constant of the PCDTBT:PC$_{60}$BM bulk heterojunction, yet the performance of the devices was reduced due to perhaps morphological issues. To minimize the effect of the introduced materials on the BHJ morphology, a solvent with high dielectric constant was therefore selected for further investigation. For the purpose of the study it is assumed that 1) the solvent effect is not limited to the surface treatment, 2) the solvent penetrates into a complex labyrinth of 3D bulk heterojunction structure and 3) some amount of solvent remains within the bulk after the fabrication process. It is understood that there is a concern regarding the remaining of the solvent within the bulk structure. It is however reported that removal of the solvent within the bulk requires rigorous elongated vacuum process together with baking.[20,21]

The Isopropyl alcohol (IPA) with the dielectric constant of 18 was chosen. The PCDTBT:PC$_{60}$BM BHJ was treated with 20 µl of IPA. The photovoltaic parameters of the solar cell devices before and after treatment with IPA are summarized in Table 4.5. The current density-voltage curves of the best efficient devices are shown in Figure 4.10. The reference devices exhibited average power conversion efficiency of 4.3 ± 0.3%. On the other hand, the IPA treatment generally leads to no significant changes in the performance devices and the IPA treated devices exhibit PCE of 4.2 ± 0.2% due to slightly decrease open-circuit potential and

Table 4.5. Current density-voltage characteristics of the PCDTBT:PC$_{60}$BM BHJ solar cell devices before and after treatment with IPA. The results are average of 8 devices for each set.

Device	V_{oc} (*mV*)	J_{sc} (*mA cm^{-2}*)	FF	PCE (%)
References	910.0 ± 7	7.8 ± 0.4	61.2 ± 3.2	4.3 ± 0.3
IPA treated	903.0 ± 4	7.6 ± 0.5	61.4 ± 1.3	4.2 ± 0.2

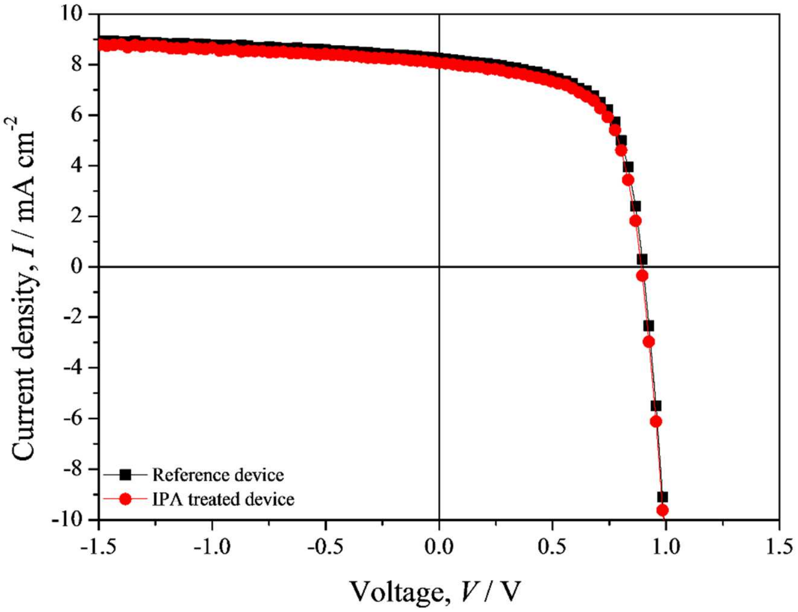

Figure 4.10. Current density-voltage curves of the PCDTBT:PC$_{60}$BM BHJ solar cell devices before and after IPA treatment.

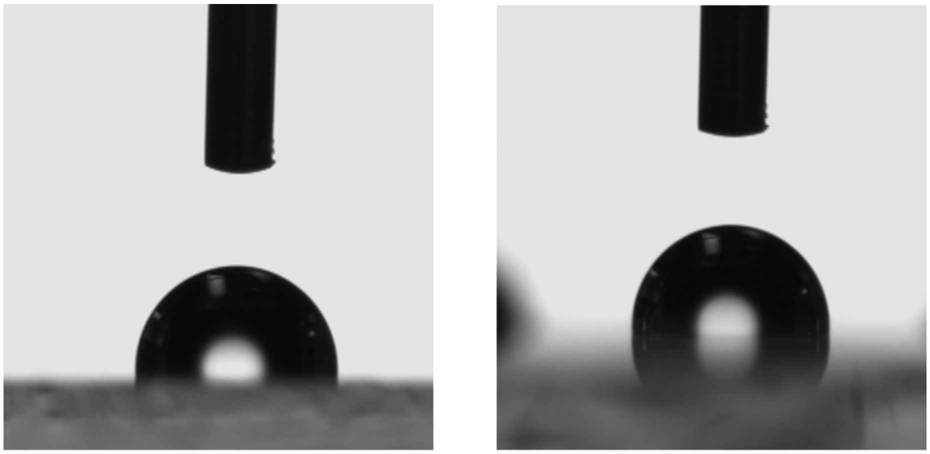

Figure 4.11. The water contact angle photos of the PCDTBT:PC$_{60}$BM BHJ film (a) before and (b) after treatment with 20 µl of IPA.

short-circuit current. A similar result has been observed in a BHJ device composed of PCDTBT:PC$_{71}$BM. The increase of the roughness and appearance an extremely uneven surface with anomalous hills after IPA treatment was accounted for the slight reduction of short-circuit current and consequently the performance.[22] It should be noted that thickness of the active layer was examined before and after the IPA treatment by using profilometer. No substantial changes were observed in the film thickness which is in agreement with the results reported in the literature.[22, 23, 26]

The water contact angle (θ) of PCDTBT:PC$_{60}$BM active layer was measured to probe the changes in top surface before and after treatment with IPA. As shown in Figure 4.11a, the water contact angle of the pristine PCDTBT:PC$_{60}$BM is 96º ± 2º, indicating a largely hydrophobic surface. The measured water contact angle of the BHJ film after IPA treatment remain almost unchanged with values around 96º ± 3º (Figure 4.11b). It is reported that surface condition of the BHJ film can be affected by the surface charge density, surface traps, surface reconstruction, and chemical composition, etc.[23-25] Given almost identical θ of the film, one may conclude that surface condition of the films has not been affected before and after treatment with isopropyl alcohol.

The UV-Vis absorption spectra of the bulk heterojunction before and after treatment with IPA is shown in Figure 4.12a. The absorption of the active layer following IPA treatment decreases in the wavelength range of 350 to 600 nm and then increases slightly thereafter. It can also be seen that the absorption peak between 500-600 nm is slightly red-shifted after the treatment. It is shown that alcohol treatment causes no observable changes in thickness of the active layer.[23] Zhang *et al.*[22] report a reduction in absorption of PCDTBT:PC$_{71}$BM film following treatment with IPA. Guo *et al.*[26] report that domain and structure sizes of PTB7:PC$_{71}$BM film shrinks after treatment with various alcohols including IPA. Therefore, the changes in the absorption after the IPA treatment may be an indication of the rearrangement of the donor and/or the acceptor within the BHJ film after IPA treatment.

Figure 4.12b shows the EQE of the devices before and after IPA treatment. The EQE of the IPA treated device decrease in the wavelength range of 500-600 nm, whereas it slightly

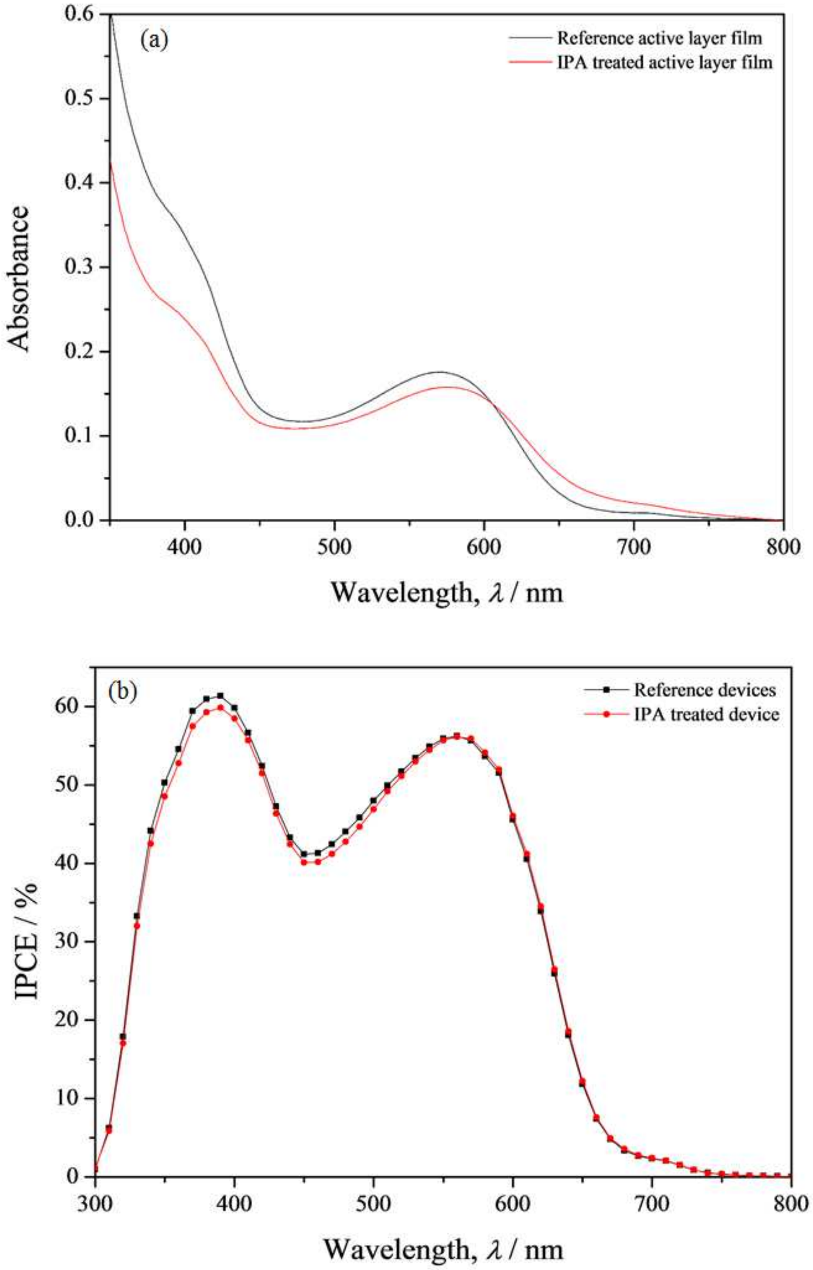

Figure 4.12. (a) UV-Vis spectra of the PCDTBT:PC$_{60}$BM BHJ film before and after treatment with IPA. The absorption spectra were corrected for absorption of bare glass. (b) External quantum efficiency of the PCDTBT:PC$_{60}$BM BHJ solar cell devices before and after IPA treatment.

enhances between 300-400 nm compared to the reference device. The J_{sc} of the devices obtained from EQE before and after the treatment are 7.91 and 7.85 *mA cm*$^{-2}$, respectively. The current values are quite similar and in good agreement with current density-voltage results. This suggests that the fundamental processes determine the performance of the devices has not been affected by IPA treatment of the bulk heterojunction.

To study the charge carrier generation and collection of the devices, photocurrent density and charge collection probability as a function of effective voltage were examined (Figure 4.14). It can be seen that both devices show similar behavior and immediately saturate in the low effective voltage (around 0.2 V). This indicates that internal electric field within the bulk heterojunction is quite comparable before and after the IPA treatment and charge carriers are effectively swept out by drift current (large internal electric field). At saturation regime, the photocurrent ($J_{ph,sat}$) is only limited by the number of the absorbed photon and can be defined as $J_{ph,sat} = edG_{max}$ where e is elementary charge, d is thickness of the active layer (80 nm) and G_{max} stands for the maximum photo-induced charge carrier generation rate per volume. The calculated G_{max} values for the reference and IPA treated devices are 6.97×10^{27} m^{-3} s^{-1} (89.34 A m^{-2}) and 6.86×10^{27} m^{-3} s^{-1} (87.95 A m^{-2}), respectively. This suggests that treatment with IPA has not altered optical (such as light absorption) and electrical characteristics of the PCDTBT:PC$_{60}$BM BHJ devices. Similar results were observed in the PCDTBT:PC$_{71}$BM BHJ treated with IPA.[22]

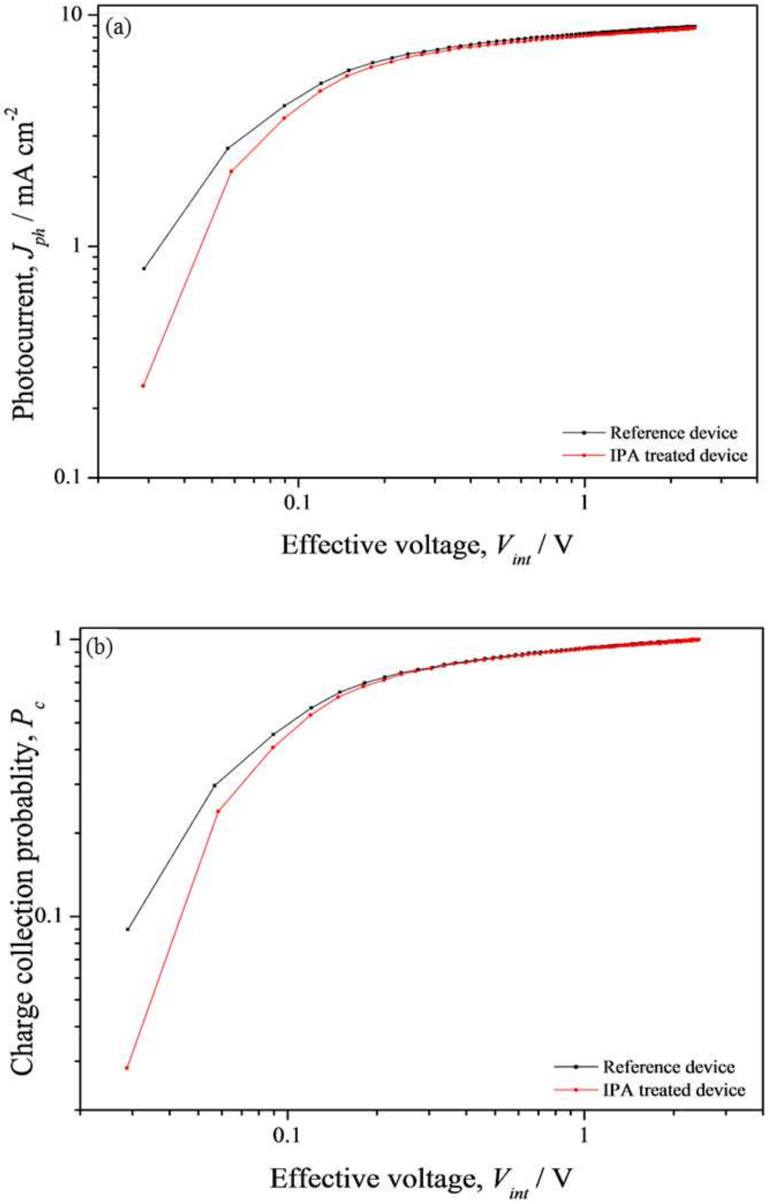

Figure 4.13. (a) Photocurrent and (b) charge collection probability as a function of effective voltage of PCDTBT:PC$_{60}$BM BHJ solar cell devices before and after treatment with 20 µl IPA.

4.3.3.2. Dielectric constant, PVD, TRCE and photo-CELIV measurements

The dark CELIV responses of the PCDTBT:$PC_{60}BM$ BHJ solar cell devices before and after IPA treatment are shown in Figure 4.14a, b. The calculated dielectric constant of the devices is reported in Table 4.6. The dielectric constant of the device following IPA treatment shows a slight increase compared to the reference device. Considering Clausius-Mossotti relation, either polarization or free volume of the bulk may be affected after treatment with IPA, resulting in a slight change of the dielectric constant.

The effect of the increase of the dielectric constant on charge carrier dynamics of the devices is examined using transient techniques. Photovoltage decay of the reference and IPA treated devices are shown in Figure 4.15a. It is clear that there is no considerable difference between photovoltage decay of the devices. The voltage decay at the early time shows that both devices have almost the same V_{oc} values (~ 0.9 V), followed by quite similar decay behavior over the course of time. However, the photovoltage decay versus extracted charge carrier density exhibits a slight downward shift in the IPA treated devices compared to the reference devices (Figure 4.15b). This may imply that recombination of charge carrier is slightly higher after IPA treatment (and a slight increase of the dielectric constant). The bimolecular recombination lifetime plot versus time shown there is no difference before and after treatment with IPA (Figure 4.16a). Moreover, bimolecular recombination coefficient is slightly higher at the longer time in the IPA treated devices, suggesting faster recombination of charge carriers (Figure 4.16b). These findings indicate that recombination dynamic of the charge carriers has not been significantly altered by changes in the dielectric constant. It is reported that the performance of PTB7-based BHJ has been improved upon treatment with IPA. The improvement was attributed to the morphological rearrangement of the bulk heterojunction, causing better charge carrier separation, transportation, and extraction.[26]

Table 4.6. The calculated dielectric constant and charge carrier mobility of PCDTBT:PC$_{60}$BM BHJ solar cell devices before and after treatment with IPA. Two devices were measured and averaged.

Device	Dielectric Constant	Mobility (*cm^2 V^{-1} s^{-1}*)
Reference	3.6 ± 0.2	2.1×10^{-5}
IPA treated	4.1 ± 0.3	1.1×10^{-5}

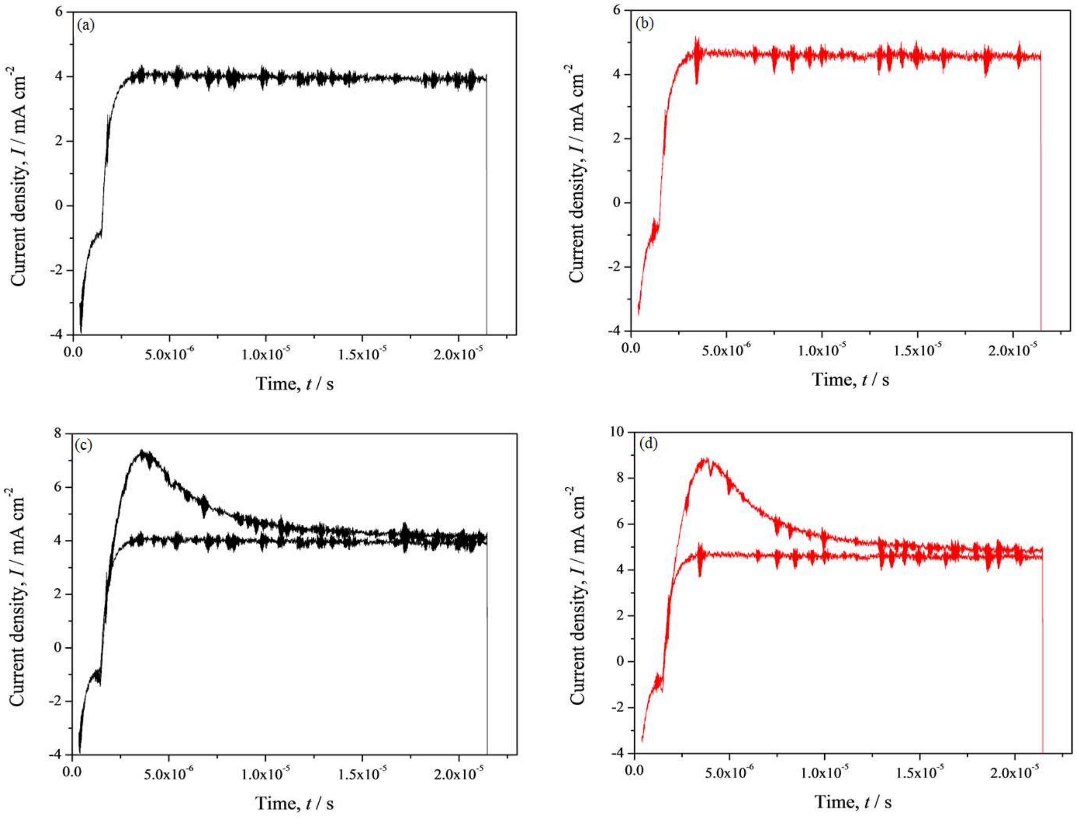

Figure 4.14. (a) and (c) Measured dark CELIV of the PCDTBT:PC$_{60}$BM BHJ solar cell devices (a) before, (b) after treatment with 20 µl IPA. (c) and (d) The photo-CELIV curves of the corresponding devices. The energy of the laser was set to 10 µj. The applied potential was 2 *V* together with a rise time of 50000 Hz (A = 100000 *V s-1*). The delay time between photogeneration and extraction of charge carrier was 2 µs. The thickness of the active layer was 80 ± 5 nm.

The effect of the IPA treatment on charge carrier transportation was studied by examining charge carrier mobility. The charge carrier mobility of the devices is summarized in Table 4.6. The corresponding photo-CELIV curves are also shown in Figure 4.13c, d. The charge carrier mobility of the devices is quite comparable, although slightly smaller value for IPA treated device. It is shown that the solvent treatment (methanol) improves hole mobility in BHJ devices consisted of PTB7:PC$_{70}$BM, leading to a more balanced charge transport and consequently higher fill factor values (an indication of less charge carrier recombination).[23] It is clear that such an effect was not observed here. Moreover, it is demonstrated in the literature that IPA treatment has not significantly improved the hole mobility in the PCDTBT:PC$_{70}$BM BHJ devices.[22]

As discussed earlier, polarizability and free volume are two important factors that influence the dielectric constant characteristics of the polymeric materials as formulated by the Clausius – Mossotti relationship. One of the aims was to increase the polarizable units per unit volume by the addition of the PFN and rhodamine 101 to the bulk heterojunction. Given the results, it appears that the incorporated amount of both PFN, rhodamine and IPA may not have been enough to substantially increase the polarizable units per unit volume. However, both materials have had a considerable impact on the performance of the devices. In a similar manner, it could also be argued that the amount of free volume within the bulk heterojunction structure may not be sufficient enough that filling it with high dielectric constant materials could give rise to significant enhancement of the dielectric constant. Another factor that could have an influence on the dielectric constant characteristics is the net polarity of the polymer structure.[6] A polymer can be polar or non-polar and what determines whether a polymer is polar or non-polar is the presence of functional groups on the neat polymer chemical structure. In addition, functional group’s configuration on the chain is important to whether the resulting dipole moments reinforce or cancel each other.[6] PCDTBT is highly likely a non-polar polymer since it does not have a big polarizable atom (bromine, chlorine) on its structure as well as its branched chain, which only contains sigma bonds (they are slightly hardly polarized when an electric field is applied). Therefore, this could be another reason explaining why the adopted

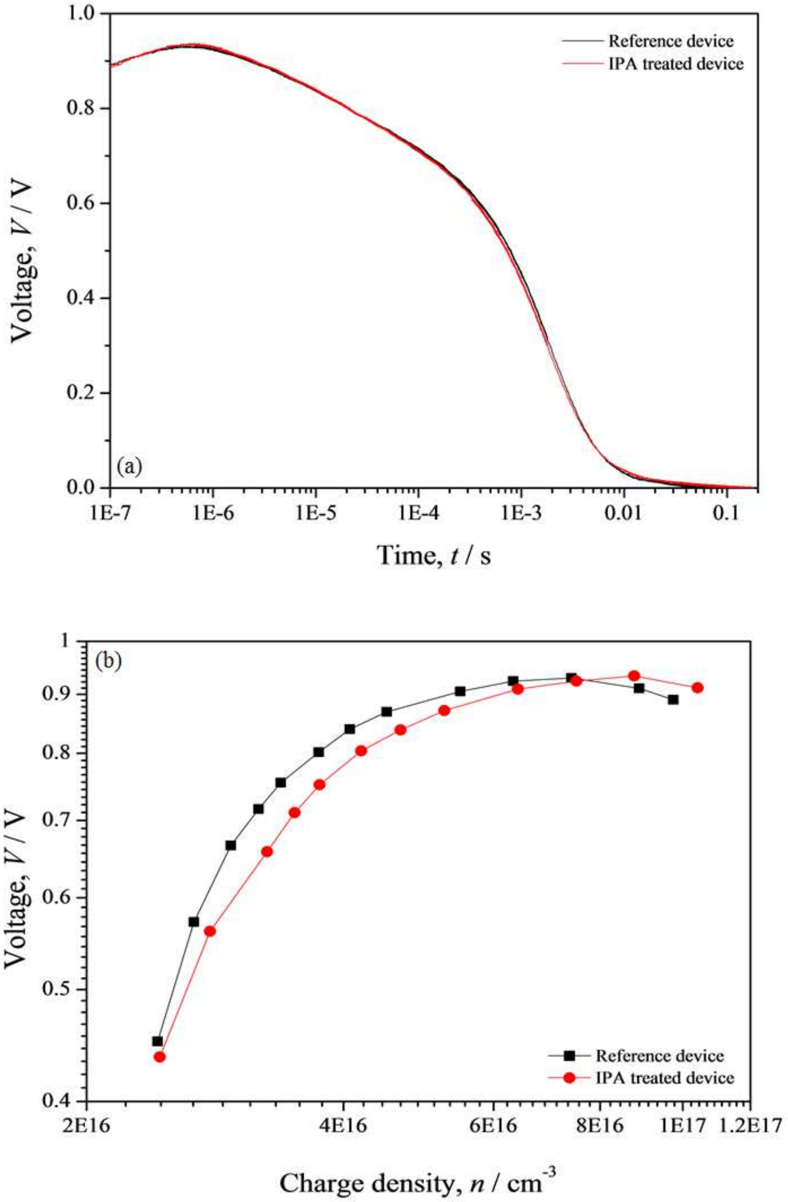

Figure 4.15. (a) Photovoltage decays of the PCDTBT:$PC_{60}BM$ BHJ solar cell devices before and after treatment with IPA. (b) Photovoltage decay as a function of extracted charge carrier density of the devices before after treatment with IPA.

approach to enhance the dielectric constant did not produce favourable results. It should also be noted that one may argue the existence of a residual solvent inside the bulk heterojunction and its impact on the dielectric constant. The fact remains that the amount of residual solvent within 3D BHJ cannot straightforwardly hardly be determined. Nevertheless, the achieved dielectric constants indicate that the amount of residual solvent is insignificant such that it cannot enhance dielectric constant or that the dielectric constant of the bulk heterojunction cannot simply be determined by the factors in the Clausius – Mossotti relationship.

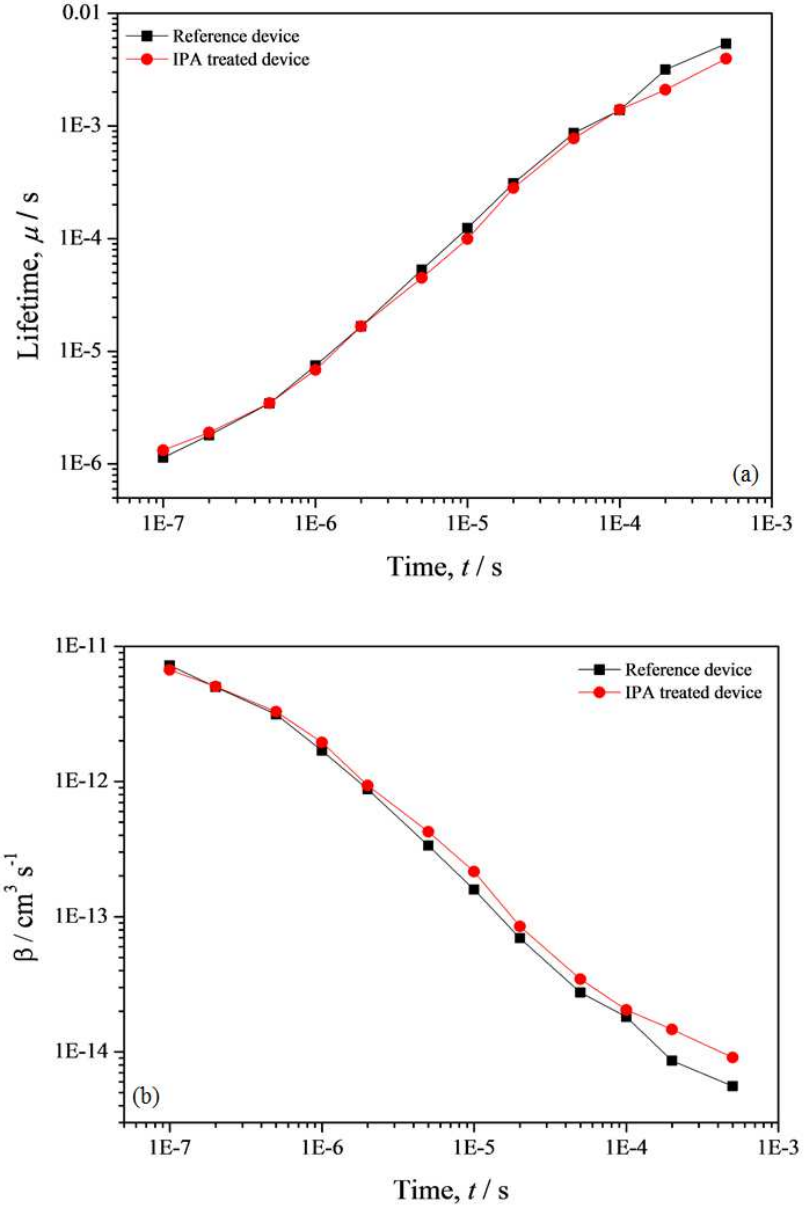

Figure 4.16. (a) bimolecular recombination lifetime, and (b) bimolecular recombination coefficient as a function of time of the PCDTBT:$PC_{60}BM$ BHJ solar cell devices before and after treatment with IPA. The energy of laser beam was 10 μj.

4.4. CONCLUSION

This chapter reports attempts to increase the dielectric constant of PCDTBT:$PC_{60}BM$ based BHJ solar cell and its impact on the charge carrier dynamics of the solar cell devices. It is assumed that free volume of the 3D complex structure of the bulk heterojunction is filled with low dielectric gasses such as air and can be replaced through introduction or treatment of the BHJ by higher dielectric constant materials. Firstly, PFN and rhodamine 101 were introduced to the bulk. It was found out both materials have no significant impact on the dielectric constant of the BHJ film. However, they reduce the performance of the solar cell devices due to increase in the charge carrier recombination. Then, the PCDTBT:$PC_{60}BM$ BHJ was treated with isopropyl alcohol. The dielectric constant of the bulk heterojunction slightly increases after the treatment. But, the increase has not led to substantial alteration of the charge carrier dynamics. Therefore, these results may imply that the dielectric constant of polymer-based solar cells can be hardly enhanced by proposed method considering only the free volume of the bulk heterojunction.

4.5. FUTURE WORK

Although the morphology of the BHJ was not investigated in this chapter, it would be beneficial to understand the morphological impact of the introduced materials or solvents. This may help to choose materials with less impact on the BHJ morphology. While AFM can provide information relevant to the surface of the BHJ film, a more in-depth study can be done by TEM.

In this study, the bulk heterojunction was composed of the conjugated polymer (PCDTBT) as donor and $PC_{60}BM$ molecule as acceptor. Hence changing host bulk heterojunction to other kinds such as polymer-polymer, small molecule-small molecule based devices would be another option to investigate.

4.6. APPENDIX

PCDTBT:PC$_{60}$BM:PFN-Inc.

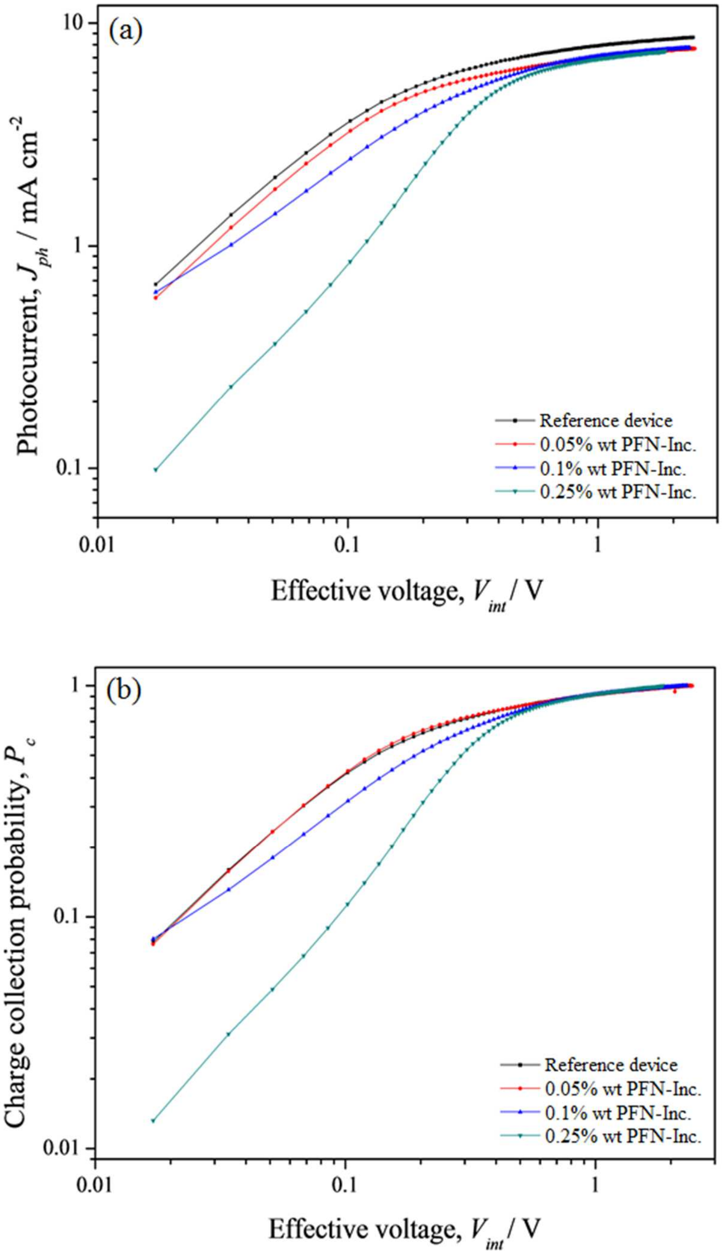

Figure 4.6.1. Photocurrent and (b) charge collection probability as a function of effective voltage of PCDTBT:PC$_{60}$BM BHJ solar cell devices before and after incorporation of PFN into bulk heterojunction.

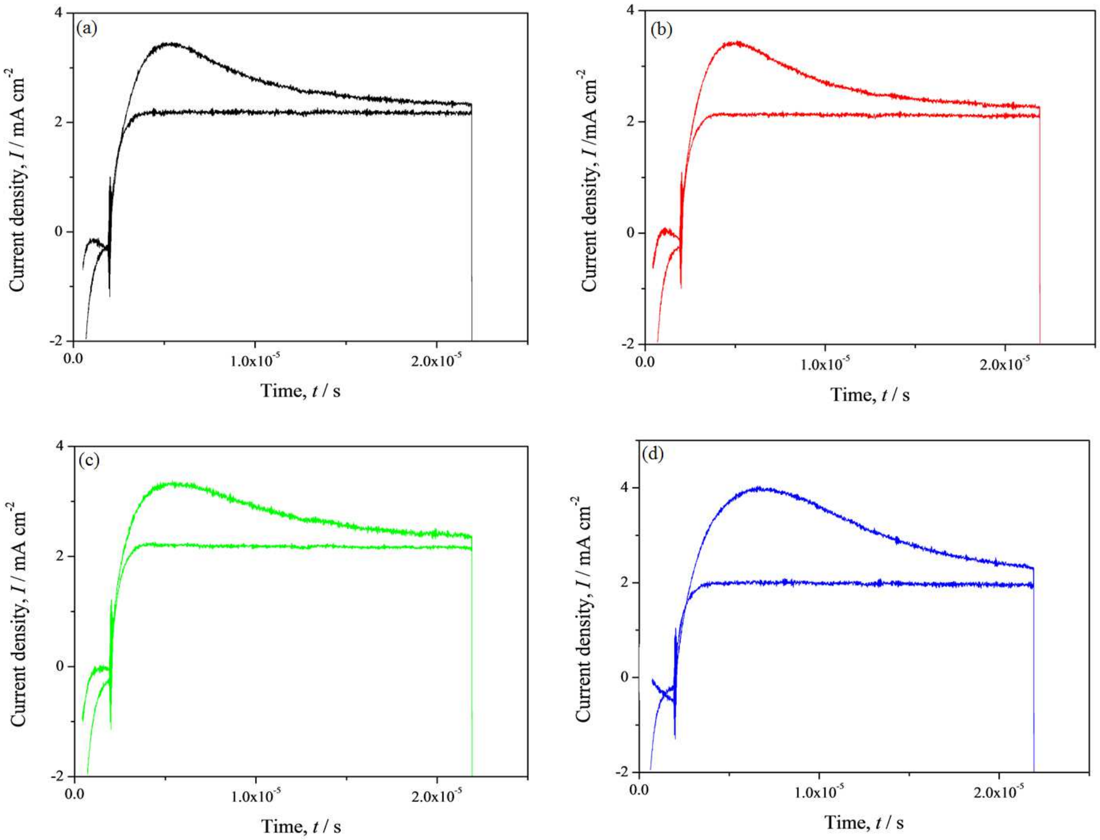

Figure 4.6.2. Photo-CELIV curves of the PCDTBT:PC$_{60}$BM BHJ solar cell devices (a) before adding PFN and after incorporation (b) 0.05%, (c) 0.1% and (d) 0.25% PFN into bulk heterojunction. The laser energy was set to 10 µj. The applied voltage was 1 V coupled with 50000 Hz rise time (A=50000 $V s^{-1}$)

PCDTBT:PC$_{60}$BM:R101-Inc.

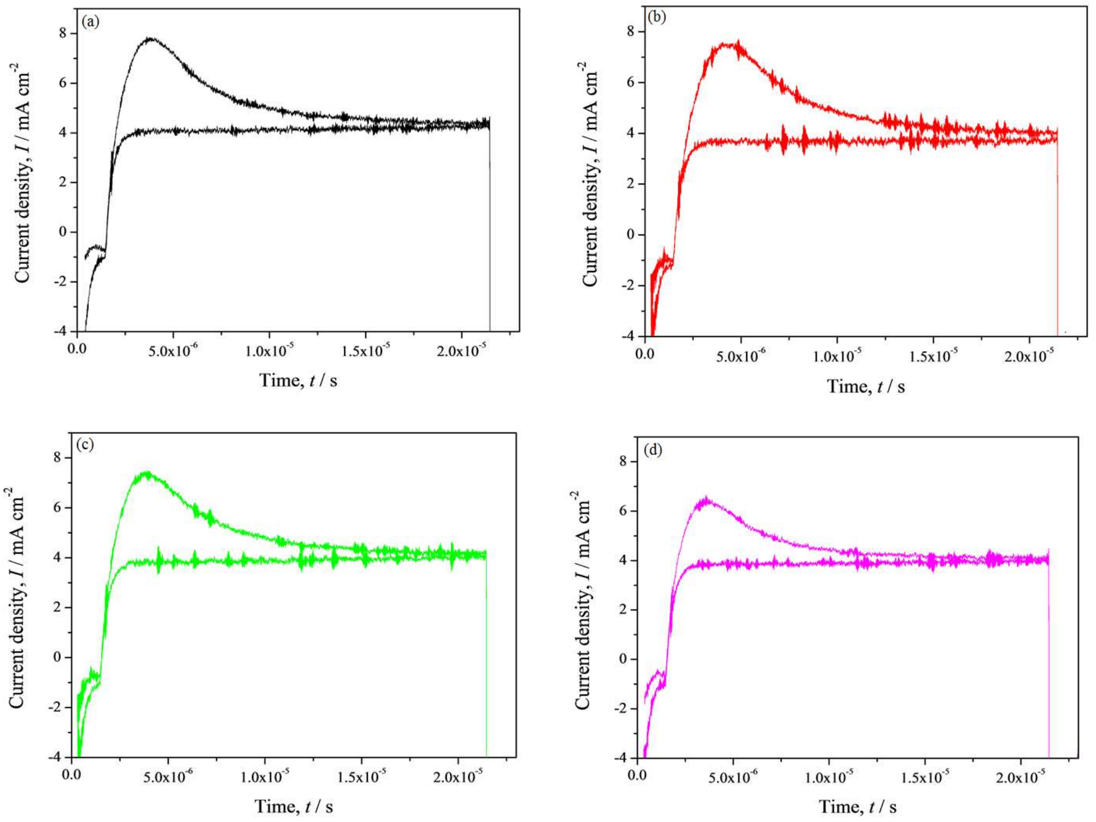

Figure 4.6.3. Photo-CELIV curves of PCDTBT:PC$_{60}$BM BHJ solar cell devices (a) without incorporation, and with incorporation of (b) 0.5%, (c) 1%, and (d) 5% rhodamine 101 into bulk heterojunction. The laser energy was set to 10 µj. The applied potential was 2 *V* coupled with 50000 Hz rise time. The delay between laser photoexcitation and extraction was set to 2 µs.

4.7. REFERENCES

(1) Koster, L. J. A.; Shaheen, S. E.; Hummelen, J. C. Pathways to a New Efficiency Regime for Organic Solar Cells. *Advanced Energy Materials* **2012,** *2* (10), 1246.

(2) Cho, N.; Schlenker, C. W.; Knesting, K. M.; Koelsch, P.; Yip, H.-L.; Ginger, D. S.; Jen, A. K. Y. High-Dielectric Constant Side-Chain Polymers Show Reduced Non-Geminate Recombination in Heterojunction Solar Cells. *Advanced Energy Materials* **2014,** *4* (10), 1301857.

(3) Torabi, S.; Jahani, F.; Van Severen, I.; Kanimozhi, C.; Patil, S.; Havenith, R. W. A.; Chiechi, R. C.; Lutsen, L.; Vanderzande, D. J. M.; Cleij, T. J.et al. Strategy for Enhancing the Dielectric Constant of Organic Semiconductors Without Sacrificing Charge Carrier Mobility and Solubility. *Advanced Functional Materials* **2015,** *25* (1), 150.

(4) Breselge, M.; Van Severen, I.; Lutsen, L.; Adriaensens, P.; Manca, J.; Vanderzande, D.; Cleij, T. Comparison of the electrical characteristics of four 2,5-substituted poly(p-phenylene vinylene) derivatives with different side chains. *Thin Solid Films* **2006,** *511–512*, 328.

(5) Hougham, G.; Tesoro, G.; Viehbeck, A.; Chapple-Sokol, J. D. Polarization Effects of Fluorine on the Relative Permittivity in Polyimides. *Macromolecules* **1994,** *27* (21), 5964.

(6) Ahmad, Z. In *Dielectric Material*; Silaghi, M. A., Ed.; InTech: Rijeka, 2012, DOI:10.5772/50638 10.5772/50638.

(7) Ramani, R.; Ramachandran, R.; Amarendra, G.; Alam, S. Direct correlation between free volume and dielectric constant in a fluorine-containing polyimide blend. *Journal of Physics: Conference Series* **2015,** *618* (1), 012025.

(8) Thran, A.; Kroll, G.; Faupel, F. Correlation between fractional free volume and diffusivity of gas molecules in glassy polymers. *Journal of Polymer Science Part B: Polymer Physics* **1999,** *37* (23), 3344.

(9) Budd, P. M.; McKeown, N. B.; Fritsch, D. Free volume and intrinsic microporosity in polymers. *Journal of Materials Chemistry* **2005,** *15* (20), 1977.

(10) Lorrmann, J.; Badada, B. H.; Inganäs, O.; Dyakonov, V.; Deibel, C. Charge carrier extraction by linearly increasing voltage: Analytic framework and ambipolar transients. *Journal of Applied Physics* **2010,** *108* (11), 113705.

(11) Hector, L. G.; Schultz, H. L. The Dielectric Constant of Air at Radiofrequencies. *Physics* **1936,** *7* (4), 133.

(12) Nian, L.; Zhou, J.; Zeng, K.; Wu, X.; Liu, L.; Xie, Z.; Huang, F.; Ma, Y. The effect of interfacial diffusion on device performance of polymer solar cells: a quantitative view by active-layer doping. *Science China Chemistry* **2015,** *58* (2), 317.

(13) Duan, C.; Cai, W.; Hsu, B. B. Y.; Zhong, C.; Zhang, K.; Liu, C.; Hu, Z.; Huang, F.; Bazan, G. C.; Heeger, A. J.et al. Toward green solvent processable photovoltaic materials for polymer solar cells: the role of highly polar pendant groups in charge carrier transport and photovoltaic behavior. *Energy & Environmental Science* **2013,** *6* (10), 3022.

(14) Constantinou, I.; Lai, T. H.; Hsu, H. Y.; Cheung, S. H.; Klump, E. D.; Schanze, K. S.; So, S. K.; So, F. Effect of Thermal Annealing on Charge Transfer States and Charge Trapping in PCDTBT:PC70BM Solar Cells. *Advanced Electronic Materials* **2015,** *1* (9).

(15) Sun, K.; Zhao, B.; Kumar, A.; Zeng, K.; Ouyang, J. Highly Efficient, Inverted Polymer Solar Cells with Indium Tin Oxide Modified with Solution-Processed Zwitterions as the Transparent Cathode. *ACS Applied Materials & Interfaces* **2012,** *4* (4), 2009.

(16) Sun, K.; Zhao, B.; Murugesan, V.; Kumar, A.; Zeng, K.; Subbiah, J.; Wong, W. W. H.; Jones, D. J.; Ouyang, J. High-performance polymer solar cells with a conjugated zwitterion by solution processing or thermal deposition as the electron-collection interlayer. *Journal of Materials Chemistry* **2012,** *22* (45), 24155.

(17) Cowan, S. R.; Leong, W. L.; Banerji, N.; Dennler, G.; Heeger, A. J. Identifying a Threshold Impurity Level for Organic Solar Cells: Enhanced First-Order Recombination Via Well-Defined PC84BM Traps in Organic Bulk Heterojunction Solar Cells. *Advanced Functional Materials* **2011,** *21* (16), 3083.

(18) Eng, M. P.; Barnes, P. R. F.; Durrant, J. R. Concentration-Dependent Hole Mobility and Recombination Coefficient in Bulk Heterojunctions Determined from Transient Absorption Spectroscopy. *The Journal of Physical Chemistry Letters* **2010,** *1* (20), 3096.

(19) Clarke, T. M.; Lungenschmied, C.; Peet, J.; Drolet, N.; Sunahara, K.; Furube, A.; Mozer, A. J. Photodegradation in Encapsulated Silole-Based Polymer: PCBM Solar Cells Investigated using Transient Absorption Spectroscopy and Charge Extraction Measurements. *Advanced Energy Materials* **2013,** *3* (11), 1473.

(20) Wang, Q.; Zhou, Y.; Zheng, H.; Shi, J.; Li, C.; Su, C. Q.; Wang, L.; Luo, C.; Hu, D.; Pei, J.et al. Modifying organic/metal interface via solvent treatment to improve electron injection in organic light emitting diodes. *Organic Electronics* **2011,** *12* (11), 1858.

(21) Kai, Z.; Zhicheng, H.; Chunhui, D.; Lei, Y.; Fei, H.; Yong, C. The effect of methanol treatment on the performance of polymer solar cells. *Nanotechnology* **2013,** *24* (48), 484003.

(22) Zhang, X.; Li, Z.; Zhang, Z.; Li, S.; Liu, C.; Guo, W.; Shen, L.; Wen, S.; Qu, S.; Ruan, S. Efficiency Improvement of Organic Solar Cells via Introducing Combined Anode

Buffer Layer To Facilitate Hole Extraction. *The Journal of Physical Chemistry C* **2016,** *120* (26), 13954.

(23) Zhou, H.; Zhang, Y.; Seifter, J.; Collins, S. D.; Luo, C.; Bazan, G. C.; Nguyen, T.-Q.; Heeger, A. J. High-Efficiency Polymer Solar Cells Enhanced by Solvent Treatment. *Advanced Materials* **2013,** *25* (11), 1646.

(24) Pingree, L. S. C.; Reid, O. G.; Ginger, D. S. Electrical Scanning Probe Microscopy on Active Organic Electronic Devices. *Advanced Materials* **2009,** *21* (1), 19.

(25) Nonnenmacher, M.; O'Boyle, M. P.; Wickramasinghe, H. K. Kelvin probe force microscopy. *Applied Physics Letters* **1991,** *58* (25), 2921.

(26) Guo, S.; Cao, B.; Wang, W.; Moulin, J.-F.; Müller-Buschbaum, P. Effect of Alcohol Treatment on the Performance of PTB7:PC71BM Bulk Heterojunction Solar Cells. *ACS Applied Materials & Interfaces* **2015,** *7* (8), 4641.

Chapter 5: A study of dielectric constant effect on the performance of bulk heterojunction solar cells Part II: Small Molecule-based solar cells

5.1. INTRODUCTION

The idea of increasing dielectric constant was presented in the previous chapter and applied to the polymer-based bulk heterojunction solar cells. The aim of this chapter is to extend the similar concept to solution-processed small molecule-based bulk heterojunction (SM BHJ) solar cells. The solution-processed small molecule donors have attracted attention during the past decade due to potential advantages over low-bandgap conjugated polymer counterparts. For example, the solubility of the SM donor in organic solvents is higher compared to the polymer analogues which facilitate purification and characterization of the donors using standard organic chemistry procedures. Moreover, the molecular framework of the donor can be fine-tuned without the complexity of variating the average molecular weight and polydispersity of BHJ polymer systems. It has been demonstrated that the solution-processed small molecule donors can become a replacement to the narrow band-gap conjugated polymer donors.[1-7] Indeed, the performance of BHJ solar cells composed of the solution-processed small molecular donor has considerably progressed in the past few years with several systems with efficiency over 8% being reported in the literature.[8-12]

Although continuous improvement of the PCE has brought the solar cells to the point where they may become commercially viable, further investigation regarding increasing efficiency and device stability is required. As predicted,[13] increasing dielectric constant may pave the way to further enhance PCE of the SM BHJ solar cell devices. Hence, small molecule BHJ solar cell devices composed of 7,7′-[4,4-Bis(2-ethylhexyl)-4H-silolo[3,2-b:4,5-b′]dithiophene-2,6-diyl]bis[6-fluoro-4-(5′-hexyl-[2,2′-bithiophen]-5-yl)benzo[c][1,2,5] thiadiazole] (p-DTS(FBBTh$_2$)$_2$) and PC$_{60}$BM are the subject of dielectric constant study in this chapter. The small molecule donor p-DTS(FBBTh$_2$)$_2$ was first introduced in 2012.[14] Its chemical structures allows to achieve better compatibility with hole transport layer PEDOT:PSS. The initial BHJ of the small molecule and PCBM shows very low efficiency due to low phase separation and intimate mixing of the molecules. Hence, an optimal small molecule device requires specific processing condition such as alteration of the solvent, using additive and post-treatment (thermal annealing).[15-19] The performance of the SM BHJ system has been progressively improved since 2012 and PCE over 8% in a single junction solar cell has been reported for the BHJ system.[19] Therefore, further enhancement of the dielectric constant may allow for achieving higher PCE in solution-processed high-performance small molecule BHJ systems.

5.2. EXPERIMENTAL

5.2.1. PFN-incorporated BHJ Devices

The small molecule-based BHJ solar cell devices were fabricated according to general procedures outlined in Chapter 2. A conventional structure composed of ITO/PEDOT:PSS/*p*-DTS(FBTTh$_2$)$_2$:PC$_{60}$BM/Al was used throughout. The *p*-DTS(FBTTh$_2$)$_2$ and PC$_{60}$BM were added to 1 ml chlorobenzene at a weight ratio of 1:1.5 with an overall concentration of 35 mg mL^{-1}. To incorporate PFN into bulk, 0.1 mg PFN was dissolved in 1 ml chlorobenzene and then 50 and 100 µl of PFN-contained CB were mixed with pure CB to prepare 1 ml solution altogether. The weight ratios of PFN to the active materials are 0.014% and 0.029% wt, respectively. The active layer films with thickness of 100 ± 5 nm were made from solutions with and without PFN and subjected to thermal treatment for 10 min at 70 ºC and 5 min at 80 Cº (inside a glovebox with oxygen concentration less than 1 ppm). The solar cell device conventional structure and chemical structures of the donor and acceptor are shown in Figure

5.2.2. Rhodamine 101-incorporated BHJ Devices

The fabrication of rhodamine 101-incorporated devices was similar to PFN-incorporated devices. The 0.1 mg rhodamine 101 was dissolved in 1 ml CB and 10 and 50 µl of rhodamine 101-contained CB solutions were mixed with pure CB solution to make 1 ml solutions. The weight ratios of the rhodamine 101 to active materials were 0.0029% and 0.014% wt, respectively. The active layers with and without embedded rhodamine 101 were subjected to thermal treatment as above.

5.2.3. Isopropyl alcohol-treated BHJ Devices

After thermal treatment of the active layer, IPA treatment was carried out by spin coating of 35 µl IPA solvent on top of the active layer at 2000 rpm for 60 s.

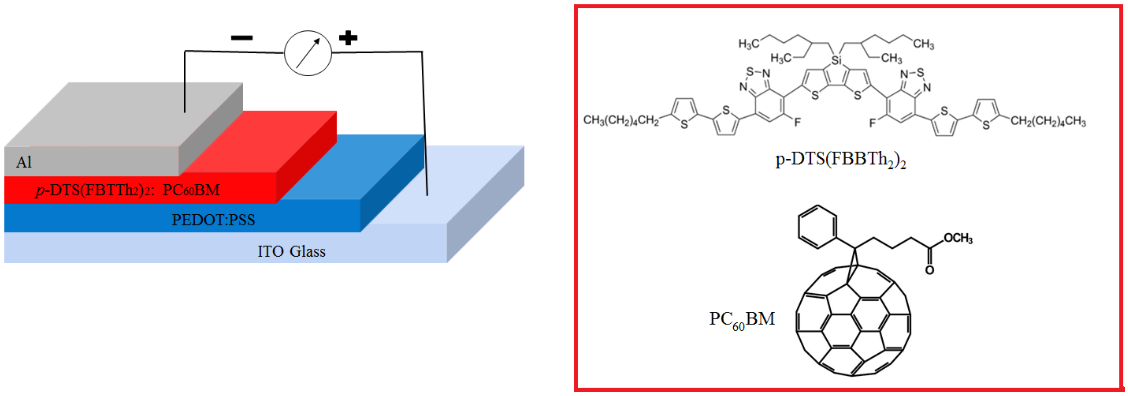

Figure 5.1. The solar cell device architecture and chemical structures of p-DTS(FBBTh$_2$)$_2$ and PC$_{60}$BM.

5.2.4. Solar cell device characterization

The current density-voltage measurement, EQE, photovoltage decay, time-resolved charge extraction and photo-CELIV measurements were performed according to the procedures described in Chapter 2. The dielectric constant of the solar cell devices was measured using dark CELIV described in Chapter 4.

5.3. RESULTS AND DISCUSSION

5.3.1. p-DTS(FBBTh2)2:PC60BM:PFN-incorporated

5.3.1.1. Photovoltaic characteristics

Figure 5.2 shows the current density-voltage curves of the representative devices fabricated from p-DTS(FBBTh$_2$)$_2$:PC$_{60}$BM without and with the incorporation of PFN. The extracted parameters from current density-voltage curves are presented in Table 5.1. The PFN was added to the bulk solution in two concentrations by weight ratio, i.e., 0.014% and 0.029% wt. The power conversion efficiency of the device was reduced after the addition of the PFN mainly due to reduction of short-circuit current and fill factor. This may indicate the enhancement of charge carrier recombination. The external quantum efficiency measurement recorded at short-circuit condition (V_{app} = 0 V) for pristine and PFN-containing devices are shown in Figure 5.3. The EQE data shows that the efficiency of photon-to-electron conversion has been decreased upon the addition of PFN. The obtained J_{sc} by integrating EQE spectrum

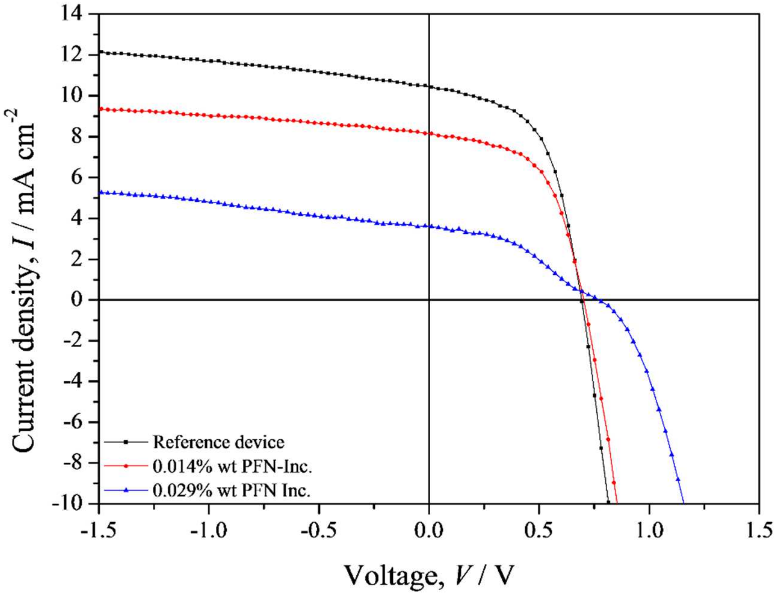

Figure 5.2. Comparison of current density-voltage characteristics of p-DTS(FBTTh$_2$)$_2$:PC$_{60}$BM BHJ solar cell devices without and with the incorporation of the PFN into bulk heterojunction.

Table 5.1. Photovoltaic parameters of p-DTS(FBTTh$_2$)$_2$:PC$_{60}$BM BHJ solar cell devices before and after introduction of PFN into bulk heterojunction. Eight devices were measured and averaged.

Devices	V_{oc} (*mV*)	J_{sc} (*mA cm*$^{-2}$)	FF	PCE (%)
Reference	690.0 ± 10	8.9 ± 1.2	54 ± 1.9	3.3 ± 0.5
0.014% wt PFN Inc.	710.0 ± 10	6.9 ± 1.2	52.2 ± 2.3	2.5 ± 0.5
0.029% wt PFN Inc.	710.0 ± 70	3.4 ± 0.8	39 ± 4.3	0.94 ± 0.3

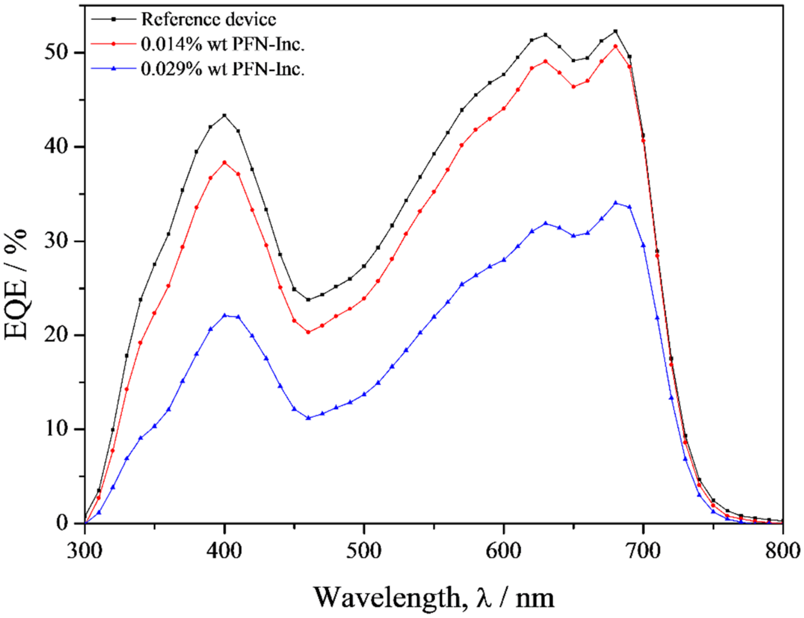

Figure 5.3. EQE curves of the p-DTS(FBTTh$_2$)$_2$:PC$_{60}$BM BHJ solar cell devices without and with PFN embedded into the bulk.

for the pristine, 0.014%, and 0.029% wt PFN-containing devices are 8.77, 8.06, and 4.11 *mA cm*$^{-2}$, respectively. These results are consistent with current density-voltage measurement. The observed reduction of external quantum efficiency can be attributed to the presence of the PFN in the bulk which obstructs generation, transportation and/or collection of charge carriers. As such, the fraction of charge carriers that can be swept out, are mitigated, resulting in a reduction in short-circuit current and fill factor in the PFN-doped devices.

To examine the effect of the PFN on the photo-generation and collection of the charge carriers, photocurrent and charge collection probability dependence on the effective voltage were investigated. Figure 5.3a shows the photocurrent of the p-DTS(FBTTh$_2$)$_2$:PC$_{60}$BM BHJ devices before and after incorporation of the PFN. It is immediately clear that the photocurrent of the PFN-doped devices was reduced across all effective voltage range compared to the reference devices. The maximum photo-induced charge carrier generation rate per volume (G_{max}) is calculated for the devices. The G_{max} values for pristine and 0.014%, 0.029% wt PFN-doped devices are 7.44×10^{27} (119.22 $A\ m^{-2}$), 5.68×10^{27} (91.056 $A\ m^{-2}$), and $3.28 \times 10^{27}\ m^{-3}\ s^{-1}$ (52.604 $A\ m^{-2}$), respectively. These values indicated that generation of charge carriers was diminished in the presence of the PFN which could potentially contribute to the lower short-circuit current observed for the PFN-doped devices. The charge collection probability of devices versus effective voltage (Figure 5.4b) also exhibited collection of charge carrier in devices doped with 0.014% wt PFN was quite similar to the reference device, whereas increasing concentration of PFN to 0.029% wt resulted in a reduced collection of charge carrier, particularly at low V_{int}. Therefore, the poor collection of charge carriers implies an enhancement of the recombination loss in the 0.029% wt PFN-doped devices, which was reflected in the considerable reduction of short-circuit current and fill factor.

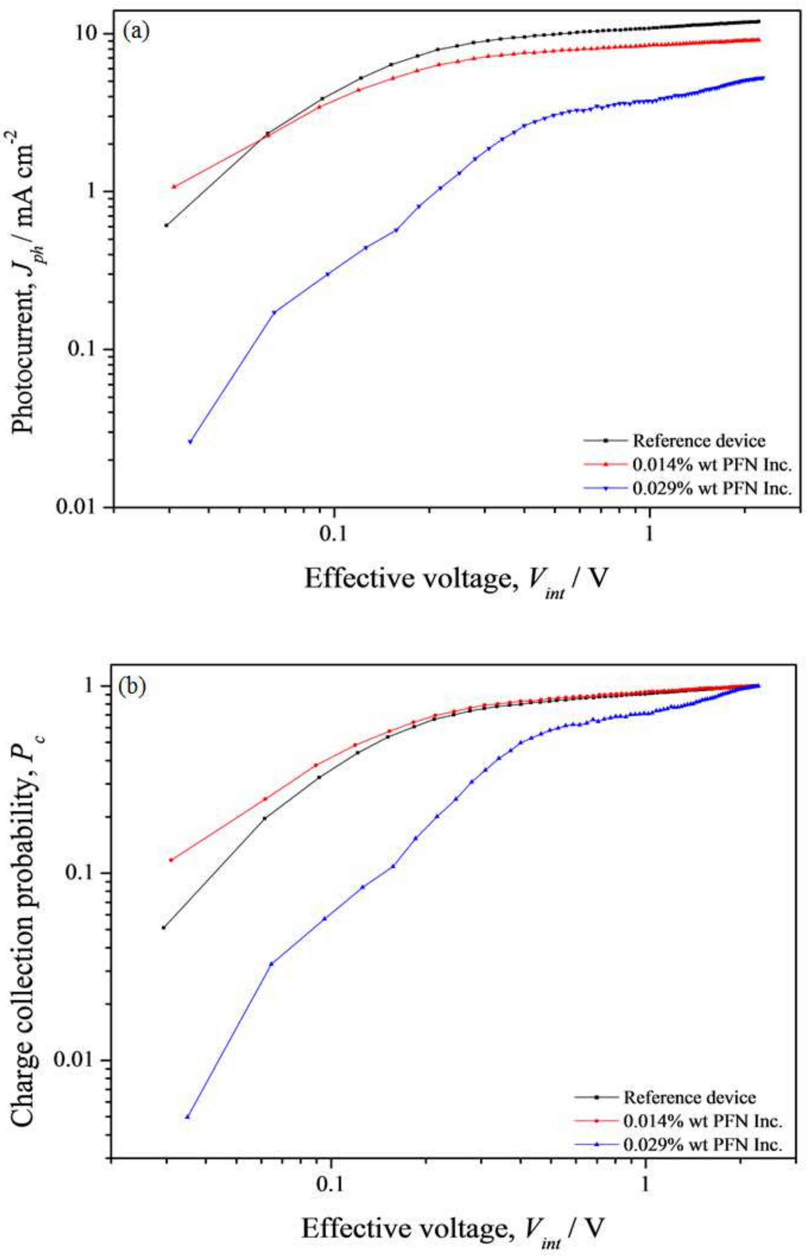

Figure 5.4. (a) Photocurrent (J_{ph}), (b) charge collection probability (P_c) as a function of effective voltage (V_{int}) of the p-DTS(FBTTh$_2$)$_2$:PC$_{60}$BM BHJ solar cell devices without and with PFN embedded into the bulk.

5.3.1.2. Dielectric constant, PVD, TRCE, and photo-CELIV measurements

The dielectric constant of the p-DTS(FBBTh$_2$)$_2$:PC$_{60}$BM BHJ solar cell devices were determined using CELIV technique (Figure 5.5). The calculated dielectric constant of the devices is listed in Table 5.2. A slight increase of the dielectric constant is observed following incorporation of the PFN into bulk heterojunction. This could be due to alteration of the polarization or free volumes within the bulk heterojunction after PFN being added. However, it appears that the added PFN interferes with internal mechanisms (generation, transportation, and collection) of the bulk heterojunction and the addition comes at cost of device's performance.

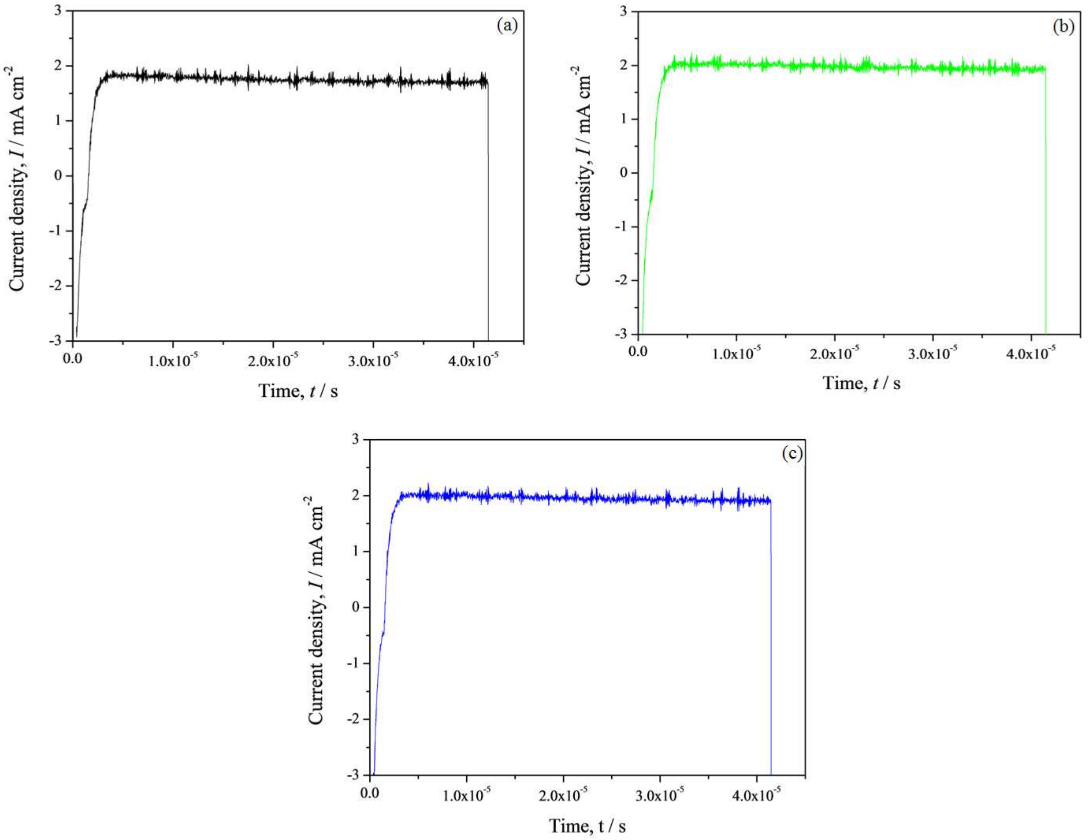

Figure 5.5. Measured dark CELIV of the p-DTS(FBTTh$_2$)$_2$:PC$_{60}$BM solar cell devices (a) without PFN (b) 0.014% wt and (c) 0.029% wt PFN-doped into the bulk. The applied voltage was 2 *V* coupled with 25000 Hz rise time (A = 50000 *V s*$^{-1}$). The thickness of the active layer was 100 ± 5 nm.

Table 5.2. Calculated dielectric constant and charge carrier mobility of p-DTS(FBTTh$_2$)$_2$:PC$_{60}$BM BHJ solar cell devices before and after incorporation of PFN. Three devices were measured and averaged.

Device	Dielectric constant	Mobility ($cm^2\ V^{-1}\ s^{-1}$)
Reference	4.0 ± 0.2	3.99×10^{-5}
0.014% loaded PFN	4.5 ± 0.2	4.08×10^{-5}
0.029% loaded PFN	4.4 ± 0.2	4.22×10^{-5}

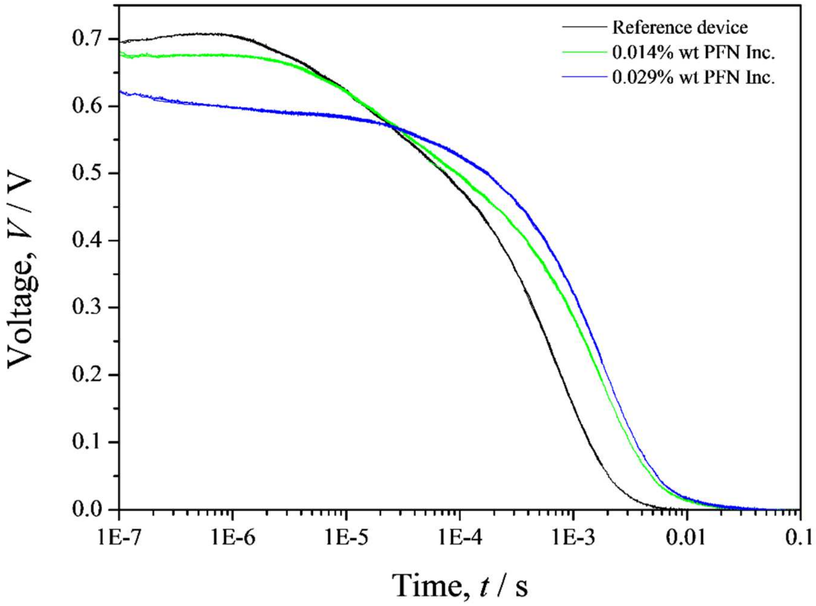

Figure 5.6. Photovoltage decay of the *p*-DTS(FBTTh$_2$)$_2$:PC$_{60}$BM solar cell devices before and after incorporation of PFN into bulk heterojunction.

Figure 5.6 shows photovoltage decay of solar cell devices over time before and after the introduction of the PFN into the p-DTS(FBBTh$_2$)$_2$:PC$_{60}$BM bulk heterojunction. The pristine device has a higher photovoltage at the early time compared to the PFN-doped devices. Moreover, at 35 μs a crossover happens such that at the longer time the PFN-doped devices have higher photovoltage. The lower photovoltage values at early time in the PFN-doped devices can be attributed to the reduction of charge carrier generation. The open-circuit potential is determined by the quasi-Fermi levels (electrons and holes) splitting which is dependent on the available charge carriers and density of state. Therefore, the reduction of the charge carrier perhaps results in the lower quasi-Fermi level and consequently photovoltage in the PFN-doped devices. However, the photovoltage values in the PFN-doped devices are lower compared to open-circuit voltage values extracted from the current density-voltage measurement. The reason for such a difference remains unknown. But, it has been suggested by Clark *et al.*[20] that variation in the results can be observed due to different nature of techniques (steady state versus transient).

In order to investigate the effect of the dielectric constant alteration upon introduction of PFN of the charge carrier density and decay dynamics, TRCE measurement was employed. The pristine device shows higher charge carrier density compared to the PFN-loaded devices at early times (Figure 5.7a). The results are in agreement with photocurrent measurement. However, after 10 μs the PFN-doped BHJ devices charge carrier density decays slowly, leading to higher charge carrier density at the longer times. This is associated with slightly higher bimolecular recombination lifetime (Figure 5.7b) and lower bimolecular recombination coefficient (Figure 5.7c) at long times in PFN-incorporated devices. These results are also consistent with the photovoltage decay results. However, there appears to be an inconsistency between these results and the constant reduction of J_{sc} upon increasing the concentration of the PFN. Clarke *et al.*[20] report similar results in a photo-degraded BHJ device composed of KP115:PCBM. The authors explain that it is probable after photodegradation, deeper and broader trap states reduce bimolecular recombination under open circuit condition (increasing charge carrier density at long times), whereas under short circuit conditions promote the recombination. Given that, one may conclude that slight enhancement of the dielectric constant (due to the addition of PFN) slows down the bimolecular recombination, giving higher charge carrier density at the longer times. However, it should be noted that considerable interference of PFN with charge carrier generation and extraction could be accounted for the loss of short-circuit current.

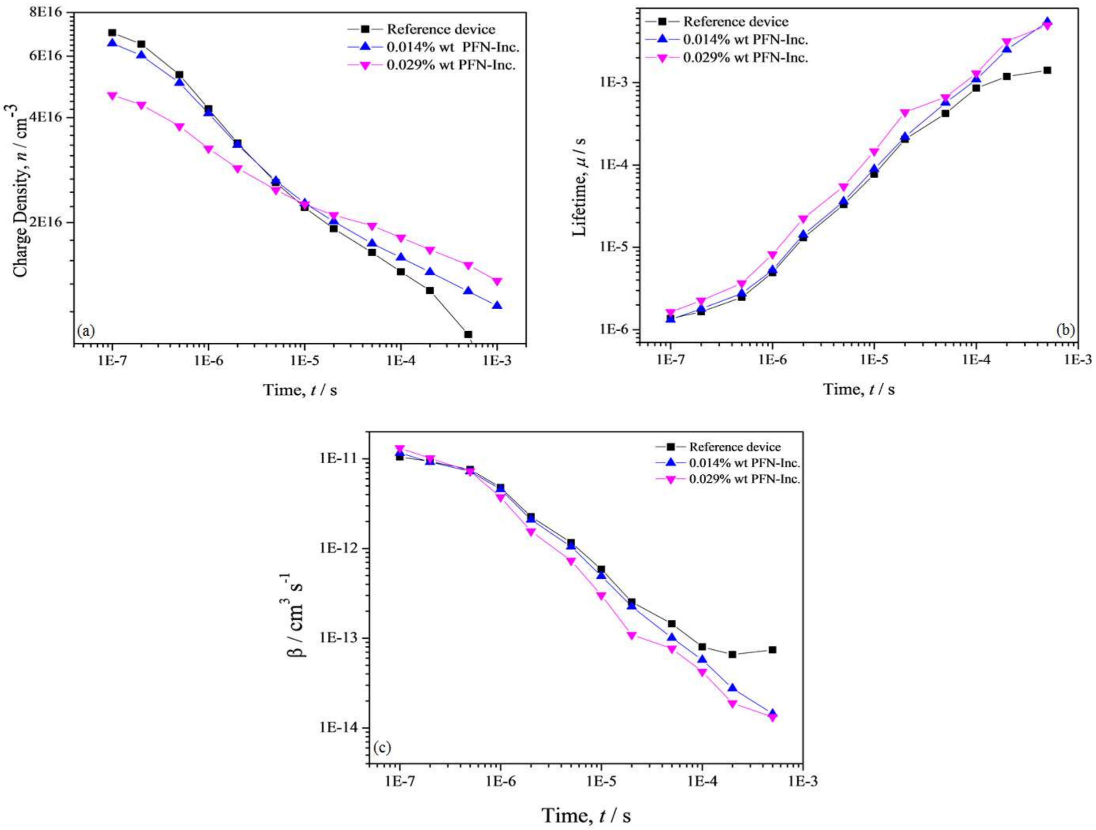

Figure 5.7. (a) charge carrier density, (b) bimolecular recombination lifetime and (c) bimolecular recombination coefficient versus time for the *p*-DTS(FBTTh$_2$)$_2$:PC$_{60}$BM BHJ solar cell devices before and after PFN incorporation into the bulk heterojunction.

The charge carrier mobility of the p-DTS(FBBTh$_2$)$_2$:PC$_{60}$BM BHJ solar cell devices before and after the addition of PFN has been accomplished using the photo-CELIV technique. The calculated mobility of the devices after 2 μs delay time are listed in Table 5.2 (the corresponding photo-CELIV curves are shown in Figure 5.6.1, Appendix). The charge carrier mobility of the device is quite comparable with slightly bigger values for the PFN-doped devices. One possibility is energetic disorders (trap states) within the bulk has not been affected by the introduction of the PFN, as it is shown that charge carrier mobility in organic semiconductor decrease with increasing trap density.[21] Another explanation is the photo-CELIV technique may not be able to observe the mobility of all charge carriers, in particular, those who are deeply trapped. Therefore, the obtained mobility values represent charge carriers that have been extracted.[20]

5.3.2. p-DTS(FBBTh2)2:PC60BM:R101-incorporated

5.3.2.1. Photovoltaic characteristics

The photovoltaic parameters of the p-DTS(FBBTh$_2$)$_2$:PC$_{60}$BM BHJ solar cell devices before and after doping with rhodamine 101 extracted from current density-voltage measurement are listed in Table 5.3. The representative current density-voltage curves are shown in Figure 5.8. The rhodamine 101-doped devices show lower power conversion efficiency compared to the pristine devices mainly because of the reduction of the fill factor. This suggests that recombination of charge carriers in the presence of the rhodamine 101 has been intensified. Figure 5.9 displays the external quantum efficiency of the devices. The EQE of rhodamine 101-doped devices was lower than that of the reference device, except slightly higher in the wavelength range 300-500 nm in 0.0029% wt device. The J_{sc} obtained from EQE for the pristine, 0.0029% wt, and 0.014% wt rhodamine 101-doped devices are 8.45, 8.24 and 7.97 $mA\ cm^{-2}$, respectively. The values were in good agreement with J_{sc} extracted from current density-voltage measurement and indicate that the efficiency of photon to electron conversion has been reduced in the rhodamine 101-doped devices (Figure 5.10).

Table 5.3. Photovoltaic parameters of the p-DTS(FBTTh$_2$)$_2$:PC$_{60}$BM BHJ solar cell devices in the absence and presence of rhodamine 101 incorporated into the bulk heterojunction. The results are an average of 8 devices.

Devices	V$_{oc}$ (*mV*)	J$_{sc}$ (*mA cm*$^{-2}$)	FF	PCE (%)
Reference	670.0 ± 10	8.5 ± 0.2	57 ± 2	3.2 ± 0.1
0.0029% wt R101-Inc.	660.0 ± 20	8.5 ± 0.4	51 ± 4	2.9 ± 0.3
0.014% wt R101-Inc.	660.0 ± 10	8.0 ± 0.4	46 ± 3	2.4 ± 0.2

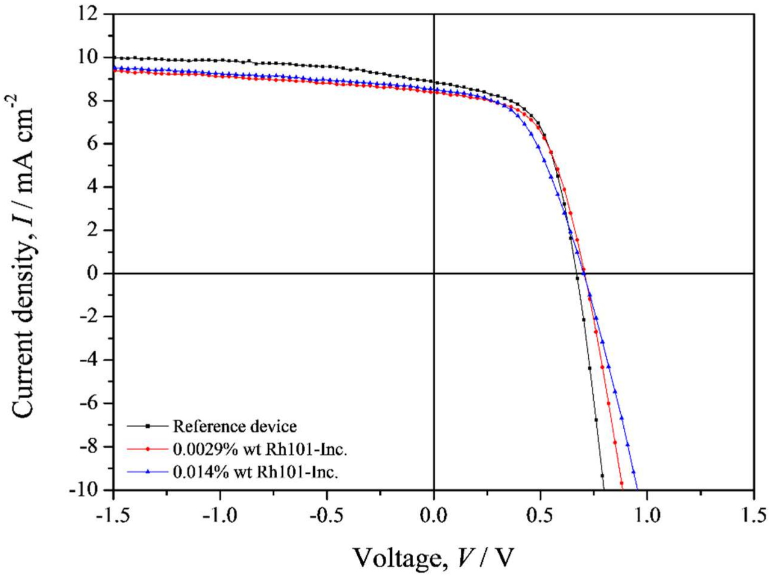

Figure 5.8. Recorded current density-voltage of p-DTS(FBTTh$_2$)$_2$:PC$_{60}$BM solar cell devices in the absence and presence of Rhodamine 101 incorporated into BHJ.

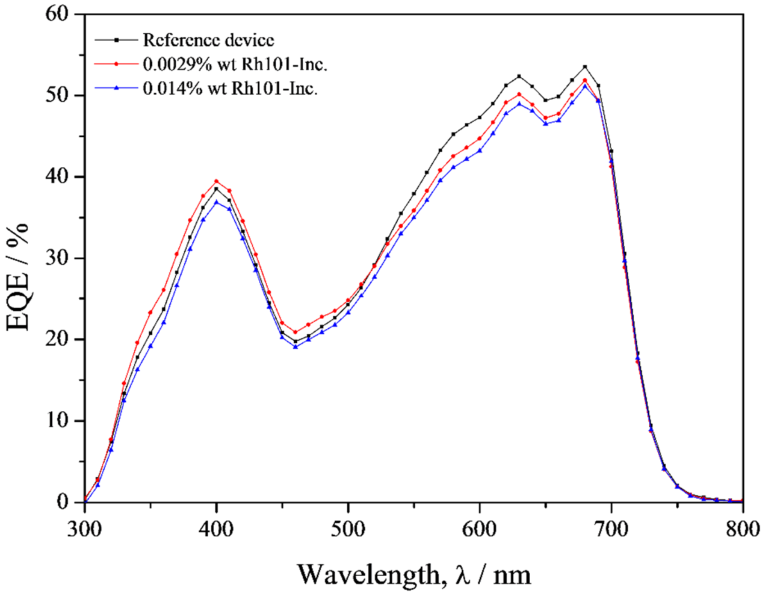

Figure 5.9. EQE curves of the p-DTS(FBTTh$_2$)$_2$:PC$_{60}$BM BHJ solar cell devices without and with Rhodamine 101 embedded into the bulk.

To understand the effect of the rhodamine 101 on the generation and collection of the charge carriers, the photocurrent (J_{ph}) and charge collection probability (P_c) of the devices were studied as a function of the effective voltage (V_{int}). The main effect of the rhodamine 101 on both photocurrent and charge collection probability emerge at the low effective voltage (< 0.3 V) where due to the weakness of the internal electric field, the bimolecular recombination plays a significant role. This means that the addition of the rhodamine 101 increase recombination loss (around open-circuit potential), especially in the 0.014% wt device. On the other hand, both photocurrent and charge collection probability of the solar cell devices at high V_{int} (> 0.3 V) are quite the same, suggesting charge carrier recombination has not been affected in the absence and presence of the rhodamine 101. The G_{max} values of the reference device, 0.0029% wt and 0.014% wt rhodamine 101-doped devices were 6.12×10^{27} (98.0256 A m^{-2}), 5.85×10^{27} (93.7571 A m^{-2}), and 5.92×10^{27} m^{-3} s^{-1} (94.8878 A m^{-2}), respectively. The values were in almost similar range, though slightly less than the rhodamine 101-doped devices. Therefore, it could be concluded that the reduction of performance in the rhodamine 101-doped devices stems from enhancing of the recombination around open-circuit conditions which manifests in low fill factor.

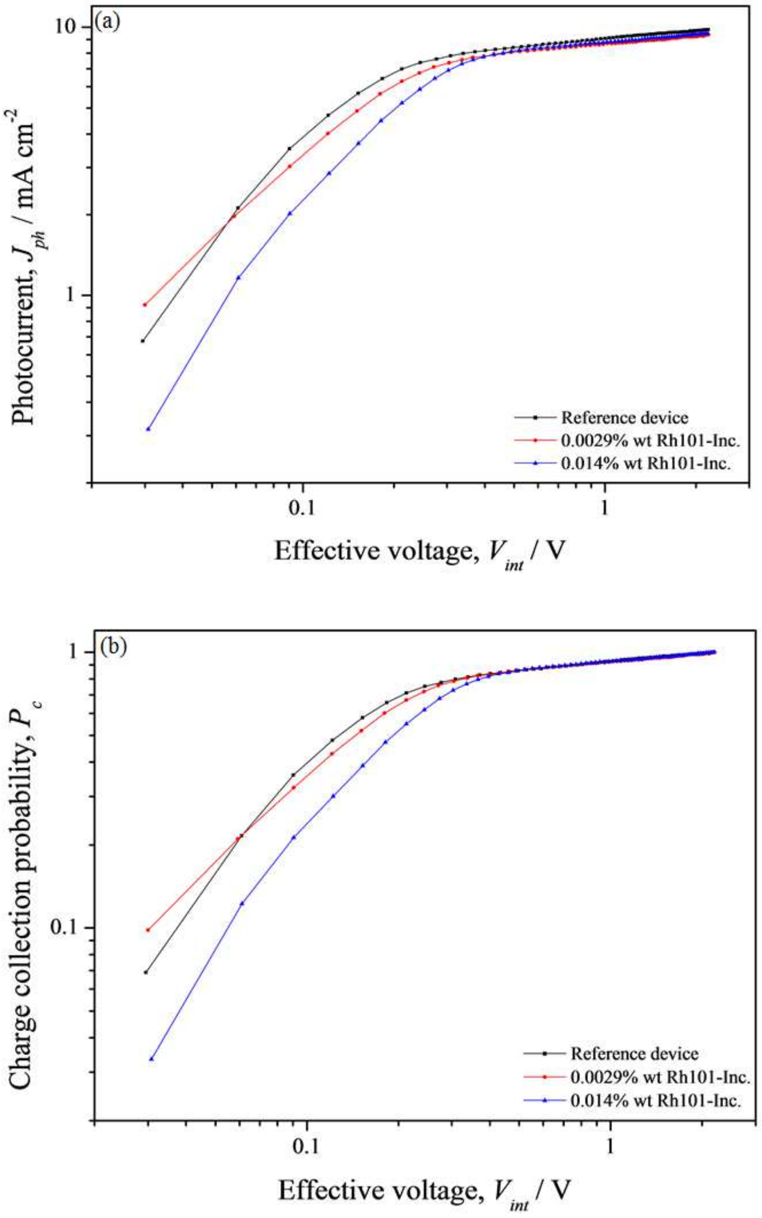

Figure 5.10. (a) Photocurrent (J_{ph}), (b) charge collection probability (P_c) as a function of effective voltage (V_{int}) of the p-DTS(FBTTh$_2$)$_2$:PC$_{60}$BM BHJ solar cell devices before and after addition of rhodamine 101 the bulk.

5.3.2.2. Dielectric constant, PVD, TRCE and photo-CELIV measurements

The dielectric constant of the p-DTS(FBBTh$_2$)$_2$:PC$_{60}$BM BHJ solar cell devices before and after doping with rhodamine 101 was calculated according to equation 4-1 using the CELIV technique. A 2 *V* potential coupled with 50,000 Hz rise time was applied to the devices and the responses were recorded by oscilloscope over 10 Ω resistance. The CELIV curves of the devices are shown in Figure 5.11. The dielectric values are presented in Table 5.4. It was observed that the incorporation of 0.0029% wt rhodamine 101 into the SM BHJ had a marginal impact, whereas increasing the dopant content to 0.014% wt moderately reduces the dielectric constant. The reduction is perhaps due to the effect of rhodamine 101 on polarization and/or free volume

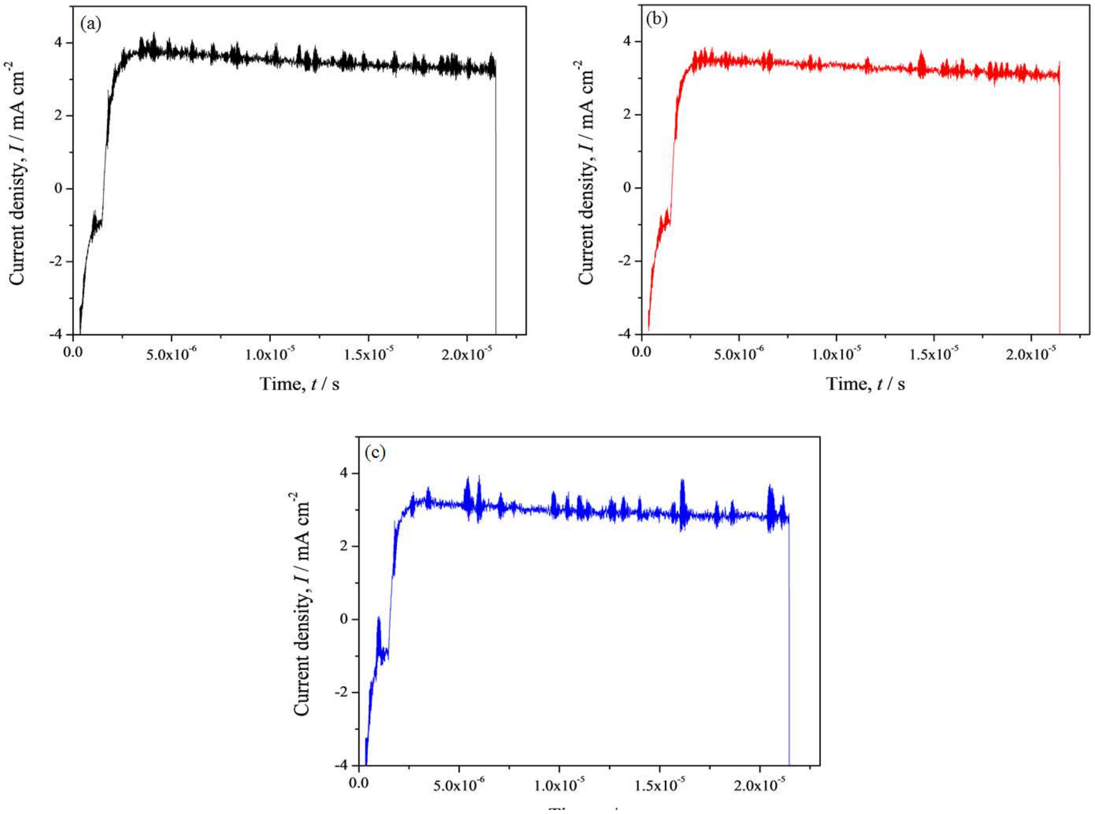

Figure 5.11. Measured dark CELIV of the *p*-DTS(FBTTh$_2$)$_2$:PC$_{60}$BM solar cell devices (a) without, and with the incorporation of (b) 0.0029% wt, and (c) 0.014% wt of rhodamine 101 into the bulk heterojunction. The voltage speed rise (A) was 100000 $V\,s^{-1}$. The thickness of the active layer was 100 ± 5 nm.

Table 5.4. The calculated dielectric constant and charge carrier mobility of the bulk heterojunction p-DTS(FBTTh$_2$)$_2$:PC$_{60}$BM solar cell devices before and after the incorporation of rhodamine 101. Three devices were measured and averaged.

Devices	**Dielectric constant**	**Mobility (*cm^2 V^{-1} s^{-1}*)**
Reference	4.0 ± 0.2	3.11×10^{-5}
0.0029% wt Rh101-loaded	3.7 ± 0.2	3.56×10^{-5}
0.014% wt Rh101-loaded	3.4 ± 0.2	3.82×10^{-5}

of the bulk, the factors determining the dielectric constant. Further investigation of the devices was accomplished by performing TRCE measurement. Figure 5.13a shows charge carrier density of the devices before and after the addition of rhodamine 101 as a function of time. The reference device has a slightly higher charge carrier density compared to the devices containing rhodamine 101. This is in agreement with better charge carrier collection at low V_{int} and higher G_{max} value in the reference device. Nevertheless, there is no appreciable discrepancy in bimolecular recombination lifetime (Figure 5.13b) and bimolecular recombination coefficient (Figure 5.13c) of the solar cell devices before and after incorporation of the rhodamine 101. This indicates that recombination dynamics of charge carrier has not been affected following the introduction of rhodamine 101 and consequently slight reduction of dielectric constant. It is reported that presence of the impurities increases energetic disorder in the solar cell and reduces the performance.[22] Hence, one may conclude that introduction of rhodamine 101 into the bulk did not increase the energetic disorder.

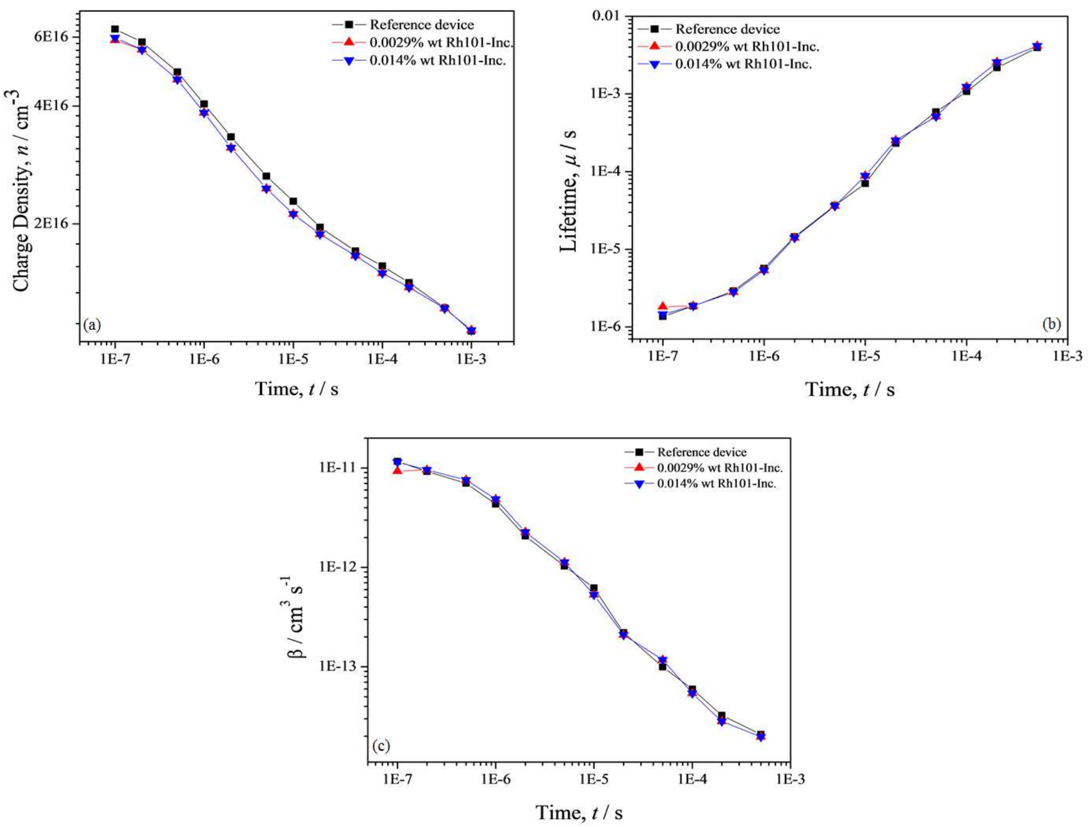

Figure 5.12. (a) Charge carrier density, (b) bimolecular recombination lifetime, and (c) bimolecular recombination coefficient as a function of time for the p-DTS(FBTTh$_2$)$_2$:PC$_{60}$BM BHJ solar cell devices before and after loading various concentration of rhodamine 101 in the bulk heterojunction.

The charge carrier mobility of the p-DTS(FBBTh$_2$)$_2$:PC$_{60}$BM BHJ solar cell device without and with rhodamine 101 was measured using the photo-CELIV technique. The mobility of the devices is listed in Table 5.4. The mobility values are quite comparable, albeit slightly increased in the device containing rhodamine 101. This may be another indication that introduction of rhodamine 101 does not exacerbate the energetic disorder within the bulk heterojunction. The increased in energetic disorder is shown to be associated with decreasing the charge carrier mobility.[21] Otherwise, this may be the inability of the photo-CELIV techniques to observer the charge carriers that are trapped as stated in the previous section.

5.3.3. p-DTS(FBTTh$_2$)$_2$:PC$_{60}$BM:IPA treated Devices

5.3.3.1. Photovoltaic characteristics

The p-DTS(FBTTh$_2$)$_2$:PC$_{60}$BM active layer was treated with 20 µl IPA and then the photovoltaic performances of the devices before and after the treatment were investigated (Table 5.5). Figure 5.13 shows current density versus voltage characteristics of the best performance devices with and without treatment with isopropyl alcohol under 100 $W\ cm^{-2}$ air mass 1.5 global illumination. The pristine devices have V_{oc} of 731 ± 14 mV, J_{sc} of 8 ± 0.8 $mA\ cm^{-2}$ and FF of 55 ± 4.2 leading to PCE of 3.24 ± 0.2%. The photovoltaic parameters of the devices remain almost unchanged after treatment with IPA. Therefore, it is clear that IPA treatment leads to no significant changes in the performance of the device. Zhou *et al.*[23] have reported that methanol treatment has no significant influence on the performance of the p-DTS(FBTTh$_2$)$_2$:PC$_{71}$BM BHJ devices.

In order to explore the effect of the treatment on the optical properties, UV-Vis absorption characteristics of the active layer film before and after treatment with IPA was probed. As can be seen from the UV-Vis absorption spectra in Figure 5.14, the pristine p-DTS(FBTTh$_2$)$_2$:PC$_{60}$BM film show absorption features in the wavelength range of 400 to 750 nm. The absorption peak observed at 680 nm is assigned to the vibronic structure of p-DTS(FBBTh$_2$)$_2$. Following the treatment with IPA, the absorption of the active layer is slightly reduced, suggesting that the molecular ordering may be lowered. It is also reported that methanol treatment of the p-DTS(FBTTh$_2$)$_2$:PC$_{71}$BM film was made no significant changes in the absorption coefficient of the film.[23]

Table 5.5. Current density-voltage characteristics of the p-DTS(FBTTh$_2$)$_2$:PC$_{60}$BM BHJ solar cell devices before and after treatment with IPA. The results are an average of 8 devices.

Device	V_{oc} (*mV*)	J_{sc} (*mA cm*$^{-2}$)	FF	PCE (%)
References	730.0 ± 10	8.0 ± 0.8	55.0 ± 4.2	3.2 ± 0.2
IPA-treated	720.0 ± 10	8.2 ± 0.6	54.0 ± 4.9	3.2 ± 0.4

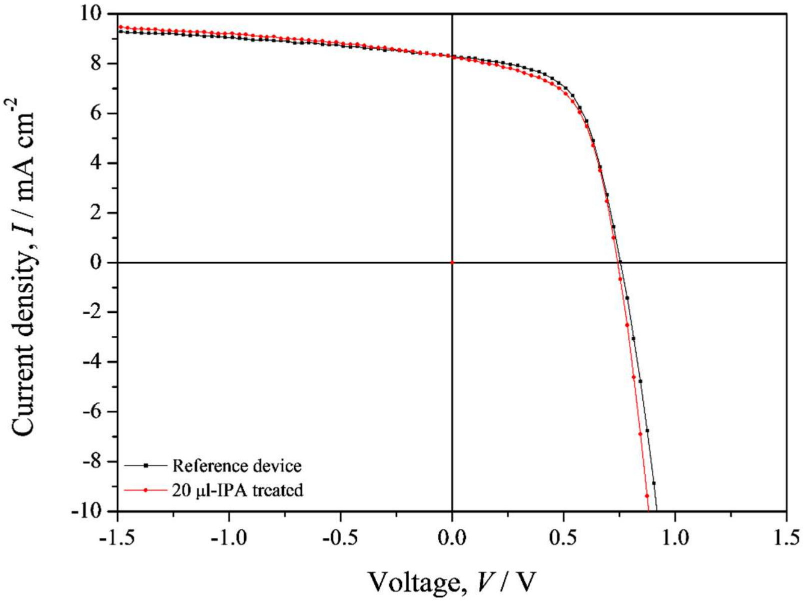

Figure 5.13. Current density-voltage curves of the p-DTS(FBTTh$_2$)$_2$:PC$_{60}$BM BHJ solar cell devices before and after IPA treatment.

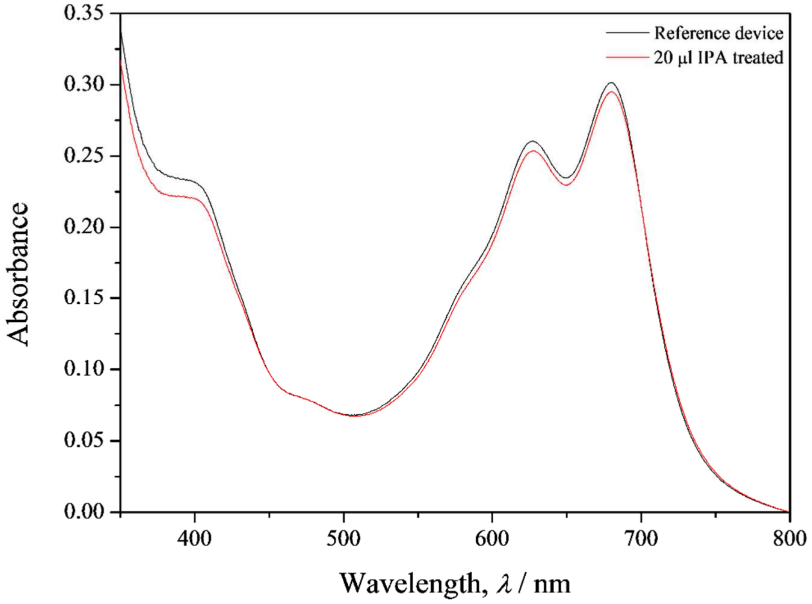

Figure 5.14. UV-Vis spectra of the *p*-DTS(FBTTh$_2$)$_2$:PC$_{60}$BM BHJ films before and after treatment with 20 μl of IPA.

The external quantum efficiency of the solar cell devices is shown in Figure 5.15. The EQE of the IPA treated device is slightly higher in the wavelength range of 300 to 500 nm, whereas it decreases slightly in the wavelength range of 500 to 800 nm compared to control device. The maximum EQE values of the solar cell devices before and after treatment with 20 μl IPA are 48.21% and 49.58% at 390 nm, respectively. The J_{sc} obtained from EQE for pristine and IPA treated devices are 8.29 and 8.22 *mA cm*$^{-2}$, respectively. The J_{sc} values are almost identical and consistent with J_{sc} extracted from the current density-voltage measurement. These results imply efficiency of conversion processes of incoming photons to collected electrons/holes at the electrodes has not been influenced by the treatment.

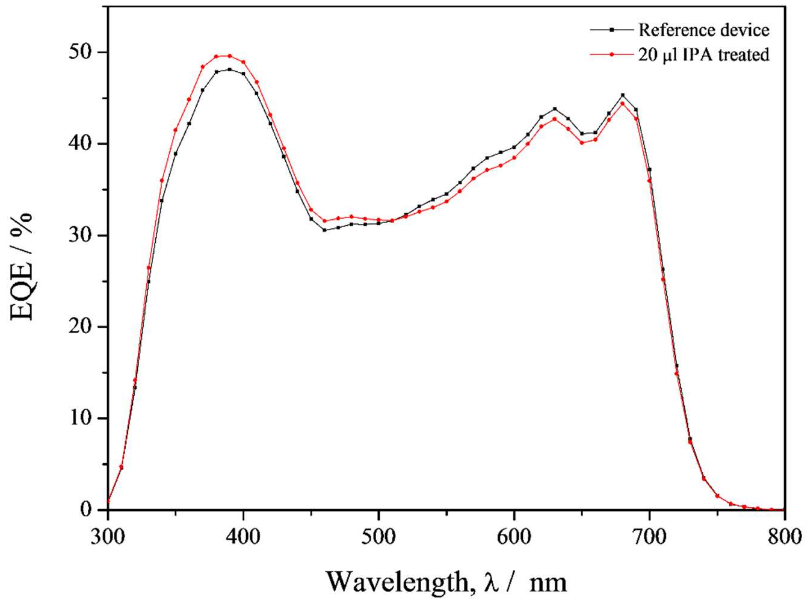

Figure 5.15. External quantum efficiency of the p-DTS(FBTTh$_2$)$_2$:PC$_{60}$BM BHJ solar cell devices before and after treatment with 20 µl IPA.

Figure 5.16 shows the photocurrent (J_{ph}) and charge collection probability (Pc) of the SM BHJ solar cell devices without and with IPA treatment as a function of effective voltage (V_{int}). There is a quite small difference between the pristine device and IPA treated device across almost all effective voltage range, indicating both J_{ph} and P_c characteristics of the devices have not been altered by the isopropyl alcohol treatment.

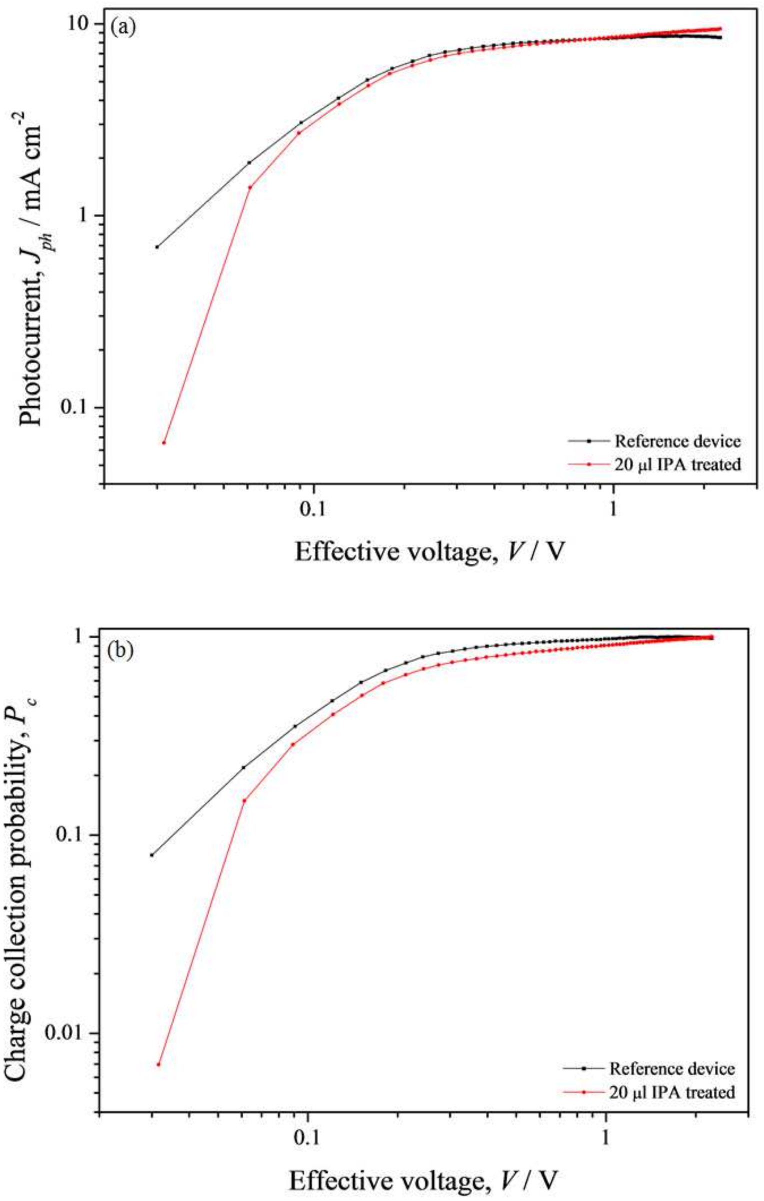

Figure 5.16. (a) Photocurrent, and (b) charge collection probability as a function of effective voltage for the p-DTS(FBTTh$_2$)$_2$:PC$_{60}$BM BHJ solar cell devices before and after treatment with 20 µl IPA.

5.3.3.2. Dielectric constant, photo-CELIV, PVD, and TRCE measurements

The bulk heterojunction solar cell devices composed of p-DTS(FBBTh$_2$)$_2$:PC$_{60}$BM were subjected to treatment with IPA. The dark CELIV characteristics of the devices were achieved by applying a 2 *V* voltage coupled with 50000 Hz rise time (10 Ω internal resistance of the oscilloscope). The CELIV curves of the solar cell devices before and after treatment with IPA are shown in Figure 5.17. The dielectric values of the devices are listed in Table 5.6. The dielectric constant of the devices slightly increases upon the treatment. This agrees with device performance results, showing no substantial difference before and after the treatment with isopropyl alcohol.

The mobility of the solar cell devices was measured using photo-CELIV techniques (Figure 5.17c, d). The charge carrier mobility results are presented in Table 5.6. The mobility of the IPA treated device is comparable to control devices with slightly smaller value. A similar result has been reported by Zhou *et al.*[23] which hole mobility in p-DTS(FBBTh$_2$)$_2$:PC$_{71}$BM BHJ solar cell device was slightly dropped upon treatment with methanol. The authors attribute the mobility decrease to the formation of isolated island structures. However, it is shown that solvent (methanol) treatment could improve hole mobility in PTB7:PC$_{71}$BM BHJ solar cell devices results in more balanced charge transport and thus reduce charge carrier recombination and increase fill factor.[24]

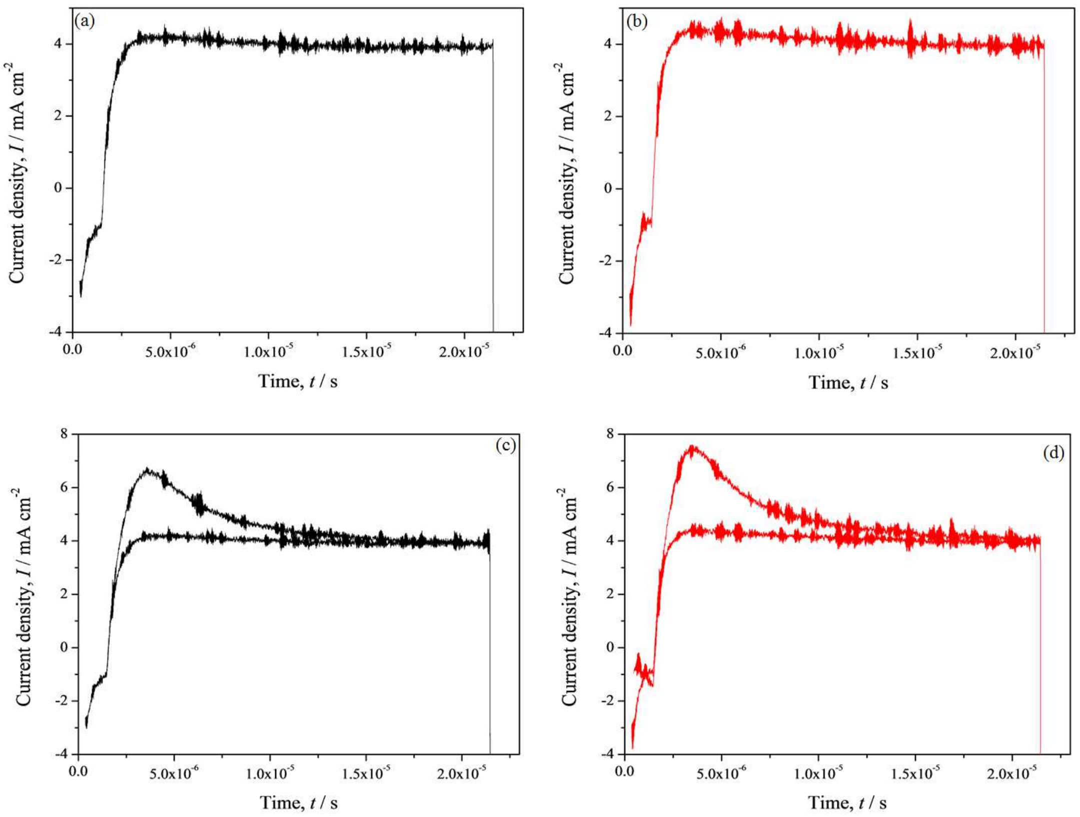

Figure 5.17. Measured dark CELIV of p-DTS(FBBTh$_2$)$_2$:PC$_{60}$BM BHJ solar cell devices (a) without, and with the treatment of (b) 20 µl IPA. The voltage speed rise was set to 100000 $V\,s^{-1}$ (2 *V* coupled with 50 kHz rise time). (c) and (d) Photo-CELIV curve of the BHJ solar cell devices before and after treatment with IPA. The laser energy was set to 10 µj. There was 2 µs delay between photogeneration and extraction.

Table 5.6. Calculated dielectric constant of p-DTS(FBTTh$_2$)$_2$:PC$_{60}$BM BHJ solar cell devices before and after treatment with IPA. Two devices were measured and averaged.

Device	Dielectric Constant	Mobility ($cm^2\ V^{-1}\ s^{-1}$)
Reference	3.9 ± 0.2	3.28×10^{-5}
20 µl IPA treated	4.1 ± 0.2	2.95×10^{-5}

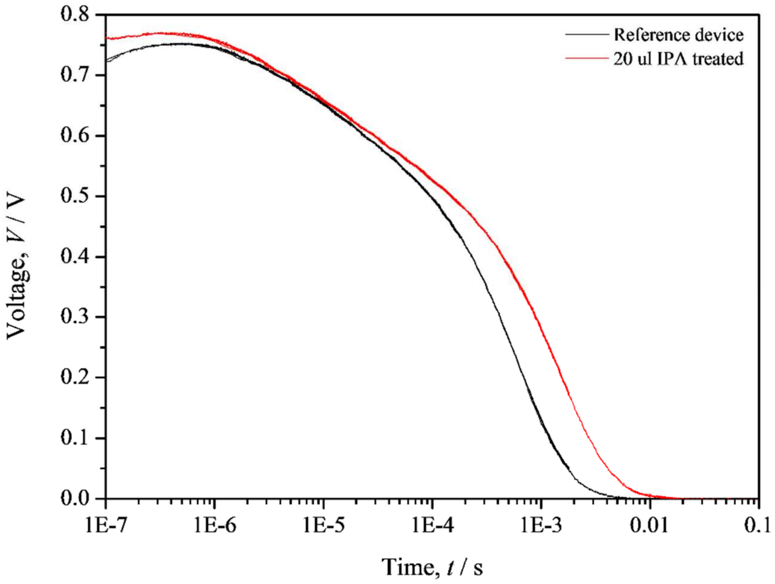

Figure 5.18. Photovoltage decay of the *p*-DTS(FBTTh$_2$)$_2$:PC$_{60}$BM BHJ solar cell devices before and after treatment with 20 µl of IPA. The laser energy was 10 µj.

Figure 5.18 displays the photovoltage decay of the solar cell devices without and with IPA treatment. The IPA treated devices shows slightly higher photovoltage at early time compared to the control device. This was consistent with higher charge carrier density (Figure 5.18a) and slightly lower bimolecular recombination lifetime (Figure 5.18c). A similar trend also was observable at the longer time as well. Moreover, the bimolecular lifetime recombination of the solar cell device after IPA treatment was slightly higher than control device (Figure 5.18b). One possible explanation for the slower recombination in IPA treated device could be suppression of the trap states. The recombination of the charge carriers occurs in the presence of an exponential distribution of trap states, especially at the longer time.[25] Hence, it may be understood that suppression of trap state will give rise to higher lifetime and slower charge carrier recombination. Another possible reason could be a slight increase of dielectric constant for the IPA treated device, as it is predicted that increasing dielectric constant could slow recombination of charge carriers.

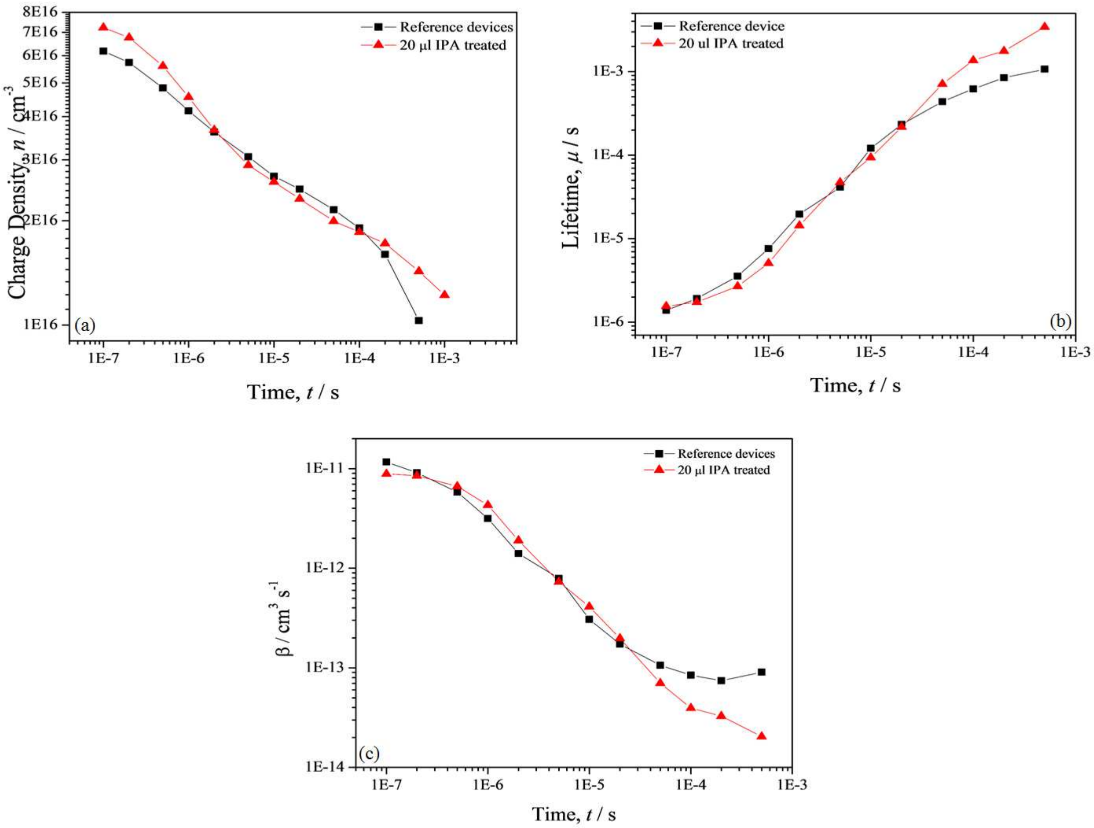

Figure 5.19. (a) Charge carrier density, (b) bimolecular recombination lifetime and (c) bimolecular recombination coefficient as a function of time of the *p*-DTS(FBTTh$_2$)$_2$:PC$_{60}$BM BHJ solar cell devices before and after treatment with 20 µl of IPA. The laser energy was 10 µj.

5.4. CONCLUSION

The enhancement of the dielectric constant in SM BHJ solar cell and its impact on the charge carrier dynamics of the solar cells was the main aim of this chapter. First, PFN and rhodamine 101 was incorporated into the p-DTS(FBBTh$_2$)$_2$:PC$_{60}$BM BHJ. Then, the bulk was treated with IPA. It was observed that PFN slightly increases the dielectric constant, whereas rhodamine 101 slightly decrease the dielectric constant. The treatment with IPA causes no significant alteration in the dielectric constant. The addition of the both PFN and rhodamine 101 into the bulk results in the reduction of the power conversion efficiency due to their influence on the charge carrier generation, collection and recombination. On the other hand, the photovoltaic properties of the BHJ solar cell devices remain unchanged following treatment with IPA. Therefore, the proposed method based on the Clausius-Mossotti relationship, to reduce free volume in the bulk by introducing material with dielectric constant higher than air, may not be an effective method to enhance the dielectric constant of small molecule BHJ solar cells and improve device performance.

5.5. FUTURE WORK

The results presented here were an exploration to examine new ways of increasing dielectric constant in BHJ systems. The effects of incorporated materials can be further investigated using spectroscopic ellipsometry and Fourier transform infrared spectroscopy spectra combined with the Kramers-Kronig relation. These techniques will provide more information on the components (ionic, electronic, and orientational) which determine polarization part of the dielectric constant.

5.6. APPENDIX

p-DTS(FBTTh$_2$)$_2$:PC$_{60}$BM:PFN-Inc.

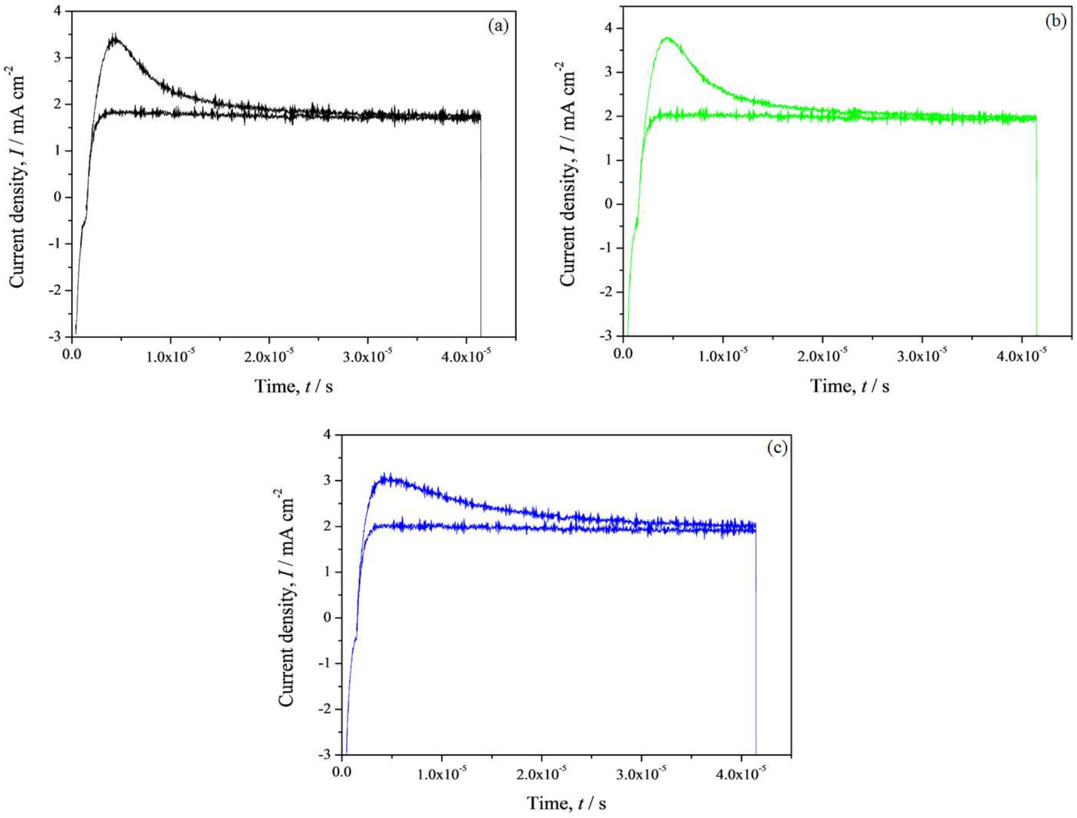

Figure 5.6.1. Photo-CELIV curves of the p-DTS(FBTTh$_2$)$_2$:PC$_{60}$BM BHJ solar cell devices (a) without, and with the incorporation of (b) 0.014% wt and (c) 0.029% wt PFN in the bulk heterojunction. The laser energy was 10 µj. The applied voltage was 2 V with speed rise of 25000 Hz. The delay between photogeneration and charge extraction was 2 µs.

p-DTS($FBTTh_2$)$_2$:PC_{60}BM:R101-Inc.

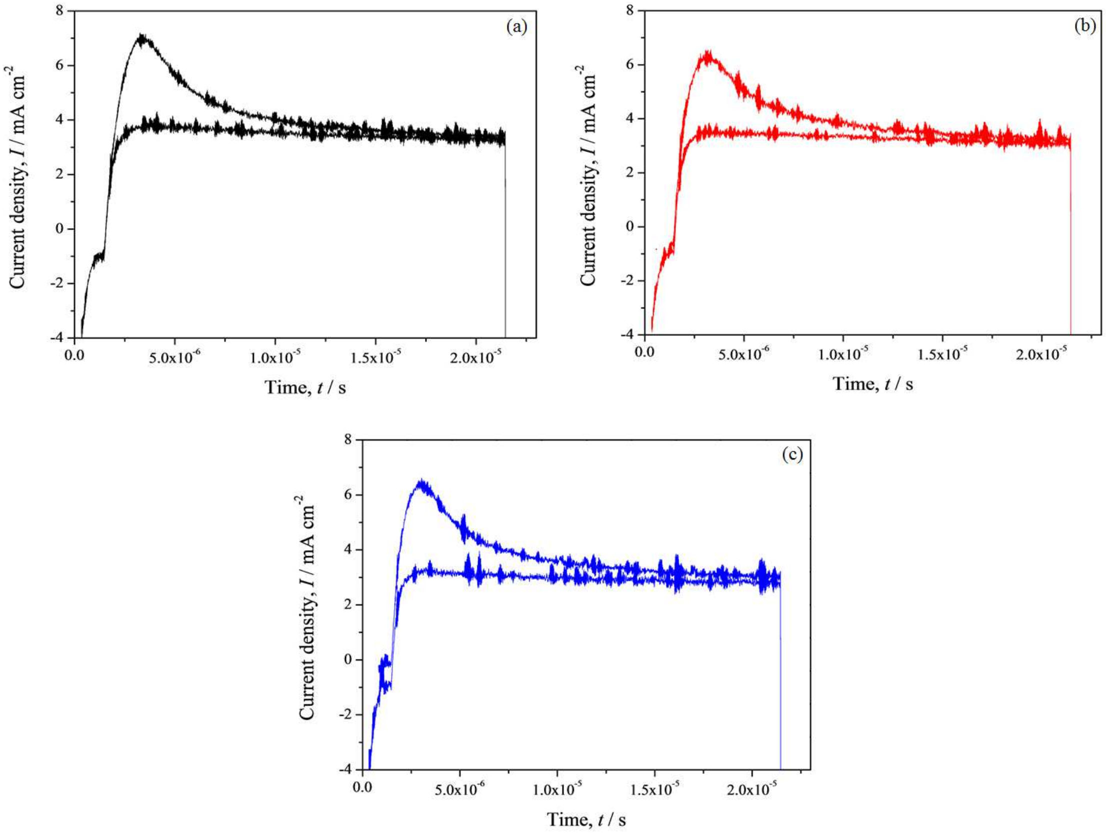

Figure 5.6.2. Photo-CELIV curve of the *p*-DTS($FBTTh_2$)$_2$:PC_{60}BM BHJ solar cell devices (a) without and with the incorporation of (b) 0.0029% wt, and (c) 0.014% wt rhodamine 101 in the bulk heterojunction. The laser energy was set to 10 µj. The applied voltage was 2 *V* together with 50000 Hz speed rise. The delay between photogeneration and charge extraction was 2 µs.

5.7. REFERENCES

(1) Roncali, J. Molecular Bulk Heterojunctions: An Emerging Approach to Organic Solar Cells. *Accounts of Chemical Research* **2009,** *42* (11), 1719.

(2) Walker, B.; Kim, C.; Nguyen, T.-Q. Small Molecule Solution-Processed Bulk Heterojunction Solar Cells. *Chemistry of Materials* **2011,** *23* (3), 470.

(3) Mishra, A.; Bäuerle, P. Small Molecule Organic Semiconductors on the Move: Promises for Future Solar Energy Technology. *Angewandte Chemie International Edition* **2012,** *51* (9), 2020.

(4) Chen, Y.; Wan, X.; Long, G. High Performance Photovoltaic Applications Using Solution-Processed Small Molecules. *Accounts of Chemical Research* **2013,** *46* (11), 2645.

(5) Roncali, J.; Leriche, P.; Blanchard, P. Molecular Materials for Organic Photovoltaics: Small is Beautiful. *Advanced Materials* **2014,** *26* (23), 3821.

(6) Ni, W.; Wan, X.; Li, M.; Wang, Y.; Chen, Y. A-D-A small molecules for solution-processed organic photovoltaic cells. *Chemical Communications* **2015,** *51* (24), 4936.

(7) Collins, S. D.; Ran, N. A.; Heiber, M. C.; Nguyen, T. Q. Small is Powerful: Recent Progress in Solution - Processed Small Molecule Solar Cells. *Advanced Energy Materials* **2017,** *7* (10).

(8) Kan, B.; Zhang, Q.; Li, M.; Wan, X.; Ni, W.; Long, G.; Wang, Y.; Yang, X.; Feng, H.; Chen, Y. Solution-Processed Organic Solar Cells Based on Dialkylthiol-Substituted Benzodithiophene Unit with Efficiency near 10%. *Journal of the American Chemical Society* **2014,** *136* (44), 15529.

(9) Kan, B.; Li, M.; Zhang, Q.; Liu, F.; Wan, X.; Wang, Y.; Ni, W.; Long, G.; Yang, X.; Feng, H.et al. A Series of Simple Oligomer-like Small Molecules Based on

Oligothiophenes for Solution-Processed Solar Cells with High Efficiency. *Journal of the American Chemical Society* **2015,** *137* (11), 3886.

(10) Zhang, Q.; Kan, B.; Liu, F.; Long, G.; Wan, X.; Chen, X.; Zuo, Y.; Ni, W.; Zhang, H.; Li, M.et al. Small-molecule solar cells with efficiency over 9%. *Nat Photon* **2015,** *9* (1), 35.

(11) Cui, C.; Guo, X.; Min, J.; Guo, B.; Cheng, X.; Zhang, M.; Brabec, C. J.; Li, Y. High - Performance Organic Solar Cells Based on a Small Molecule with Alkylthio - Thienyl - Conjugated Side Chains without Extra Treatments. *Advanced Materials* **2015,** *27* (45), 7469.

(12) Badgujar, S.; Lee, G.-Y.; Park, T.; Song, C. E.; Park, S.; Oh, S.; Shin, W. S.; Moon, S.-J.; Lee, J.-C.; Lee, S. K. High-Performance Small Molecule via Tailoring Intermolecular Interactions and its Application in Large-Area Organic Photovoltaic Modules. *Advanced Energy Materials* **2016,** *6* (12), 1600228.

(13) Koster, L. J. A.; Shaheen, S. E.; Hummelen, J. C. Pathways to a New Efficiency Regime for Organic Solar Cells. *Advanced Energy Materials* **2012,** *2* (10), 1246.

(14) Poll, T. S. v. d.; Love, J. A.; Nguyen, T. Q.; Bazan, G. C. Non - Basic High - Performance Molecules for Solution - Processed Organic Solar Cells. *Advanced Materials* **2012,** *24* (27), 3646.

(15) Kyaw, A. K. K.; Wang, D. H.; Luo, C.; Cao, Y.; Nguyen, T.-Q.; Bazan, G. C.; Heeger, A. J. Effects of Solvent Additives on Morphology, Charge Generation, Transport, and Recombination in Solution-Processed Small-Molecule Solar Cells. *Advanced Energy Materials* **2014,** *4* (7), n/a.

(16) Love, J. A.; Proctor, C. M.; Liu, J.; Takacs, C. J.; Sharenko, A.; van der Poll, T. S.; Heeger, A. J.; Bazan, G. C.; Nguyen, T.-Q. Film Morphology of High Efficiency

Solution-Processed Small-Molecule Solar Cells. *Advanced Functional Materials* **2013,** *23* (40), 5019.

(17) Mukherjee, S.; Proctor, C. M.; Tumbleston, J. R.; Bazan, G. C.; Nguyen, T.-Q.; Ade, H. Importance of Domain Purity and Molecular Packing in Efficient Solution-Processed Small-Molecule Solar Cells. *Advanced Materials* **2015,** *27* (6), 1105.

(18) Zalar, P.; Kuik, M.; Ran, N. A.; Love, J. A.; Nguyen, T.-Q. Effects of Processing Conditions on the Recombination Reduction in Small Molecule Bulk Heterojunction Solar Cells. *Advanced Energy Materials* **2014,** *4* (14), n/a.

(19) Kyaw, A. K. K.; Wang, D. H.; Wynands, D.; Zhang, J.; Nguyen, T.-Q.; Bazan, G. C.; Heeger, A. J. Improved Light Harvesting and Improved Efficiency by Insertion of an Optical Spacer (ZnO) in Solution-Processed Small-Molecule Solar Cells. *Nano Letters* **2013,** *13* (8), 3796.

(20) Clarke, T. M.; Lungenschmied, C.; Peet, J.; Drolet, N.; Sunahara, K.; Furube, A.; Mozer, A. J. Photodegradation in Encapsulated Silole - Based Polymer: PCBM Solar Cells Investigated using Transient Absorption Spectroscopy and Charge Extraction Measurements. *Advanced Energy Materials* **2013,** *3* (11), 1473.

(21) Eng, M. P.; Barnes, P. R. F.; Durrant, J. R. Concentration-Dependent Hole Mobility and Recombination Coefficient in Bulk Heterojunctions Determined from Transient Absorption Spectroscopy. *The Journal of Physical Chemistry Letters* **2010,** *1* (20), 3096.

(22) Kaake, L.; Dang, X.-D.; Leong, W. L.; Zhang, Y.; Heeger, A.; Nguyen, T.-Q. Effects of Impurities on Operational Mechanism of Organic Bulk Heterojunction Solar Cells. *Advanced Materials* **2013,** *25* (12), 1706.

(23) Zhou, W.; Xie, Y.; Hu, X.; Zhang, L.; Meng, X.; Zhang, Y.; Ma, W.; Chen, Y. Surface treatment by binary solvents induces the crystallization of a small molecular donor for

enhanced photovoltaic performance. *Physical Chemistry Chemical Physics* **2016,** *18* (2), 735.

(24) Zhou, H.; Zhang, Y.; Seifter, J.; Collins, S. D.; Luo, C.; Bazan, G. C.; Nguyen, T. Q.; Heeger, A. J. High - Efficiency Polymer Solar Cells Enhanced by Solvent Treatment. *Advanced Materials* **2013,** *25* (11), 1646.

(25) Clarke, T. M.; Peet, J.; Denk, P.; Dennler, G.; Lungenschmied, C.; Mozer, A. J. Non-Langevin bimolecular recombination in a silole-based polymer:PCBM solar cell measured by time-resolved charge extraction and resistance-dependent time-of-flight techniques. *Energy & Environmental Science* **2012,** 5 (1), 5241.

Chapter 6: Studying S-shaped Current-Voltage characteristics in High-Performance Solution-Processed Small Molecule based Bulk Heterojunction Solar Cells

6.1. INTRODUCTION

Solution-processed small molecule-based BHJ solar cells are of keen interest as they have shown the potential to compete with traditional conjugated polymer-based solar cells.[1,2] The well- defined chemical structure, batch-to-batch reproducibility, simple synthesis and purification, monodispersity coupled with relatively high mobility are some of their advantages over polymer counterparts.[2-4] Enhancement of the small molecule-based solar cells has been mainly achieved via the new molecular framework,[5-8] engineering bulk heterojunction morphology,[9-12] and device architecture modification.[13] Of particular importance is the morphological characteristics of the small molecule (SM) BHJ which significantly influence generation and extraction of charge carriers.[11,12] An optimized morphology is a trade-off between domain size and domain purity of the donor and acceptor within the bulk film. The former (domain size) mostly controls charge carrier generation, while the latter provides uninterrupted paths for charge carrier collection at the electrode. Consequently, any morphological deformation within the bulk or at the electrode contact could potentially result in a poor performance solar cell device.

S-shape characteristic is one of the efficiency-restricted phenomena that has been observed in organic photovoltaic systems. The origin of the S-shaped current-voltage curve has been ascribed to the morphological host or interfacial issues, leading to inefficient extraction of one of the charge carrier type. The so-called “kink” appears in the fourth quadrant of the current-voltage curve and is usually associated with significant reduction of fill factor (FF) and power conversion efficiency (PCE). Several underlying causes have been suggested for the appearance of the S-shaped current-voltage curves in the literature including, vertical phase separation,[14,15] defect or surface dipoles at the interface,[16-18] energy barrier,[19-21] and imbalance mobility of charge carriers.[22] A few models have also been proposed to address the physical underlying mechanism of the s-shape. Dyakonov *et al.*[23] developed a numerical model and introduced reduced surface recombination velocity of the majority carriers to explain the S-shape current-voltage curve. Yang *et al.*[24] suggested that the formation of a dipole is responsible for the kink in the current-voltage curve. Schwartz *et al.*[25] reported a model based on the vertical phase separation of the active layer, suggesting that the mismatch in electron and hole mobility in conjunction with an abrupt change in the mobility at the interface can lead to the S-shape curve. Huh, *et al.*[26] also reported a numerical model based on P3HT:PCBM solar cell devices. The authors proposed the S-shape curve appears provided that large imbalance mobility between charge carriers, accumulation of charge carriers at one of the electrodes and strong Langevin-type bimolecular recombination present at the same time in the system. While the appearance of the S-shaped current-voltage curve have been extensively investigated in the polymer-based organic solar cell, there are very few reports on the origin of the S-curve phenomenon in solution-process small molecule BHJ solar cells.[27]

In this study, the appearance of the S-shaped current density-voltage curve in high-performance solution-processed small molecule bulk heterojunction solar cells composed of 7,7′-(4,4-bis(2-ethylhexyl)-4H-silolo[3,2-b:4,5-b′]dithiophene-2,6-diyl)bis(6-fluoro-4-(5′-hexyl-[2,2′-bithiophen]-5-yl) benzo[c][1,2,5] thiadiazole), and [6,6]-phenyl C70 butyric acid methyl ester, (*p*-DTS(FBTTh$_2$)$_2$:PC$_{70}$BM) is investigated. The aim was to find a solution to revive the normal current-voltage curve. After that, the focus of the study was to understand the origin of the phenomenon and its effect on the photovoltaic characteristics of the BHJ solar cell devices. To achieve that, a range of steady state and transient techniques were employed. The photovoltaic performance of the devices was studied using current density-voltage, IPCE, and UV-Vis measurements. Atomic force microscopy was employed to study the top surface of the bulk heterojunction films. The charge carrier generation and collection of the devices were compared through analysis of photocurrent density-voltage curves. Finally, photovoltage decay, time-resolved charge extraction, and photo-CELIV techniques were carried out to investigate the effect of the S-curve phenomenon on the charge carrier extraction, recombination, and mobility.

6.2. EXPERIMENTAL

6.2.1. Device Fabrication

The solution-processed small molecule BHJ solar cell devices were fabricated according to the general procedures outlined in chapter 2. The solar cells' structure was conventional throughout the experiments and comprised of ITO/PEDOT:PSS/*p*-DTS($FBTTh_2$)$_2$:$PC_{70}BM$/Al. The schematic structure of the solar cell device, molecular structure of *p*-DTS($FBBTh_2$)$_2$ and $PC_{70}BM$ and energy level diagram of the solar SMBHJ solar cell devices are shown in Figure 1. The acceptor and donor materials were blended together in four different weight ratios, namely 1.5:1 (acceptor-rich, AR device), 1:1, 1:1.5 (donor-rich, DR device) and 1:2 in chlorobenzene solvent with 0.4% (v/v) of 1,8-diiodooctane (DIO) processing additive. The total concentration of the solutions was 35 mg/ml. The active materials were cast on top of the PEDOT:PSS layer at 2000 rpm for 45 s. The thickness of active layers was determined by Dektak 150 (Veeco) profilometer and was around 100 nm (± 5). In order to remove the residual solvent within the active layer, the substrates were heated at 70 ºC for 10 min and at 80 ºC for 5 min inside the glovebox. Finally, a 100 nm of aluminum (cathode electrode) was deposited on top of the active layer by metal evaporation technique. The active area of the solar cell devices was 0.06 cm^2.

6.2.2. Film Characterization

The surface morphology of the acceptor-rich (AR) and donor-rich (DR) BHJ films was studied using atomic force microscopy (AFM) (Asylum Research, MFP-3D) in tapping mode. The sample BHJ films for the AFM measurement were prepared on top of the ITO coated with PEDOT:PSS. The BHJ film samples for the UV-Vis absorption measurements were cast on microscope glass slides. The UV-Vis absorption measurements were performed using a UV-

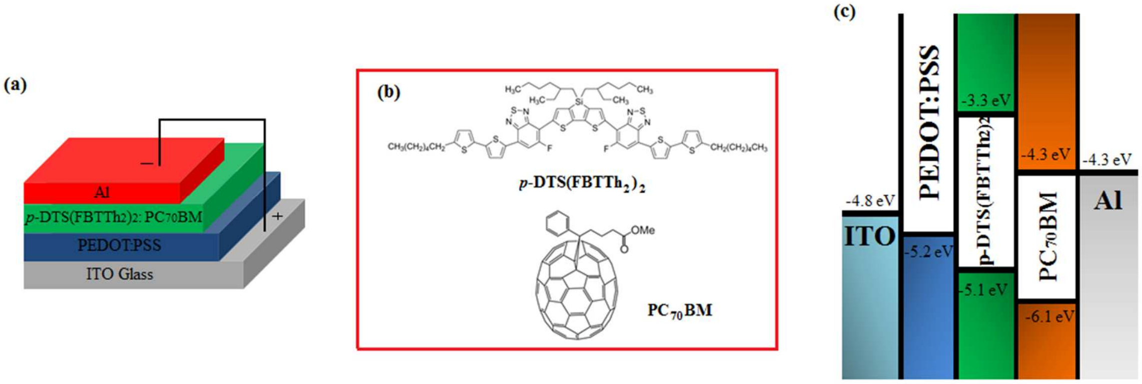

Figure 6.1. (a) Schematic of device architecture. (b) Molecular structures of p-DTS(FBTTh$_2$)$_2$ and PC$_{70}$BM. (c) Energy level diagram of SM bulk heterojunction solar cell comprised of ITO/PEDOT:PSS/p-DTS(FBTTh$_2$)$_2$:PC$_{70}$BM/Al cathode. The energy levels were obtained from ref. [11, 13].

VIS-NIR spectrophotometer (Shimadzu, UV-3600). All spectra were scanned from 800 nm to 300 nm, although only the section between 350 and 800 nm was shown in the figure. The baseline was corrected for the absorption of the glass at a single point at 800 nm.

6.2.3. Device Characterization

The current density-voltage, IPCE, light-intensity dependency, photovoltage decay, charge extraction and Photo-CELIV measurement were carried out according to the procedures outlined in Chapter 2.

6.3. RESULTS AND DISCUSSION

6.3.1. Interface Modification

It is reported that interfacial features such as partial metal coverage or top electrode corrosion could lead to imperfect interfaces between the BHJ and the cathode electrode. As a result, extraction of the charge carriers at the cathode side is obstructed, causing the appearance of the S-shaped current-voltage curve. To examine the nature of the interface between the SM BHJ and the cathode electrode, solar cell devices with TiO_x and ZnO electron transport layers were fabricated. The TiO_x and ZnO were prepared based on the work of Kim *et al.*[28] and Kyaw *et al.*[13], respectively. The photovoltaic parameters of the solar cell devices without and with electron transport layers are summarized in Table 6.1. The current density-voltage curves of the devices are shown in Figure 6.2. It is obvious that the insertion of the TiO_x and ZnO at the interface does not resolve the S-shaped current-voltage characteristics and the fabricated devices with incorporated ETLs exhibit low fill factor together with PCE comparable to the reference device. This indicates that the S-curve phenomenon is not an interface-driven process and the imperfection of the interface due to thermal evaporation cathode electrode cannot account for the appearance of the S-shaped current-voltage curve and low-performance solar cell devices.

Table 6.1. Photovoltaic parameters of p-DTS(FBTTh$_2$)$_2$:PC$_{70}$BM BHJ solar cell device without and with two incorporated electron transport layers. The results are average 8 devices.

ETL	V_{oc} (*mV*)	J_{sc} (*mA cm*$^{-2}$)	FF	PCE (%)
-	721.0 ± 10	10.2 ± 0.5	0.35 ± 0.01	2.6 ± 0.3
TiO_x	738.0 ± 90	9.6 ± 0.4	0.4 ± 0.3	2.7 ± 0.3
ZnO	735.0 ± 10	9.6 ± 0.6	0.36 ± 0.04	2.6 ± 0.3

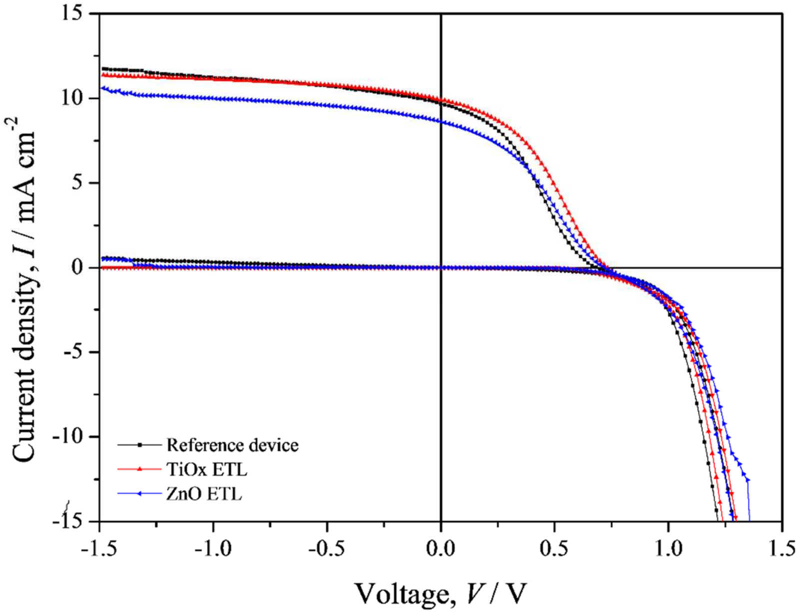

Figure 6.2. Current density-voltage curves of the *p*-DTS(FBTTh$_2$)$_2$:PC$_{70}$BM BHJ solar cell device without and with incorporated TiO$_x$ and ZnO electron transport layers in the dark and under illumination.

There have been reports that the appearance of the S-shaped current-voltage curve was assigned to the interface between the active layer and cathode electrode. Vogel *et al.*[29] report a bilayer structure device composed of ITO/ZnPc/C60/Al showed S-curve phenomenon. It was further shown that the S-curve phenomenon was removed by the insertion of a bathocuproine (BCP) interfacial layer. It was claimed that penetration of the aluminum into active layer results in a "structured interface" which either quench the excitons or enhance the exciton recombination at the interface.[29] The authors concluded that insertion BCP prevents the recombination or quenching the exciton at the interface by increasing the distance between the excited molecules and the metal surface. Jin *et al.*[30] have shown that oxidized Ca cathode electrode or poorly deposited Ca cathode electrode in the P3HT:PCBM BHJ devices gives rise to S-shaped current-voltage curve. They attributed the former to the chemical degradation of the Ca-polymer interface and the latter to the inefficient charge transfer at the polymer-metal interface. It was proposed that insertion of 5 nm CdS interlayer could alleviate imperfect interface effects and revive normal diode-like current-voltage curve.[30] The chemical degradation of metal-polymer interface or partial coverage of metal electrode over the polymer were also suggested by Gupta *et al.*[16] The authors show that a normal current-voltage curve was revived when the cathode electrode was replaced with a low melting point alloy metal electrode (In-Sn-Pb-Bi). It is apparent that our findings are in contradiction of the abovementioned results in which interface modification is not the key to reviving the normal diode-like current-voltage curve and the S-curve phenomenon originates from the small molecule bulk heterojunction and probably its morphological characteristics.

6.3.2. DIO Effect

Given that the interface between the active layer and the cathode is not the culprit for the appearance of the S-shaped current-voltage curve, the remaining option is the bulk heterojunction. The performance of the *p*-DTS(FBBTh$_2$)$_2$:PC$_{70}$BM solar cell devices relies crucially upon the BHJ morphology. Moreover, the processing additive DIO which has been widely used to optimize the small molecule BHJ morphology may be responsible for the S-curve phenomenon. In this section, the results of devices fabricated with a range of DIO concertation from 0 to 0.6% is presented. The photovoltaic parameters of the additive-processed devices are summarized in Table 6.2. It is apparent that the devices fabricated with DIO clearly show S-shaped current density-voltage curve and suffer from low fill factor (Figure 6.3). This indicates that despite the impressive impact of the DIO on the solar cell performance, the kink near the V_{oc} that dramatically change the shape of the current density-voltage curve appears regardless of the DIO concentration and therefore cannot be ascribed to DIO-driven morphological defects. It has been shown in the literature that the performance of small molecule devices can be vastly improved via incorporation of the small amount of the solution additive DIO in the casting solution.[5,6,9,31-33] Recently, Love *et al.*[27] report a reduction of the

Table 6.2. The photovoltaic characteristics of the solar cell devices fabricated with various concentration of DIO. Four devices were measured and averaged.

DIO concentration	V_{oc} (*mV*)	J_{sc} (*mA cm*$^{-2}$)	FF	PCE (%)
0%	550.0 ± 30	2.45 ± 0.2	0.25 ± 0.6	0.33 ± 0.01
0.2%	720.0 ± 20	9.34 ± 0.3	0.31 ± 0.03	2.1 ± 0.5
0.4%	740.0 ± 10	11.5 ± 0.3	0.41 ± 0.02	3.5 ± 0.2
0.6%	700.0 ± 50	2.4 ± 0.4	0.16 ±0.02	0.24 ± 0.03

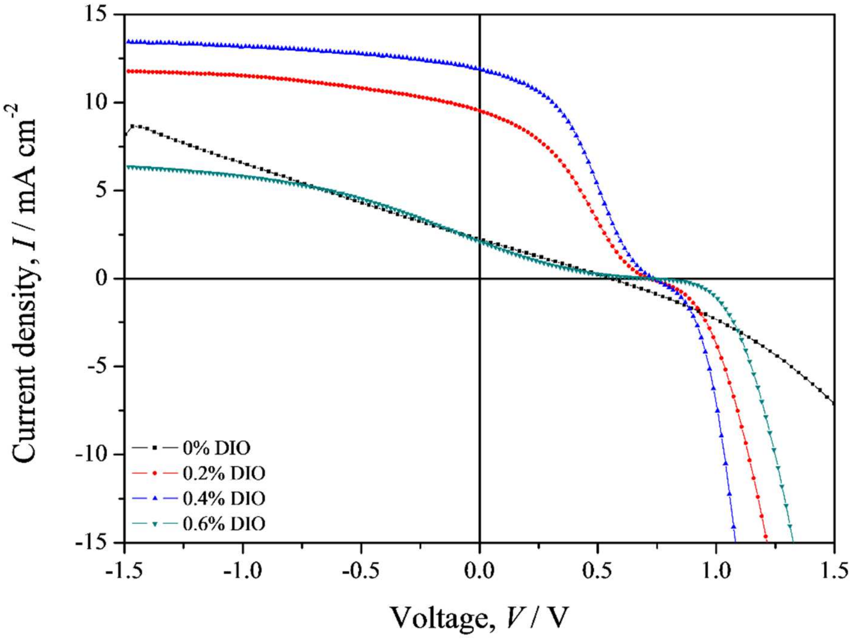

Figure 6.3. Current density-voltage curves of *p*-DTS(FBTTh$_2$)$_2$:PC$_{70}$BM fabricated with various concentration of DIO solution additive under illumination.

S-shape of current-voltage curve in the small molecule devices composed of *p*-SIDT(FBTThCA8)$_2$:PC$_{71}$BM. It is, however, apparent that S-curve phenomenon in our system is independent of the DIO.

6.3.3. Donor and Acceptor Ratio

It is widely accepted that donor and acceptor form an interpenetrating network throughout the bulk heterojunction. The efficient exciton dissociation and charge carrier generation within the bulk depends on the interfacial area between donor and acceptor, whereas efficient charge carrier collection relies upon percolation pathways composed of pure donor/acceptor phase. A high-performance device has a large interfacial area over the bulk, yet long percolation paths toward electrodes. As a result, any morphological defects such as aggregation of donor/acceptor could potentially undermine the generation, transportation or collection of charge carriers, resulting in low-performance solar cell devices. In the last section, the results of DIO concentration on the device performance were presented. In this section, we examined the effect of the donor/acceptor ratio on the appearance of the S-curve phenomenon. The current density-voltage characteristics of the p-DTS(FBTTh$_2$)$_2$:PC$_{70}$BM solar cell devices fabricated with 1.5:1, 1:1, 1.5:1, and 1:2 donor/acceptor (D/A) weight ratio are listed in Table 6.3. It is observed that the devices with 1.5:1 and 1:1 (D/A) weight ratio shows S-shaped current density-voltage curve, whereas normal diode-like curves are obtained for devices with higher content of PC$_{70}$BM (1:1.5 and 1:2 weight ratio).

Table 6.3. Photovoltaic parameters of *p*-DTS(FBTTh$_2$)$_2$:PC$_{70}$BM BHJ solar cell device fabricated with various weight ratios of donor and acceptor.

Donor:Acceptor ratio	**V$_{oc}$ (*mV*)**	**J$_{sc}$ (*mA cm^{-2}*)**	**FF**	**PCE (%)**	**Average**
1.5 : 1	780.0 ± 30	11.1 ± 0.8	0.39 ± 0. 03	3.3 ± 0.3	16
1 : 1	740.0 ± 90	12 ± 0.4	0.44 ± 0.03	3.9 ± 0.4	8
1 : 1.5	740.0 ± 12	14 ± 0.4	0.56 ± 0.04	6 ± 0.2	16
1 : 2	740.0 ± 60	13 ± 0.4	0.55 ± 0.01	5.2 ± 0.2	12

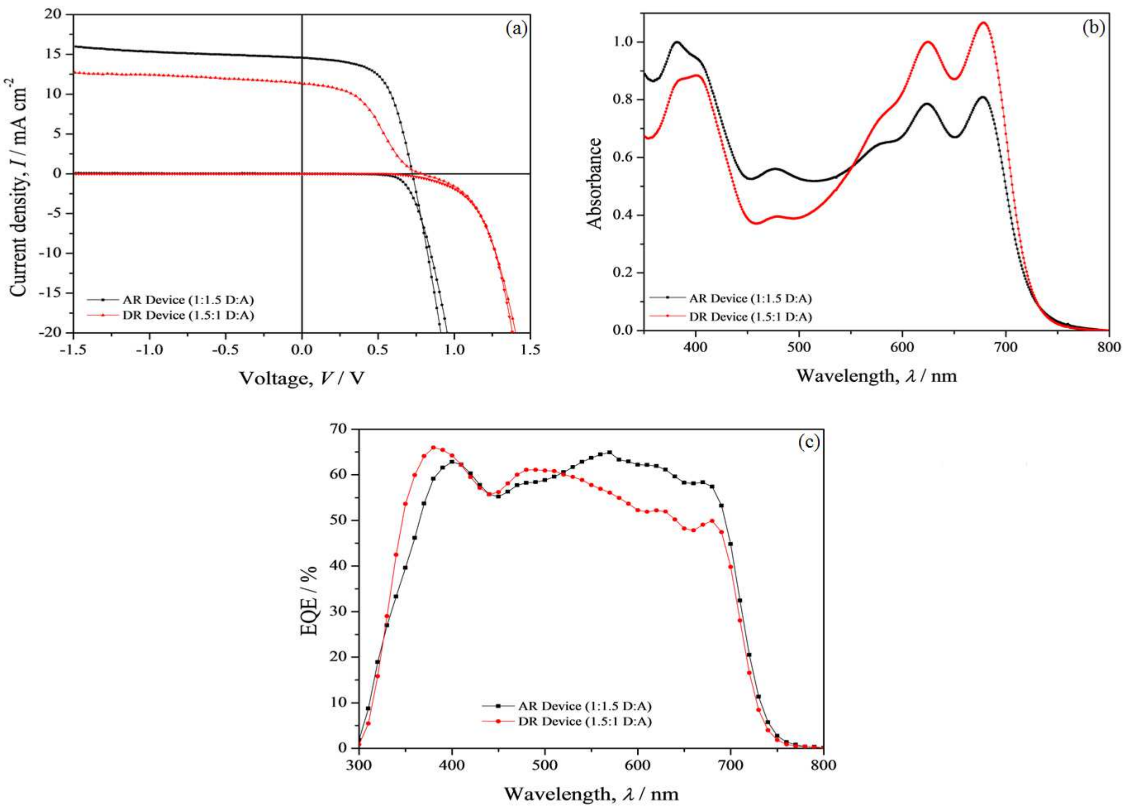

Figure 6.4. (a) Current density-voltage characteristics of solar cell devices composed of p-DTS(FBTTh2)2:PC$_{70}$BM with 1.5 : 1 (DR Device, red) and 1 : 1.5 (AR Device, black) weight ratio of donor/acceptor, (b) Normalized UV-Vis absorption spectra of the corresponding photoactive layers, (c) External quantum efficiency of DR (red) and AR (black) solar cell devices.

It is clear that the S-shaped curve stems from the bulk heterojunction (it is a morphology issue) and is significantly alleviated when the donor/acceptor ratio is altered. It is found that the best ratio to obtain a relatively high fill factor and short circuit current is 1:1.5 (D/A). The 1:2 ratio devices show normal current density curves, but lower performance (compared to 1:1.5 devices) due to lower J_{sc}. Moreover, the devices fabricated with 1:1 donor/acceptor ratio also demonstrate S-shaped curves, although slightly less pronounced as indicated by the higher fill factor (0.44 ± 0.03). Hence, solar cell devices with 1:1.5 ratio (donor-rich, DR) and 1:1.5 (acceptor-rich, AR) were selected for further investigation. The current density-voltage curve of donor-rich and acceptor rich devices measured under 1 sun simulated illumination (100 *mW*

cm^{-2}, AM 1.5) and in the dark, are presented in Figure 6.4a (the current density-voltage curves of devices with 1:1 and 1:2 D/A ratio are shown in Figure 6.6.1, Appendix). It can be seen that acceptor-rich devices demonstrate a power conversion efficiency (6 ± 0.2%) almost twice as large as donor-rich devices (3.3 ± 0.3%). In terms of current density-voltage curve, it is apparent that devices using DR active layer show an inflection point near the V_{oc} and a clear kink in the fourth quadrant, whereas the AR devices show normal diode-like behavior. While open circuit potential of DR devices is slightly higher, the fill factor of the devices is 31% lower compared to the AR devices. Moreover, the forward bias injection potential for the DR device is shifted 0.5 V to higher potential both in the dark and under illumination conditions.

The current density-voltage curves suggest the presence of an injection/extraction barrier in the DR devices which is manifested by the S-curve behavior. It is speculated that accumulation of the donor materials and formation a thin donor-rich layer near and/or in contact with electron extracting cathode electrode could be the physical origin of the barrier. The extraction barrier would then stem from the voltage loss arising from the low electron conductivity (high electric resistance) of the donor-rich surface region. The increment of the acceptor content in the AR devices has probably caused better distribution of donor and acceptor throughout the bulk, leaving more $PC_{70}BM$ on the surface of active layer necessary for efficient charge carrier extraction.

In Figure 6.4b, UV-Vis absorption spectra are shown for the donor-rich (1:1.5 D/A ratio) and acceptor-rich (1:1.5 D/A ratio) active layer thin films. The spectra were normalized to the absorption peak of $PC_{70}BM$ at 383 nm. The absolute absorbance values were in the range of 0.25 to 0.5 depending on the wavelength. The donor-rich UV-Vis spectrum shows two absorption features at 380 nm and at 550 to 700 nm. This matches the reported absorption spectrum of the donor *p*-DTS$(FBTTh_2)_2$ with contribution from $PC_{70}BM$ absorption at 400 nm.[9] The acceptor-rich film exhibits similar phenomenology; however, the relative strength of absorbance is weakened within the 550 nm to 700 nm wavelength range. This may suggest that the solid-state ordering of *p*-DTS(FBTTh$_2$)$_2$ is reduced in AR devices.

External quantum efficiency (EQE) of the solar cell devices is shown in Figure 6.4c. It is clear that the EQE values of the DR devices are lower up to 10% compared to the AR devices within the 550 nm to 700 nm wavelength range, despite the fact that the absorption was found to be higher at the same range for the DR active layer film. The obtained J_{sc} values by integrating the EQE spectrum convoluted with a standard AM 1.5G spectrum are 13.7 $mA\ cm^{-2}$ and 11.8 $mA\ cm^{-2}$ for the AR and DR devices respectively, which is consistent with J_{sc} obtained experimentally. The lower EQE values suggest that lower charge separation and/or collection in the DR type devices.[6]

6.3.4. Surface Morphology Studies

The surface morphology of the DR and AR devices were evaluated with atomic force microscopy (AFM) technique. The AFM topographic and corresponding image phases of the sample are represented in Figure 6.5. It is clear from AFM images that there are no large-scale topographic features (such as aggregation of either the donor or the acceptor) presents in both AR and DR films but randomly oriented fibrillar-like structures. A root-mean-square (RMS) surface roughness of 1.73 nm (average of four measurements) was obtained for DR films, whereas AR films show smoother surface roughness (RMS of 0.84 nm) and smaller grain sizes.

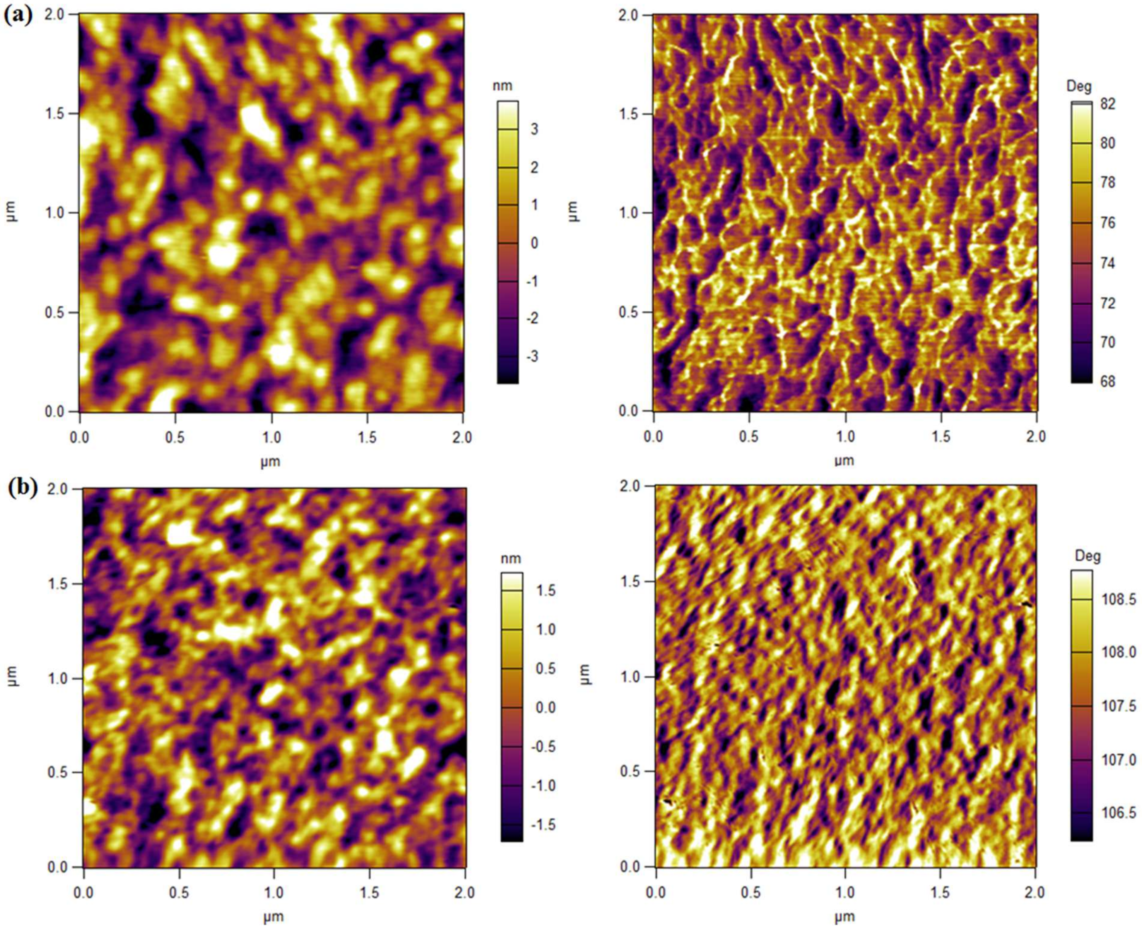

Figure 6.5. Tapping mode AFM topography (left) and corresponding phase images (right) of p-DTS(FBTTh$_2$)$_2$:PC$_{70}$BM film fabricated with (a) 1.5 : 1 weight ratio of donor : acceptor (top) (b) 1 : 1.5 weight ratio of donor : acceptor (bottom), respectively.

The AFM surface topography suggests that both domain size and surface roughness has been changed upon increasing the content of the $PC_{70}BM$ in AR film. Both properties could indicate changes at the top of the active layer. The extraction barrier in the DR devices would be reasonably expected if a thin donor-rich layer formed at the top of the active layer due to for example the solubility differences between the donor and acceptor materials.

It is shown that DIO controls the crystallinity of the small molecule bulk heterojunction film and higher domain size and fibrillar structures together with rougher surface were reported with higher concentration of the solution additive.[10] As such, the reduction of the surface roughness in AR film may imply the reduction of crystallinity. Given that the DIO content of the both DR an AR active solution is identical, the lowering content of small molecule donor in AR film may be accounted for the reduction of the crystallinity and subsequent surface roughness.

6.3.5. Charge Carrier Generation and Collection

To understand the impact of the extraction/injection barrier on the performance of the solar cell devices, photocurrent (J_{ph}) of both donor-rich and acceptor-rich devices was inspected as a function of the effective voltage (V_{int}). The photocurrent, $J_{ph} = J_L - J_D$, is defined as a current density measured upon illumination subtracted from the current density measured in the dark (J_D). The effective voltage, $V_{int} = V_{BI} - V_{app}$, is voltage difference between the applied voltage (V_{app}) and the voltage at which the photocurrent is zero (V_{BI}).[13,34,35] Noteworthy that the effective voltage determines the strength of internal electric field within the device, indicating driving force for the extraction of charge carriers. In Figure 6.6a, the photocurrent of the DR device and AR device are shown as a function of the effective voltage. The J_{ph} of AR device increases proportionally and in a linear fashion at the low effective voltage ($V_{BI} - V_{app} < 0.2\ V$) and reaches a saturation regime at higher effective voltage ($V_{int} < 0.3\ V$). In the DR device, the photocurrent does not follow a linear trend at low V_{int} and saturation regime occurs at nearly 0.6 V. This indicated that the internal electric field within the DR device is reduced by the presence of the barrier.

The internal electric field is small at the low effective voltage and therefore gives rise to a competition between drift and diffusion of photo-generated carriers towards contacts. At high effective voltage, On the other hand, the internal electric field is strong enough to sweep out all charge carriers and the photocurrent is independent of the voltage, tending to saturate. Hence, the photocurrent at the saturation regime is limited only by the number of absorbed photons and can be expressed as below:[13,34,35]

$$J_{ph,sat} = edG_{max} \qquad (6\text{-}1)$$

where e is elementary charge, d stands for thickness, and G_{max} is maximum photo-induced charge carrier generation rate per unit volume. The G_{max} value for the DR device was calculated as $7.811\times10^{27}\ m^{-3}\ s^{-1}$ ($J_{ph,sat} = 126.5\ A\ m^{-2}$), whereas the G_{max} value for the AR device was

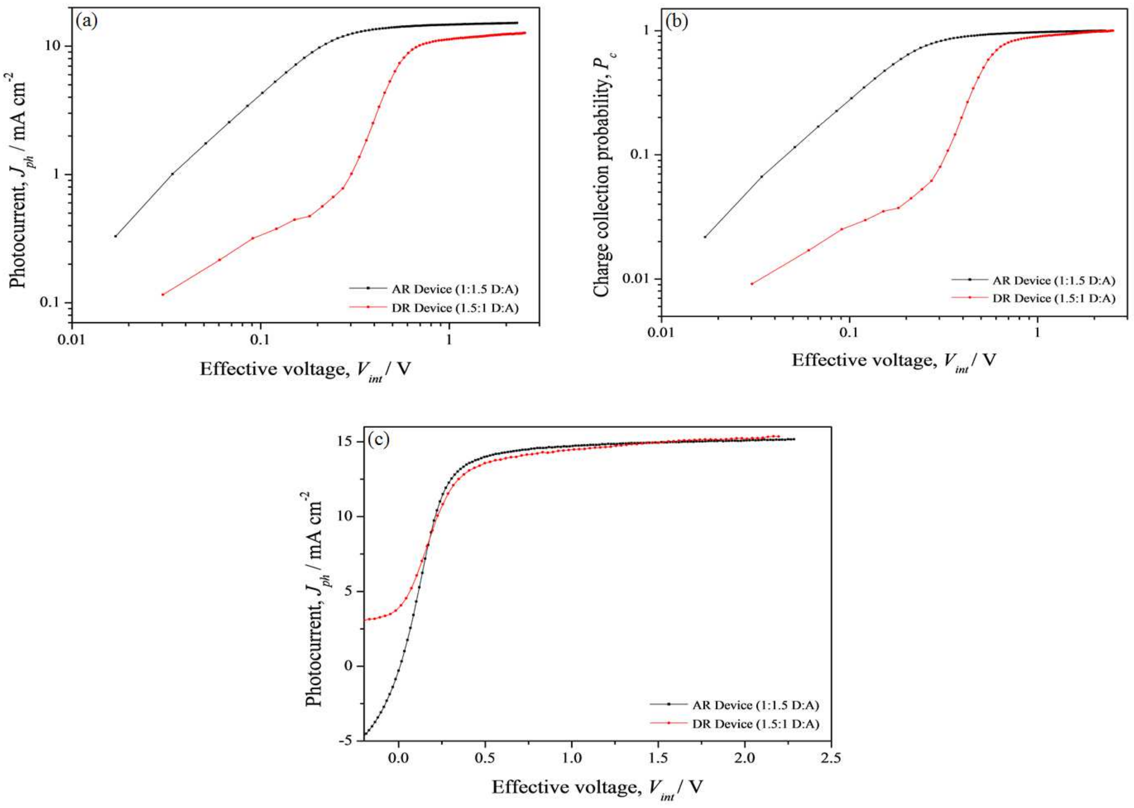

Figure 6.6. (a) Photocurrent density and (b) Charge collection probability (Pc) as a function of effective voltage, of DR (red) and AR (black) solar cell devices. (c) Photocurrent overlay of DR device to AR device by subtracting - 0.32 V from effective voltage and adding 2.8 $mA\ cm^{-2}$ to the photocurrent density.

found to be 17% higher at 9.47×10^{27} $m^{-3}\ s^{-1}$ ($J_{ph,sat}$ = 151.7 $A\ m^{-2}$). This indicates that generation of charge carriers in the DR device is reduced, albeit higher concentration of p-DTS(FBTTh$_2$)$_2$. This is probably due to low charge carrier generation yield in the thin donor-rich layer. As such, the 20% lower J_{sc} in the donor-rich devices can be attributed to the lower charge carrier generation.

Figure 6.6b shows charge collection probability (P_c) of the solar cell devices with respect to the effective voltage. The photocurrent of a solar cell can be written as [13,34,35]

$$J_{ph} = edG_{max}P_c \qquad (6\text{-}2)$$

considering the equations (6-1) and (6-2), charge collection probability can be calculated by dividing J_{ph} on $J_{ph,sat}$ ($P_c = J_{ph}/J_{ph,sat}$). Higher values of P_c are calculated for the AR device across the entire range of applied voltage. At short circuit conditions (high internal voltage), the difference in P_c is small (0.96 vs. 90). However, at a lower effective voltage close to open circuit potential ($\cong V_{int}$ - 0.1 V), the P_c values are one order of magnitude higher in the AR devices. This suggests that charge carrier extraction is limited in the DR devices due to the lower internal electric field. The internal electric field is reduced due to the presence of the extraction barrier.

To estimate the size of extraction barrier, the J_{ph} versus V_{int} of the donor-rich devices was replotted to match the acceptor-rich device curve. To achieve a reasonably good overlay of the two solar cells curves, the photocurrent was adjusted by adding 2.8 $mA\ cm^{-2}$ and the V_{int} was shifted 0.32 V (Figure 6.6c). The added value to the measured photocurrent was consistent with the difference in J_{sc} and the EQE results and stem from less charge carrier generation in the DR devices as explained above. Given that the calculated V_{int} is higher in the DR devices by approximately 0.2 V (The V_{BI} was 0.8 and 1 V for AR and DR device, respectively), the additional barrier in the DR device is approximately 0.1 V.

6.3.5. Equivalent Circuit Model

It is shown in the literature that a typical organic solar cell can be represented by an equivalent circuit comprised of a photocurrent source (J_{ph}), diode, series resistance, (R_s) and shunt resistance (R_{sh}).[36,37] The photocurrent source is the characteristics of the photo-generated current by the solar cell via converting of absorbed photons to free charge carriers. The diode represents the recombination of charge carrier within the devices. The series resistance accounts for the resistance of the bulk and the electrode to flow of the electric current, and leakage current (through pinholes or at the edge of devices) is modeled by the shunt resistance.[36,37]

Having said that, however, the devices with S-shaped current density-voltage do not seem to be represented fully by the simple one-diode model and addition of another diode would be necessary for the description of the S-curve phenomenon. As discussed earlier, the S-shape of the current density-voltage curves is due to an extraction barrier originating from a thin donor-rich layer on top of the active layer. Electrically, such a barrier would manifest the second diode in series to the bulk heterojunction diode, as illustrated in Figure 6.7. Under steady state conditions, a similar amount of current flows through both diodes. But, depending on the resistance, the voltage drop is divided between the two diodes. Given the current density-voltage curve in Figure 6.4a, the second diode (D2, donor-rich layer), 1) the second diode opens at higher applied voltage (0.5 *V*) compared to the first diode (D1, bulk heterojunction), and

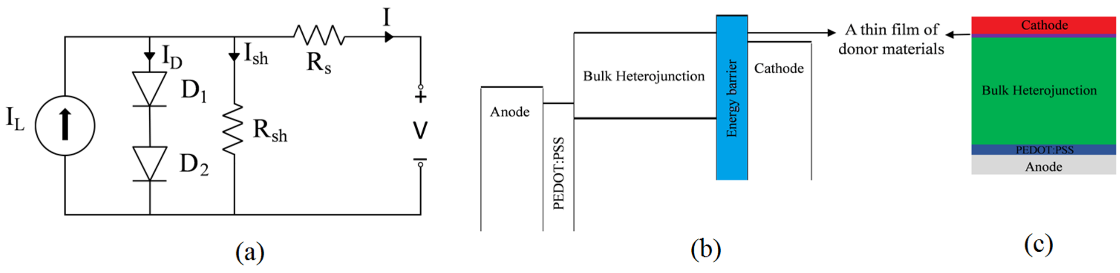

(a) (b) (c)

Figure 6.7. (a) Equivalent circuit, (b) energy diagram, (c) schematic presentation of the DR devices in the presence of a thin donor-rich layer.

2) the second diode generates marginal photocurrent compared to the bulk heterojunction diode under illumination. This marginal, albeit non-zero photocurrent of the second diode, is likely the reason for the slightly increased V_{oc} and V_{BI} in the current density-voltage curves of S-shaped donor-rich devices. Therefore, due to the additional voltage expended to facilitate charge extraction through the second diode is reduced, the charge carrier collection efficiency near the open circuit conditions is diminished, manifesting in a low fill factor and S-shaped current density-voltage curves. Tada reports the S-shaped current-voltage curves for devices fabricated from PTB7-Th/C70 composite using halogen-free solvent.[38] An opposed two-diode equivalent circuit model was used to analyze the current-voltage curve. The diodes were accounted for normal characteristics of the photocell and a parasitic part responsible for the S-curve. It was shown that the best fitting results were achieved when the parasitic part was assumed light-insensitive.

6.3.6. Charge Carrier Recombination at Steady State Conditions

Recombination order of charge carrier at steady state condition can be determined using the light-intensity dependency current density-voltage technique, as described in section 2.3.3. The donor-rich and acceptor-rich devices were subjected to various incident light intensities ranging from 100 $mW\ cm^{-2}$ to 1 $mW\ cm^{-2}$ and their current density-voltage responses were recorded. Figure 6.8a shows short circuit current of the devices as a function of the incident light intensities. It is widely accepted that charge carriers are collected effectively at the electrodes at short circuit conditions due to the strong built-in electric field. Hence a power dependency is often observed between light intensity and short circuit current ($J_{sc} \propto I^{\alpha}$) where α is close to unity when the first-order recombination is dominant.[13,34,35] The α values for donor-rich and acceptor rich devices are 0.78555 and 0.77473, respectively. This indicates that other factors contribute to the annihilation of charge carriers at short circuit condition such as bimolecular recombination,[34,39] space charge effect and charge carrier mobility imbalance.[34] The measured mobility of the DR and AR devices are quite similar (discussed in section 6.3.9). Thus, deviation of α from unity can be correlated to the bimolecular recombination of charge carriers. Moreover, analysis of the light intensity dependence of 4 DR and 5 AR devices shows slightly lower α values for the DR devices (Table 6.6.1 and Table 6.6.2, Appendix). This may be an indication of slightly higher bimolecular recombination of charge carrier at short circuit condition in the DR devices. However, it is reported that loss of current due to bimolecular recombination at short-circuit conditions is very small (2%-17% depending on the system and preparation procedure), given the fact that the concentration of charge carrier is low.[40,41] Hence, bimolecular recombination cannot be accounted for the lower short-circuit current in the donor-rich devices and the difference in J_{sc} between the devices is mainly due to the difference in the charge carrier generation, as discussed in section 6.3.5.

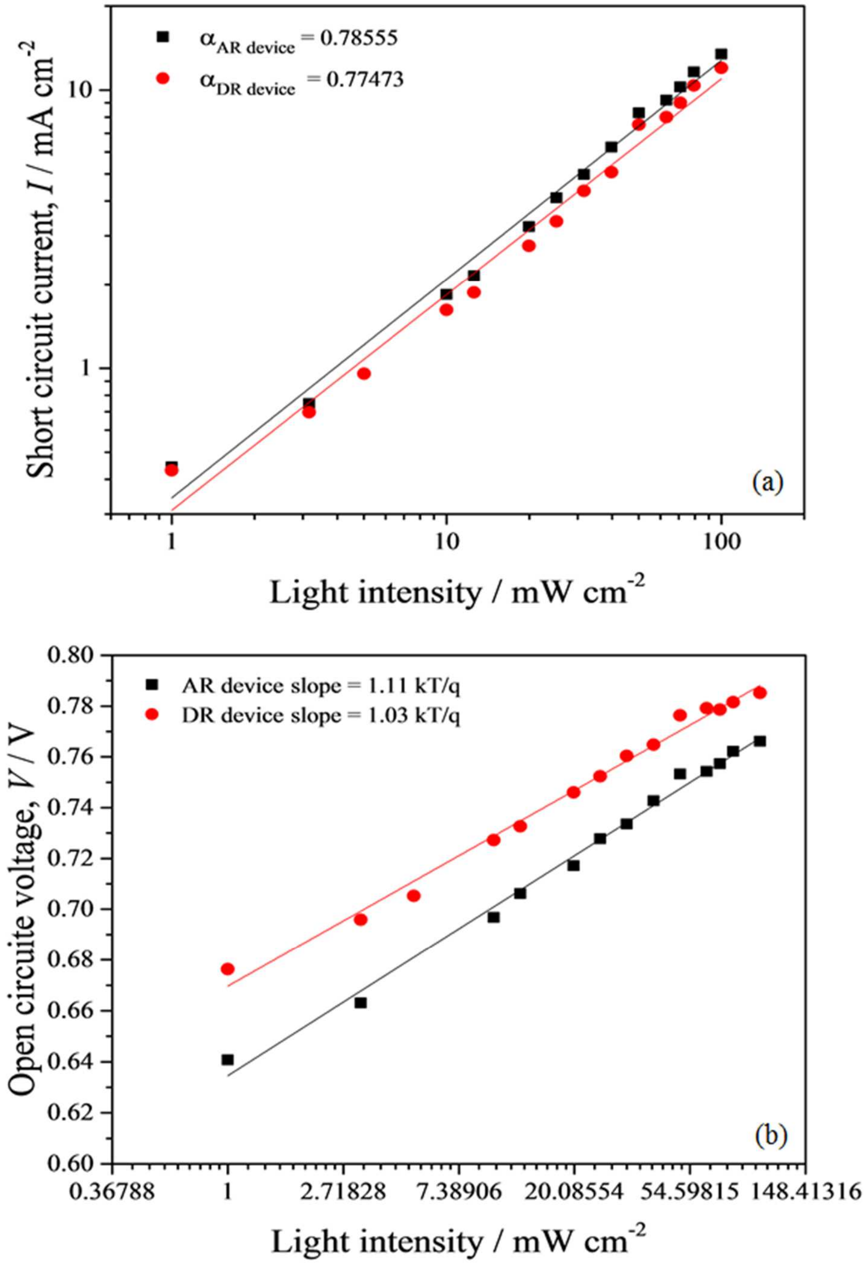

Figure 6.8. Measured (a) short circuit current, and (b) open circuit potential as a function of incident light intensity (100 to 1 mW cm^{-2}) for donor-rich (red) and acceptor-rich (black) solar cell devices.

At open circuit condition, the net extraction of charge carrier is zero J = 0, therefore all charge carriers must recombine. As such, the concentration of charge carriers is high and higher-order recombination is expected. Of particular interest is bimolecular recombination which has been shown depends only on temperature and light intensity (section 2.3.3) at open circuit. For pure bimolecular recombination, the predicted slope of the V_{oc} versus the natural logarithm of the light intensity is *kT/e*.[13,34,35] In Figure 6.8b, the V_{oc} of the DR and AR devices as a function of light intensity are depicted. The slope for both devices is similar and close to *kT/e*, implying that bimolecular recombination is dominant at the open circuit conditions. Further studying of 4 DR devices and 5 AR devices shows that the donor-rich devices have a slightly smaller slope than *kT/e* (0.98125), whereas the acceptor-rich devices possess slightly higher slope than *kT/e* (1.142). The higher measured value than *kT/e* in AR devices shows the stronger dependence of the open circuit on the light intensity. This can be attributed to SRH recombination of the charge carriers due to the presence of the interfacial traps between the cathode electrode (aluminum) and the bulk heterojunction.[35] Nevertheless, there is a marginal difference between slopes of the devices and one can conclude that the interface in donor-rich devices and acceptor-rich devices acts quite similar. As such, the S-shaped current density-voltage curve is not brought about morphological defection (due to penetration of aluminum to the active layer) or charge trapping at the interface.

6.3.7. Recombination Dynamics under Transient Conditions

Charge carrier density decay of the solar cell devices composed of AR and DR active layer measured by the TRCE techniques are presented in Figure 6.9a. Initially, the acceptor-rich devices have higher charge density. These results are similar to those obtained from photocurrent versus voltage studies. At the longer time scales, however, the AR devices declines faster compared to the DR devices.

Figure 6.9b compares photovoltage decay of the AR and DR devices. Initially, both devices show a similar photovoltage of around 0.76 *V*, which is close to the open circuit potential of the devices measured under steady-state conditions (1 sun illumination). The photovoltage decay of the DR devices features two distinguished regimes (<1 μs and > 1μs), while the photovoltage of the AR devices decays monotonously over time. This difference shows a faster photovoltage decay of the donor-rich devices in the in the 10^{-6} to 10^{-4} s time region, likely indicating an existence of a faster (transient) component of recombination near one of the contacts (the aluminum contact based on aforementioned discussion). Faster recombination in a donor-rich layer is feasible if electrons are localized in a scarce acceptor phase.

The measured photovoltage decay for each solar cell devices depends on the charge density and the energetics (density of states (DOS)) of charge transport sites near the contacts. Plotting charge carrier density of the devices versus photovoltage (Figure 6.10a), both obtained from transient measurement, suggests no major differences between the energy level of the AR and DR devices, i.e. the same charge density leads to similar open circuit potential in the devices. This suggests that the difference in the photovoltage decay between acceptor-rich and donor-rich devices is related to the dynamics of the charge carrier density at the electrodes.

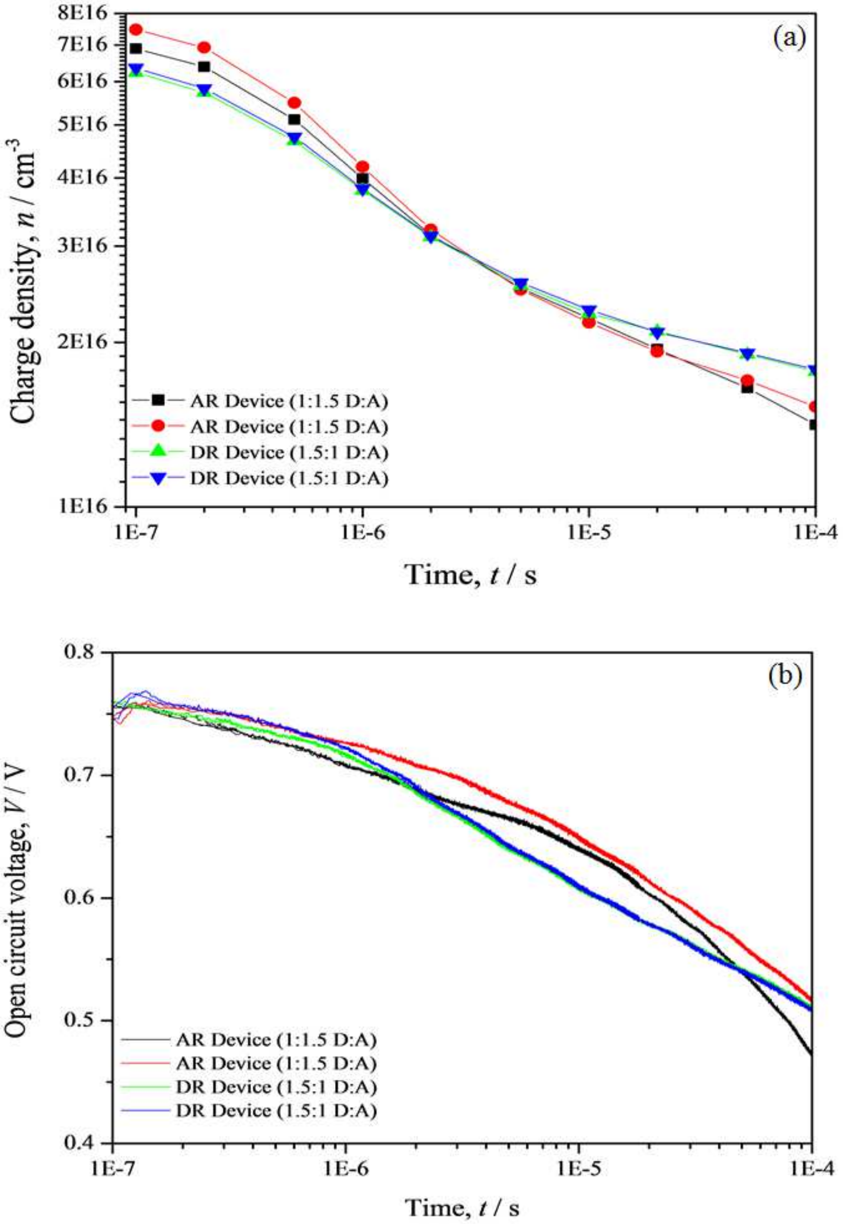

Figure 6.9. (a) Charge carrier density decay and (b) Photovoltage decay over time of acceptor-rich (black and red) and donor-rich (green and blue) solar cell devices.

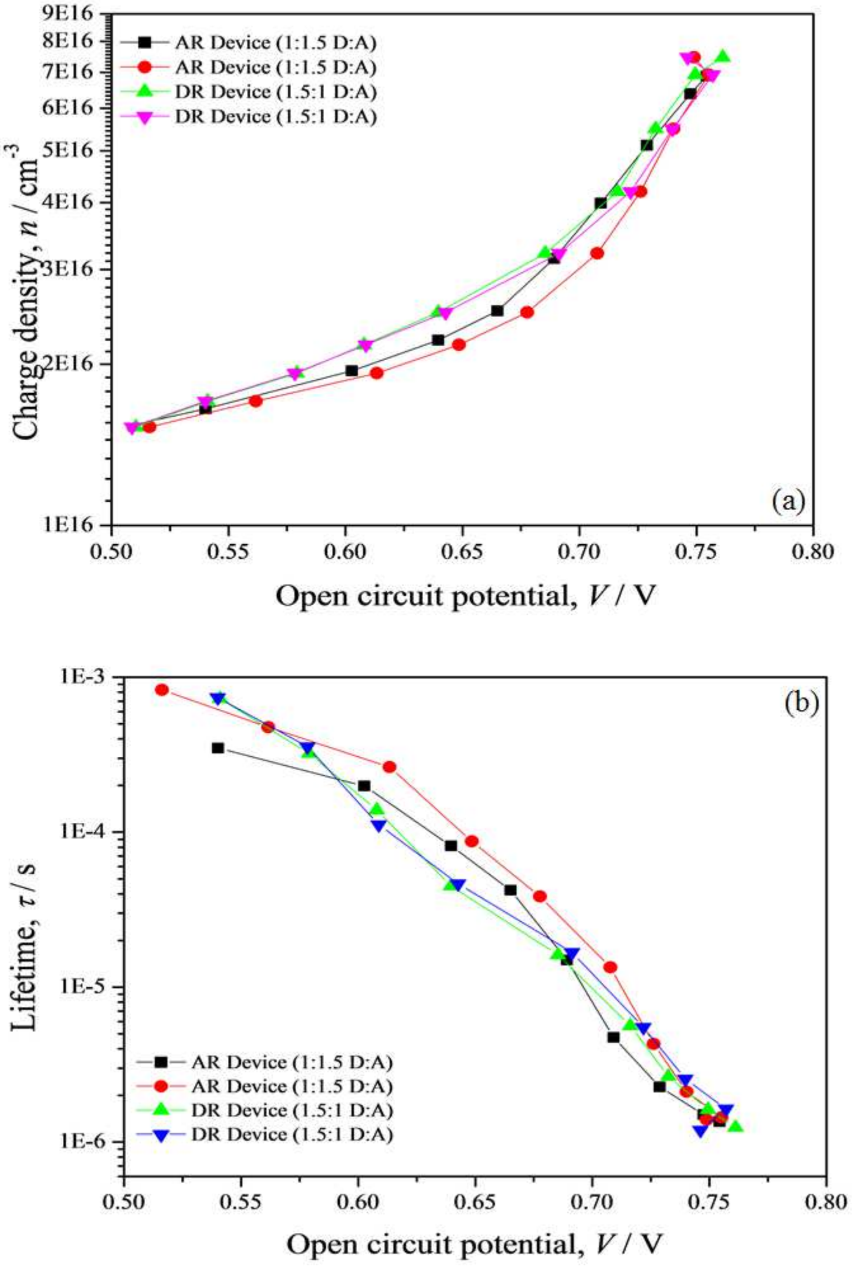

Figure 6.10. (a) Charge carrier density and (b) charge carrier lifetime versus open circuit potential of acceptor-rich (black and red) and donor-rich (green and blue) solar cell devices.

The bimolecular recombination lifetime of the devices was calculated and plotted against the photovoltage (Figure 6.10b). A longer charge carrier lifetime is observed for the AR derive in the 1 μs to 10 μs (corresponding to 0.7 to 0.6 *V* in Figure 6b) time window. This explains the larger photovoltage for the AR devices.

6.3.8. Charge Carrier Mobility

Photo-induced charge extraction using linearly increasing voltage (photo-CELIV) is used to measure charge carrier mobility of donor-rich and acceptor-rich devices. In this technique, the charge carriers are extracted by a linearly increasing voltage pulse ($A = \Delta U/\Delta t$) after an adjustable dealy time between photogeneration and extractions. The photo-CELIV curves of the devices are shown in the Figure 6.11. It is immediately clear that the photo-CELIV curves shows only one extraction peak, implying that charge carrier mobile is fairly balanced within the active layer and both charge carriers (electrons and holes) possess similar mobility within experimental error. The calculated mobility for the DR an AR device are shown in Table 6.4. The calculated mobility values for both devices are quite similar with slightly higher value for the donor-rich devices. Therefore, it can be concluded that asymmetry between the mobility of the holes and electrons is not the main reason for the appearance of the S-shaped current density-voltage curve in the DR devices. It must be noted that the photo-CELIV technique relies upon the extraction of charge carriers after an adjustable delay time. The fact that a difference in charge carrier mobility between DR and AR devices was not observed, does not preclude the presence of the thin donor-rich layer with diminished electron mobility on the surface of the active layer. Given the experimental condition and smallness of the photo-generation in the thin donor-rich layer, transience charge extracting from this layer would not be visible. Under steady state condition, on the other hand, electrons must be transported through this layer limiting the total current through the devices.

Table 6.4. Calculated values of the charge carrier mobility, electron (hole) density, and charge carrier sweep-out time for DR and AR devices.

Devices	**Mobility ($cm^2\ V^{-1}\ s^{-1}$)**	n_{sc} **(cm^{-3})**	τ_s **(s)**
Donor-rich	4.19×10^{-5}	9.46×10^{15}	1.193×10^{-6}
Acceptor-rich	3.25×10^{-5}	1.82×10^{16}	1.923×10^{-6}

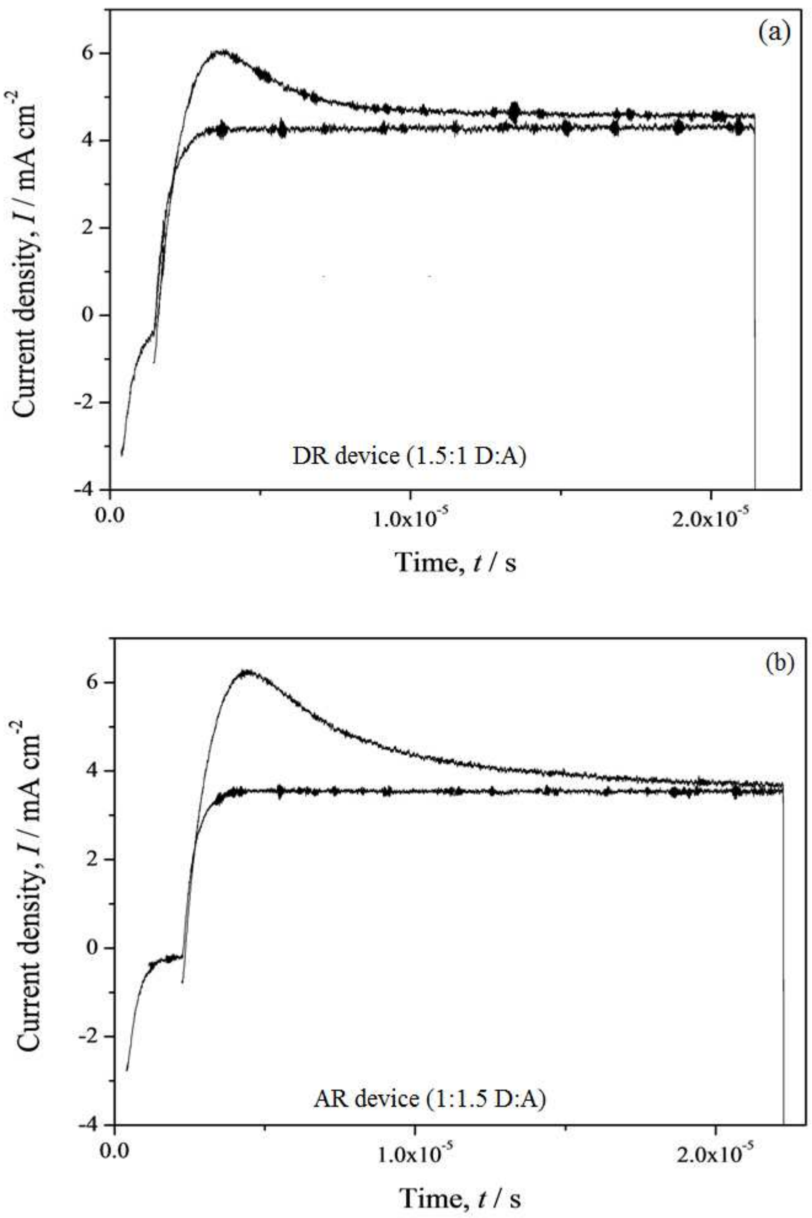

Figure 6.11. The photo-CELIV curves of and DR (top) and AR (bottom) solar cell devices measured. The laser energy was set to 10 µj. The delay time between extraction and photoexcitation was 2 µs. The applied voltage was 2 *V* coupled with 50000 Hz rising time. The dark CELIV traces are also shown.

Tremolet de Villers *et al.*[14] report S-shaped current-voltage curve in a P3HT:PCBM solar cell results in the appearance of two peaks in photo-CELIV curves correlated to an imbalance between the mobility of electrons and holes. The authors claim that vertical phase segregation during spin coating drives PCBM component toward the bottom electrode (ITO), causing a P3HT-rich surface in contact with cathode electrode. It was shown that adding a layer of the PCBM on top of the active layer resolves the s-curve phenomenon and the asymmetry mobility between the charge carriers. However, Huh *et al.*[26] show the imbalanced mobility cannot be solely accounted for the appearance of the S-curve and two other conditions are required to meet, i.e. accumulation of charge carriers at the electrodes and strong Langevin bimolecular recombination. The imbalance of the mobility between the electron and hole is not observed in the data presented here.

Having calculated mobilities, two electrical characteristics of the AR and DR devices are estimated, i.e. electron (hole) density (τ_s) and charge carrier sweep-out time (n_{sc}) at short circuit conditions, using equation (6-3) and (6-4) respectively:[34]

$$J_{ph,sat} = edG_{max} = 2en_{sc}\,\mu\frac{V_{int}}{d} \qquad (6\text{-}3)$$

$$\tau_s = \frac{d^2}{2\mu V_{bi}} \qquad (6\text{-}4)$$

where μ is the mobility of charge carriers. The calculated values for both n_{sc} and τ_s are shown in Table 6.4. Although both devices possess quite similar sweep-out time, the acceptor-rich device has a higher electron (hole) density at the short circuit conditions. This indicates that the difference between acceptor-rich and donor-rich devices at short circuit conditions comes from the generation of charge carriers, otherwise, the internal electric field in both devices is strong enough to suppress any barrier and extract all charge carriers into the respective electrodes.

6.4. CONCLUSION

In this chapter, the appearance of the S-shaped current density-voltage curve in BHJ solar cells based on DTS(FBBTh$_2$)$_2$:PC$_{70}$BM has been investigated. The formation of a thin donor-rich layer on top of bulk heterojunction is proposed as the origin. The lower electron conductivity near the electron extracting electrode leads to an additional barrier of 0.1 *V*. As a result, the collection of electrons is hampered, giving rise to a low fill factor and consequently lower power conversion efficiency. It is determined that the key to the recovery of normal device behavior is to increase the PCBM content of the bulk heterojunction. The recombination dynamics of charge carrier in both S-shaped and normal devices are studied using both steady state and transient techniques. While the recombination dynamics for both devices are quite similar under steady state condition, transient technique results show that in the S-curve devices charge carriers recombine slightly faster.

6.5. FUTURE WORK

While the presented results in this chapter are consistent, it would be advantageous to directly determine the lateral morphology including the chemical compositions of the bulk heterojunction, e.g. by using secondary ion mass spectrometry,[42] or x-ray reflectivity measurements.[43] This may be lead to deeper understanding of the S-curve physical origin.

6.6. APPENDIX

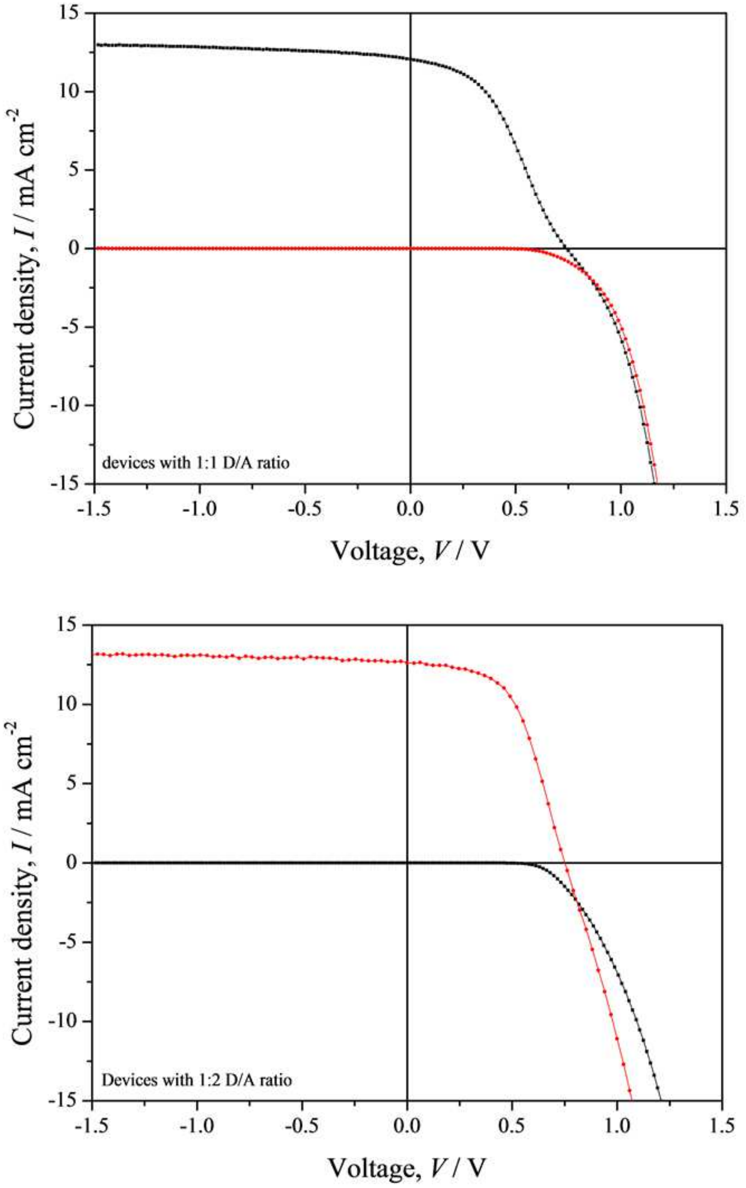

Figure 6.6.1 Current density-voltage curves of *p*-DTS(FBTTh$_2$)$_2$:PC$_{70}$BM BHJ solar cell devices fabricated with 1:1 (top) and 1:2 (bottom) donor/acceptor ratio.

Table 6.6.1. Photovoltaic parameters of 5 donor-rich devices and analysis of light intensity dependency of their short circuit current and open circuit potential

ID	V_{oc}	J_{sc}	FF	PCE	J_{sc} slope	R-square	V_{oc} slope(kT/q)	R-square
DR 1	0.7888	10.101	42	3.35	0.74418	0.97481	0.97	0.99172
DR 2	0.7852	11.989	41.1	3.87	0.77473	0.98084	1.03	0.98955
DR 3	0.7895	10.203	40.2	3.24	0.76028	0.98189	0.95	0.988
DR 4	0.7881	12.197	39.4	3.78	0.78169	0.98456	0.975	0.98868
Average	0.7879 ± 0.002	11.1225 ± 1.12	40.675 ± 1.12	3.56 ± 0.3	0.76522 ± 0.016	0.980525 ± 0.004	0.98125 ± 0.03	0.9894875 ± 0.002

Table 6.6.2. Photovoltaic parameters of 4 acceptor rich devices and analysis of light intensity dependency of their short circuit current and open circuit potential

ID	V_{oc}	J_{sc}	FF	PCE	J_{sc} Slope	R-Square	V_{oc} slope(kT/q)	R-Square
AR 1	0.7306	13.702	47.1	4.72	0.78957	0.9859	1.14	0.9332
AR 2	0.7662	13.454	50.2	5.17	0.78555	0.98717	1.11	0.99185
AR 3	0.7441	13.653	54.1	5.50	0.794	0.98264	1.18	0.98465
AR 4	0.7531	13.225	54.3	5.41	0.7939	0.98344	1.14	0.99
AR5	0.7603	13.613	51.5	5.33	0.7904	0.98	1.14	0.98503
Average	0.75086 ± 0.014	13.5294 ± 0.19	51.44 ± 3	5.226 ± 0.3	0.790684 ± 0.0035	0.98383 ± 0.003	1.142 ± 0.025	0.976946 ± 0.025

R-square is the coefficient of determination and shows how close data are to the plotted line.

6.7. REFERENCES

(1) Lin, Y.; Li, Y.; Zhan, X. Small molecule semiconductors for high-efficiency organic photovoltaics. *Chemical Society Reviews* **2012,** *41* (11), 4245.

(2) Walker, B.; Kim, C.; Nguyen, T.-Q. Small Molecule Solution-Processed Bulk Heterojunction Solar Cells. *Chemistry of Materials* **2011,** *23* (3), 470.

(3) Mishra, A.; Bäuerle, P. Small Molecule Organic Semiconductors on the Move: Promises for Future Solar Energy Technology. *Angewandte Chemie International Edition* **2012,** *51* (9), 2020.

(4) Tong, M.; Cho, S.; Rogers, J. T.; Schmidt, K.; Hsu, B. B. Y.; Moses, D.; Coffin, R. C.; Kramer, E. J.; Bazan, G. C.; Heeger, A. J. Higher Molecular Weight Leads to Improved Photoresponsivity, Charge Transport and Interfacial Ordering in a Narrow Bandgap Semiconducting Polymer. *Advanced Functional Materials* **2010,** *20* (22), 3959.

(5) Sun, Y.; Welch, G. C.; Leong, W. L.; Takacs, C. J.; Bazan, G. C.; Heeger, A. J. Solution-processed small-molecule solar cells with 6.7% efficiency. *Nat Mater* **2012,** *11* (1), 44.

(6) van der Poll, T. S.; Love, J. A.; Nguyen, T.-Q.; Bazan, G. C. Non-Basic High-Performance Molecules for Solution-Processed Organic Solar Cells. *Advanced Materials* **2012,** *24* (27), 3646.

(7) Ni, W.; Li, M.; Liu, F.; Wan, X.; Feng, H.; Kan, B.; Zhang, Q.; Zhang, H.; Chen, Y. Dithienosilole-Based Small-Molecule Organic Solar Cells with an Efficiency over 8%: Investigation of the Relationship between the Molecular Structure and Photovoltaic Performance. *Chemistry of Materials* **2015,** *27* (17), 6077.

(8) Zhang, Q.; Kan, B.; Liu, F.; Long, G.; Wan, X.; Chen, X.; Zuo, Y.; Ni, W.; Zhang, H.; Li, M.et al. Small-molecule solar cells with efficiency over 9%. *Nat Photon* **2015,** *9* (1), 35.

(9) Love, J. A.; Proctor, C. M.; Liu, J.; Takacs, C. J.; Sharenko, A.; van der Poll, T. S.; Heeger, A. J.; Bazan, G. C.; Nguyen, T.-Q. Film Morphology of High Efficiency Solution-Processed Small-Molecule Solar Cells. *Advanced Functional Materials* **2013,** *23* (40), 5019.

(10) Kyaw, A. K. K.; Wang, D. H.; Luo, C.; Cao, Y.; Nguyen, T.-Q.; Bazan, G. C.; Heeger, A. J. Effects of Solvent Additives on Morphology, Charge Generation, Transport, and Recombination in Solution-Processed Small-Molecule Solar Cells. *Advanced Energy Materials* **2014,** *4* (7), n/a.

(11) Zalar, P.; Kuik, M.; Ran, N. A.; Love, J. A.; Nguyen, T.-Q. Effects of Processing Conditions on the Recombination Reduction in Small Molecule Bulk Heterojunction Solar Cells. *Advanced Energy Materials* **2014,** *4* (14), n/a.

(12) Mukherjee, S.; Proctor, C. M.; Tumbleston, J. R.; Bazan, G. C.; Nguyen, T.-Q.; Ade, H. Importance of Domain Purity and Molecular Packing in Efficient Solution-Processed Small-Molecule Solar Cells. *Advanced Materials* **2015,** *27* (6), 1105.

(13) Kyaw, A. K. K.; Wang, D. H.; Wynands, D.; Zhang, J.; Nguyen, T.-Q.; Bazan, G. C.; Heeger, A. J. Improved Light Harvesting and Improved Efficiency by Insertion of an Optical Spacer (ZnO) in Solution-Processed Small-Molecule Solar Cells. *Nano Letters* **2013,** *13* (8), 3796.

(14) Tremolet de Villers, B.; Tassone, C. J.; Tolbert, S. H.; Schwartz, B. J. Improving the Reproducibility of P3HT:PCBM Solar Cells by Controlling the PCBM/Cathode Interface. *The Journal of Physical Chemistry C* **2009,** *113* (44), 18978.

(15) Orimo, A.; Masuda, K.; Honda, S.; Benten, H.; Ito, S.; Ohkita, H.; Tsuji, H. Surface segregation at the aluminum interface of poly(3-hexylthiophene)/fullerene solar cells. *Applied Physics Letters* **2010,** *96* (4), 043305.

(16) Gupta, D.; Bag, M.; Narayan, K. S. Correlating reduced fill factor in polymer solar cells to contact effects. *Applied Physics Letters* **2008,** *92* (9), 093301.

(17) Jin, H.; Tuomikoski, M.; Hiltunen, J.; Kopola, P.; Maaninen, A.; Pino, F. Polymer−Electrode Interfacial Effect on Photovoltaic Performances in Poly(3-hexylthiophene):Phenyl-C61-butyric Acid Methyl Ester Based Solar Cells. *The Journal of Physical Chemistry C* **2009,** *113* (38), 16807.

(18) Kumar, A.; Sista, S.; Yang, Y. Dipole induced anomalous S-shape I-V curves in polymer solar cells. *Journal of Applied Physics* **2009,** *105* (9), 094512.

(19) Tress, W.; Leo, K.; Riede, M. Influence of Hole-Transport Layers and Donor Materials on Open-Circuit Voltage and Shape of I–V Curves of Organic Solar Cells. *Advanced Functional Materials* **2011,** *21* (11), 2140.

(20) Wagner, J.; Gruber, M.; Wilke, A.; Tanaka, Y.; Topczak, K.; Steindamm, A.; Hörmann, U.; Opitz, A.; Nakayama, Y.; Ishii, H.et al. Identification of different origins for s-shaped current voltage characteristics in planar heterojunction organic solar cells. *Journal of Applied Physics* **2012,** *111* (5), 054509.

(21) Tress, W.; Corvers, S.; Leo, K.; Riede, M. Investigation of Driving Forces for Charge Extraction in Organic Solar Cells: Transient Photocurrent Measurements on Solar Cells Showing S-Shaped Current–Voltage Characteristics. *Advanced Energy Materials* **2013,** *3* (7), 873.

(22) Tress, W.; Petrich, A.; Hummert, M.; Hein, M.; Leo, K.; Riede, M. Imbalanced mobilities causing S-shaped IV curves in planar heterojunction organic solar cells. *Applied Physics Letters* **2011,** *98* (6), 063301.

(23) Wagenpfahl, A.; Rauh, D.; Binder, M.; Deibel, C.; Dyakonov, V. S-shaped current-voltage characteristics of organic solar devices. *Physical Review B* **2010,** *82* (11), 115306.

(24) Wang, J. C.; Ren, X. C.; Shi, S. Q.; Leung, C. W.; Chan, P. K. L. Charge accumulation induced S-shape J–V curves in bilayer heterojunction organic solar cells. *Organic Electronics* **2011,** *12* (6), 880.

(25) Finck, B. Y.; Schwartz, B. J. Understanding the origin of the S-curve in conjugated polymer/fullerene photovoltaics from drift-diffusion simulations. *Applied Physics Letters* **2013,** *103* (5), 053306.

(26) Huh, Y. H.; Park, B.; Hwang, I. Investigating the origin of S-shaped photocurrent-voltage characteristics of polymer:fullerene bulk-heterojunction organic solar cells. *Journal of Applied Physics* **2014,** *115* (12), 124504.

(27) Love, J. A.; Chou, S.-H.; Huang, Y.; Bazan, G. C.; Nguyen, T.-Q. Effects of solvent additive on “s-shaped” curves in solution-processed small molecule solar cells. *Beilstein J. Org. Chem.* **2016,** *12*, 2543.

(28) Kim, J. Y.; Kim, S. H.; Lee, H. H.; Lee, K.; Ma, W.; Gong, X.; Heeger, A. J. New Architecture for High-Efficiency Polymer Photovoltaic Cells Using Solution-Based Titanium Oxide as an Optical Spacer. *Advanced Materials* **2006,** *18* (5), 572.

(29) Vogel, M.; Doka, S.; Breyer, C.; Lux-Steiner, M. C.; Fostiropoulos, K. On the function of a bathocuproine buffer layer in organic photovoltaic cells. *Applied Physics Letters* **2006,** *89* (16), 163501.

(30) Jin, T. M.; Sivasayan, K. R.; Zhongxing, Z.; Vijila, C.; Wei, C. Understanding Carrier Lifetime in Inverted Polymer Solar Cells with a Thick Electron Selective Layer. *ECS Solid State Letters* **2014,** *3* (11), Q82.

(31) Takacs, C. J.; Sun, Y.; Welch, G. C.; Perez, L. A.; Liu, X.; Wen, W.; Bazan, G. C.; Heeger, A. J. Solar Cell Efficiency, Self-Assembly, and Dipole–Dipole Interactions of Isomorphic Narrow-Band-Gap Molecules. *Journal of the American Chemical Society* **2012,** *134* (40), 16597.

(32) Love, J. A.; Collins, S. D.; Nagao, I.; Mukherjee, S.; Ade, H.; Bazan, G. C.; Nguyen, T.-Q. Interplay of Solvent Additive Concentration and Active Layer Thickness on the Performance of Small Molecule Solar Cells. *Advanced Materials* **2014,** *26* (43), 7308.

(33) Love, J. A.; Nagao, I.; Huang, Y.; Kuik, M.; Gupta, V.; Takacs, C. J.; Coughlin, J. E.; Qi, L.; van der Poll, T. S.; Kramer, E. J.et al. Silaindacenodithiophene-Based Molecular Donor: Morphological Features and Use in the Fabrication of Compositionally Tolerant, High-Efficiency Bulk Heterojunction Solar Cells. *Journal of the American Chemical Society* **2014,** *136* (9), 3597.

(34) Cowan, S. R.; Roy, A.; Heeger, A. J. Recombination in polymer-fullerene bulk heterojunction solar cells. *Physical Review B* **2010,** *82* (24), 245207.

(35) Kyaw, A. K. K.; Wang, D. H.; Gupta, V.; Leong, W. L.; Ke, L.; Bazan, G. C.; Heeger, A. J. Intensity Dependence of Current–Voltage Characteristics and Recombination in High-Efficiency Solution-Processed Small-Molecule Solar Cells. *ACS Nano* **2013,** *7* (5), 4569.

(36) Servaites, J. D.; Ratner, M. A.; Marks, T. J. Organic solar cells: A new look at traditional models. *Energy & Environmental Science* **2011,** *4* (11), 4410.

(37) Qi, B.; Wang, J. Fill factor in organic solar cells. *Physical Chemistry Chemical Physics* **2013,** *15* (23), 8972.

(38) Tada, K. Validation of opposed two-diode equivalent-circuit model for S-shaped characteristic in polymer photocell by low-light characterization. *Organic Electronics* **2017,** *40*, 8.

(39) Koster, L. J. A.; Mihailetchi, V. D.; Xie, H.; Blom, P. W. M. Origin of the light intensity dependence of the short-circuit current of polymer/fullerene solar cells. *Applied Physics Letters* **2005,** *87* (20), 203502.

(40) Koster, L. J. A.; Kemerink, M.; Wienk, M. M.; Maturová, K.; Janssen, R. A. J. Quantifying Bimolecular Recombination Losses in Organic Bulk Heterojunction Solar Cells. *Advanced Materials* **2011,** *23* (14), 1670.

(41) Cowan, S. R.; Banerjib, N. In *Organic Solar Cells Fundamentals, Devices, and Upscaling*; Rand, B. P.;Richter, H., Eds.; CRC Press, 2014.

(42) Franquet, A.; Conard, T.; Voroshazi, E.; Poleunis, C.; Cheyns, D.; Vandervorst, W. Characterization of organic solar cell materials by G-SIMS. *Surface and Interface Analysis* **2013,** *45* (1), 430.

(43) Paci, B.; Generosi, A.; Albertini, V. R.; Perfetti, P.; Bettignies, R. d.; Firon, M.; Leroy, J.; Sentein, C. In situ energy dispersive x-ray reflectometry measurements on organic solar cells upon working. *Applied Physics Letters* **2005,** *87* (19), 194110.

Chapter 7: Conclusion

7.1. SUMMARY

Investigations into three key issues influencing the photovoltaic performance of the organic solar cells were carried out. Firstly, the interface between bulk heterojunction and the cathode electrode was modified by PFN electron transport layer and charge carrier dynamics of devices as a function of PFN film were probed. Followed by, an exploratory based concept to enhance dielectric constant of the bulk heterojunction. Finally, the performance of solution-processed small molecule bulk heterojunction was investigated with regard to the appearance of the S-shaped current density-voltage curve, in order to study the impact of the phenomenon on the charge carrier generation, collection, mobility, and recombination.

7.2. PFN ELECTRON TRANSPORT LAYER

At this point, it is helpful to revisit the hypotheses presented in Chapter 1. The first hypothesis stated that PFN can affect the charge carrier dynamics and therefore increase the power conversion efficiency of bulk heterojunction solar cells. In order to examine this hypothesis, the interface between Poly[N-9′-heptadecanyl-2,7-carbazole-alt-5,5-(4′,7′-di-2-thienyl-2′,1′,3′-benzothiadiazole)] (PCDTBT)-based bulk heterojunction and the cathode electrode (aluminum) were modified with a wide range of PFN interlayer films. The films were made from solutions with concentration ranging from 0.5 to 0.2 mg/ml spin cast at 1000 to 8000 rpm. Photovoltaic characteristics of devices were then examined as a function of the PFN film thicknesses. It was observed that PFN layer induced no significant enhancement in open-circuit potential, short-circuit current, fill factor and therefore PCE of the solar cell devices. This finding was contrary to what has been reported in the literature. This was further confirmed with almost comparable external quantum efficiency, charge carrier generation and collection with regard to reference devices. It was proposed that either the interface is almost ideal, which cannot be further improved/modified by the PFN film or the PFN interlayer may have been destroyed during thermal evaporation of cathode electrode. A further investigation of the devices by several techniques including light intensity dependency, photovoltage decay (PVD) and time-resolved charge extraction (TRCE) allowed evaluating the effect of the PFN film on the recombination of charge carriers. It was determined that introduction of PFN interlayer could not have a substantial influence on the recombination dynamics of charge carriers. Moreover, a relatively faster recombination was observed in the PFN-based devices. It was surmised that the PFN interlayer on top of the active layer may act as trap states, enhancing trap-assisted recombination. Comparable charge carrier mobility in the absence and presence of the PFN film revealed that transportation of charge carriers was not also affected. These results led to conclude that under circumstances explored the hypothesis was inconclusive and further investigation is warranted.

7.3. DIELECTRIC CONSTANT

The second hypothesis investigated the incorporation of materials with dielectric constant higher than air to occupy free volume within the active layer to enhance dielectric constant and consequently increase the efficiency of the bulk heterojunction solar cells. This hypothesis was based on the Clausius-Mossotti relationship which determines polarization and free volume as key parameters influencing the dielectric constant in polymeric materials. It was assumed that the free volume content (air or other low dielectric constant gases) within the bulk heterojunction could be replaced with a higher dielectric material. Hence, poly[(9,9-bis(3′-(N,N-dimethylamino)-propyl)-2,7-fluorene)-alt-2,7-(9,9-dioctyl)-fluorene] (PFN) (dielectric constant = 2.16) and rhodamine 101 (dielectric constant = 4.73) were directly incorporated into the bulk heterojunction. The bulk was composed of either Poly[N-9′-heptadecanyl-2,7-carbazole-alt-5,5-(4′,7′-di-2-thienyl-2′,1′,3′-benzothiadiazole)] (PCDTBT) (conjugated polymer) or 7,7′-[4,4-Bis(2-ethylhexyl)-4H-silolo[3,2-b:4,5-b′]dithiophene-2,6-diyl]bis[6-

fluoro-4-(5′-hexyl-[2,2′-bithiophen]-5-yl)benzo[c][1,2,5] thiadiazole] (p-DTS(FBBTh$_2$)$_2$) (small molecule) as donor and 1-[3-(Methoxycarbonyl)propyl]-1-phenyl-[6.6]C$_{60}$ (PC$_{60}$BM) as acceptor. In this study changes in dielectric constant taken via this approach were found to be minimum in the polymer-based bulk heterojunctions. In addition, the photovoltaic performance of the solar cells was noted to be degraded. The generation and collection of charge carriers were reduced especially at low effective voltage (around open-circuit conditions) when the content of both PFN and rhodamine 101 was increased in the bulk heterojunction. This was mostly due to increasing of charge carrier recombination as consequences of the incorporation of the materials. However, bimolecular recombination lifetime derived from TRCE results and mobility of charge carriers measured by photo-CELIV technique showed insignificant changes before and after the introduction of materials. Similar impacts were observed for the small molecule based-bulk heterojunction when PFN and rhodamine 101 were added. The bulk heterojunctions were also treated with isopropyl alcohol (dielectric constant = 17.9). While dielectric constant of polymer-based BHJ increased slightly, it remained almost unchanged in SM based-BHJ. Moreover, the open-circuit potential, short-circuit current, fill factor, and PCE of devices were almost similar before and after treatment with IPA. While absorption of the PCDTBT-based film was decreased following IPA treatment, IPA-treated SM-based film absorption was quite similar to pristine film. Both charge carrier generation and collection were not influenced upon treatment with isopropyl alcohol. Charge carrier dynamics of the solar cell devices including bimolecular recombination lifetime, bimolecular recombination coefficient and mobility were not substantially affected following IPA treatment in both polymer and SM-based devices. These results imply that the adopted method derived from the Clausius-Mossotti relationship did not significantly enhance the dielectric constant and therefore the efficiency of the bulk heterojunction solar cells.

7.4. S-SHAPED CURRENT DENSITY-VOLTAGE CURVE IN SM BHJ

The third hypothesis was to evaluate whether the idea that the alteration of the donor and acceptor ratio may resolve the S-shaped current density-voltage curve in solution-processed small molecule bulk heterojunction solar cells. To determine the origin of the S-curve phenomenon, the interface between the bulk and the cathode electrode was initially evaluated. Two electron transport layers (ETLs), i.e., ZnO and TiOx, were employed to modify the interface. The devices modified with ETLs demonstrated current density-voltage associated with S-curve characteristics. This revealed that the bulk heterojunction was responsible for the deformed current density-voltage curve. The characteristics of the bulk heterojunction and consequently devices performance was also investigated as a function of 1,8-diiodooctane (DIO) concentration. It was noted that regardless of DIO concentration, the device exhibited low power conversion efficiency due to S-shaped characteristics. Eventually, a normal diode-like curve was retrieved when the PCBM content of the small molecule bulk heterojunction (SM BHJ) was increased. A further investigation of normal and S-curve devices was carried out using several steady state and transient techniques. Although UV-Vis absorption profile was higher in S-curve devices, external quantum efficiency (EQE) curves showed around 10% decrease within the wavelength range of 550-700 nm when compared to the normal diode-like curve device. This was consistent with lower short-circuit current (20% reduction) and it was pointed out that generation/collection of charge carriers were likely hindered in S-curve devices. Investigation of photocurrent and charge collection probability as a function of effective voltage confirmed the reduction of charge carrier generation/collection particularly around open-circuit voltage (low effective voltage). The atomic force microscopy (AFM) study of the bulk film revealed that S-curve devices' bulk film was rougher with bigger grain size compared to normal device bulk. These results coupled with a 0.5 *V* shift of forward injection to higher potentials led to correlation between the appearance of the S-curve and an energy barrier stemming from the formation of a small molecule rich thin film on top of the active layer. The energy barrier value was estimated to be around 0.1 V. An equivalent circuit was presented to model the S-curve device using an additional diode to account for the energy barrier. The light-intensity dependency measurement of the devices revealed that there was a slight difference regarding recombination of charge carriers at short-circuit and open-circuit conditions between the S-curve and normal curve devices. However, faster charge carrier recombination in S-curve devices was detected by the photovoltage decay and time-resolved charge extraction techniques. Given the fact that both normal and S-curve devices possessed comparable photovoltages (showing similar energy levels in both devices), the faster recombination was attributed to the dynamics of the charge carriers near the electrodes. Furthermore, charge carrier mobility of the devices was measured using the photo-CELIV technique and appeared to be in the same range. This indicated that mobility imbalance between hole and electron and the subsequent space charge effect cannot be the reason for the appearance of the S-shaped current density-voltage curve. Here, a new approach based on the alteration of donor an acceptor ratio was evaluated to resolve the S-shaped current density-voltage curve in solution processed SM BHJ solar cells. From this, it was apparent that the approach could be used to revive the normal behavior of the current density-voltage curve and significantly alleviate the energy barrier hindering generation and collection of charge carriers within the bulk heterojunction.

7.5. CONCLUSION

The work in this thesis represents a novel piece of work in relation to bulk heterojunction solar cells. It investigated the potential of novel exploratory approaches to enhance the dielectric constant of the bulk heterojunction. This involved an extensive study regarding the use of PFN as an electron transport layer and its impact on the charge carrier dynamics of the solar cells. It proposed a novel, yet simple method to mitigate S-curve phenomenon and revive a normal current density-voltage curve. These investigations gave rise to interesting results and provided new avenues for further research and development.